Implementation of a new transition prediction method in

Predicting transition in suction boundary layers

December 13, 2006

J. Bongers

Faculty of Aerospace Engineering

Delft University of Technology

Implementation of a new transition prediction method in *Predicting transition in suction boundary layers*

Afstudeerverslag

ter verkrijging van de titel MSc
aan de Technische Universiteit Delft,
op gezag van de voorzitter van de leerstoel Aërodynamica
prof. dr. ir. P.G. Bakker,

op donderdag 24 augustus 2006, 14.00u

door

Jeroen Bongers

student Luchtvaart- en Ruimtevaarttechniek
geboren te Venray

Dit afstudeerverslag is goedgekeurd door de examencommissie.

Samenstelling examencommissie:

Prof. dr. ir. P.G. Bakker (**voorzitter**)	Technische Universiteit Delft
Prof. dr. ir. J.L. van Ingen	Technische Universiteit Delft
Dr.ir. B. W. van Oudheusden	Technische Universiteit Delft
Ir. L. L. M. Boermans	Technische Universiteit Delft

Prof. dr. ir. J.L. van Ingen en Ir. L. L. M. Boermans hebben in belangrijke mate bijgedragen aan de totstandkoming van dit afstudeerverslag.

I T B

Preface

This report was written to obtain the Master of Science degree in Aerospace Engineering at the Delft University of Technology. It is the result of almost a year and a half of work, done at the Low Speed Laboratory of the Department of Aerodynamics in Delft. In this time I got to work together with prof. Van Ingen. For me as a student it was a great opportunity to work with a professor as highly regarded in the field of aerodynamics as prof. Van Ingen. He has been a great inspiration during this past year and a half, and was so kind to devote much of his time to sharing his experience with me and helping me with my research. I would like to thank prof. Van Ingen for the many pleasant and (for me) instructive meetings we had. I would also like to thank mr. Boermans for his time and advice given to me during this thesis project. I would like to mention Leo Molenwijk for his help in practical affairs and some good laughs at the Low Speed Laboratory.

In a formal way this masters thesis concludes only the last 2 years of my study, as in my time at the Delft University of Technology a switch was made in educational organization from the older Dutch model to the Bachelors-Masters structure. To me however it still counts as the conclusion of my whole study in aerospace engineering. In this light I would like to thank the people who enabled me to finish this study. First of all my thanks go out to both my parents. Sadly enough my father has not been granted to witness me graduating, but nonetheless I take this opportunity to thank him here for always supporting me and taking a lot of interest in my study. I also thank my mother for her continuing support in good and bad times. Also I thank my girlfriend Marieke for her support and love.

Then there's a lot of people that I want to thank, and the few words here actually don't do justice to my thanks, but I will try anyway. Alex for being my brother, Peter for being a splendid roommate and friend, Frank, Koen, Jordi, Patrick and Edwin for their friendship and support over all the years and for studying together which made even the worst courses fun to go to. Pim, Siddharth, Ruud, Roel, Jouri, Maaike, Fleur, Helleke, Bas, Vincent, or JC Zarja for the good times and their support and friendship. Furthermore I would like to thank my roommates at "Blok 8 Boven" and at "Partycentrum Bagijnhof" for a great time in Delft. Last but not least I would like to thank my friends not specifically named here, just for being my friends.

Abstract

To reduce drag on wings, aerodynamicists have long been trying to keep the boundary layer on the wings laminar and to postpone transition to a turbulent boundary layer. To achieve this, laminar flow control by means of boundary layer suction can be used. At the Delft University of Technology has been adapted to design airfoils using boundary layer suction. This version is called . The use of this design program was restricted because the transition point prediction methods in could not predict the damping of disturbances in the boundary layer when suction was used. The objective of this study was therefore to implement a reliable transition prediction method into that could predict transition for boundary layers with and without suction.

To achieve this a new database e^N method was implemented into . This new method, dubbed the Improved e^N-method, was developed by Van Ingen with some assistance from the present author. It uses the solutions of the Orr-Sommerfeld equation as calculated by Arnal, that describe the stability diagrams for fifteen values of $Re_{\theta_{crit}}$. These fifteen values of $Re_{\theta_{crit}}$ represent boundary layers with shapefactors between 2.216 and 35.944. As characteristic parameter, the boundary layer shapefactor is used to correlate arbitrary boundary layers to a $Re_{\theta_{crit}}$ value. By scaling and shifting some parameters, the data is stored in splines suitable for interpolation and some extrapolations. It was found that when using the Improved e^N-method in due to the interaction between the boundary layer iterations and the transition prediction, most solutions would not converge. A method using forced transition was developed to remedy this problem. Using this method, convergence of the boundary layer solution is achieved without affecting the accuracy. The Improved e^N-method was found to be able to accurately predict transition in boundary layers with and without suction.

After the implementation of the Improved e^N method a study into the quality of s laminar boundary layer calculations revealed that the shapefactor can sometimes be a bit off, compared to a finite difference method using the pressure distribution as calculated in . This has an impact on the predicted transition point. Another problem is that for high suction velocities the shapefactor can go below the value of 2, which is considered erroneous. Further research into this is recommended.

A case study concerning the DU99 airfoil, originally designed for the standard class ASW-28 sailplane, was done using the Improved e^N-method. For this airfoil a suction distribution is designed that results in a 50 to 75 % reduction in drag in the low drag bucket, excluding the suction drag. The suction drag is excluded because it is highly dependant on the suctionsystem. Also the $C_{l_{max}}$ value is increased from 1.4 to 1.7. This airfoil is therefore well suited for further testing in a windtunnel.

List of Symbols

A	wave amplitude	[-]
A_0	wave amplitude at $x = x_0$ (spatial), or $t = t_0$ (temporal)	[-]
C_d	airfoil drag coeffiecient	[-]
C_l	airfoil liftcoeffient	[-]
C_m	airfoil moment coefficient	[-]
C_p	pressure coeffient	[-]
C_q	suction flow coefficient	[-]
c	chord	[m]
$\bar{c}$	$c_r + ic_i$	[-]
d	distance	[m]
f	nondimensional streamfunction	[-]
H	shapefactor	[-]
H_k	kinematic shape factor	[-]
H^*	$\frac{\theta^*}{\theta}$	[-]
L	lift	[N]
l	$\frac{\tau_o \theta}{\mu U}$	[-]
M	Mach number	[-]
m_T	$\left(\frac{\partial^2 \bar{u}}{\partial \bar{y}^2}\right)_0$	[-]
N	amplification factor	[-]
p	static pressure	[Pa]
$\bar{p}$	mean static pressure	[Pa]
p'	fluctuation of static pressure	[Pa]
$\tilde{p}$	$\bar{p} + p'$	[-]
q	dynamic pressure	[Pa]
r	$Re_\theta - Re_{\theta_{crit}}$	[-]
r_{top}	r corresponding to T_{maxmax}	[-]
Re_c	Reynolds number with respect to chord length	[-]
Re_θ	Reynolds number with respect to momentum thickness	[-]
$Re_{\theta_{crit}}$	critical Reynolds number with respect to momentum thickness	[-]
s	coordinate along (airfoil) surface	[m]
T	amplification rate of unstable disturbances	[-]
T_{max}	maximum value of T at specific Re_θ and $Re_{\theta_{crit}}$	[-]
T_{maxmax}	maximum value of T at specific $Re_{\theta_{crit}}$	[-]
Tu	Turbulence level	[%]

U	boundary layer edge velocity, parallel to surface	$\left[\frac{m}{s}\right]$
U_∞	freestream velocity	$\left[\frac{m}{s}\right]$
$\overline{U}$	$\frac{U}{U_\infty}$	[-]
u	tangential velocity in boundary layer	$\left[\frac{m}{s}\right]$
$\overline{u}$	mean tangential velocity in boundary layer	$\left[\frac{m}{s}\right]$
u'	tangential velocity fluctuation in boundary layer	$\left[\frac{m}{s}\right]$
$\tilde{u}$	$\overline{u} + u'$	[-]
v	normal velocity in boundary layer	$\left[\frac{m}{s}\right]$
$\overline{v}$	mean normal velocity in boundary layer	$\left[\frac{m}{s}\right]$
v'	normal velocity fluctuation in boundary layer	$\left[\frac{m}{s}\right]$
$\tilde{v}$	$\overline{v} + v'$	[-]
v_0	normal velocity at the wall	$\left[\frac{m}{s}\right]$
x	distance along airfoil	[m]
$\overline{x}$	$\frac{x}{c}$	[-]
y	distance normal to surface	[m]
$\overline{y}$	$\frac{y}{\theta}$	[-]

Greek symbols

α	angle of attack	[deg]
$\overline{\alpha}$	$\alpha_r + i\alpha_i$	[-]
α_i	spatial growth rate of disturbances	[-]
α_r	wave number	[-]
$\overline{\beta}$	$\beta_r + i\beta_i$	
β_i	temporal growth rate of disturbances	[-]
β_r	frequency	[Hz]
Γ	circulation	[-]
γ	ratio of specific heats (1.4 for air)	[-]
δ	infinitesimal change	[-]
δ^*	displacement thickness of the boundary layer	[m]
η	nondimensionalized y-coordinate in boundary layer	[-]
θ	momentum loss thickness of the boundary layer	[m]
θ	angle of potential flow	[deg]
θ^*	kinetic momentum thickness	[-]
θ_{crit}	θ at instability point	[m]
Λ	source strength	[-]
μ	viscosity	$[Pa \cdot s]$
ν	kinematic viscosity	$[\frac{m^2}{s}]$
ξ	nondimenionalized x-coordinate	[-]
ρ	(air) density	$\left[\frac{kg}{m^3}\right]$

σ	amplification factor (old notation)	[-]
σ	source strength	[-]
τ	shear stress	[Pa]
τ_0	wall shear stress	[Pa]
ϕ	velocity potential	[-]
ψ	streamfunction	[-]
ω	frequency	[Hz]

Subscripts

∞	freestream
c	chord
crit	instability point
i	i-th interval
j	j-th interval
max	local maximum
maxmax	global maximum
scale	frequency difference between upper neutral curve and global maximum
scaled	frequency divided by ”scale”
top	global maximum

Contents

Preface **v**

Abstract **vii**

List of Symbols **ix**

1 Introduction **1**
1.1 Introduction . . . 1
1.2 Previous work . . . 1
1.2.1 Preliminary work on transition . . . 1
1.2.2 e^N-method . . . 2
1.3 Recent work at . . . 3
1.4 Objectives of present study . . . 4
1.5 Approach of present study . . . 5
1.6 Outline . . . 5

2 Theory **7**
2.1 Boundary layer equations . . . 7
2.1.1 Navier-Stokes equation . . . 7
2.1.2 Prandtl's Boundary-layer Equations . . . 8
2.1.3 Similarity Solutions . . . 9
2.2 Linear Stability Theory . . . 11
2.3 e^N method . . . 12
2.4 Finite Difference Method . . . 14
2.4.1 Solution procedure . . . 16

3 The improved e^N method **19**
3.1 Introduction . . . 19
3.2 Characteristic parameter . . . 19
3.3 Basic concept . . . 28

4 XFOIL **47**
4.1 Introduction . . . 47
4.2 Inviscid formulation in . . . 47
4.3 Viscous formulation in . . . 49
4.4 Solution procedure . . . 53
4.4.1 Newton solution . . . 54

4.5 Transition routines . . . 55
4.5.1 Drela Transition method . . . 55
4.5.2 Van Ingen method . . . 57

5 Modifications to 61
5.1 General principles of adapting code . . . 61
5.2 Flowchart . . . 62
5.3 Implementation of improved e^N . . . 65
5.3.1 . . . 66
5.3.2 . . . 67
5.3.3 Convergence . . . 68

6 Validation 73
6.1 Test Airfoils . . . 73
6.2 Abandoned Test Cases . . . 81
6.3 Grid convergence . . . 84
6.4 Validation of transition method . . . 87

7 Results of the finite difference boundary layer calculation 93

8 Transition method comparison 99

9 Case study DU99 airfoil 109
9.1 Performance without suction . . . 109
9.2 Suction distribution . . . 110

10 Conclusions and Recommendations 117
10.1 Conclusions . . . 117
10.2 Recommendations . . . 118

A User Guide Transition 119
A.1 . . . 119
A.1.1 2nd order Drela method . . . 119
A.1.2 Van Ingens e^N method . . . 120
A.1.3 Improved Van Ingens e^N method . . . 120
A.2 . . . 120
A.2.1 Safety factor method . . . 121
A.2.2 Nlimit method . . . 121
A.2.3 Forcing method . . . 121
A.2.4 No convergence improvement . . . 122

B Airfoil Grids 123

C Validation figures 127

List of Figures

2.1 3 point approximation 15
2.2 2 point approximation 15

3.1 m vs l for Hartree and $\overline{u} = 1 - \overline{x}^n$ 20
3.2 Hartree case 6, velocity 23
3.3 Hartree case 17, velocity 24
3.4 Hartree case 20, velocity 24
3.5 Hartree case 22, velocity 25
3.6 Hartree case 6, curvature 25
3.7 Hartree case 17, curvature 26
3.8 Hartree case 20, curvature 26
3.9 Hartree case 22, curvature 27
3.10 correlation between $^{10}log(Re_{\theta_{crit}})$ and $^{10}log(H)$ 27
3.11 Stability diagrams with and without inflexion point 30
3.12 Basic data 30
3.13 Shifted stability diagram 31
3.14 Crossection of stability diagram 31
3.15 locations of T_{max} values on axis 32
3.16 diagram of all T_{max} for 1 case 32
3.17 scaled diagram of all T_{max} for 1 case 33
3.18 location of top and $\left(\frac{\omega\theta}{U}\right)_{scale}$ in stability diagram 33
3.19 cross-cut curves in $\left(\frac{\omega\theta}{U}\right)$ and T 34
3.20 cross-cut curves in $\overline{\left(\frac{\omega\theta}{U}\right)}$ and T 34
3.21 cross-cut curves in $\overline{\left(\frac{\omega\theta}{U}\right)}$ and $\overline{T}$ 35
3.22 Display of datapoints from Arnal 37
3.23 axis of T_{max} on log scale 38
3.24 Display of interpolated and extrapolated splines 39
3.25 3d representation of T surface for the flat plate case 40
3.26 $\overline{T}$ versus $\overline{r}$ for all 15 cases 41
3.27 Approximation of T_{max} by $T_{max} = \overline{r}e^{1-\overline{r}}$ for all 15 cases 41
3.28 $^{10}log(T_{maxmax})$ versus $^{10}log(Re_{\theta_{crit}})$, all 15 cases 42
3.29 r_{top} versus $^{10}log(Re_{\theta_{crit}})$ 42
3.30 $\left(\frac{\omega\theta}{U}\right)_{scale}$ versus $^{10}log(Re_{\theta_{crit}})$ 43
3.31 $^{10}log(F)_{top}$ versus $^{10}log(Re_{\theta_{crit}})$ 43
3.32 correlation between $^{10}log(Re_{\theta_{crit}})$ versus $^{10}log(H)$ 44

3.33 Schematic roadmap 45

4.1 panelling in 48
4.2 Closure relation for H^* & 50
4.3 Closure relation for $Re_\theta \frac{C_f}{2}$ & 51
4.4 Closure relation for $Re_\theta \frac{C_D}{H^*}$ & 51
4.5 Envelope approximation Drela method 56
4.6 $^{10}log(Re_{\theta_{crit}})$ and $^{10}log(H)$ for the Drela method 57
4.7 $\theta \frac{\delta N}{\delta \xi}$ and H for the Drela method 58
4.8 $^{10}log(Re_{\theta_{crit}})$ and $^{10}log(H)$ for the Van Ingen method 59
4.9 discontinuities in Van Ingen method 59

5.1 Flowchart of transition related subroutines in 64
5.2 interpolation in 9 points 67
5.3 interpolation in 3 points 67
5.4 Safety factor prediction method 69
5.5 Forcing method 70

6.1 C_p NACA0012 for $\alpha = 3°$, $Re_c = 1 \cdot 10^6$, no suction 74
6.2 C_p for NACA0012 at $\alpha = 0°$, $Re_c = 1 \cdot 10^6$, no suction 75
6.3 C_p for NACA0012 at $\alpha = 0°$, $Re_c = 1 \cdot 10^6$, base suction 75
6.4 C_p for NACA0012 at $\alpha = 0°$, $Re_c = 1 \cdot 10^6$, $2 \cdot$ base suction 76
6.5 suction distribution *base* for NACA0012 $\alpha = 0°$, $Re_c = 1 \cdot 10^6$ 76
6.6 suction distribution $2 \cdot base$ for NACA0012 $\alpha = 0°$, $Re_c = 1 \cdot 10^6$ 76
6.7 C_p for NACA0018 at $\alpha = 2°$, $Re_c = 1 \cdot 10^5$ 77
6.8 C_f for NACA0018 at $\alpha = 2°$, $Re_c = 1 \cdot 10^5$, upper surface (red), lower surface (cyan) 78
6.9 C_p for "flat plate airfoil" at $\alpha = 1.33°$, $Re_c = 5 \cdot 10^6$ 78
6.10 Comparison of Re_θ for the "flat plate airfoil" and the Blasius solution 79
6.11 Zoomed in comparison of Re_θ for the "flat plate airfoil" and the Blasius solution . . . 79
6.12 H for flat plate airfoil at $\alpha = 1.33°$,$Re_c = 5 \cdot 10^6$ 79
6.13 C_p for uncorrected NACA64$_2$-A-215 at $\alpha = 0°$, $Re_c = 2.75 \cdot 10^6$ 80
6.14 C_p for corrected NACA64$_2$-A-215 at $\alpha = 0°$, $Re_c = 2.75 \cdot 10^6$ 81
6.15 C_p for flat plate suction airfoil at $\alpha = 1.33°$, $Re_c = 5 \cdot 10^6$ 82
6.16 v_0 for flat plate suction airfoil at $\alpha = 1.33°$, $Re_c = 5 \cdot 10^6$ 82
6.17 H for flat plate suction airfoil at $\alpha = 1.33°$, $Re_c = 5 \cdot 10^6$, lower surf. 83
6.18 H for flat plate suction airfoil at $\alpha = 1.33°$, $Re_c = 5 \cdot 10^6$, upper surf. 83
6.19 N for flat plate suction airfoil at $\alpha = 1.33°$, $Re_c = 5 \cdot 10^6$, lower surf. 83
6.20 N for flat plate suction airfoil at $\alpha = 1.33°$, $Re_c = 5 \cdot 10^6$, upper surf. 83
6.21 $x_{transition}$ lower surface for NACA0012 $\alpha = 3°$, $Re_c = 1 \cdot 10^6$ 84
6.22 $x_{transition}$ upper surface for NACA0012 $\alpha = 3°$, $Re_c = 1 \cdot 10^6$ 84
6.23 $x_{transition}$ lower surface for NACA0012 $\alpha = 0°$, $Re_c = 1 \cdot 10^6$, no suction 84
6.24 $x_{transition}$ upper surface for NACA0012 $\alpha = 0°$, $Re_c = 1 \cdot 10^6$, no suction 84
6.25 $x_{transition}$ lower surface for NACA0012 $\alpha = 0°$, $Re_c = 1 \cdot 10^6$, suction *base* 85
6.26 $x_{transition}$ upper surface for NACA0012 $\alpha = 0°$, $Re_c = 1 \cdot 10^6$, suction *base* 85
6.27 $x_{transition}$ lower surface for NACA0012 $\alpha = 0°$, $Re_c = 1 \cdot 10^6$, suction $2 \cdot base$ 85
6.28 $x_{transition}$ upper surface for NACA0012 $\alpha = 0°$, $Re_c = 1 \cdot 10^6$, suction $2 \cdot base$ 85
6.29 $x_{transition}$ lower surface for NACA0018 $\alpha = 2°$, $Re_c = 1 \cdot 10^5$ 85

6.30 $x_{transition}$ upper surface for NACA0018 $\alpha = 2°$, $Re_c = 1 \cdot 10^5$ 85
6.31 $x_{transition}$ lower surface for flat plate airfoil$\alpha = 1.33°$, $Re_c = 5 \cdot 10^6$, ... 86
6.32 $x_{transition}$ upper surface for flat plate airfoil $\alpha = 1.33°$, $Re_c = 5 \cdot 10^6$ 86
6.33 $x_{transition}$ lower surface for NACA64$_2$-A-215 $\alpha = 0°$, $Re_c = 2.75 \cdot 10^6$ 86
6.34 $x_{transition}$ upper surface for NACA64$_2$-A-215 $\alpha = 0°$, $Re_c = 2.75 \cdot 10^6$ 86
6.35 H for NACA0012 $\alpha = 3°$, $Re_c = 1 \cdot 10^6$, lower surf. 87
6.36 H for NACA0012 $\alpha = 3°$, $Re_c = 1 \cdot 10^6$, upper surf. 87
6.37 Re_θ and $Re_{\theta_{crit}}$ for NACA0012 $\alpha = 3°$, $Re_c = 1 \cdot 10^6$, lower surf. 88
6.38 Re_θ and $Re_{\theta_{crit}}$ for NACA0012 $\alpha = 3°$, $Re_c = 1 \cdot 10^6$, upper surf. 88
6.39 N for NACA0012 $\alpha = 3°$, $Re_c = 1 \cdot 10^6$, lower surf. 88
6.40 N for NACA0012 $\alpha = 3°$, $Re_c = 1 \cdot 10^6$, upper surf. 88
6.41 N for NACA0012 at $\alpha = 0°$, $Re_c = 1 \cdot 10^6$, no suction, lower surf. 88
6.42 N for NACA0012 at $\alpha = 0°$, $Re_c = 1 \cdot 10^6$, no suction, upper surf. 88
6.43 N for NACA0012 at $\alpha = 0°$, $Re_c = 1 \cdot 10^6$, base suction, lower surf. 89
6.44 N for NACA0012 at $\alpha = 0°$, $Re_c = 1 \cdot 10^6$, base suction, upper surf. 89
6.45 N for NACA0012 at $\alpha = 0°$, $Re_c = 1 \cdot 10^6$, $2 \cdot$ base suction, lower surf. 89
6.46 N for NACA0012 at $\alpha = 0°$, $Re_c = 1 \cdot 10^6$, $2 \cdot$ base suction, upper surf. 89
6.47 N for NACA0018 at $\alpha = 2°$, $Re_c = 1 \cdot 10^5$, lower surf. 89
6.48 N for NACA0018 at $\alpha = 2°$, $Re_c = 1 \cdot 10^5$, upper surf. 89
6.49 N for flat plate airfoil at $\alpha = 1.33°$, $Re_c = 5 \cdot 10^6$, lower surf. 90
6.50 N for flat plate airfoil at $\alpha = 1.33°$, $Re_c = 5 \cdot 10^6$, upper surf. 90
6.51 N for NACA64$_2$-A-215 at $\alpha = 0°$, $Re_c = 2.75 \cdot 10^6$, lower surf. 90
6.52 N for NACA64$_2$-A-215 at $\alpha = 0°$, $Re_c = 2.75 \cdot 10^6$, upper surf. 90

7.1 H at lower surface for NACA0012 $\alpha = 3°$, $Re_c = 1 \cdot 10^6$ 94
7.2 H at upper surface for NACA0012 $\alpha = 3°$, $Re_c = 1 \cdot 10^6$ 94
7.3 N at lower surface for NACA0012 $\alpha = 3°$, $Re_c = 1 \cdot 10^6$ 94
7.4 N at upper surface for NACA0012 $\alpha = 3°$, $Re_c = 1 \cdot 10^6$ 94
7.5 H at lower surface for NACA0012 $\alpha = 0°$, $Re_c = 1 \cdot 10^6$, no suction 94
7.6 H at upper surface for NACA0012 $\alpha = 0°$, $Re_c = 1 \cdot 10^6$, no suction 94
7.7 N at lower surface for NACA0012 $\alpha = 0°$, $Re_c = 1 \cdot 10^6$, no suction 95
7.8 N at upper surface for NACA0012 $\alpha = 0°$, $Re_c = 1 \cdot 10^6$, nosuction 95
7.9 H at lower surface for NACA0012 $\alpha = 0°$, $Re_c = 1 \cdot 10^6$, suction *base* 95
7.10 H at upper surface for NACA0012 $\alpha = 0°$, $Re_c = 1 \cdot 10^6$, suction *base* 95
7.11 N at lower surface for NACA0012 $\alpha = 0°$, $Re_c = 1 \cdot 10^6$, suction *base* 95
7.12 N at upper surface for NACA0012 $\alpha = 0°$, $Re_c = 1 \cdot 10^6$, suction *base* 95
7.13 H at lower surface for NACA0012 $\alpha = 0°$, $Re_c = 1 \cdot 10^6$, suction $2 \cdot$ *base* 96
7.14 H at upper surface for NACA0012 $\alpha = 0°$, $Re_c = 1 \cdot 10^6$, suction $2 \cdot$ *base* 96
7.15 N at lower surface for NACA0012 $\alpha = 0°$, $Re_c = 1 \cdot 10^6$, suction $2 \cdot$ *base* 96
7.16 N at upper surface for NACA0012 $\alpha = 0°$, $Re_c = 1 \cdot 10^6$, suction $2 \cdot$ *base* 96
7.17 H at lower surface for NACA0018 $\alpha = 2°$, $Re_c = 1 \cdot 10^5$ 96
7.18 H at upper surface for NACA0018 $\alpha = 2°$, $Re_c = 1 \cdot 10^5$ 96
7.19 N at lower surface for NACA0018 $\alpha = 2°$, $Re_c = 1 \cdot 10^5$ 97
7.20 N at upper surface for NACA0018 $\alpha = 2°$, $Re_c = 1 \cdot 10^5$ 97
7.21 H at lower surface for flat plate airfoil $\alpha = 1.33°$, $Re_c = 5 \cdot 10^6$ 97
7.22 H at upper surface for flat plate airfoil $\alpha = 1.33°$, $Re_c = 5 \cdot 10^6$ 97
7.23 N at lower surface for flat plate airfoil $\alpha = 1.33°$, $Re_c = 5 \cdot 10^6$ 97

7.24 N at upper surface for flat plate airfoil $\alpha = 1.33°$, $Re_c = 5 \cdot 10^6$ 97
7.25 H at lower surface for naca 64_2-A-215 $\alpha = 0°$, $Re_c = 2.75 \cdot 10^6$ 98
7.26 H at upper surface for naca 64_2-A-215 plate airfoil $\alpha = 0°$, $Re_c = 2.75 \cdot 10^6$ 98
7.27 N at lower surface for naca 64_2-A-215 $\alpha = 0°$, $Re_c = 2.75 \cdot 10^6$ 98
7.28 N at upper surface for naca 64_2-A-215 $\alpha = 0°$, $Re_c = 2.75 \cdot 10^6$ 98

8.1 $^{10}log(Re_{\theta_{crit}}) - ^{10} log(H)$ for all three transition methods 100
8.2 N for NACA0012 $\alpha = 3°$, $Re_c = 1 \cdot 10^6$ 101
8.3 N for NACA0012 $\alpha = 0°$, $Re_c = 1 \cdot 10^6$, no suction 102
8.4 N for NACA0012 $\alpha = 0°$, $Re_c = 1 \cdot 10^6$, suction $base$ 103
8.5 N for NACA0012 $\alpha = 0°$, $Re_c = 1 \cdot 10^6$, suction $2 \cdot base$ 104
8.6 N for NACA0018 $\alpha = 2°$, $Re_c = 1 \cdot 10^5$ 105
8.7 N for flat plate airfoil $\alpha = 1.33°$, $Re_c = 5 \cdot 10^6$ 106
8.8 N for NACA64_2-A-215 $\alpha = 0°$, $Re_c = 2.75 \cdot 10^6$ 107

9.1 DU99 airfoil with the 360 panel grid 109
9.2 DU99 polar without suction 111
9.3 DU99 suction distribution no. 1 112
9.4 DU99 polar with suction distribution no. 1 113
9.5 DU99 suction distribution no. 2 114
9.6 DU99 suction distribution no. 1 & 2 114
9.7 DU99 polar with suction distribution no. 2 115
9.8 DU99 polar, without suction, and both suction distributions 116

B.1 NACA0012 with 160 panels 123
B.2 NACA0012 with 360 panels 123
B.3 NACA0018 with 160 panels 124
B.4 NACA0018 with 360 panels 124
B.5 Flat plate airfoil with 160 panels 124
B.6 Flat plate airfoil with 360 panels 124
B.7 NACA 64_2-A-215 with 160 panels 125
B.8 NACA 64_2-A-215 with 360 panels 125

C.1 C_p NACA0012 for $\alpha = 0°$ 127
C.2 H for NACA0012 $\alpha = 0°$,$Re_c = 1 \cdot 10^6$, no suction, lower surf. 128
C.3 H for NACA0012 $\alpha = 0°$,$Re_c = 1 \cdot 10^6$, no suction upper surf. 128
C.4 Re_θ and $Re_{\theta_{crit}}$ for NACA0012 $\alpha = 0°$,$Re_c = 1 \cdot 10^6$, no suction, lower surf. 128
C.5 Re_θ and $Re_{\theta_{crit}}$ for NACA0012 $\alpha = 0°$,$Re_c = 1 \cdot 10^6$, no suction, upper surf. 128
C.6 N for NACA0012 at $\alpha = 0°$,$Re_c = 1 \cdot 10^6$, no suction, lower surf. 128
C.7 N for NACA0012 at $\alpha = 0°$,$Re_c = 1 \cdot 10^6$, no suction, upper surf. 128
C.8 C_p for NACA0012 at $\alpha = 0°$,$Re_c = 1 \cdot 10^6$, base suction 129
C.9 H for NACA0012 at $\alpha = 0°$,$Re_c = 1 \cdot 10^6$, base suction, lower surf. 130
C.10 H for NACA0012 at $\alpha = 0°$,$Re_c = 1 \cdot 10^6$, base suction, upper surf. 130
C.11 Re_θ and $Re_{\theta_{crit}}$ for NACA0012 at $\alpha = 0°$,$Re_c = 1 \cdot 10^6$, base suction, lower surf. . . . 130
C.12 Re_θ and $Re_{\theta_{crit}}$ for NACA0012 at $\alpha = 0°$,$Re_c = 1 \cdot 10^6$, base suction, upper surf. . . . 130
C.13 N for NACA0012 at $\alpha = 0°$,$Re_c = 1 \cdot 10^6$, base suction, lower surf. 130
C.14 N for NACA0012 at $\alpha = 0°$,$Re_c = 1 \cdot 10^6$, base suction, upper surf. 130
C.15 C_p for NACA0012 at $\alpha = 0°$,$Re_c = 1 \cdot 10^6$, 2·base suction 131

C.16 H for NACA0012 at $\alpha = 0°$,$Re_c = 1 \cdot 10^6$, 2·base suction, lower surf. 132
C.17 H for NACA0012 at $\alpha = 0°$,$Re_c = 1 \cdot 10^6$, 2·base suction, upper surf. 132
C.18 Re_θ, $Re_{\theta_{crit}}$ for NACA0012 at $\alpha = 0°$,$Re_c = 1 \cdot 10^6$, 2·base suction, lower surf. 132
C.19 Re_θ, $Re_{\theta_{crit}}$ ffor NACA0012 at $\alpha = 0°$,$Re_c = 1 \cdot 10^6$, 2·base suction, upper surf. 132
C.20 N for NACA0012 at $\alpha = 0°$,$Re_c = 1 \cdot 10^6$, 2·base suction, lower surf. 133
C.21 N for NACA0012 at $\alpha = 0°$,$Re_c = 1 \cdot 10^6$, 2·base suction, upper surf. 133
C.22 C_p for NACA0018 at $\alpha = 2°$,$Re_c = 1 \cdot 10^5$ 133
C.23 H for NACA0018 at $\alpha = 2°$,$Re_c = 1 \cdot 10^5$, lower surf. 134
C.24 H for NACA0018 at $\alpha = 2°$,$Re_c = 1 \cdot 10^5$, upper surf. 134
C.25 Re_θ and $Re_{\theta_{crit}}$ for NACA0018 at $\alpha = 2°$,$Re_c = 1 \cdot 10^5$, lower surf. 134
C.26 Re_θ and $Re_{\theta_{crit}}$ for NACA0018 at $\alpha = 2°$,$Re_c = 1 \cdot 10^5$, upper surf. 134
C.27 N for NACA0018 at $\alpha = 2°$,$Re_c = 1 \cdot 10^5$, lower surf. 134
C.28 N for NACA0018 at $\alpha = 2°$,$Re_c = 1 \cdot 10^5$, upper surf. 134
C.29 C_p for flat plate airfoil at $\alpha = 1.33°$,$Re_c = 5 \cdot 10^6$ 135
C.30 H for flat plate airfoil at $\alpha = 1.33°$,$Re_c = 5 \cdot 10^6$, lower surf. 136
C.31 H for flat plate airfoil at $\alpha = 1.33°$,$Re_c = 5 \cdot 10^6$, upper surf. 136
C.32 Re_θ and $Re_{\theta_{crit}}$ for flat plate airfoil at $\alpha = 1.33°$,$Re_c = 5 \cdot 10^6$, lower surf. 136
C.33 Re_θ and $Re_{\theta_{crit}}$ for flat plate airfoil at $\alpha = 1.33°$,$Re_c = 5 \cdot 10^6$, upper surf. 136
C.34 N for flat plate airfoil at $\alpha = 1.33°$,$Re_c = 5 \cdot 10^6$, lower surf. 136
C.35 N for flat plate airfoil at $\alpha = 1.33°$,$Re_c = 5 \cdot 10^6$, upper surf. 136
C.36 C_p for NACA64$_2$-A-215 at $\alpha = 0°$,$Re_c = 2.75 \cdot 10^6$ 137
C.37 H for NACA64$_2$-A-215 at $\alpha = 0°$,$Re_c = 2.75 \cdot 10^6$, lower surf. 138
C.38 H for NACA64$_2$-A-215 at $\alpha = 0°$,$Re_c = 2.75 \cdot 10^6$, upper surf. 138
C.39 Re_θ and $Re_{\theta_{crit}}$ for NACA64$_2$-A-215 at $\alpha = 0°$,$Re_c = 2.75 \cdot 10^6$, lower surf. 138
C.40 Re_θ and $Re_{\theta_{crit}}$ for NACA64$_2$-A-215 at $\alpha = 0°$,$Re_c = 2.75 \cdot 10^6$, upper surf. 138
C.41 N for NACA64$_2$-A-215 at $\alpha = 0°$,$Re_c = 2.75 \cdot 10^6$, lower surf. 138
C.42 N for NACA64$_2$-A-215 at $\alpha = 0°$,$Re_c = 2.75 \cdot 10^6$, upper surf. 138

List of Tables

3.1 *H* for Hartree solutions 23
3.2 summary for data from Arnal 29

5.1 Transition points for different convergence improvements 71

6.1 Studied Airfoils 73

Chapter 1

Introduction

1.1 Introduction

For a very long time aerodynamicists are trying to reduce drag on airplanes by trying to achieve laminar flow over as large an area of the wings as possible. For the lower surface, at a not too high Reynolds number, natural laminar flow is a good way of achieving almost total laminar boundary layer flow. For the upper wing surface a combination of natural laminar flow and boundary layer suction holds most perspective for achieving the same for wings with not too high sweep angles. Research into boundary layer suction has been ongoing since the late 1930s. This study hopes to contribute to application of boundary layer suction by providing a tool for analyzing the influence of boundary layer suction to the transition point as well as enabling aerodynamicists to design airfoils for use with boundary layer suction.

1.2 Previous work

1.2.1 Preliminary work on transition

The first person to see that boundary layer suction could have huge benefits is Ludwig Prandtl [28] in 1904. He saw in boundary layer suction a method of delaying separation. A problem since the formulation of the boundary layer theory is to predict transition from laminar to turbulent flow in the boundary layer, a phenomenon first observed in pipe flow by Reynolds [34](1883). Orr [27](1907) and Sommerfeld [40](1908), derived the equations for the analysis of small disturbances in viscous parallel flows from the Navier-Stokes equations but were unable to find instability according to Herbert [20]. In 1929 Tollmien [49] solved the Orr-Sommerfeld equation for the Blasius flow, and calculated a neutral curve, outside of which the laminar flow is stable. Schlichting [36] in 1933 calculated growth rates for the instable laminar fluctuations in the boundary layer flow. Also in 1933 Squire [41] showed that the 3D problem of disturbances could be rewritten into an equivalent 2D problem. This meant

that the transition is governed (in parallel flows) by 2D waves, while the turbulent fluctuations are 3D. Rayleigh, Tollmien, Schlichting, Lin and others ([49], [37], [25]) developed the linear stability theory. Linear stability theory considers a laminar boundary layer on which small disturbances are superimposed. These disturbances can be damped or amplified, depending on the flow conditions. Taylor [46](1936) objected to linear stability theory being connected to transition, as he found that turbulence in the free stream causes fluctuations inside the boundary layer and that these cause local separation followed by transition. In 1941 (some sources give 1943) it was found that this mechanism is not valid for less than 0.1% turbulence in the free stream and the relevance of linear stability theory was shown by Schubauer & Skramstad [38]. This was not published until 1947 due to wartime restrictions on research publications. They experimentally showed the existence of the so-called Tollmien-Schlichting waves in the boundary layer.

1.2.2 e^N-method

Liepmann [24] found in 1943 (but due to war-time classification published after the war) the idea of using the criterion of A/A_0 as a measure for the amplification, with A_0 the unknown but small initial amplitude, and A the wave amplitude. If one solves the Orr-Sommerfeld equation for real frequencies to obtain the spatial growth rate α_i from the complex wavenumber $\alpha = \alpha_r + i\alpha_i$ then the amplitude ratio is then given by:

$$\sigma = ln\frac{A}{A_0} = -\int_{x_0}^{x} \alpha(\xi, \omega)d\xi \tag{1.1}$$

More detailed information considering the Orr-Sommerfeld equation is given in section 2.2. After this came the creation of the e^N-method for transition prediction (1956, Smith and Gamberoni [39], and Van Ingen [50]). This method allows the part of the transition mechanism with linear growth of disturbances dominated by Tollmien-Schlichting waves to be predicted very well. As the growth of the disturbances can be considered linear from $N = 0$ up to $N = 7$, a large part of the entire growth regime is approximated very well. The success of the e^N method lies partly in that extrapolation into the section with non-linear disturbance growth is only necessary in the small last part ($N > 7$) of the entire curve, when assuming a critical N-factor of 9. Initially it was called the e^9-method, due to the fact that in many cases, in flight as well as in low-turbulence wind tunnel testing, a critical N-factor of 9 correlated well with the transition region. Later it was found that the critical N factor was dependent on (mainly) the free stream turbulence level, and that this factor should be adapted to the flowcase to which the method was applied.
The advantage of this method is it's fast calculation and ease of use. Disadvantages are the fact that it relies on a good choice of the (empirical) N_{crit}-factor: the amplification level at which transition to turbulent boundary layer is assumed to occur. The method is still very popular today. The method was used for boundary layer suction in [51], and a version capable of calculating very limited amounts of damping of the N-factor was implemented in an airfoil design program ( ) in 2002 although it suffered some drawbacks. Since the discovery of the e^N-method in 1956 many advances have been made in transition modelling, mainly in extending the method for 3D flowcases and supersonic flows.

1.3 Recent work at

The Department of Aerodynamics at the Delft University of Technology, and more specifically the Low Speed Aerodynamics section, has taken an interest in boundary layer suction techniques for Laminar Flow Control for many years now. The main focus is to reduce drag by using boundary layer suction as a tool to delay boundary layer transition and boundary layer separation. Current developments in hole-drilling techniques are taking away some of the most pressing practical issues connected with the use of boundary layer suction. Also advances in research concerning boundary layer suction (e.g. Steffens, [42]) are taking away barriers for the practical use of boundary layer suction. For instance advances have been made in estimating the maximum suction velocity without inducing transition and in hole drilling techniques that allow for many very small suction holes without compromising the wing structure. With these advances there comes a desire for an airfoil design tool that can cope with boundary layer suction. Using boundary layer suction on existing airfoils may reduce drag and/or increase performance. To study this phenomena and to be able to put the technique to practical use a software program is needed that is adapted for use with boundary layer suction. The effect of the boundary layer suction can be calculated with some of the existing software packages. However these programs require the user to have expert knowledge of aerodynamics and suction phenomena and are usually focussed on extensive analysis of the flow. Due to their long calculation time and time consuming pre- and postprocessing cycles they are also slow in use. Therefore they do not meet the demands which aerodynamic design programs make, such as fast iteration cycles to take into account changes fast and user-friendliness to knowledgeable but not quite expert users.
To take full advantage of the benefits of boundary layer suction an airfoil design tool that can cope with the aspects of boundary layer suction is definitely necessary. At the Delft University of Technology a choice was made to adapt several programs to cope with boundary layer suction. These programs are:

- XFOIL, the 2D single element airfoil design program by M. Drela ([9], [10], [12], [13]) of , the modified version for boundary layer suction was named . This version however was incomplete as the transition routine could predict only very limited damping of the N-factor, which is the main driver behind the wish for such an adapted program.
- MSES, the 2D multiple element airfoil design program similar to XFOIL also by M. Drela ([9], [11])of . This program has the same drawback as the , only very limited amounts of damping of the N-factor can be taken into account.
- xSoaring a sailplane performance program developed at the Low Speed Laboratory ( ) at the ([17], [22], [47])

Adaptation of these programs for boundary layer suction has been ongoing since 2002 by several workers([1], [14], [17], [22], [47], [48]). The focus of the present study is on .

In 2004 two transition methods were present in . One being the original version by M. Drela [9], which is an envelope e^N method, and a full e^N method, originally written by Van Ingen and implemented by Ferreira [14]. This method is based on Van Ingens e^N method as described in [50] and [51] and was further developed over the years. Presently prof. Van Ingen is working on an overview of his 50 years involvement with the e^N-method. This overview will end with a new database method.

The present author assisted prof. Van Ingen in the new development and could consult a draft version of this new method. More about the new method will be explained in chapter 3. From here the e^N method as implemented by Ferreira in 2002 in will be called the Van Ingen method. To avoid confusion the method implemented in in this study (the new database method) will be named the Improved e^N method.

In Broers [1] deficiencies were found in both transition methods present at the time in .

- The standard transition method by Drela is not able to predict decreasing amplification factors that may occur when boundary layer suction is used. When suction is used the Drela method can not cope with a growth rate of anything less than (or even equal to) zero. In the Drela method always a very small mimimum growth rate of N is used (see figure 4.7), unless the Re_θ is below the $Re_{\theta_{crit}}$, then the N-factor is kept constant. Never will a H occur at which the amplification rate ($\frac{dN}{dx}$) will be less than zero. Obviously this is not correct as damping will occur in a stable boundary layer.
- The full e^N method by Van Ingen as implemented by Ferreira [14] does not have the drawback of not being able to calculate negative or zero values of the amplification rate, although these negative amplification rates can only be quite small in this method. So the method can predict a decreasing N-factor, but has another flaw with regard to using it as a design tool in airfoils employing boundary layer suction. The curve used in determining whether the boundary layer is stable or not, the $Re_{\theta_{crit}} - H$ curve, cannot cope with a boundary layer in which the Re_θ-value is smaller that the $Re_{\theta_{crit}}$, if this happens, an amplification rate ($\frac{dN}{dx}$) of zero is given.

1.4 Objectives of present study

With the problems in transition prediction in as mentioned in the previous section (1.1) objectives for the present study can be formulated. The main objective of this study is:

To implement an improved transition region prediction method in that achieves reliable results for boundary layers on airfoils with and without boundary layer suction.

Connected with this 2 sub-objectives can be formulated:

- **To make a comparison between the newly implemented transition region prediction method and the ones already present in .**
- **A short practical study to recalculate the airfoil performance of an airfoil using boundary layer suction and that is designed with the older transition region prediction methods.**

Fulfilling the main objective should enable aerodynamicists to take full advantage of this study and of earlier work done on , as up until now the limiting factor in designing for boundary layer

suction was the transition region prediction method. Fulfilling the sub-objectives gives further insight in the quality and user-friendliness of the newly added functions.

1.5 Approach of present study

This study will use as the new transition region prediction method the improved version by Van Ingen [53] of the e^N-method (Smith and Gamberoni [39] and Van Ingen [50]) This improved version of the e^N-method was developed by Van Ingen, using [58]. The new method will be a database method that uses a set of stability diagrams calculated by Arnal [4] for a series of Falkner-Skan boundary layers. The later phases of the development of the code were performed by prof. Van Ingen concurrently with the work of the present author on the implementation in Fortran 77 for inclusion in . Some suggestions for improvement by the present author were implemented in both the and Fortran version of the method, after preliminary tests revealed some flaws. The in implemented version of this code (written in Fortran 77) was made by the present author based on the version and differs in some respects due to the different programming language used. The function or results of both versions of the method do not differ.
So first the improved e^N transition method was implemented into . Then some modifications were made to the program to maximize the functionality and ease of use. Then the method was extensively tested, which revealed some areas in which improvement was needed, notably in the convergence of the boundary layer solution. Resolving this, a validation study was made, to prove that the method implemented in is the same as the method. As this method is proven to handle the data taken from Arnal ([4]) correctly, the same then holds for the implementation. This validation is done using 7 test cases. After this is done a study is made of the possible errors introduced by the boundary layer calculations in . The variables used for input in the improved e^N-method are then also generated using a finite difference method developed by Van Ingen [52]. After this the results of the improved e^N-method are compared for these two sets of boundary layer variables. Then a comparative study is made between the transition methods present in . This being the Drela method, the Van Ingen e^N-method and the newly added Improved e^N-method. A study of the first two was already done by Ferreira [14] and Broers [1].
As a final exercise a previously designed airfoil using boundary layer suction is evaluated. It was designed using the Drela and Van Ingen transition methods, and now using the Improved e^N-method the performance is re-calculated and a new suction velocity distribution is designed. Also the newly added functions and routines in are evaluated in this way to ensure user-friendliness and functionality of the added features.

1.6 Outline

In chapter 1 an introduction into the subject of this study is given, along with a summary of the previous work done on this subject by other workers. Also the objectives of this study are given in this chapter. In chapter 2 an introduction into the theory of the subject is presented, including some elements of the potential flow, boundary layer theory, the linear stability theory, the classic e^N-method and the finite difference theory. Chapter 3 will explain the Improved e^N-method. In chapter 4 and

the present state of will be discussed. Chapter 5 gives a description of the modifications made by the present author to in implementing the improved e^N-method. In chapter 6 a validation study is made to see if the results given by the e^N-method in correspond with the values generated by the version of the method. Also in this chapter a short grid convergence study is presented. Chapter 7 gives the results of a comparative study of and a finite difference method by Van Ingen to compare the boundary layer solutions of both methods and their effect on the transition point prediction. In chapter 9 the results of a case study in (re)designing a suction distribution for an airfoil is made. This is done on the DU99 airfoil that was designed especially for boundary layer suction but which suction distribution was designed with the older transition methods in . Chapter 10 will give the conclusions and recommendations that follow from this study. In appendix A a user guide for users of is given, providing future users some explanations and practical information on the new functions in the program. Appendix B gives the used airfoil grids and appendix C gives additional figures that were made in the validation study but not included in chapter 6.

Chapter 2

Theory

As in the next chapters some concepts and theories will be used without detailed information to go with it, some basic theory will be introduced here.

2.1 Boundary layer equations

2.1.1 Navier-Stokes equation

For two dimensional incompressible viscous flows the fluid properties are governed by the Navier-Stokes (by Navier [26] and Stokes [44], here taken from White [56]) equations, together with the continuity equation. Omitting the body forces these equations can be written for a 2-dimensional flow as follows:

$$\frac{\partial u}{\partial t} + u\frac{\partial u}{\partial x} + v\frac{\partial u}{\partial y} = -\frac{1}{\rho}\frac{\partial p}{\partial x} + \nu\left(\frac{\partial^2 u}{\partial x^2} + \frac{\partial^2 u}{\partial y^2}\right) \tag{2.1}$$

$$\frac{\partial v}{\partial t} + u\frac{\partial v}{\partial x} + v\frac{\partial v}{\partial y} = -\frac{1}{\rho}\frac{\partial p}{\partial y} + \nu\left(\frac{\partial^2 v}{\partial x^2} + \frac{\partial^2 v}{\partial y^2}\right) \tag{2.2}$$

$$\frac{\partial u}{\partial x} + \frac{\partial v}{\partial y} = 0 \tag{2.3}$$

In this equations 2.1 and 2.2 are the momentum equations in respectively x and y direction. Equation 2.3 is the continuity equation. The notation is as commonly used, where u and v are the x and y components of the velocity, p is the pressure, ρ stands for density, and ν is the kinematic viscosity coefficient. The Navier-Stokes equations are difficult to solve for any but the most simplest geometries. For flows with high Reynolds numbers, with the Reynolds number defined as 2.4

$$Re = \frac{U_\infty c}{\nu} \tag{2.4}$$

(with c a characteristic lenght, for instance airfoil chord, U_∞ the freestream velocity, and ν is the kinematic viscosity coefficient), a thin layer near the wall exists where the tangential velocity decreases from the free stream value at a small distance from the wall to zero at the wall surface quite rapidly. This region is called the boundary layer.

2.1.2 Prandtl's Boundary-layer Equations

In 1904 Prandtl [28] simplified the Navier-Stokes equations to form a set of boundary layer equations. The boundary layer equations for steady flow along a plane wall are:

$$u\frac{\partial u}{\partial x} + v\frac{\partial u}{\partial y} = -\frac{1}{\rho}\frac{\partial p}{\partial x} + \nu\frac{\partial^2 u}{\partial y^2} \tag{2.5}$$

$$\frac{\partial u}{\partial x} + \frac{\partial v}{\partial y} = 0 \tag{2.6}$$

The continuity equation is untouched by Prandtl's simplifications, but the y-momentum equation has been reduced to:

$$\frac{\partial p}{\partial y} = 0 \tag{2.7}$$

So that

$$p = p(x) \tag{2.8}$$

The observation made by Prandtl was that the pressure is a known variable in boundary-layer analysis, with $p = p(x)$ impressed on the boundary-layer by the inviscid outer flow.
The boundary-layer equations only hold for flows where the boundary-layer can be considered thin with respect to the reference length scale (such as flat plate length). Equations 2.5 and 2.6 are also valid for curved surfaces, where the boundary-layer thickness is small with respect to the radius of curvature of the surface and the change in curvature $\frac{dr}{dx}$ remains small. Because the assumption of a thin boundary layer is only valid at high Reynolds numbers the boundary layer equations are also only valid at high Reynolds numbers. ($Re_x > 1000$, according to White [56]).

In Schlichting [6] the following observation is made: Outside the boundary layer the velocity gradient $\frac{\partial u}{\partial y}$ can be neglected en therefore equation 2.5 reduces to

$$U\frac{dU}{dx} = -\frac{1}{\rho}\frac{dp}{dx} \tag{2.9}$$

using this, 2.5 can be written as:

$$u\frac{\partial u}{\partial x} + v\frac{\partial u}{\partial y} = U\frac{dU}{dx} + \nu\frac{\partial^2 u}{\partial y^2} \tag{2.10}$$

Together with the continuity equation 2.3 this equation determines the development of the boundary layer flow downstream of an initial station $x = x_0$ when the velocity profile at $x = x_0$ is known. The

following boundary conditions should be accounted for:

$$y = 0: \qquad u = 0, v = v_0(x) \tag{2.11}$$

$$y \to \infty: \qquad u \to U \tag{2.12}$$

2.12 implies that the suction or blowing that occurs on the wall is usually assumed to be strictly normal to the wall.

2.1.3 Similarity Solutions

Equations 2.3 and 2.10 are partial differential equations (PDE) that in special cases can be reduced to ordinary differential equations (ODE) using the idea of similarity of boundary layer flows. Similarity means that the velocity profiles at all stations x can be reduced to a single curve by scaling the y and u variables with scaling factors depending on x. Similarity can only be achieved in a limited number of (free stream) velocity distributions. There are a number of similar boundary layers, of which 3 will be looked at closer here:

- The flat plate flow by Blasius
- The wedge flow by Falkner-Skan
- The asymptotic suction boundary layer

Flat plate flow

Blasius [5] introduced the scaled variable

$$\eta = \frac{y}{x}\sqrt{\frac{Ux}{\nu}} \tag{2.13}$$

The stream function can then be written as:

$$\psi = \sqrt{\nu U x} f(\eta) \tag{2.14}$$

where f is a function to be determined. With the stream function defined, expressions for u and v are:

$$u = \frac{\partial \psi}{\partial y} = U f'(\eta) \tag{2.15}$$

$$v = -\frac{\partial \psi}{\partial x} = -\frac{1}{2}\sqrt{\frac{\nu U}{x}} f(\eta) - \sqrt{\nu x U}\frac{\partial \eta}{\partial x} f'(\eta) \tag{2.16}$$

Substitution of *u* and *v* into equation 2.10 yields:

$$f''' + \frac{1}{2} f f'' = 0 \tag{2.17}$$

This is the classic Blasius equation, which has no exact solution in closed form, but can numerically be solved by for example a shooting method such as the Runge-Kutta method.

Wedge flow

For wedge type similar flow the free stream velocity distribution can be written as:

$$U = u_1 x^m \tag{2.18}$$

The non-dimensionalised scaled variable η is:

$$\eta = \frac{y}{x}\sqrt{\frac{Ux}{\nu}} \tag{2.19}$$

and the stream function becomes:

$$\psi(x,y) = \sqrt{\frac{2\nu u_1}{m+1}} x^{\frac{m+1}{2}} f(\eta) \tag{2.20}$$

u and v can again be denoted as follows:

$$u = \frac{\partial \psi}{\partial y} \tag{2.21}$$

$$v = -\frac{\partial \psi}{\partial x} \tag{2.22}$$

and by combining 2.19 and 2.20 u and v can be rewritten as:

$$u = U f'(\eta) \tag{2.23}$$

$$v = -\sqrt{\frac{m+1}{2}\nu u_1 x^{m-1}}\left[f + \frac{m-1}{m+1}\eta f'\right] \tag{2.24}$$

where primes denote differentiation with respect to η. Now the boundary layer equation reduces to:

$$f''' + \frac{m+1}{2} f f'' + m(1 - f'^2) = 0 \tag{2.25}$$

with

$$\beta = \frac{2m}{1+m} \tag{2.26}$$

Equation 2.25 is a rewritten form of the Falkner-Skan equation. For a flat plate ($\beta = 0$) the equation reduces to the Blasius equation.

Hartree [18] solved the Falkner-Skan equation numerically for several values of β. For $\beta > 0$ always only one solution exists. For $\beta < 0$ an infinite number of solutions exist. Hartree defined a condition (now called the Hartree condition) that the correct solution of the Falkner-Skan equation is the one in which the velocity in the velocity profile goes most quickly to 1 without overshoot. Stewartson [43] showed (with complying to the Hartree condition) that there were also solutions with backflow near the wall for $\beta < 0$.

Asymptotic suction boundary layer

This similarity solution is special because it not only gives a similar velocity profile at different values of x, these profiles are even identical. This so called asymptotic suction boundary layer occurs on a flat plate with constant suction velocity ($-v_0$) for $x \to \infty$. The velocity profile can be found by looking for a solution of equations 2.5 to 2.8 that is independent of x. For equation 2.6 this gives

$$\frac{\partial v}{\partial y} = 0 \tag{2.27}$$

So that v will be constant and equal to a value v_0. Then with equation 2.5 this gives the following for the velocity profile:

$$\frac{u}{U} = 1 - e^{\frac{v_0 y}{\nu}} \tag{2.28}$$

From 2.28 the following values are found (irrelevant of the actual magnitude of v_0, as long as v_0 or x is sufficiently large) :

$$\frac{-v_0\delta^*}{\nu} = 1 \quad and \quad \frac{-v_0\theta}{\nu} = 0.5 \tag{2.29}$$

so that:

$$H = \frac{\delta^*}{\theta} = 2 \tag{2.30}$$

Hence a shape factor H of 2 can be seen as the asymptotic limit for flows with boundary layer suction.

2.2 Linear Stability Theory

After having looked at the boundary layer equations we now take a look at the Linear Stability Theory. The Linear Stability Theory is a way of predicting the growth of disturbances in a laminar boundary layer. For a large part (from the first instability to about $N = 7$) this growth has a linear character. In flows with transition dominated by Tollmien Schlichting waves ([49], [36]) this linear growth plays a major role in the transition process. By accurately predicting the amplification of disturbances a good estimate for the point where transition occurs, is acquired. The basis of Laminar Stability Theory is the Orr-Sommerfeld equation which was derived from the above mentioned Navier-Stokes equations 2.1.1. The derivation goes as follows: u, v and p are assumed to fluctuate about their respective mean values ($\overline{u}$, $\overline{v}$, $\overline{p}$) so that they can be represented as:

$$\begin{aligned} \tilde{u} &= \overline{u} + u'(x,y,t) \\ \tilde{v} &= v'(x,y,t) \\ \tilde{p} &= \overline{p}(x) + p'(x,y,t) \end{aligned} \tag{2.31}$$

Then 2.31 is introduced into the Navier-Stokes equations at 2.1, 2.2 and 2.3 and these equations are then linearized. If one notices that 2.1, 2.2 and 2.3 hold for both the disturbed and undisturbed equations and one eliminates the fluctuating pressure p' the following equations can be written down:

$$\frac{\partial^2 u'}{\partial t \partial y} - \frac{\partial^2 v'}{\partial t \partial x} + u\left(\frac{\partial^2 u'}{\partial x \partial y} - \frac{\partial^2 v'}{\partial x^2}\right) + v'\frac{\partial^2 u}{\partial y^2} = \nu\left(\frac{\partial^3 u'}{\partial x^2 \partial y} + \frac{\partial^3 u'}{\partial y^3} - \frac{\partial^3 v'}{\partial x^3} - \frac{\partial^3 v'}{\partial x \partial y^2}\right) \tag{2.32}$$

$$\frac{\partial u'}{\partial x} + \frac{\partial v'}{\partial y} = 0 \tag{2.33}$$

If then a periodic disturbance is assumed with the following stream function:

$$\psi(x, y, t) = \phi(y) e^{i(\bar{\alpha}x - \bar{\beta}t)} \tag{2.34}$$

with:

$$u' = \frac{\partial \psi}{\partial y} \quad and \quad v' = -\frac{\partial \psi}{\partial x} \tag{2.35}$$

the continuity equation is satisfied. For some time the temporal stability theory ($\bar{\alpha}$ real, $\bar{\beta}$ complex) was used but the spatial version ($\bar{\alpha}$ complex, $\bar{\beta}$ real) has proven ([15]) to be more representative of the transition problem on airfoils. Despite the fact that the original e^N-method used a temporal approach that was transformed into the spatial form, here the newer approach of using the spatial approach right away, is introduced. For the spatial version β is real and $\bar{\alpha}$ is complex ($\bar{\alpha} = \alpha_r + i\alpha_i$), so that the wavelength $\lambda = \frac{2\pi}{\omega}$ (as $\beta = \beta_r = \omega$) and for the frequency $f = \frac{\omega}{2\pi}$. In this -α_i determines whether the disturbances are unstable, neutrally stable or stable; this corresponds respectively to a positive, zero of negative $-\alpha_i$. Furthermore use is made of the propagation speed c. Using equations 2.32, 2.34 and 2.35 and nondimensionalising using:

$$\bar{u} = \frac{u}{U}; \qquad \bar{y} = \frac{y}{\theta}; \qquad \alpha_* = \bar{\alpha}\theta; \qquad \bar{c} = \frac{c}{U}; \qquad \phi = \frac{\phi}{U\theta} \tag{2.36}$$

The following equation is derived:

$$(\bar{u} - \bar{c})\left[\phi'' - \alpha_*^2 \phi\right] - \bar{u}''\phi = \frac{-i}{(\alpha_* Re_\theta)}\left[\phi'''' - 2\alpha_*^2 \phi'' + \alpha_*^4 \phi\right] \tag{2.37}$$

Equation 2.37 is known as the Orr-Sommerfeld equation([27], [40]). One of the reasons for this equation being difficult to solve stems from the right hand side, as due to the Reynoldsnumber a large coefficient is paired with the highest derivative of the equation. The non trivial solutions of the resulting eigenvalue problem form the basis of the Laminar Stability Theory.

2.3 e^N method

From the Orr-Sommerfeld equation the -α_i value that determines amplification or damping of disturbances can be calculated. An equation can be derived that governs the growth or decay of these disturbances. It follows from the stream function as displayed in 2.34. The amplification ratio of $\frac{a}{a_0}$ where a_0 is the amplification at coordinate x_0 can be displayed as:

$$d(ln(a)) = -\alpha_i \, dx \tag{2.38}$$

or in integral form:

$$ln\left(\frac{a}{a_0}\right) = \int_{x_0}^{x} -\alpha_i \, dx \tag{2.39}$$

or in different notation:

$$\frac{a}{a_0} = e^{\sigma_a} \quad where: \quad \sigma_a = \int_{x_0}^{x} -\alpha_i \, dx \tag{2.40}$$

Where σ_a is an older notation for the amplification factor, which is later renamed N. Then equation 2.40 can be nondimensionalised to:

$$\sigma_a = \frac{U_\infty c}{\nu} \cdot 10^{-6} \cdot \int_{\bar{x}_0}^{\bar{x}} T\bar{U}d\bar{x} \tag{2.41}$$

with:

$$T = \frac{-\alpha_i \theta}{Re_\theta} \cdot 10^6 \tag{2.42}$$

and $\bar{x} = \frac{x}{c}$ with c a constant reference lenght (in airfoils usually the chord) and T the amplification rate. T can be calculated as a function of $\bar{x}$ for a given value of the frequency if the velocity profile and $\frac{U\theta}{\nu}$ are known functions of $\bar{x}$. To calculate the T using the e^N method, the stability diagrams for the specific velocity profile would have to be known.

Many versions of the e^N method exist since its discovery by Smith and Gamberoni [39] and independently by Van Ingen [50]. Different versions exist using sometimes different stabilitydiagrams to calculate T (and thus the σ or N factor). The first version (1956) by Van Ingen employed the stability diagrams by Pretsch([29], [30], [33]). The second version (1965) used still only the Pretsch diagrams, but to widen the application of the method to include suction profiles the assumption was made that all possible stabilitydiagrams with arbitrary pressure gradient and suction form a one parameter family with the critical Reynolds number as a parameter. Later on more stability diagrams were included in the method([23], [45], [54]).

For some time the critical N-factor was assumed to be constant at values between 7 and 10. (a value of 9 is still often the default critical N-factor in many computer applications) The critical N-factor however depends on the flow parameters such as turbulence spectrum in the freestream. A workable method was derived assuming that the critical value of N (or σ) at which transition starts and ends is influenced by the freestream turbulence level (Tu in %) in the following way (from [19]):

$$N_1 = 2.13 - 6.18^{10} log(Tu) \tag{2.43}$$

$$N_2 = 5 - 6.18^{10} log(Tu) \tag{2.44}$$

with N_1 the value at which the transition region starts and N_2 where the transition region ends and the boundary layer is fully turbulent. The freestream turbulence level alone is not sufficient to describe the variation of the N-factor with all possible disturbances. This is due to the fact that not all turbulence

will influence the transition region (due to differences in frequency), and moreover not all disturbing factors may be included in the freestream turbulence level. Most importantly the receptivity of the boundary layer to disturbances originating from outside the boundary layer but also the sound level are not included in the regular turbulence level but both do indeed influence the location of the transition region. By using an effective Tu-level a better correlation can be achieved. This can be defined by comparing the measured and calculated amplification ratios. The critical N-factor will then become a parameter that represents the flowquality of a windtunnel. The N-factor should not be seen as a magic number but be treated as a factor to bring into agreement experiments and theory.

2.4 Finite Difference Method

Apart from integral relations (of which some will be discussed in chapter 4) for the boundary layer, a numerical calculation can be made by means of a finite difference method. The finite difference method discussed here is one made by Van Ingen and an earlier version of this method can be found in [52]. The calculation method remains in principle unchanged, however the more recent version used in this study employs a Richardson extrapolation to reduce the error due to the grid spacing. The basic idea behind this finite difference method will be briefly discussed here. It should be noted that only the laminar form of this method is discussed because in this study it will only be used for laminar boundary calculations. A turbulent form can be made using the eddy viscosity concept. The form of the boundary layer equations used in this method is developed by Görtler [16] and is the same as used in the Smith and Clutter method:

$$f''' + \frac{M+1}{2} f f'' + M\left[1 - (f')^2\right] = x\left[f' \frac{\partial f'}{\partial x} - f'' \frac{\partial f}{\partial x}\right] \tag{2.45}$$

in which the following scaling is used:

$$\eta = \frac{y}{x}\sqrt{\frac{Ux}{\nu}} \tag{2.46}$$

When the streamwise coordinate x is divided in a 1D non-uniform grid and a 3 point form discretization is used (figure 2.1) for an arbitrary variable g one can express $\frac{\partial g}{\partial x}$ at point x_m in the values g_m, g_{m-1} and g_{m-2} as follows:

$$\left(\frac{\partial g}{\partial x}\right)_m = c_0 g_m + c_1 g_{m-1} + c_2 g_{m-2} \tag{2.47}$$

with:

$$\begin{aligned} c_0 &= \frac{1}{d_1} + \frac{1}{d_3} \\ c_1 &= -\frac{d_3}{d_1 d_2} \\ c_2 &= \frac{d_1}{d_2 d_3} \end{aligned} \tag{2.48}$$

The 2-point approximation, shown in figure 2.2, which is used in the startup of the calculation can also be expressed in the three point form as shown in equation 2.47 but now using coefficients as shown in

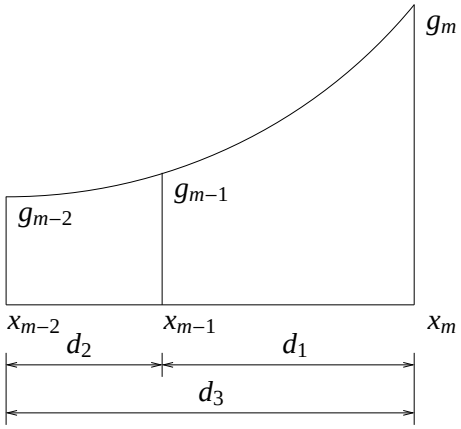

Figure 2.1: 3 point approximation

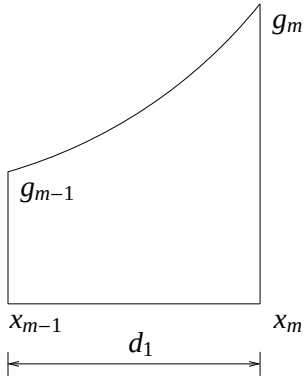

Figure 2.2: 2 point approximation

2.49:

$$\begin{aligned} c_0 &= \frac{1}{d_1} \\ c_1 &= -\frac{1}{d_1} \\ c_2 &= 0 \end{aligned} \tag{2.49}$$

Then:

$$\left(\frac{\partial f}{\partial x}\right)_m = c_0 f_m + c_1 f_{m-1} + c_2 f_{m-2} \tag{2.50}$$

$$\left(\frac{\partial f'}{\partial x}\right)_m = c_0 f'_m + c_1 f'_{m-1} + c_2 f'_{m-2} \tag{2.51}$$

and introducing these equations into equation 2.45 leads to:

$$f'''_m + \left[\frac{M+1}{2} f_m + c_0 x f_m + c_1 x f_{m-1} + c_2 x f_{m-2}\right] f''_m + \left[-c_1 x f'_{m-1} - c_2 x f'_{m-2}\right] f'_m + M - [M + c_0 x](f'_m)^2 = 0 \tag{2.52}$$

This equation can be linearized and reduced to a linear, second order differential equation written as:

$$\bar{u}''_m + S_1 \bar{u}'_m + [S_2 + 2\tilde{u}_m S_3]\,\bar{u}_m = -M + (\tilde{u}_m)^2 S_3 \tag{2.53}$$

with:

$$\begin{aligned} S_1 &= \frac{M+1}{2} f_m + c_0 x f_m + c_1 x f_{m-1} + c_2 x f_{m-1} \\ S_2 &= -c_1 x \bar{u}_{m-1} - c_2 x \bar{u}_{m-2} \\ S_3 &= -M - c_0 x \end{aligned} \tag{2.54}$$

and when writing:

$$\begin{aligned} P(\eta) &= S_1 \\ Q(\eta) &= S_2 + 2\tilde{u}_m S_3 \\ R(\eta) &= -M + (\tilde{u}_m)^2 S_3 \end{aligned} \tag{2.55}$$

the equations can be put into a 3-diagonal system of equations, easily solved by the Thomas algorithm. The Thomas algorithm solves a tri-diagonal system of equations by changing the system into an upper bidiagonal system. This is done by changing the main diagonal term and the right hand side of each equation. Then the last equation of the system will be solvable, as it has only one unknown. From that the other equations can be solved. A good and detailed description of the Thomas algorithm can be found in [3].

To decrease the error due to the spacing of the points through the boundary layer at which the solution is obtained, a Richardson extrapolation is used. This was not used in the finite difference method described in [52]. In this method any three grids can be used as long as the ratio to the coarsest grid are 2 and 4 for respectively the second and third grids. The author used for the first and coarsest grid 201 evenly spaced points resulting in 200 intervals. The second grid consists of 401 points and the third of 801 points. By decreasing the cell size by a factor 4 and applying the Richardson extrapolation twice, the order of the total method is increased from h^2 to h^6. The formula for u using the Richardson extrapolation is as follows:

$$u_{extrap} = \frac{64u_4(4n-3) - 20u_2(2n-1) + u_1(n)}{45} \tag{2.56}$$

In this u_4 stands for the u as calculated in grid 4, and so on. Please note that in using splines in this method these splines are the limiting factor in the numerical accuracy.

2.4.1 Solution procedure

The solution procedure is such that at the start for the first point a Falkner-Skan profile is assumed. From equation 2.52 it follows that at $x = 0$ the right hand side is taken out of the equation and the solution starts as a member of the Falkner-Skan family. For the second point the same Falkner-Skan velocity profile is assumed. This can also be explained using 2.52, as for x is small, and if the behaviour of the righthand side term is regular, the solution will be nearly the same as that for $x = 0$. For airfoils this method is accurate enough, for some other cases a series solution near $x = 0$ has been derived. From here the 2-point form can be used to acquire the third point and from that onwards the three point form is used. For every station a first guess for $\bar{u_m}$ for the start of the iteration is made. For the first and second point this is the value supplied by the starting profile and for the third point a linear extrapolation from the first two points is used. From the third point onwards a linear extrapolation based on the two previous points is used. This approximation is then improved by the iteration process.

The skin friction is determined by:

$$c_f = \frac{\tau_0}{\frac{1}{2}\rho U^2} = \frac{2f''(0)}{\sqrt{\frac{Ux}{\nu}}} \tag{2.57}$$

$f''(0)$ is used to characterize the wall shear stress as a function of x. $f''(0)$ is determined by fitting a fourth degree polynomial through the 5 points closest to the wall. The other boundary layer variables (δ^*,θ and H) are determined from the calculated velocity profile. A check is performed to make sure

that in the next step no separation will be encountered, because due to the Goldstein singularity no accurate boundary layer solution can be acquired there. In this method the squared value of τ_0 is used to ease the extrapolation to $\tau_0 = 0$. The separation point is approached using small steps in x and by making sure $\tau_0 > 0.0001$.

Chapter 3

The improved e^N method

3.1 Introduction

In this chapter the newly made improved e^N method will be discussed. This method has been developed by prof. Van Ingen with assistance from the author. Like similar developments the method did not emerge suddenly in it's present form but has been the result of an idea that evolved due to new insights and elaborate testing and will continue to do so. In this process frequent communication and cooperation between prof. Van Ingen and the author, while simultaneously implementing and testing the new method in different programming languages, has led to the method in it's present form. The full description of the method can be found in a yet to appear publication by prof. Van Ingen. The following chapter is based on information from a draft version of the publication [53] by Van Ingen and from many private conversations between the author and prof. Van Ingen. References to this article refer to the draft version where the improved e^N-method is discussed in full. Here the new method will be discussed in a slightly more condensed form.

3.2 Characteristic parameter

In Van Ingen [51] the working hypothesis was made that all stability diagrams can be assumed to form a one-parameter family with the critical Reynolds number ($Re_{\theta_{crit}}$, with as reference length the momentum thickness θ) as the parameter. Some supporting arguments were given in [51], these will be reproduced in [53]. The $Re_{\theta_{crit}}$ value is the lowest value of Re_θ for which one or more frequencies become unstable. The critical Reynolds number was related to a suitable form parameter of the velocity profile, using Lin's approximate formula [35]. Now a different characteristic parameter is sought to correlate an arbitrary boundary layer to this critical Reynolds number in order to find the corresponding stability diagram. Only then can one calculate the amplification of disturbances and the transition point for an arbitrary boundary layer. In the first version of the e^N-method only stability diagrams were available for the Hartree solutions of the Falkner-Skan equation. At that time, a correlation was made between β and λ (from the Pohlhausen method) to correlate the stability diagrams

made by Pretsch of the Hartree boundary layers to other boundary layers. In the improved method more stability diagrams are available, and because β as the characteristic parameter does not allow suction profiles it cannot be used here. Many workers have used the velocity profile shape parameter H to correlate with the critical Reynolds number. Some research was done to find a better parameter.

The Orr-Sommerfeld equation found in 2.37 depends highly on both the velocity profile as well as the curvature profile of the boundary layer as can be seen from the $\overline{u}$ and $\overline{u}''$ present in the left hand side of the Orr-Sommerfeld equation in 2.37. Also it is visible in the stability diagrams as a velocity profile with an inflection point has a finite value for the amplification rate as $Re_\theta \to \infty$ while the amplification rate goes to zero when such an inflection point is absent.

The shape factor is known to correlate well for the velocity profile, but there is some uncertainty about it when the curvature profile is considered. Could perhaps a parameter connected to the curvature function as the correlation parameter? Starting with the curvature it will be shown here that using the curvature profile is inadequate for this use. The nondimensional curvature and slope at the wall are denoted by

$$m_T = \left(\frac{\partial^2 \overline{u}}{\partial \overline{y}^2}\right)_{y=0}; \qquad l = \left(\frac{\partial \overline{u}}{\partial \overline{y}}\right)_{y=0} \tag{3.1}$$

In figure 3.1 a graph (taken from [52]) shows the Hartree parameters l and m_T. In the graph it can be seen that the Hartree curve for m_T has a range smaller than necessary to account for other boundary layers such as occur for $\overline{U} = 1 - \overline{x}^n$. Therefore using m as the characteristic parameter is not possible, as it simply cannot account for all occurring boundary layers.

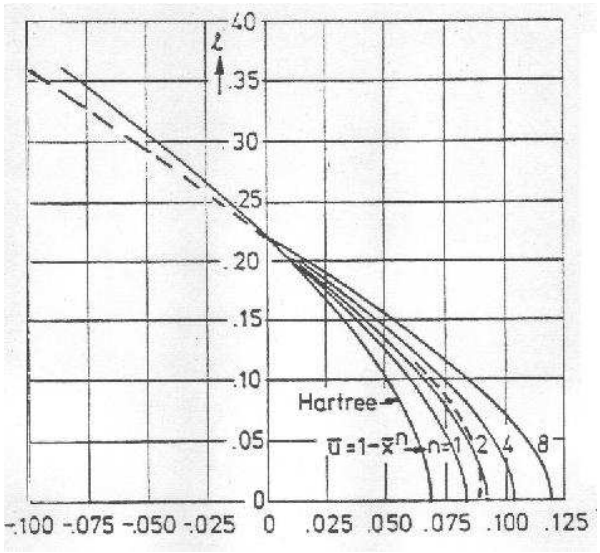

Figure 3.1: m vs l for Hartree and $\overline{u} = 1 - \overline{x}^n$

As an alternative for the curvature then the shape parameter H is considered. It has been used already in this fashion and there is some support for using the shape parameter as the characteristic parameter. This gives good correlation for the velocity, but the quality of correlation is unknown for the curvature profile. When using the boundary layer equation in the form of 2.10 and using the continuity equation

2.6:

$$u\frac{\partial u}{\partial x} + v\frac{\partial u}{\partial y} = U\frac{dU}{dx} + \nu\frac{\partial^2 u}{\partial y^2} \tag{3.2}$$

$$\frac{\partial u}{\partial x} + \frac{\partial v}{\partial y} = 0 \tag{3.3}$$

and one wants to focus on the wall curvature, using

$$y = 0 \qquad u = 0 \qquad v = v_0 \tag{3.4}$$

then equation 3.2 becomes:

$$v_0\left(\frac{\partial u}{\partial x}\right)_0 = U\frac{dU}{dx} + \nu\left(\frac{\partial^2 u}{\partial y^2}\right)_0 \tag{3.5}$$

if this is non dimensionalised with:

$$\bar{u} = \frac{u}{U} \qquad \bar{y} = \frac{y}{\theta} \qquad l = \left(\frac{\partial \bar{u}}{\partial \bar{y}}\right)_0 \qquad m = \left(\frac{\partial^2 \bar{u}}{\partial \bar{y}^2}\right)_0 \qquad K = \frac{\theta^2}{\nu}\frac{dU}{dx} \qquad w = \frac{v_0\theta}{\nu} \tag{3.6}$$

This leads to:

$$w \cdot l = K + m_T \tag{3.7}$$

which means that without suction ($w = 0$):

$$m_T = -K = -\frac{\theta^2}{\nu}\frac{dU}{dx} \tag{3.8}$$

and if one differentiates 3.2 with respect to y and uses 3.3, one finds for $y = 0$:

$$v_0\left(\frac{\partial^2 u}{\partial y^2}\right)_0 = \nu\left(\frac{\partial^3 u}{\partial y^3}\right)_0 \tag{3.9}$$

so that:

$$w \cdot m_T = \left(\frac{\partial^3 \bar{u}}{\partial \bar{y}^3}\right)_0 \tag{3.10}$$

This means that:

$$\left(\frac{\partial^3 \bar{u}}{\partial \bar{y}^3}\right)_0 = 0 \quad , for\ zero\ suction \tag{3.11}$$

This means that the third derivative of u to y is always zero for boundary layers without suction, irrespective of the pressure gradient. Then the curvature m will have a vertical tangent when plotted in a $m, \bar{y}$ diagram. With this in mind, some suction boundary layers are observed. As an example a series of solutions of the Falkner-Skan equation is created for the boundary layer velocity and curvature profiles using a flat plate boundary layer with suction and blowing. 22 of these solutions were created in the range of H-values from 2.2 to 4, thus comparable to the full range Hartree profiles. The results compare very well, when the H value is made to be (nearly) equal. The exact values of H for both the Hartree solution with suction/blowing and with the pressure gradient for 4 representative cases are shown in table 3.1 The velocity profile looks very similar, and maybe even more important the curvature profile is very similar in a large region as well. The only appreciable difference is in the curvature profile near the wall, and this difference gets increasingly larger for larger values of H. As was shown, the third derivative of $\bar{u}$ with respect to y is zero for non-suction boundary layers and can

be non-zero for suction boundary layers. How this difference in curvature close to the wall influences the solutions of the Orr-Sommerfeld equation and therefore the comparison of the stability diagram is as yet unknown. Specific calculations solving the Orr-Sommerfeld equation for both curvature profiles (for a number of cases) can provide an answer to this, but this is found to be beyond the scope of this study. 4 representative cases from the 22 studied can be seen in figures 3.3 through 3.9 of which the first four figures show velocity plots of cases 6, 17, 20 and 22, and the latter four show the curvature plot of these cases. As case 17 represents the flat plate, no suction or blowing is applied. The great similarities in both the velocity and curvature profiles strengthen the case for using H as the characteristic parameter, which will be used as such in the Improved e^N-method. Figure 3.10 shows the correlation between ${}^{10}log(Re_{\theta_{crit}}) - H$. The curve is made up from a ${}^{10}log(Re_{\theta_{crit}})$ of 4.3642 for $H = 2$, as calculated by Hughes [21] and 15 values for ${}^{10}log(Re_{\theta_{crit}})$ for 15 different shapefactors as calculated by Arnal ([4]).

Table 3.1: *H* for Hartree solutions

case #	*H* pressure	*H* for suction/blowing employed on a flat plate
6	2.2696	2.2696
17	2.5911	2.5911
20	3.0909	3.0909
22	4.0995	4.1010

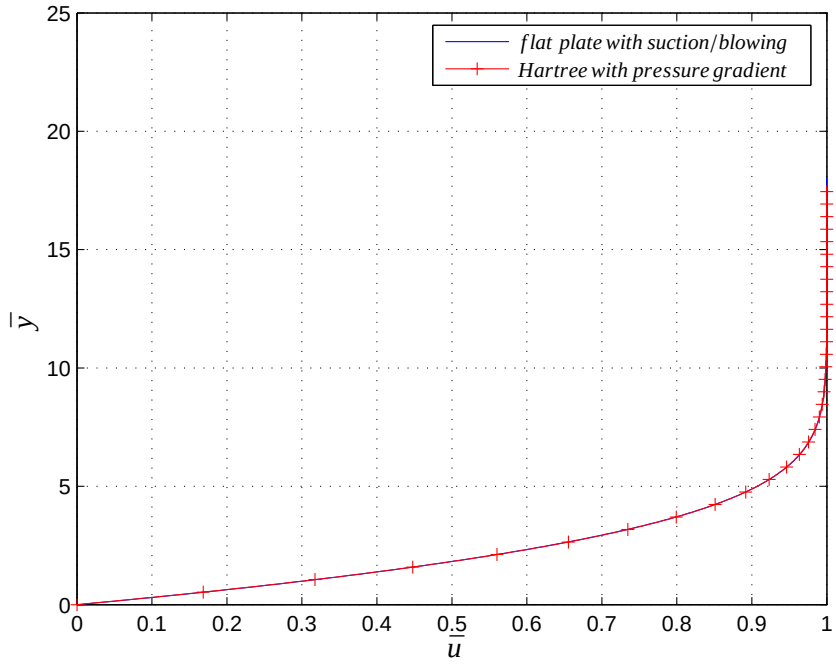

Figure 3.2: Hartree case 6, velocity

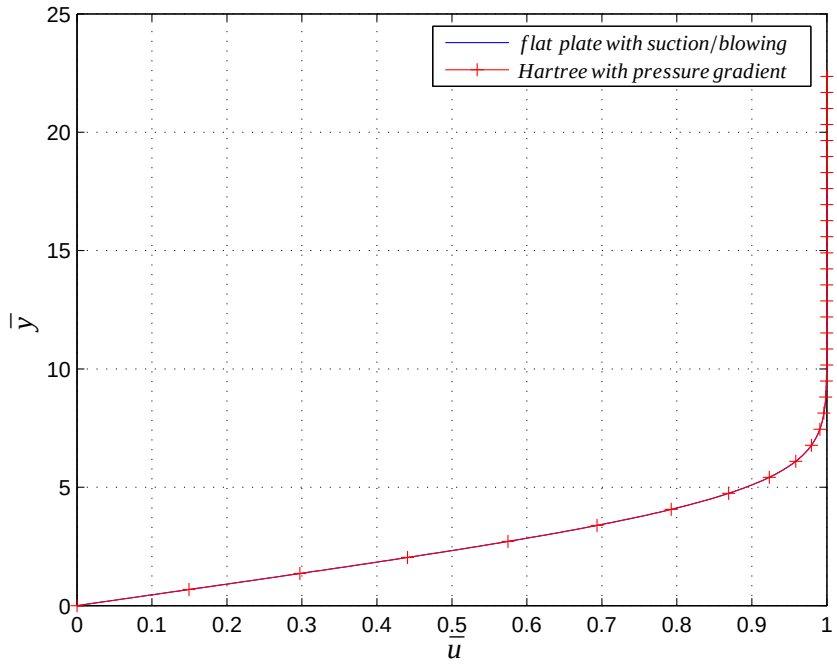

Figure 3.3: Hartree case 17, velocity

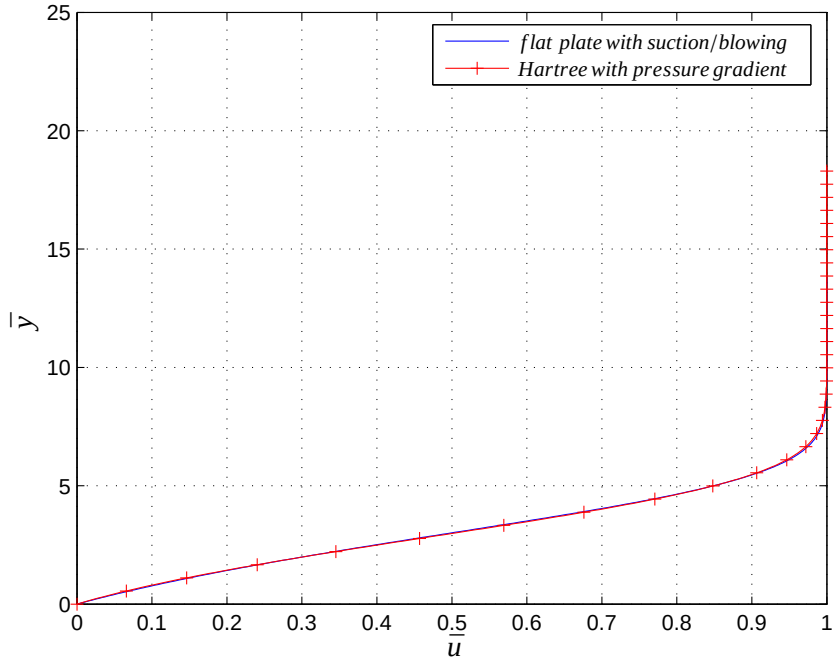

Figure 3.4: Hartree case 20, velocity

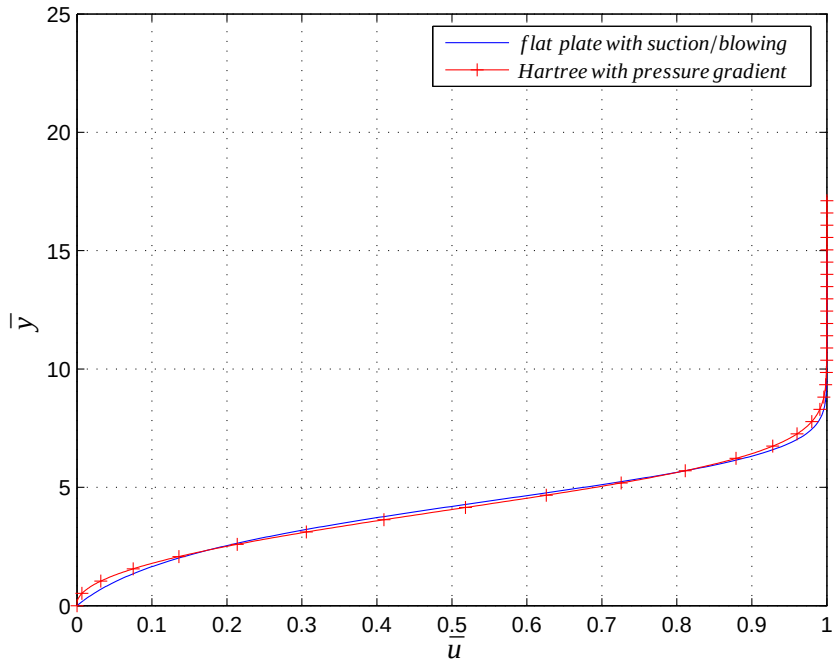

Figure 3.5: Hartree case 22, velocity

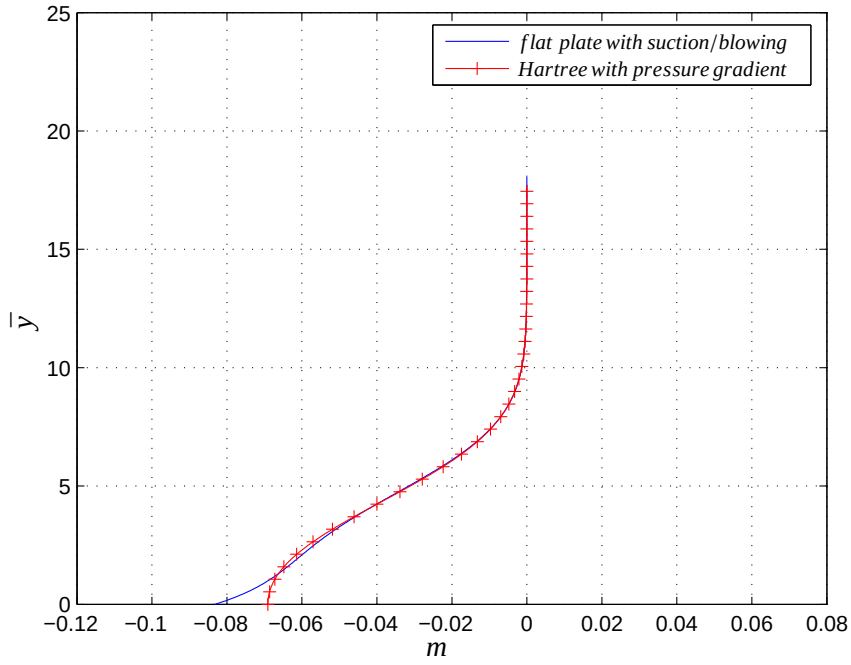

Figure 3.6: Hartree case 6, curvature

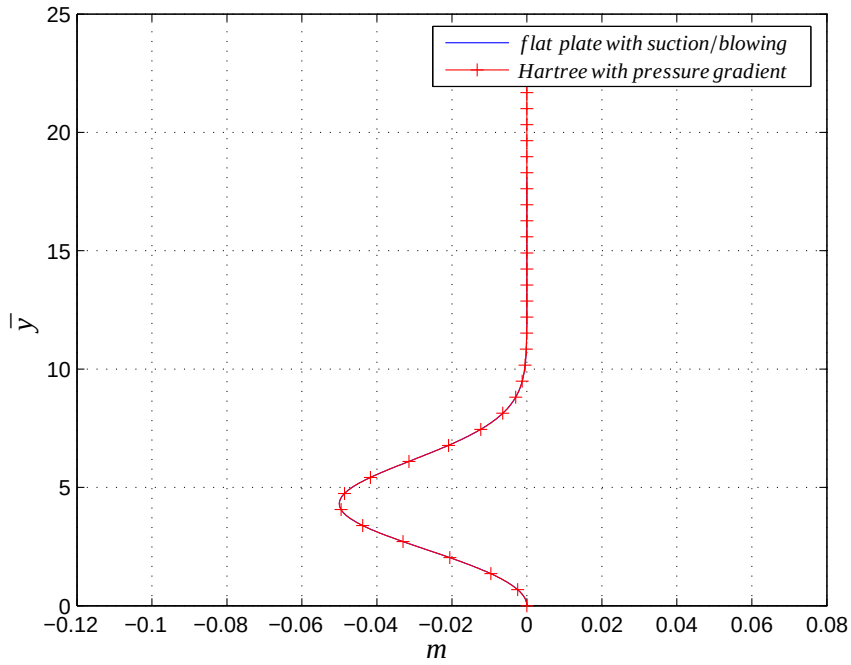

Figure 3.7: Hartree case 17, curvature

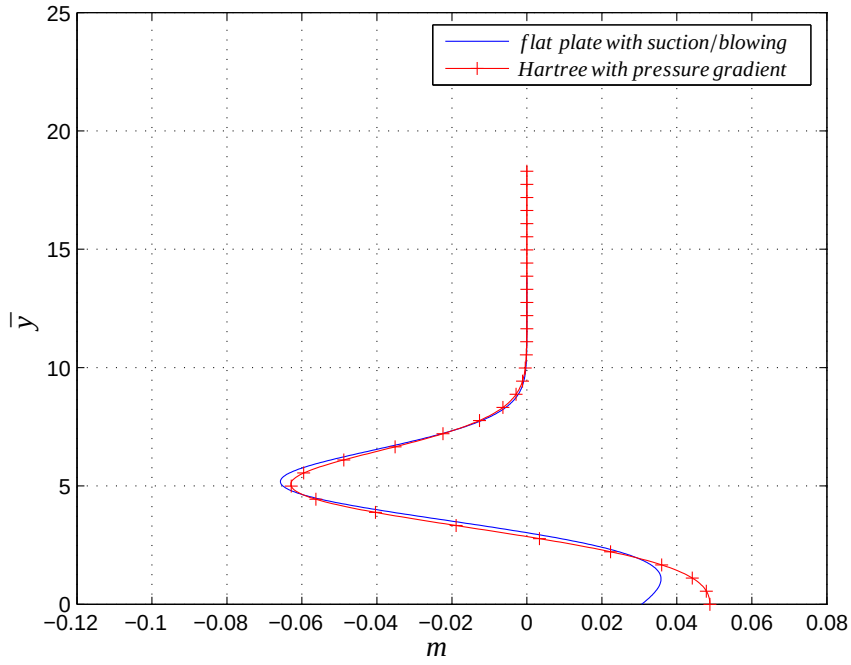

Figure 3.8: Hartree case 20, curvature

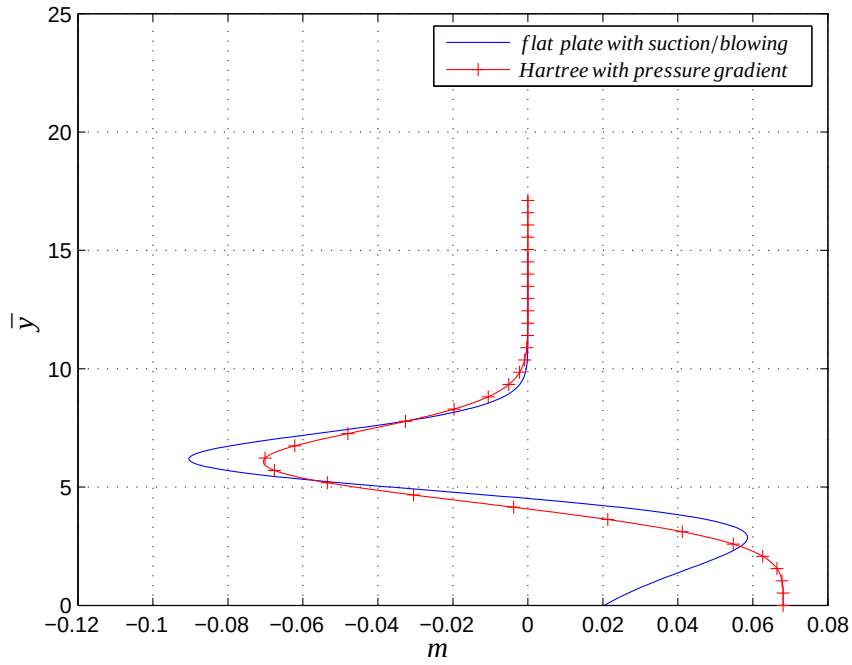

Figure 3.9: Hartree case 22, curvature

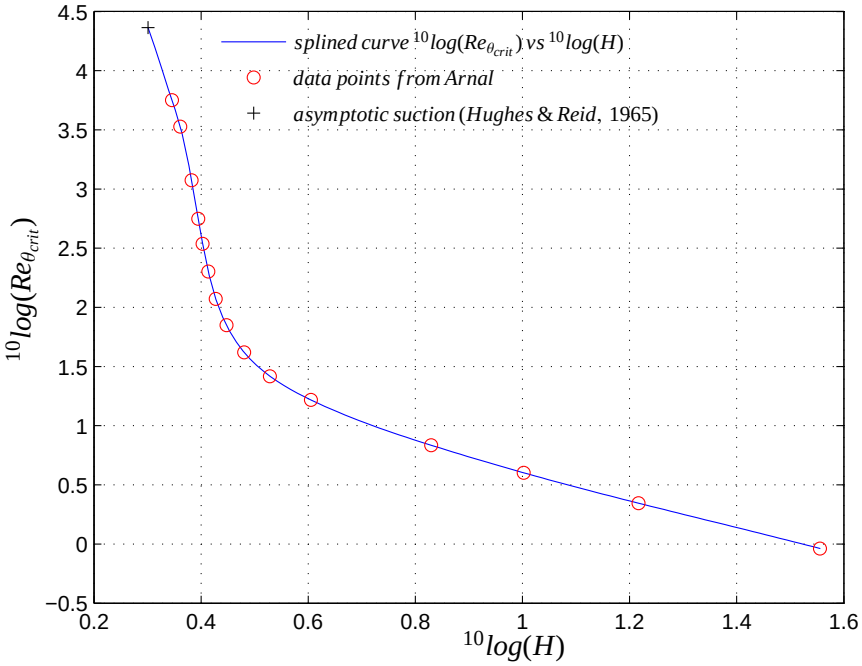

Figure 3.10: correlation between $^{10}log(Re_{\theta_{crit}})$ and $^{10}log(H)$

3.3 Basic concept

The improved e^N method is based on the well known e^N method in the spatial form. In section 2.3 the original e^N-method was already discussed but using some slightly different (older) notations. The most important equations are therefore repeated here with the newer notations. In the spatial form the amplification of disturbances grows as $e^{-\alpha_i x}$. For the ratio of amplitudes between station x_1 and x_2 one can write:

$$ln\left(\frac{a}{a_0}\right) = \int_{x_1}^{x_2} -\alpha_i \, dx \tag{3.12}$$

from this equation the N-factor (the former σ) can be written:

$$N = ln\left(\frac{a}{a_0}\right) = \int_{x_{instab}}^{x} -\alpha_i \, dx \tag{3.13}$$

with x_{instab} is the value of x for a specific frequency at which this frequency becomes unstable. Then

$$N = \int_{x_{instab}}^{x} \frac{-\alpha_i \theta}{\theta} \frac{U}{U} \frac{U_\infty}{U_\infty} c \, d\left(\frac{x}{c}\right) \tag{3.14}$$

so that:

$$N = \frac{U_\infty c}{\nu} \cdot 10^{-6} \int_{x_{instab}}^{x} \frac{-\alpha_i \theta}{Re_\theta} \cdot 10^6 \frac{U}{U_\infty} \, d\left(\frac{x}{c}\right) \tag{3.15}$$

Which can be written as:

$$N = Re_{c_{reduced}} \int_{x_{instab}}^{x} T \cdot \bar{U} \, d\bar{x} \tag{3.16}$$

with:

$$Re_{c_{reduced}} = \frac{U_\infty c}{\nu} \cdot 10^{-6} \tag{3.17}$$

$$T = \frac{-\alpha_i \theta}{Re_\theta} \cdot 10^6 \tag{3.18}$$

$$\bar{U} = \frac{U}{U_\infty} \tag{3.19}$$

$$d\bar{x} = d\left(\frac{x}{c}\right) \tag{3.20}$$

This improved e^N method is a database method. The data used for this method come from stability calculations performed by Arnal [4]. These calculations give values of $\alpha_i \delta^*$ for 15 values of H (ranging from $H = 2.216$ to $H = 35.944$) with cross-cuts for 13 to 19 different values of R_{δ^*}, and all of this for up to 33 different frequencies denoted as $\frac{\omega \delta^*}{U}$ and as $\frac{\omega \nu}{U^2}$. These variables are converted so that for the amplification rate we use T instead of $-\alpha_i \theta$, for the boundary layer Reynolds number we use Re_θ and for the frequencies we use $\frac{\omega \theta}{U}$ and $\frac{\omega \nu}{U^2}$. For the latter frequency sometimes the logarithmic value

$^{10}log(\frac{\omega\nu}{U^2})$ is used. Please note that no suction boundary layers are included in the data from Arnal. A summary of the different boundary layer calculated by Arnal is shown in table 3.2. Added to these 15 cases is the asymptotic suction profile. Although no stability diagram is available for this profile, the scaling parameters for this are available and will be used later on.

Table 3.2: summary for data from Arnal

case #	H	$^{10}log(Re_{\theta_{crit}})$	description	inflection point present?
0	2.000	4.3643	asymptotic suction	no
1	2.216	3.7514	stagnation point	no
2	2.297	3.5279		no
3	2.411	3.0738		no
4	2.481	2.7479		no
5	2.529	2.5371		no
6	2.591	2.3024	flat plate	no
7	2.676	2.0711		yes
8	2.802	1.8487		yes
9	3.023	1.6198		yes
10	3.378	1.4179		yes
11	4.029	1.2174	separated flow	yes
12	6.752	0.8352		yes
13	10.056	0.6019		yes
14	16.467	0.3455		yes
15	35.944	-0.0378		yes

The converted data from Arnal can be scaled and represented in a way that makes it possible to store the data in splines which can be easily interpolated and extrapolated. In the following this will be explained using some schematic diagrams. In figure 3.11 one can see 2 neutral stability curves in a $\frac{\omega\theta}{U} - Re_\theta$ plane showing schematic representation of a stability diagram of boundary layers with and without an inflexion point. Also some typical graphs will be shown, these are taken from the flat plate stability diagram.

A typical stability diagram for an arbitrary $Re_{\theta_{crit}}$ is shown in figure 3.12 with several cross-cuts at the dotted lines, representing the data by Arnal and the critical Re_θ number of this particular curve. The values of $Re_{\theta_{crit}}$ will later be correlated with the shape factor in accordance with section 3.2.

Then this curve is scaled by using a different coordinate at the horizontal axis. The coordinate used is:

$$r = ^{10} log(Re_\theta) - ^{10} log(Re_{\theta_{crit}}) \tag{3.21}$$

This means that for negative values of r the T will be negative as well. The stability diagram will look as shown in figure 3.13.

In figure 3.14 a typical shape of the amplification data in the $T - \frac{\omega\theta}{U}$ plane is shown. For all cross-cuts at different Re_θ, then the maximum value of T, called T_{max}, is determined. The lines on which the points of T_{max} lie for each case will be called the *axis* and is shown in figure 3.15.

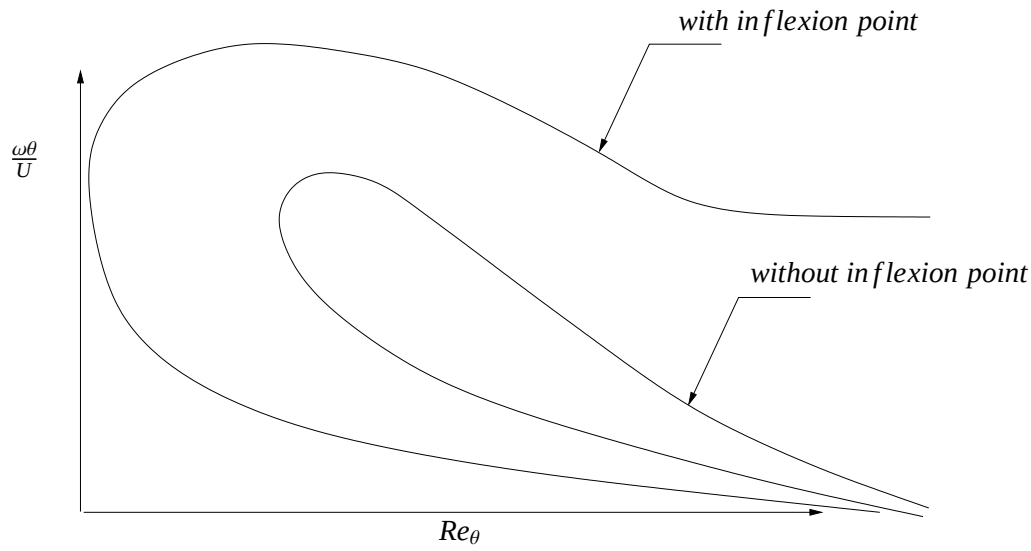

Figure 3.11: Stability diagrams with and without inflexion point

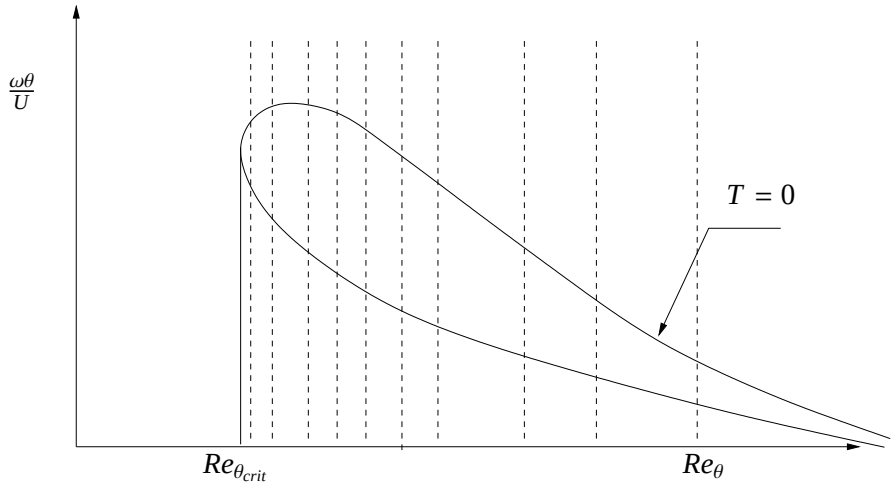

Figure 3.12: Basic data

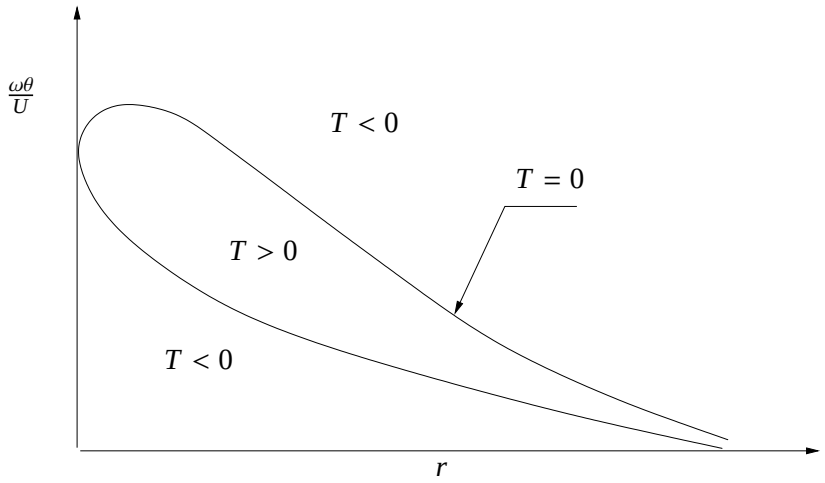

Figure 3.13: Shifted stability diagram

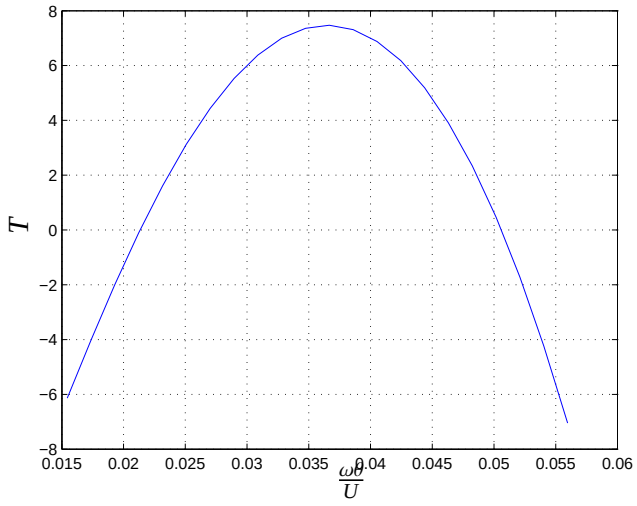

Figure 3.14: Crossection of stability diagram

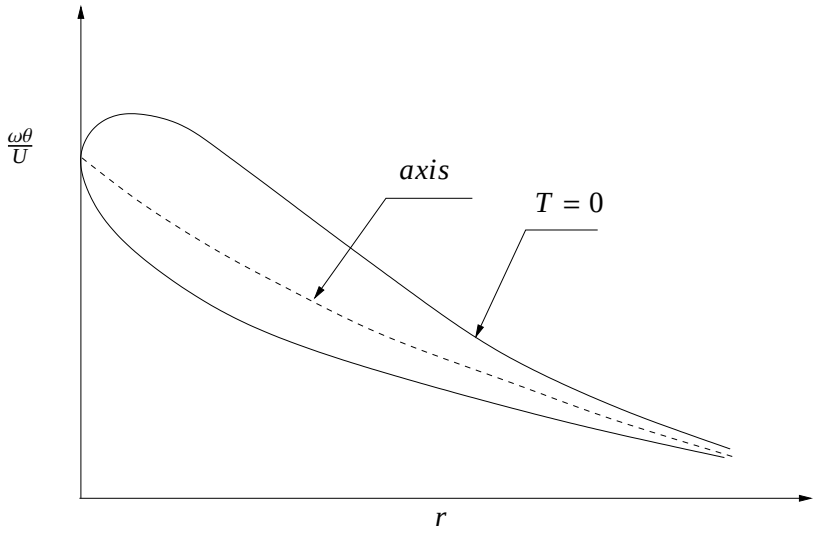

Figure 3.15: locations of T_{max} values on axis

The values of T_{max} on this *axis* in the $T-r$ diagram are plotted in figure 3.16. A T_{maxmax} can be found that is the global maximum of T for that case (i.e. that specific value of $Re_{\theta_{crit}}$). So there will be 15 values of T_{maxmax} for the 15 cases present in the data plus a value for the asymptotic suction profile.

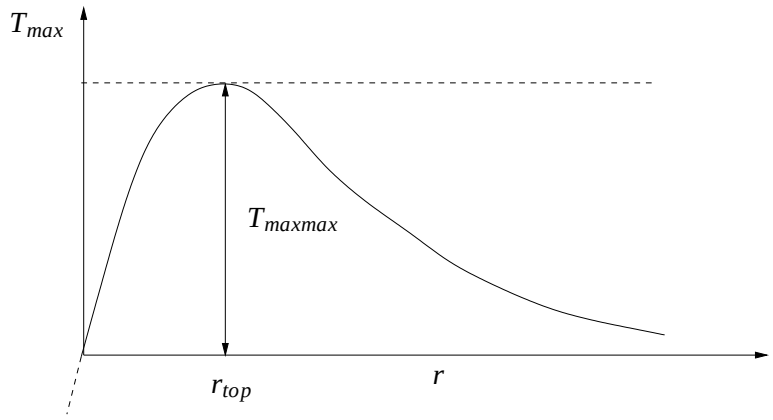

Figure 3.16: diagram of all T_{max} for 1 case

Now one can scale the curve of figure 3.16 in vertical direction as $\frac{T_{max}}{T_{maxmax}}$ and in horizontal direction with $\frac{r}{r_{top}}$ so that figure 3.17 appears. Although the 15 (+1) cases look very much alike when scaled, the T_{maxmax} values differ greatly in reality. The range for T_{maxmax} runs from around .1 to over 5000. A curve for T_{maxmax} and a curve for r_{top} with respect to $Re_{\theta_{crit}}$ are stored in splines. When putting the axes of the cases together in a logarithmic plot in the ${}^{10}log\left(\frac{\omega\nu}{U^2}\right) - r$ plane these axes will be straight lines. Now yet again a scaling is used to account for differences in frequency where the maximum value for $\alpha_i\theta$ (and thus for T) occurs. The scaling used is the distance from the "top" of the stability diagram (with the value of T_{maxmax}) to the frequency where for the same $\overline{r}$, T becomes zero (so on the neutral curve). Figure 3.18 shows this scaling parameter now called $\left(\frac{\omega\theta}{U}\right)_{scale}$.

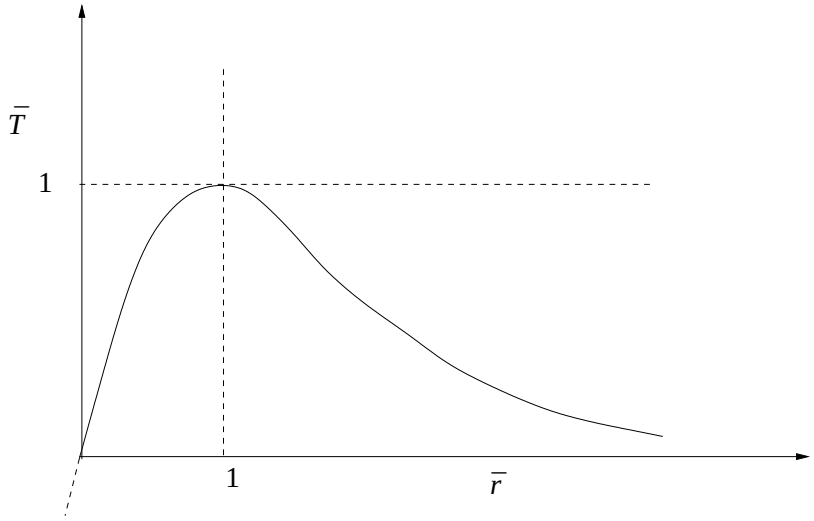

Figure 3.17: scaled diagram of all T_{max} for 1 case

For the frequency, F_∞ is used that is defined as 601 logarithmically spaced values between 10^{-7} and 10^{-1} with:

$$F_\infty = \frac{\omega\nu}{U_\infty^2} \tag{3.22}$$

The frequency $\frac{\omega\theta}{U}$ is determined by multiplying F_∞ by the present values for Re_θ and $\left(\frac{U_\infty}{U}\right)^2$. By using so many frequencies almost in every case there are enough frequencies between $-2 \leq \overline{\left(\frac{\omega\theta}{U}\right)} \leq 3$, which is the range of interest for our calculations. Almost always this is sufficient to give an accurate description of the amplification rate but for some very small values of H combined with high values for Re_θ too few frequencies are available for this range so that the range has to be expanded.

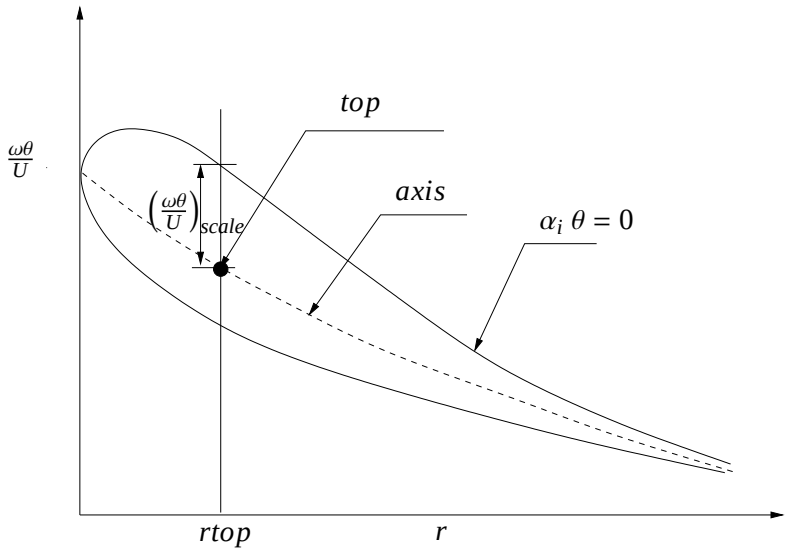

Figure 3.18: location of top and $\left(\frac{\omega\theta}{U}\right)_{scale}$ in stability diagram

Then the crosscut curves are plotted versus the new parameter that also scales it against each points

local value of $\left(\frac{\omega\theta}{U}\right)_{axis}$, defined as equation 3.23.

$$\overline{\left(\frac{\omega\theta}{U}\right)} = \frac{\left(\frac{\omega\theta}{U}\right) - \left(\frac{\omega\theta}{U}\right)_{axis}}{\left(\frac{\omega\theta}{U}\right)_{scaled}} \tag{3.23}$$

The effect of this can be seen in the typical figures 3.19 and 3.20. These curves have some resemblance to parabolic functions, but are in fact not exactly so. Therefore splines were favoured over an analytical representation to store these curves.

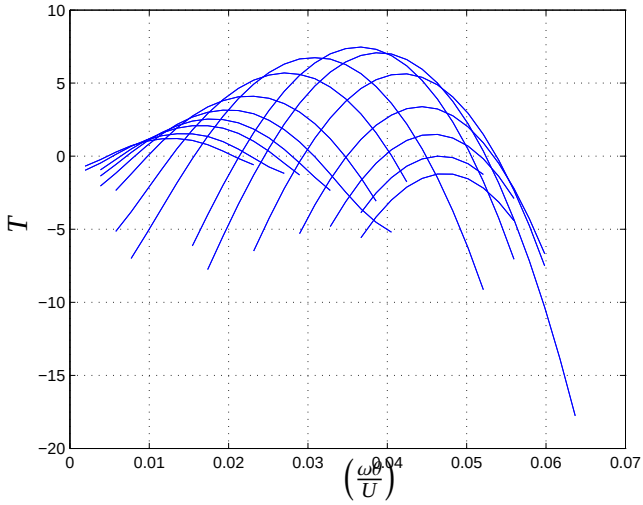

Figure 3.19: cross-cut curves in $\left(\frac{\omega\theta}{U}\right)$ and T

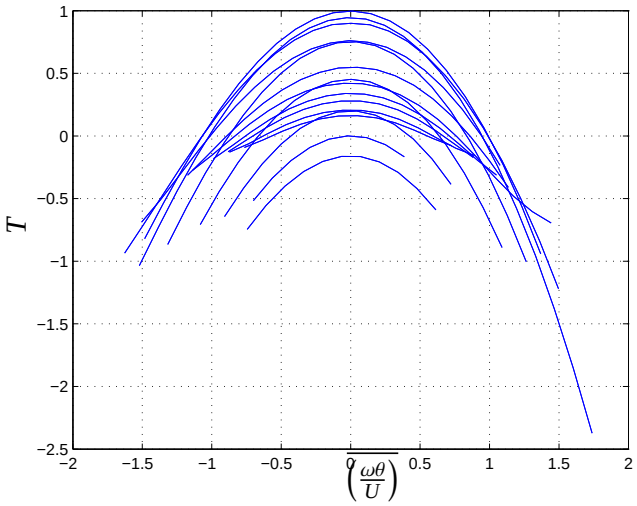

Figure 3.20: cross-cut curves in $\overline{\left(\frac{\omega\theta}{U}\right)}$ and T

After this all the curves are shifted down a distance T_{max} (each over it's own T_{max}) so that all maximum values end up at the horizontal axis. This makes the final scaling on this axis to be as shown in equation

3.24.

$$\bar{T} = \frac{T - T_{max}}{T_{maxmax}} \tag{3.24}$$

The graphical representation can be seen in figure 3.21.

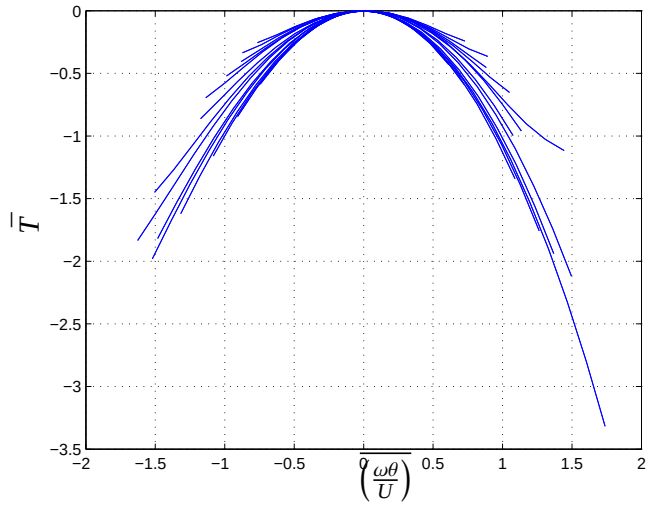

Figure 3.21: cross-cut curves in $\overline{\left(\frac{\omega\theta}{U}\right)}$ and $\bar{T}$

All shifting and converting of the data provided by Arnal is essentially done by only a few parameters. These scaled and converted variables are stored in splines. The advantage of storing these parameters in splines is that it is then easy to interpolate and to extrapolate. For extrapolation in the frequency, as in some applications the values of $\left(\frac{\omega\theta}{U}\right)$ fall outside the $-2 < \left(\frac{\omega\theta}{U}\right) < 3$ interval, the splines are forced to be linear functions near the endpoints as extrapolation of a spline will give faulty results due to the fact that the 2^{nd} and 3^{rd} order terms are only meaningful on the interval in which the spline is generated. These stored variables can be subdivided in three groups:

- Variable $\bar{T}$ is the main variable in this method, it stands for the amplification rate. It is defined in almost the whole of the data area and has a different value for each different r and $Re_{\theta_{crit}}$ and is stored in splines. In figure 3.22 each circle represents an Arnal datapoint. Then the splines are interpolated and redistributed in the r direction, to ease the use of the splines and to make sure an accurate description of the stability diagram for each case is made. Therefore a 1-D Lagrangian interpolation is used to find 59 distributed splines from the Arnal data and the extrapolated Arnal data. The 1-D Lagrange interpolation is shown in equation 3.25.

$$\begin{aligned} Y(i) &= c_1x_1 + c_2x_2 + c_3x_3 \\ c_1 &= \frac{(x_i - x_2)(x_i - x_3)}{(x_1 - x_2)(x_1 - x_3)} \\ c_2 &= \frac{(x_i - x_1)(x_i - x_3)}{(x_2 - x_1)(x_2 - x_3)} \\ c_3 &= \frac{(x_i - x_1)(x_i - x_2)}{(x_3 - x_1)(x_3 - x_2)} \end{aligned} \tag{3.25}$$

  with x_i the value to be interpolated and $x_1 \leq x_i \leq x_3$. It can be seen (figure 3.22) that not the whole range of r is filled with data points, especially for the cases with a higher value of $Re_{\theta_{crit}}$. To remedy this, an extrapolation is made into the higher r values. The T_{max} curve can be easily extrapolated (using $T_{max} = \bar{r}e^{1-\bar{r}}$), and the shape of the $\bar{T}$ curve is taken to be similar to that of the last known $\bar{T}$ splines. The extrapolation of *axis* is a bit more difficult. This is because *axis* is a straight line when plotted in a logarithmic scale, with a kink in it for velocity profiles with an inflexion point. Before the kink the slope is about $-\sqrt{2}$, after is the slope is -1. Figure 3.23 shows these kinks for the cases with an inflexion point, that is cases 7 through 15. These cases are the ones for which the α_i will not go to zero for $Re_\theta \to \infty$, but as $T = -\frac{\alpha_i\theta}{Re_\theta}$, T will go to zero for $Re_\theta \to \infty$. The location of these kinks have been made into a function, as the data from Arnal does not specifically locate these kinks.

  In figure 3.24 the result is shown. With this the dataset for $\bar{T}$ in r direction is now defined from $0 < r < 2.5$. Frequency wise the curves in the $T - \frac{\omega\theta}{U}$ plane faintly resemble parabolic functions, and these are all defined in the range of $-2 < \frac{\omega\theta}{U} < 3$. But because of the scaling of the frequency at large values of Re_θ and corresponding low values of $\left(\frac{\omega\theta}{U}\right)_{scaled}$ the $\left(\overline{\frac{\omega\theta}{U}}\right)$ values can grow to up to 16.000. To account for such large values of $\left(\overline{\frac{\omega\theta}{U}}\right)$ the stability curve in the $T - \left(\overline{\frac{\omega\theta}{U}}\right)$ plane needs to be extrapolated. Due to the approximately linear behaviour near $\left(\overline{\frac{\omega\theta}{U}}\right) = 3$ of this curve a linear extrapolation is used. Please note that this area of the stability diagram is hardly used. Most boundary layer flows have transitioned to turbulent boundary layer flow long before they reach the values of Re_θ necessary for these high (scaled) frequencies. However as the choice of

frequency in which to evaluate the data is not case specific a large number of frequencies will be calculated every time to accommodate almost all possible cases.

A combination of all $\overline{T}$ values for one $Re_{\theta_{crit}}$ value make up the stability diagram and can be represented as spanning a (3D) surface in the $\frac{\omega\theta}{U} - r - T$ space. A visualization of T for the flat plate case can be seen in figure 3.25.

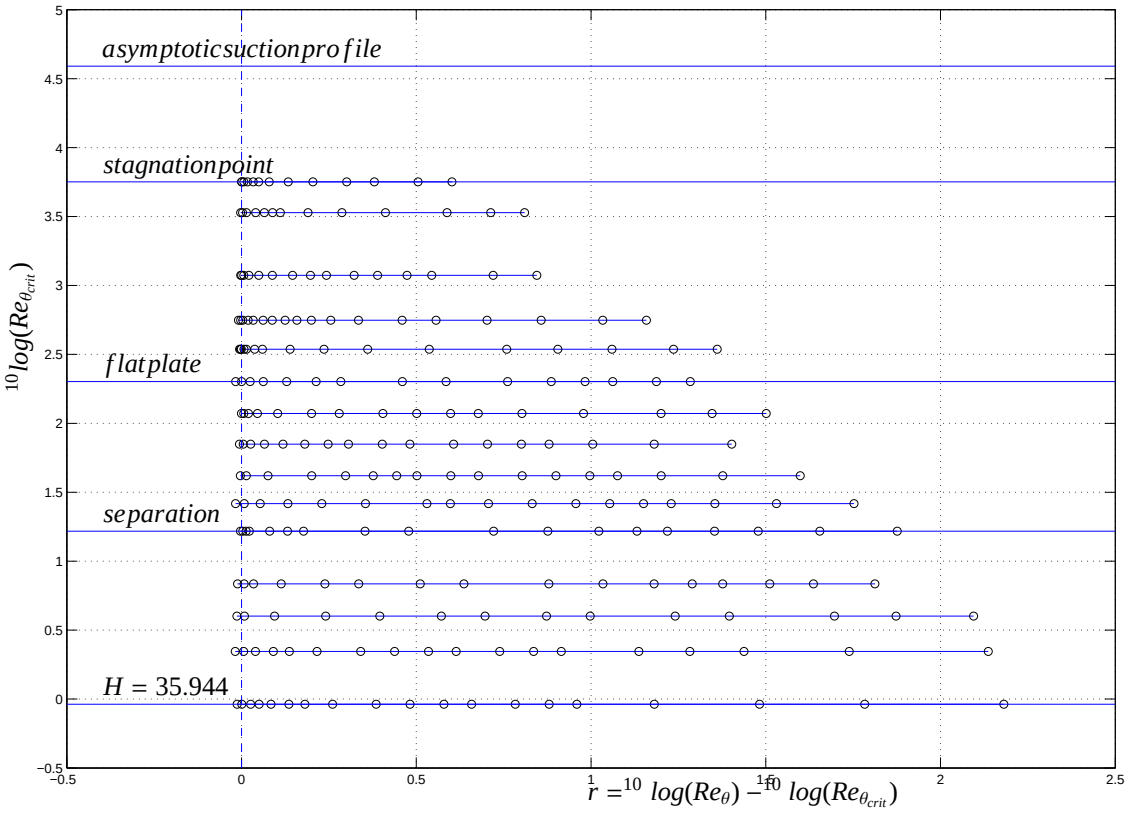

Figure 3.22: Display of datapoints from Arnal

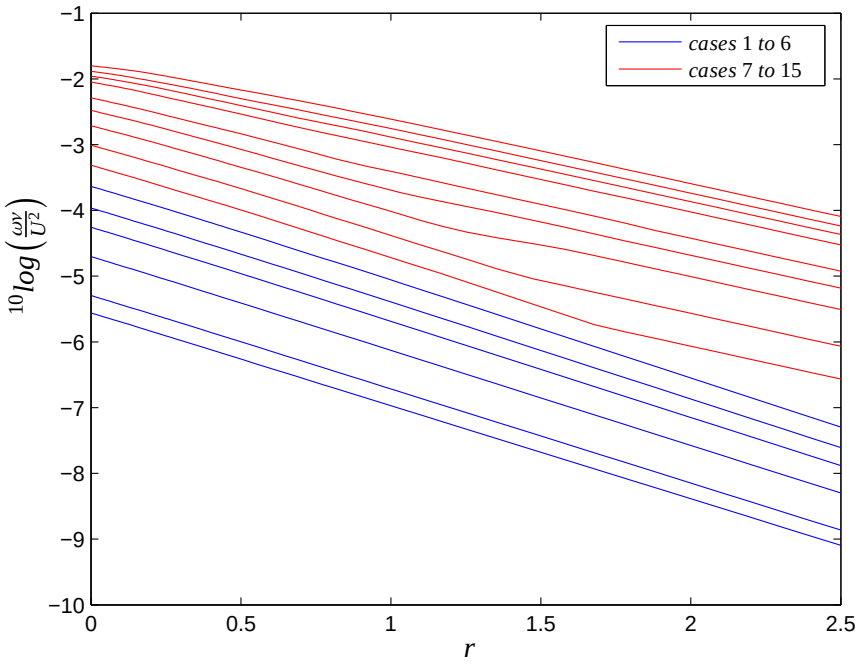

Figure 3.23: axis of T_{max} on log scale

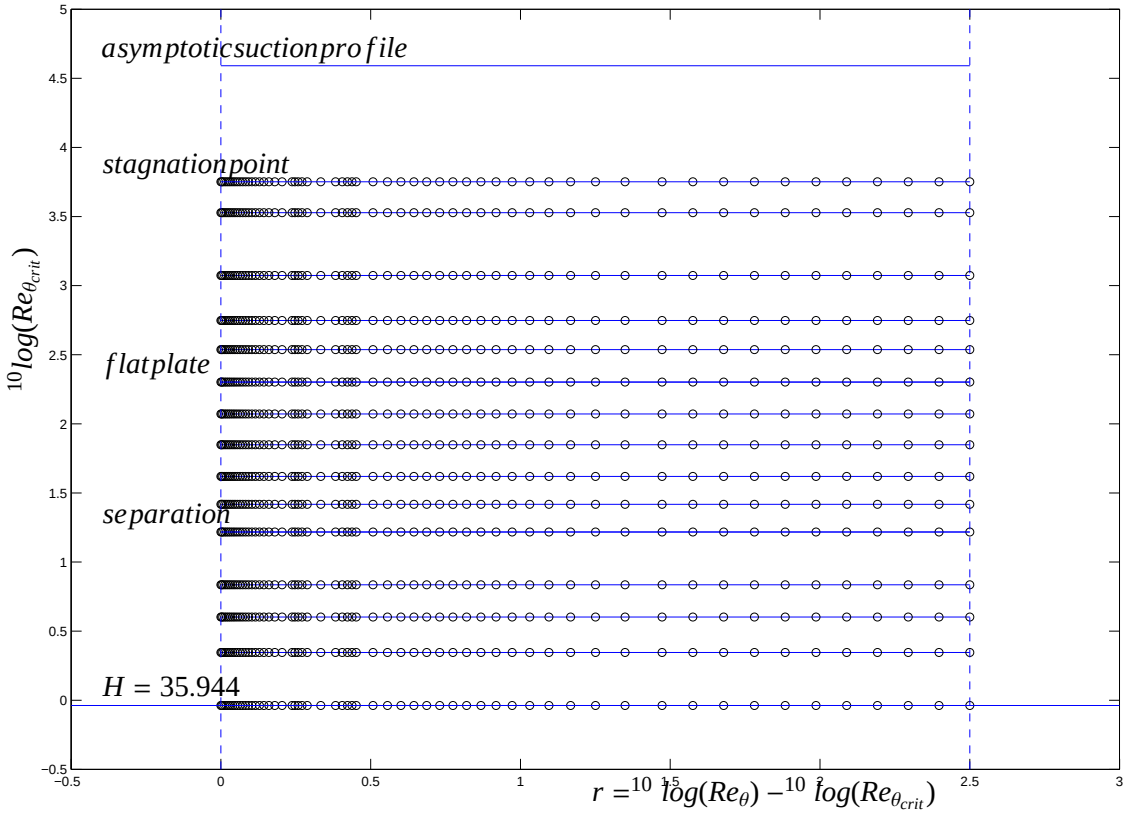

Figure 3.24: Display of interpolated and extrapolated splines

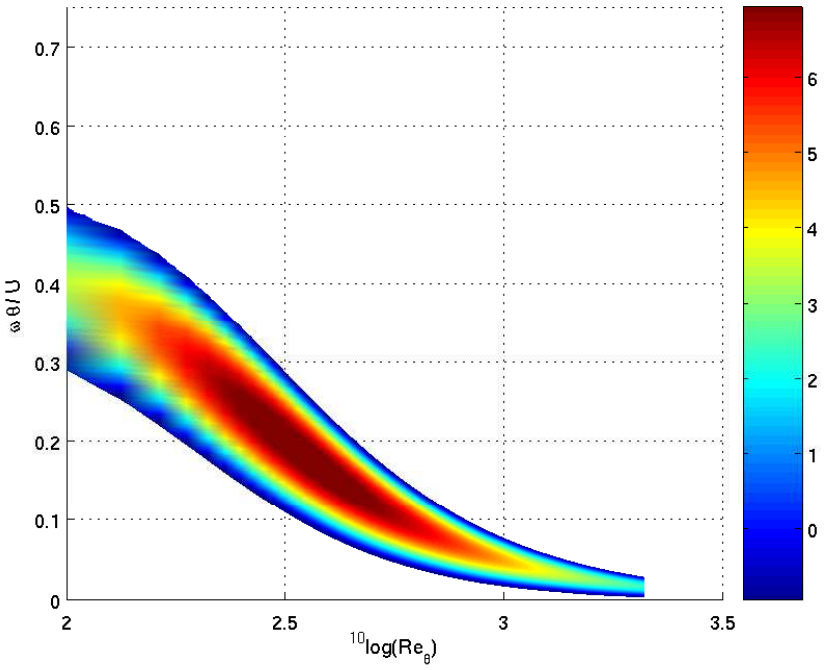

Figure 3.25: 3d representation of T surface for the flat plate case

- Two of the scaling variables are stored in splines for each of the 15 cases separately. These are T_{max} and $axis$. T_{max} is a line in the $T - r$ plane and $axis$ a line in the ${}^{10}log(\frac{\omega\nu}{U^2}) - r$ plane. Plots of both are shown in figures 3.23 and 3.26, where in figure 3.26 all 15 cases from Arnal are plotted. For extrapolation purposes T_{max} can be approximated by $T_{max} = \overline{r}e^{1-\overline{r}}$. This approximation is shown in figure 3.27, where again all 15 cases from Arnal are plotted, now together with the approximating function. For extrapolation of $axis$, linear extrapolation from the endpoints suffices when this extrapolation is needed in $\overline{r}$-direction. Shifting of the $axis$ is necessary when extrapolation in ${}^{10}log(\frac{\omega\nu}{U^2})$ direction is wanted. For the shifting of $axis$ the $axis$ point of the T_{maxmax}, r_{top} point is used as an anchorpoint. The distance over which is shifted can be determined using ${}^{10}log(F)_{top}$, of which the graph is shown in figure 3.31.

- The variables T_{maxmax}, r_{top}, $\left(\frac{\omega\theta}{U}\right)_{scale}$, ${}^{10}log(F)_{top}$ and $R_{theta_{crit}}$ can each be represented by a single curve. These variables are stored as splines against $Re_{\theta_{crit}}$ and are defined from ${}^{10}log(Re_\theta) = -0.5$ to ${}^{10}log(Re_\theta) = 4.5$, which spans all necessary values of ${}^{10}log(Re_\theta)$, so no extrapolations will be needed. The curves of T_{maxmax}, r_{top}, $\left(\frac{\omega\theta}{U}\right)_{scaled}$ and ${}^{10}log\left(\frac{\omega\theta}{U}\right)_{top}$ can be seen in figures 3.28, 3.29, 3.30 and 3.31. Figure 3.32 shows the graph of $Re_{\theta_{crit}}$ versus ${}^{10}log(H)$ and is the same as 3.10 but included here for completeness.

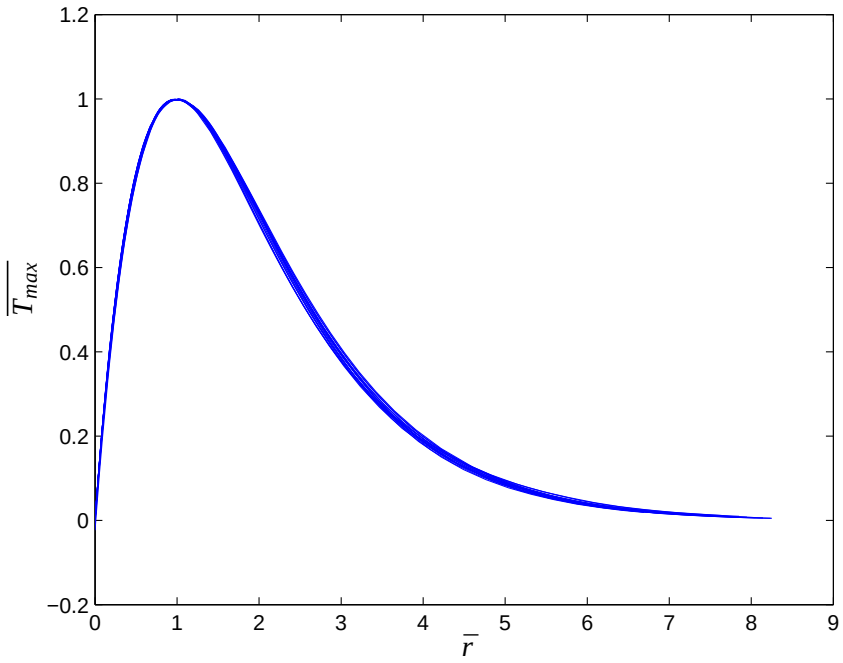

Figure 3.26: $\overline{T}$ versus $\overline{r}$ for all 15 cases

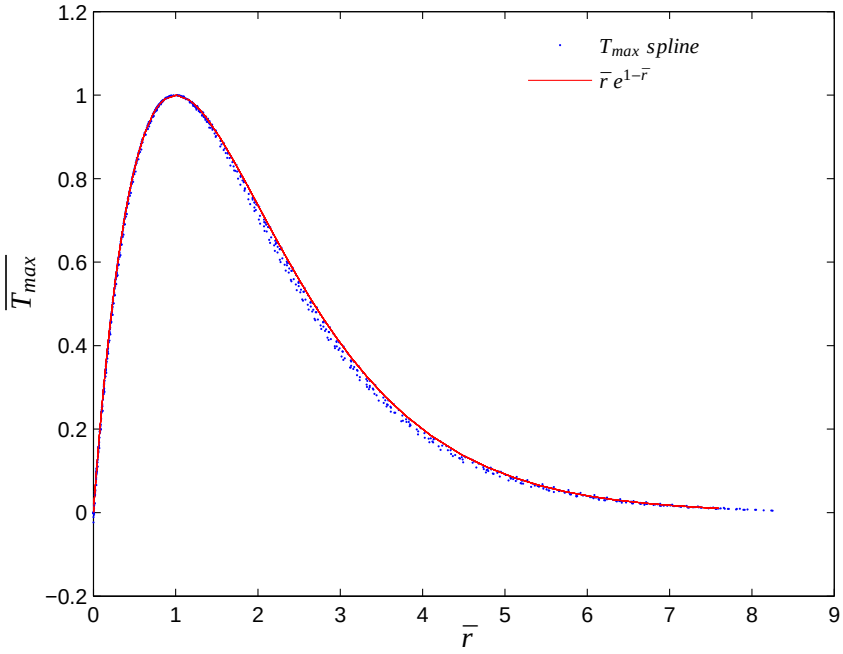

Figure 3.27: Approximation of T_{max} by $T_{max} = \overline{r}e^{1-\overline{r}}$ for all 15 cases

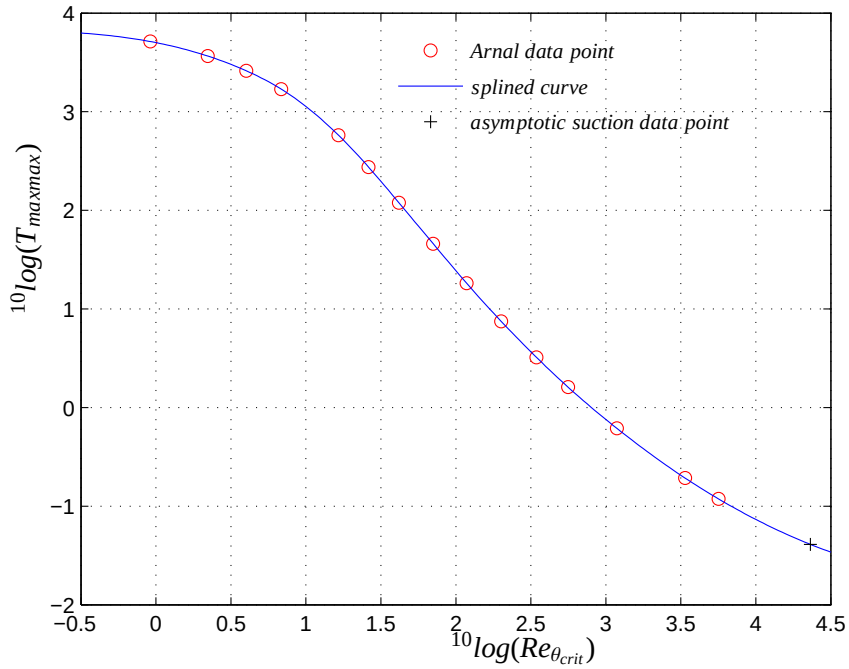

Figure 3.28: $^{10}log(T_{maxmax})$ versus $^{10}log(Re_{\theta_{crit}})$, all 15 cases

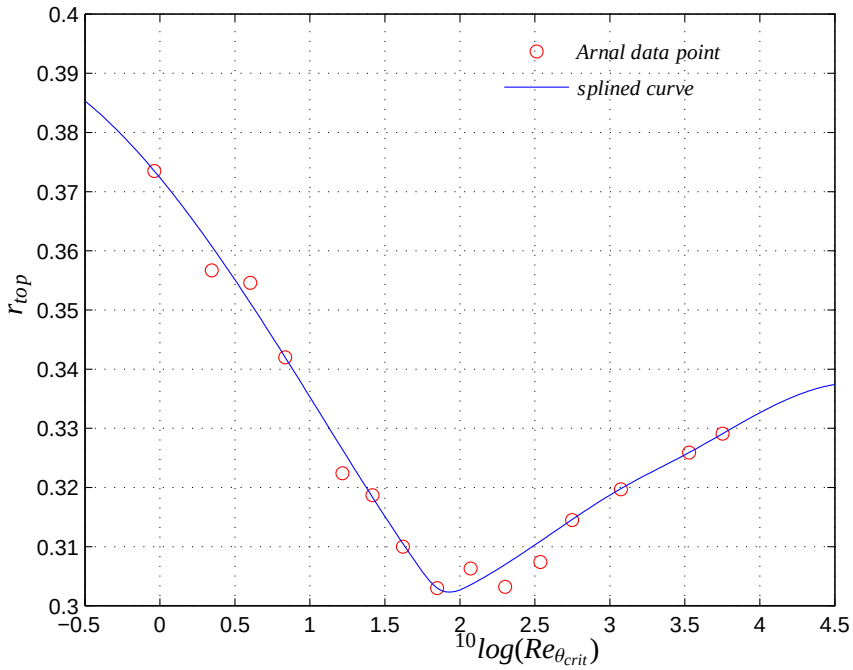

Figure 3.29: r_{top} versus $^{10}log(Re_{\theta_{crit}})$

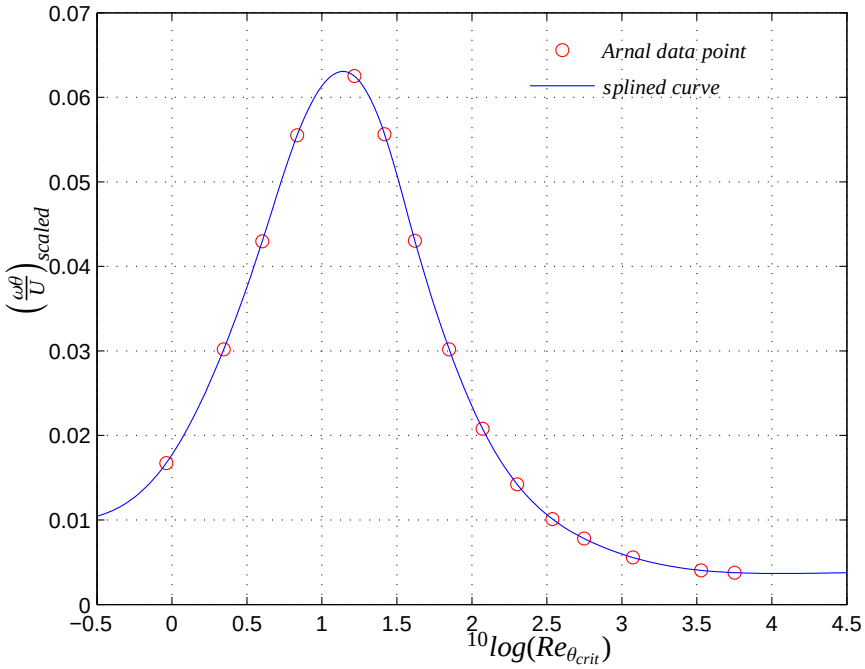

Figure 3.30: $\left(\frac{\omega\theta}{U}\right)_{scale}$ versus $^{10}log(Re_{\theta_{crit}})$

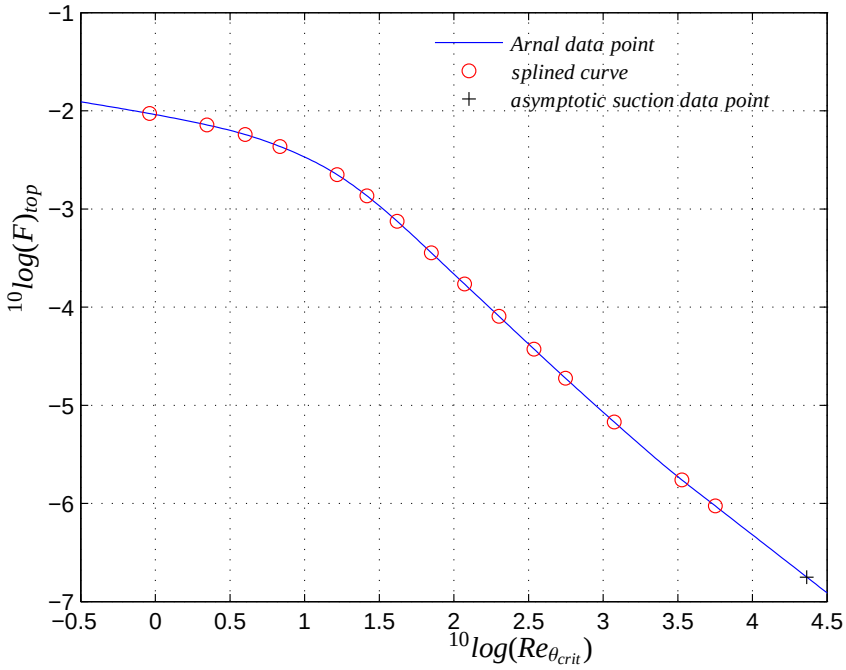

Figure 3.31: $^{10}log(F)_{top}$ versus $^{10}log(Re_{\theta_{crit}})$

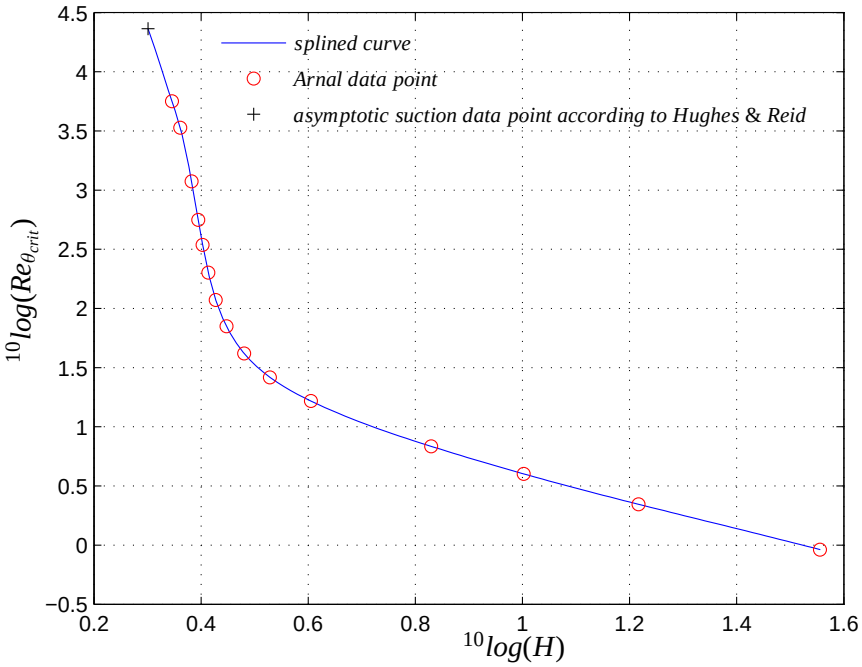

Figure 3.32: correlation between $^{10}log(Re_{\theta_{crit}})$ versus $^{10}log(H)$

The basic data is now with some extrapolations defined in the area from $0 < r < 2.5$ and from $-2 < \overline{\left(\frac{\omega\theta}{U}\right)} < 3$, as well as from $-0.038 <^{10} log(Re_{\theta_{crit}}) < 3.75$. Now a view is taken from a broader perspective to look at the range of variables where this data is to be used. Figure 3.33 (in which the $^{10}log(Re_{\theta_{crit}})$ is replaced by the shapefactor H using figure 3.32, though all inter -and extrapolation is still done using $^{10}log(Re_{\theta_{crit}})$) gives an overview of the areas where the basic data is to be used and where it is known. Using this data and the scaling parameters within the area where the basic data is defined as well as outside it using some extrapolations, the amplification of disturbances is calculated. Each area in figure 3.33 will be discussed on how values of T are calculated. Please note that the stability diagrams that are mentioned are in reality a collection of 59 splines of $\overline{T}$ connected with a single $Re_{\theta_{crit}}$.

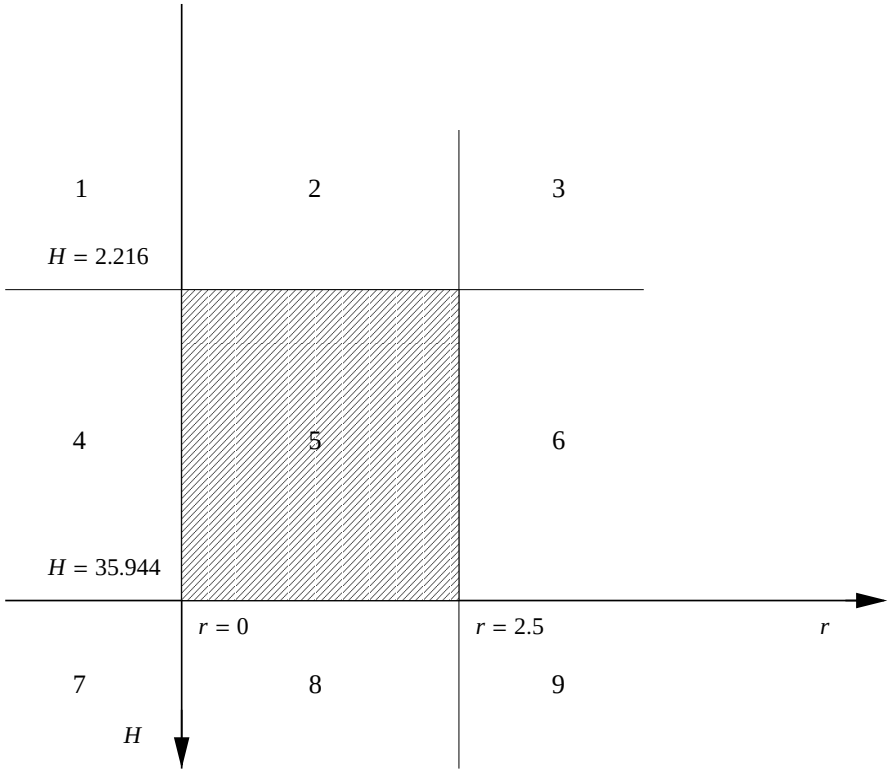

Figure 3.33: Schematic roadmap

- Area 1 is the area with $H < 2.216$ and $r < 0$. A special form of extrapolation is used here. As the stability diagrams of the six cases without inflection point are very much similar in size and form it is assumed that in shifting the stability diagram of the stagnation point case ($H = 2.216$) a good approximation is achieved for the stability diagrams up to $H = 2$. The curve for $\overline{T_{max}}$ is taken to be $\overline{T_{max}} = \overline{r}e^{1-\overline{r}}$ and needs to be extrapolated towards $\overline{r} < 0$. The *axis* is devised by shifting the *axis* curve of the stagnation point down according to $^{10}log(F)_{top}$. Then a linear extrapolation for *axis* is also needed for $\overline{r} < 0$. The correlation between $^{10}log(Re_{\theta_{crit}})$ and $^{10}log(H)$ is known from figure 3.32. The parameters r_{top} and $\left(\frac{\omega\theta}{U}\right)_{scale}$ can be interpolated from their splined functions shown in figures 3.29 and 3.30. T_{maxmax} and $^{10}log(F)_{top}$ just have to be interpolated as they contain values for the asymptotic suction profile.

- Area 2 uses the same $\overline{T}$ and (shifted) *axis* as area 1, but without the extrapolation for *axis* or $\overline{T_{max}}$. The correlation between $^{10}log(Re_{\theta_{crit}})$ and $^{10}log(H)$ is known from figure 3.32. The parameters r_{top} and $\left(\frac{\omega\theta}{U}\right)_{scale}$ can be interpolated from their splined functions. T_{maxmax} and $^{10}log(F)_{top}$ just have to be interpolated as they contain values for the asymptotic suction profile.

- Area 3 is also much the same as area 1, the only difference being that $\overline{T_{max}}$ and *axis* need to be extrapolated in the $r > 2.5$ direction. To approximate $\overline{T_{max}}$ again $\overline{r}e^{1-\overline{r}}$ is used to extrapolate. The parameters r_{top} and $\left(\frac{\omega\theta}{U}\right)_{scale}$ can be interpolated from their splined functions. T_{maxmax} and $^{10}log(F)_{top}$ just have to be interpolated as they contain values for the asymptotic suction profile.

- In area 4 the splines for $\overline{T}$ of the stability diagrams are interpolated using the one dimensional Lagrangian method that uses (in $Re_{\theta_{crit}}$-direction) the closest stability diagram of the three nearest cases and in this way a new interpolated stability diagram is made. The $\overline{T_{max}}$(again approximated by $\overline{r}e^{1-\overline{r}}$) and *axis* need to be linearly extrapolated into the direction of $\overline{r} < 0$. No shifting of the *axis* is required, so $^{10}log(F)_{top}$ is not used. T_{maxmax}, r_{top} and $\left(\frac{\omega\theta}{U}\right)_{scale}$ can just be interpolated.

- Area 5 is the area where no extrapolations are needed except for the ones already performed to extend the range of usable frequencies and the higher r values. Here a two dimensional Lagrangian interpolation using the nine closest stability diagrams in the $^{10}log(Re_{\theta_{crit}}) - r$ plane is made to find the current stability diagram. Then the scaling parameters (found also by interpolating) are used to rescale the splined and scaled stability diagram. This area is the most used area of all.

- In area 6 the splines of the stability diagrams of the Arnal cases are interpolated using the one dimensional Lagrangian method that uses the closest (in $Re_{\theta_{crit}} or H$ -direction) stability diagram of the three nearest cases and in this way a new interpolated stability diagram is made. The scaling parameters $\overline{T_{max}}$ (again approximated by $\overline{r}e^{1-\overline{r}}$) and *axis* need to be linearly extrapolated into the direction of $r > 2.5$. T_{maxmax}, r_{top} and $\left(\frac{\omega\theta}{U}\right)_{scale}$ can be just be interpolated.

- Area 7 occurs for very high values of H, but in the unlikely event of this occurring a simple linear extrapolation for the splines for $\overline{T}$ of the stability diagrams is made from the two cases with the lowest $Re_{\theta_{crit}}$ values and a linear extrapolation is done for T_{maxmax}, r_{top} and $\left(\frac{\omega\theta}{U}\right)_{scale}$. *axis* is not shifted. The scaling parameters $\overline{T_{max}}$ (again approximated by $\overline{r}e^{1-\overline{r}}$) and *axis* need to be linearly extrapolated into the direction of $r < 0$.

- Area 8 occurs for very high values of H, but in the unlikely event of this occurring a simple linear extrapolation for the splines for $\overline{T}$ of the stability diagrams is made from the two cases with the lowest $Re_{\theta_{crit}}$ values. $\overline{T_{max}}$ is linearly extrapolated from the $\overline{T_{max}}$ defined by the two (in $Re_{\theta_{crit}}$ direction) cases and *axis* is not shifted. T_{maxmax}, r_{top} and $\left(\frac{\omega\theta}{U}\right)_{scaled}$ need to be extrapolated.

- Area 9 occurs for very high values of H, but in the unlikely event of this occurring a simple linear extrapolation for the splines for $\overline{T}$ of the stability diagrams is made from the two cases with the lowest $Re_{\theta_{crit}}$ values and a linear extrapolation is done for T_{maxmax}, r_{top} and $\left(\frac{\omega\theta}{U}\right)_{scaled}$. The *axis* is not shifted. The parameters $\overline{T_{max}}$ (again approximated by $\overline{r}e^{1-\overline{r}}$) and *axis* need to be linearly extrapolated into the direction of $r > 2.5$.

Chapter 4

XFOIL

4.1 Introduction

As explained on 's website [59] " *is an interactive program for the design and analysis of subsonic isolated airfoils.*" The program has been around since 1986 and consists of a high-order (2D) panel method combined with a strong coupled viscid-inviscid interaction method. Since 1986 many changes were made to the program, usually improving the program and adding new features. Since 2001 the code was frozen, and significant changes were no longer implemented by its creators, M. Drela and H. Youngren. The version of as discussed here is 6.93.

4.2 Inviscid formulation in

The inviscid formulation as used in is discussed in detail in [12]. Here a short overview of the inviscid formulation is given to give the reader a basic understanding of the working of the inviscid part of . The inviscid flowfield is constructed by the superposition of a freestream flow, a vortex sheet of on the airfoil surface and a source sheet on the airfoil surface as well as on the wake panels. In figure 4.1 an overview is seen from the panelling in . The graph is taken from [12]. In this configuration the streamfunction is given by equation 4.1

$$\Psi(x,y) = u_\infty y - v_\infty x + \frac{1}{2\pi}\int \gamma(s) ln\, r(s;x,y) ds + \frac{1}{2\pi}\int \sigma(s)\theta(s;x,y) \tag{4.1}$$

with s the coordinate along the vortex and source sheets, r the magnitude of the vector between the point at s and the field point x,y. θ is the vector's angle and $u_\infty = q_\infty cos(\alpha)$ and $v_\infty = q_\infty sin(\alpha)$ the freestream velocity components. Each airfoil panel has a linear vorticity distribution and a constant source strength. The wake panels only have a source strength. From the streamfunction finally a linear system can be created that requires the streamfunction to be equal to some constant value Ψ_0 at each

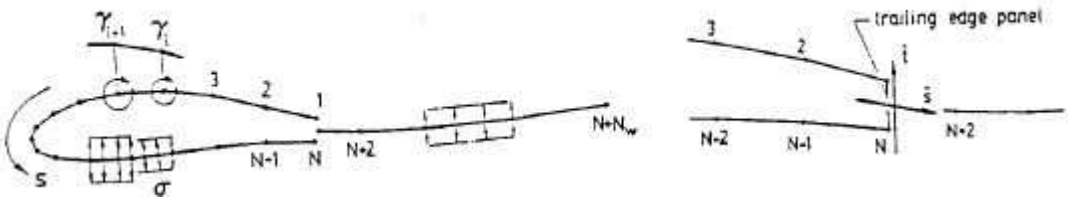

Figure 4.1: panelling in

node of the airfoil. The linear system is given in equation 4.2.

$$\sum_{j=1}^{N} a_{ij}\gamma_j - \Psi_0 = -u_\infty y_i + v_\infty x_i - \sum_{j=1}^{N+Nw-1} b_{ij}\sigma_j \tag{4.2}$$

with N the number of panels on the airfoil, N_w the number of panels in the wake, a_{ij} and b_{ij} the coefficient matrices. By setting $\sigma_i = 0$ one gets the inviscid solution, for a specified angle of attack. Since the flow inside the airfoil is stagnant, the u_i on the airfoil is simply equal to the local vorticity γ on the suction side, and $-\gamma$ on the pressure side as seen in equation 4.3.

$$u_{e_i} = \pm\gamma; \qquad 1 \le i \le N \tag{4.3}$$

The influence of the viscous layer on the potential flow is properly modelled by the wall transpiration concept if the local source strength is equal to the local gradient of the mass defect $m \equiv u_e\delta^*$

$$\sigma_i = \frac{dm}{d\xi} = \pm\frac{m_{i+1} - m_i}{s_{i+1} - s_i} \tag{4.4}$$

For the trailing edge two approaches exist, one for blunt trailing edges and one for sharp trailing edges. For the blunt trailing edges a panel of uniform source strength σ_{TE} is placed across the gap. For smooth flow off the trailing edge the trailing edge panel strengths σ_{TE}, γ_{TE} must be related to the local airfoil surface velocity by:

$$\sigma_{TE} = \frac{1}{2}(\gamma_1 - \gamma_N)|\hat{s}\cdot\hat{t}| \qquad \gamma_{TE} = \frac{1}{2}(\gamma_1 - \gamma_N)|\hat{s}\times\hat{t}| \tag{4.5}$$

Where $\hat{s}$ is the unit vector bisecting the trailing edge angle, and $\hat{t}$ is the unit vector along the trailing edge panel as shown in figure 4.1. For the sharp trailing edge the nodes i and N coincide, and their corresponding equations are identical. This results in a singular system, and has to be circumvented. This is done by discarding the $i = N$ equation in 4.2 and replacing it by an extrapolation of the mean γ (between top and bottom) to the trailing edge as given in 4.6.

$$(\gamma_3 - 2\gamma_2 + \gamma_1) - (\gamma_{N-2} - 2\gamma_{N-1} + \gamma_N) = 0 \tag{4.6}$$

For both the sharp and blunt trailing edge the following Kutta condition is used in as in equation 4.7.

$$\gamma_1 + \gamma_N = 0 \tag{4.7}$$

with sub 1 and sub N as in figure 4.1. After the combination of the linear system from 4.2 with the Kutta condition a $(N+1)\times(N+1)$ system for N node values γ_i (when considering the inviscid solution $\sigma_j = 0$) and airfoil surface streamfunction Ψ_0 is acquired. This system can be solved using a Gaussian elimination and gives as inviscid solution for the surface vorticity values equation 4.8.

$$\gamma_i = \gamma_{0_i} cos\ \alpha + \gamma_{90_i} sin\ \alpha + \sum_{j=1}^{N+N_w-1} b'_{ij}\sigma_j \quad 1 \leq i \leq N \tag{4.8}$$

with γ_0 and γ_{90} the inviscid vorticity distribution corresponding to a freestream α of 0° and 90°, and with $b'_{ij} = -a_{ij}^{-1} b_{ij}$ is the source-influence matrix. The C_p can finally be calculated to be:

$$C_p = 1 - \left(\frac{\gamma}{q_\infty}\right)^2 \tag{4.9}$$

For the viscous solution the boundary layer equations have to come into play, with which we shall deal in the next section.

4.3 Viscous formulation in

The most recent viscous formulation of can be found in [12] appended by [13]. Here a short overview is given of the laminar boundary layer formulation found in . The viscous formulation in exists of a 2 integral equation model consisting of equations 4.10 and 4.11.

$$\frac{d\theta}{d\xi} + (2 + H - M_e^2)\frac{\theta}{u_e}\frac{du_e}{d\xi} = \frac{C_f}{2}\left(+\frac{v_0}{u_e}\right) \tag{4.10}$$

$$\theta\frac{dH^*}{d\xi} + (2H^{**} + H^*(1-H))\frac{\theta}{u_e}\frac{du_e}{d\xi} = 2C_D - H^*\frac{C_f}{2}\left(+(1-H^*)\frac{v_0}{u_e}\right) \tag{4.11}$$

With ξ the streamwise arc lenght coordinate and the righthand side parts in brackets the additional parts added by Ferreira [14] in the version. This is to incorporate boundary layer suction into the boundary layer equations. One extra equation is added to the existing two. For turbulent boundary layers a lag equation for the maximum shear stress coefficient C_τ is included. In the laminar region a rate equation (see 4.12) for the growth of the amplitude $\tilde{n}$ of the most amplified Tollmien Schlichting wave is included.

$$\frac{d\tilde{n}}{d\xi} = \frac{d\tilde{n}}{dRe_\theta}(H_k)\frac{dRe_\theta}{d\xi}(H_k, \theta) \tag{4.12}$$

The empirical relation $\frac{d\tilde{n}}{d\xi}(H_k)$ is a correlation of spatial growth rates computed from solutions of the Orr-Sommerfeld equation, and $\frac{dRe_\theta}{d\xi}(H_k, 0)$ is obtained from the properties of the Falkner-Skan profile family. The transition point is defined by the location where $\tilde{n}$ reaches some user defined value $\tilde{n}_{crit}$. In section 4.5 the transition routines are discussed in more detail. To close these boundary layer equations the following dependencies are used:

$$\begin{aligned} H^* &= H^*(H_k, M_e, Re_\theta) \\ H^{**} &= H^{**}(H_k, M_e) \\ C_f &= C_f(H_k, M_e, Re_\theta) \\ C_D &= C_D(H_k, M_e, Re_\theta) \end{aligned} \tag{4.13}$$

Here H^* is defined in equation 4.14 and H_k is the kinematic shape parameter correlated by Whitfield [55] for adiabatic flows in air as in equation 4.15.

$$H^* = \frac{\theta^*}{\theta} = \frac{\int_0^\infty \frac{u}{U}\left(1-\left(\frac{u}{U}\right)^2\right)dy}{\int_0^\infty \frac{u}{U}\left(1-\left(\frac{u}{U}\right)\right)dy} \tag{4.14}$$

$$H_k = \frac{H - 0.290M_e^2}{1 + 0.113M_e^2} \tag{4.15}$$

Note that for $M = 0$, $H_k = H$. The laminar closure relations are written in equations 4.16 to 4.19 and can be found in [13]. Graphical representations are shown in figures 4.2 to 4.4.

$$H^* = \begin{cases} 1.528 + 0.0111\frac{(H_k-4.35)^2}{H_k+1} - 0.0278\frac{(H_k-4.35)^3}{H_k+1} - 0.0002(H_k-4.35)^2H_k^2, & H_k < 4.35 \\ 1.528 + 0.015\frac{(H_k-4.35)^2}{H_k}, & H_k > 4.35 \end{cases} \tag{4.16}$$

$$H^{**} = \left(\frac{0.064}{H_k - 0.8} + 0.251\right)M_e^2 \tag{4.17}$$

$$Re_\theta \frac{C_f}{2} = \begin{cases} -0.07 + 0.0727\frac{(5.5-H_k)^3}{H_k+1}, & H_k < 5.5 \\ -0.07 + 0.015\left(1 - \frac{1}{H_k-4.5}\right)^2, & H_k > 5.5 \end{cases} \tag{4.18}$$

$$Re_\theta \frac{2C_D}{H^*} = \begin{cases} 0.207 + 0.00205(4-H_k)^{5.5}, & H_k < 4 \\ 0.207 - 0.0016\frac{(H_k-4)^2}{(1+0.02(H_k-4)^2)}, & H_k > 4 \end{cases} \tag{4.19}$$

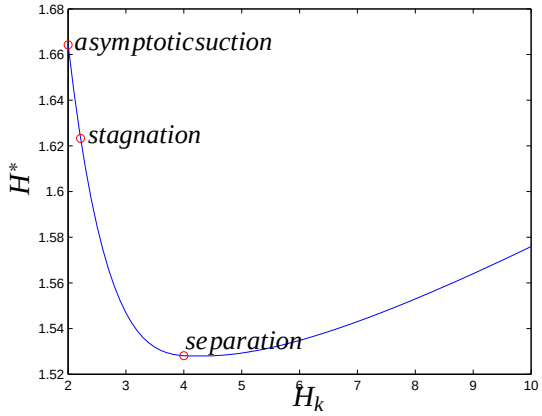

Figure 4.2: Closure relation for H^* &

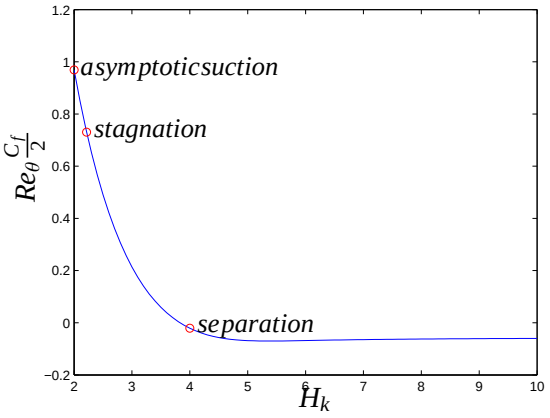

Figure 4.3: Closure relation for $Re_\theta \frac{C_f}{2}$ &

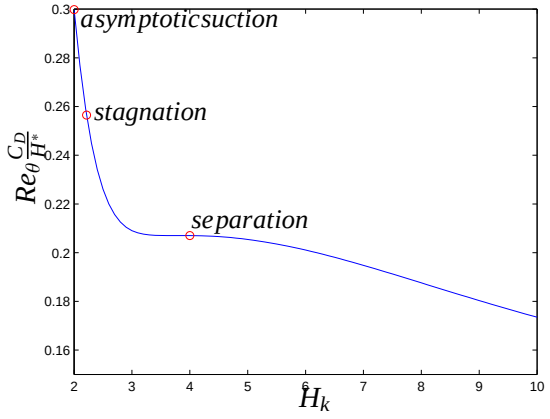

Figure 4.4: Closure relation for $Re_\theta \frac{C_D}{H^*}$ &

The closure relations will normally be used only from $H = 2.216$ (stagnation point) up to around $H = 10$. In cases of high Mach numbers the kinetic shape factor can be lower, and up to $H = 2$, but with suction this can also be achieved. These low H numbers will be reached in a different manner so it needs to be checked if the closure relations agree with the asymptotic suction boundary layer solution for $H = 2$. To do this the value of the closure relations are calculated assuming the asymptotic suction boundary layer. For H^* as in equation 4.14 can be written as:

$$H^* = \frac{\theta^*}{\theta} = \frac{\int_0^\infty \frac{u}{U}\left(1 - \left(\frac{u}{U}\right)^2\right) dy}{\int_0^\infty \frac{u}{U}\left(1 - \left(\frac{u}{U}\right)\right) dy} \tag{4.20}$$

For the asymptotic suction profile this is written as:

$$\begin{aligned}
\theta^* &= \int_0^\infty \left(1 - e^{\frac{v_0 y}{\nu}}\right)\left(1 - \left(1 + e^{\frac{v_0 y}{\nu}}\right)^2\right) dy \\
&= -\frac{5}{6}\frac{\nu}{v_0} \\
\theta &= \int_0^\infty \left(1 - e^{\frac{v_0 y}{\nu}}\right)\left(1 - \left(1 + e^{\frac{v_0 y}{\nu}}\right)\right) dy \\
&= -\frac{\nu}{2v_0}
\end{aligned}$$

This gives for H^*:

$$\frac{-\frac{5}{6}\frac{\nu}{v_0}}{-\frac{\nu}{2v_0}} = \frac{10}{6} \approx 1.667 \tag{4.21}$$

which agrees with the value of equation 4.16 and figure 4.2.

Then for C_f:

$$C_f = \frac{\tau_w}{\frac{1}{2}\rho U^2} \tag{4.22}$$

and for the asymptotic suction profile:

$$u = U\left(1 - e^{\frac{v_0 y}{\nu}}\right) \tag{4.23}$$

then:

$$\mu\frac{\partial u}{\partial y} = \mu U\left(-\frac{v_0}{\nu}e^{\frac{v_0 y}{\nu}}\right) \tag{4.24}$$

then for $y = 0$ this can be written:

$$\tau_w = \mu U\left(-\frac{v_0}{\nu}\right) \tag{4.25}$$

so that:

$$C_f = \frac{\tau_w}{\frac{1}{2}\rho U^2} = \frac{2\mu U\left(\frac{-v_0}{\nu}\right)}{\rho U^2} = 2\left(\frac{-v_0}{\nu}\right) \tag{4.26}$$

and as for the asymptotic suction profile the following holds:

$$\begin{aligned} \frac{-v_0\theta}{\nu} &= \frac{1}{2} \\ \frac{-v_0}{U} &= \frac{1}{2}\frac{\nu}{\theta U} \end{aligned} \tag{4.27}$$

gives the same solution as given by equation 4.18 and figure 4.3:

$$\frac{C_f}{2} Re_\theta = 1 \tag{4.28}$$

For C_D:

$$C_D = \frac{\mu}{\rho U_e^3} \int_0^\infty \left(\frac{\partial u}{\partial y}\right)^2 dy \tag{4.29}$$

with:

$$\tau = \mu \frac{\partial u}{\partial y} = \mu U \left(-\frac{v_0}{\nu} e^{\frac{v_0 y}{\nu}}\right) \tag{4.30}$$

gives:

$$\begin{aligned} C_D &= \frac{\mu}{\rho U_e^3} \int_0^\infty U_e^2 \left(\frac{v_0}{\nu}\right)^2 e^{\frac{2v_0 y}{\nu}} dy \\ &= \frac{1}{2}\frac{1}{2}\frac{\nu}{\theta U_e} \\ &= \frac{1}{4}\frac{1}{Re_\theta} \end{aligned}$$

which gives with the previous acquired value of 1.667 for H^* for $C_D \frac{2Re_\theta}{H^*}$ the value of 0.30, which agrees with equation 4.19 and figure 4.4 Thus it can be concluded that the closure relations for and can account for shapefactors up to $H = 2$, and will be valid for the asymptotic suction boundary layer.

This being established, next the governing equations are discretized using 2-point central differences (the trapezoidal rule) . The boundary layer variables θ, δ^*, C_τ or $\tilde{n}$ and u_e are defined to be located at the panel nodes (although u_e is originally calculated on the panels itself and then an average value is taken for the node). Each airfoil and wake panel therefore has three coupled nonlinear equations associated with it. The focus of the next section will be on the solution procedure of these equations.

4.4 Solution procedure

The solution procedure is described in detail in [12] and will be summarized here with a focus on the airfoil panels. The panels in the wake are treated slightly different, but as this has little effect on the

general course of the calculation it is left out of this summary. If the solution for the airfoil vorticity values of equation 4.8 is substituted into equation 4.3 this gives equation 4.31.

$$u_{e_i} = u_{inv_i} + \sum_{j=1}^{N+N_w+1} d_{ij} m_j; \qquad 1 \leq i \leq N + N_w \tag{4.31}$$

This very general expression gives the potential flow about the airfoil for any distribution of mass defect on the airfoil and wake. The u_{e_i} in this formulation is essentially split in an inviscid part and a viscous part. The inviscid part (u_{inv}) is determined completely independent from the viscous part, and only influenced by airfoil and wake geometry and the freestream angle of attack. The same holds for the mass-influence matrix d_{ij}. The viscous part of u_{e_i} is determined first by an iterative method marching through the boundary layer, shown in equation 4.32. In this equation VS_1 and VS_2 are the equation matrices for nodes #1 and #2 of the current panel, made up of equations 4.10, 4.11 and 4.12. The δA stands for the amplification of the T-S waves and the VS_r stands for the righthand side (residue) of the equations.

$$\begin{bmatrix} & VS_1 & \end{bmatrix} \begin{Bmatrix} \delta A_1 \\ \delta\theta_1 \\ \delta\delta_1^* \\ \delta u_{e_1} \\ \delta\xi_1 \end{Bmatrix} + \begin{bmatrix} & VS_2 & \end{bmatrix} \begin{Bmatrix} \delta A_2 \\ \delta\theta_2 \\ \delta\delta_2^* \\ \delta u_{e_2} \\ \delta\xi_2 \end{Bmatrix} = \begin{Bmatrix} \\ VS_r \\ \\ \end{Bmatrix} \tag{4.32}$$

After iterating and solving this system, the $\delta\theta$, $\delta m (= \delta(u_{e_i} \cdot \delta^*))$ and $\tilde{n}$ are inserted into the (global) Newton method to couple the viscous part of u_{e_i} with the inviscid solution. The coupling consists in the form the mass-influence matrix d_{ij}. It is important to note that d_{ij} embodies the effect of the local m_j near the trailing edge on the global u_{e_i} distribution via its effect on the Kutta condition.

4.4.1 Newton solution

Equation 4.31 closed the discrete boundary layer equations. This nonlinear system of equations is now rendered elliptic by the global mass influence on u_e and is solved using a so-called full Newton-method. In the Newton method a system of nonlinear equations can be written as:

$$F(Q) = 0 \tag{4.33}$$

where Q is the vector of variables and F the vector of equations. At some iteration level k the solution procedure can be written as follows:

$$F^k + \left(\frac{\delta F}{\delta Q}\right)^k \delta Q^k = 0 \tag{4.34}$$

$$Q^{k+1} = Q^k + \delta Q^k \tag{4.35}$$

The unknown vector δQ contains the iterates of the variables: $\delta\theta$, δm_j and for the laminar part of the boundary layer $\delta\tilde{n}$. Variable δm_i is chosen over the $\delta\delta^*$ as the former will generate a matrix with

only significant values at some diagonals to solve, which can be solved more efficiently than a regular matrix.

$$\begin{bmatrix} & & \\ & J_{ij} & \\ & & \end{bmatrix} \begin{Bmatrix} \delta\theta_j \\ \delta m_j \\ \delta\tilde{n}, \delta C_{\tau j} \end{Bmatrix} = \begin{Bmatrix} \\ -R_i \\ \\ \end{Bmatrix}; \qquad 1 \leq i \leq N + N_w \tag{4.36}$$

In equation 4.36 matrix J_{ij} is quite large, and almost sparse. By neglecting the small off-diagonal values a sparse matrix is generated. The elements in the vector containing $\delta\theta$, δm_j and $\delta\tilde{n}$ are grouped together corresponding to each streamwise station. The equations in J_{ij} are grouped in a similar fashion to create the tri-diagonal form of the matrix. This is then solved using a custom solver completing one iteration of the global Newton procedure.

4.5 Transition routines

4.5.1 Drela Transition method

The transition routines in have been point of discussion for some time by several different authors. First the working of the transition prediction is explained here. As we will discuss 2 other transition prediction methods we will name this method the Drela transition method after its author. The Drela method uses a linear approximation of the envelopes of the spatial amplification curves of the Orr-Sommerfeld solutions for the Falkner-Skan profile family. This approximation of the curves by straight lines is shown in figure 4.5. Any influence by behaviour of separate frequencies is eliminated by only approximating the envelopes. Dini [8] showed that the Drela method is not strictly correct, and only applicable in case of similar boundary layers. Drela argues that the error is small and overruled by other uncertainties in the code and the choice of the N_{crit}. However in chapter 8 it can be seen that these differences are substantial when compared to the Van Ingen, or Improved e^N-method. In the code the Drela method is implemented as follows. The slope of the amplification curve is given by:

$$\frac{\delta N}{\delta \xi} = \frac{AF \cdot DADR}{\theta} RFAC \tag{4.37}$$

with:

$$AF = -0.05 + 2.7\left(\frac{1.0}{H_k - 1}\right) - 5.5\left(\frac{1.0}{H_k - 1}\right)^2 + 3.0\left(\frac{1.0}{H_k - 1}\right)^3 \tag{4.38}$$

$$DADR = 0.028(H_k - 1.0) - 0.0345e^{-(3.87\frac{H_k}{H_k - 1} - 2.52)^2} \tag{4.39}$$

$$RFAC = \begin{cases} 0.0 & ;RNORM < 0 \\ 3.0 \cdot RNORM^2 - 2.0 \cdot RNORM^3 & ;0 \leq RNORM \leq 1 \\ 1.0 & ;RNORM \geq 1 \end{cases} \tag{4.40}$$

$$RNORM = \frac{^{10}log(Re_\theta) - (^{10}log(Re_{\theta_{crit}})) - 0.08}{2 \cdot 0.08} \tag{4.41}$$

$$^{10}log(Re_{\theta_{crit}}) = 2.492\left(\frac{1}{H_k - 1}\right)^{0.43} + 0.7\left(tanh\left(14.0\left(\frac{1}{H_k - 1}\right) - 9.24\right) + 1\right) \tag{4.42}$$

This gives for the correlation between $^{10}log(Re_{\theta_{crit}})$ and H for the Drela method figure 4.6. From

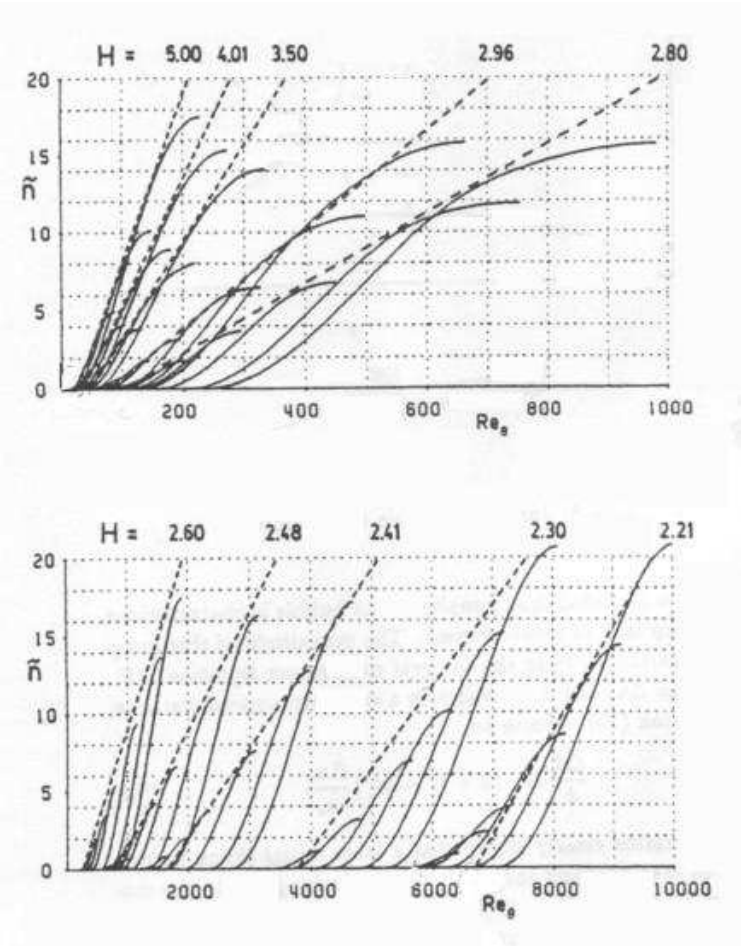

Figure 4.5: Envelope approximation Drela method

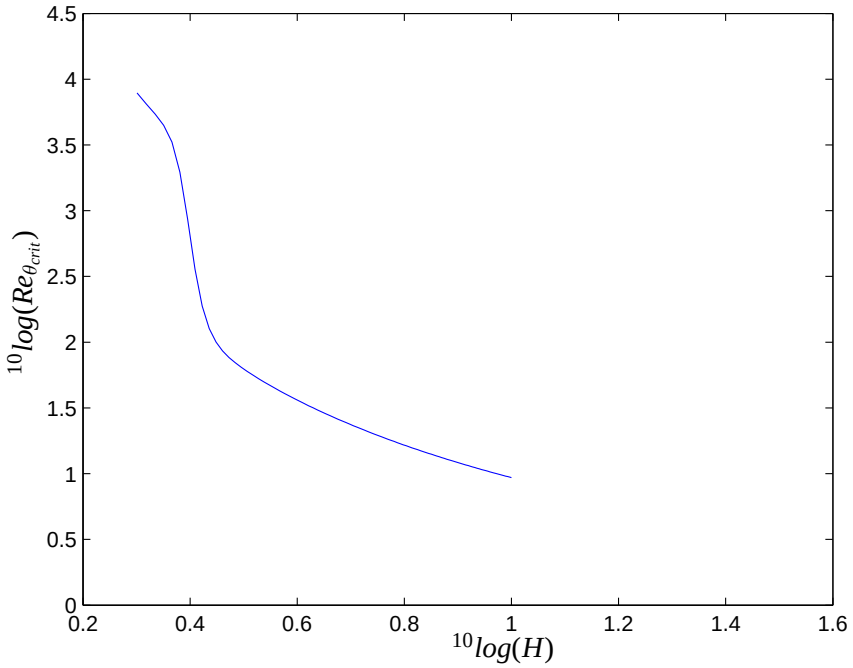

Figure 4.6: $^{10}log(Re_{\theta_{crit}})$ and $^{10}log(H)$ for the Drela method

equations 4.37 to 4.42 also a curve depicting $\theta\frac{\delta N}{\delta \xi}$ is made and shown in figure 4.7. In this figure $RFAC$ is made to be 1, which is true unless $Re_\theta \cong Re_{\theta_{crit}}$. It can be seen that close to $H = 2$ the $\theta\frac{\delta N}{\delta \xi}$ does not go into the stable (negative) area, it does not even become zero. Therefore the Drela method cannot cope with damping of the T-S waves as would possibly occur in suction boundary layers. Instead when using suction with the Drela method for transition the Re_θ will become less than $Re_{\theta_{crit}}$ at which point the amplification will be set to be zero. This is also not correct as the amplification should also be allowed to decrease. It must be remarked that the Drela method was never intended to cope with damping of T-S waves by using boundary layer suction, and therefore should not be expected to do so.

4.5.2 Van Ingen method

In the adapted version of named which is made suitable for handling boundary layer suction with the boundary layer equations another transition method is present. This method is called the (full) Van Ingen method, after its author and was implemented by Ferreira [14] and later modified by Broers [1]. This method was implemented to overcome the difficulties encountered with the Drela method when employing boundary layer suction. This method uses no straight line approximation of the envelope of the Orr-Sommerfeld solutions. It calculates the contribution of 100 frequencies to the amplification and can predict damping of the T-S waves. Unfortunately it stops the calculation when the $^{10}log(Re_\theta)$ value is lower than $^{10}log(Re_{\theta_{crit}})$, and will keep the amplification factor constant. This way the only damping that occurs is when still the $^{10}log(Re_\theta)$ value is higher than $^{10}log(Re_{\theta_{crit}})$ (so

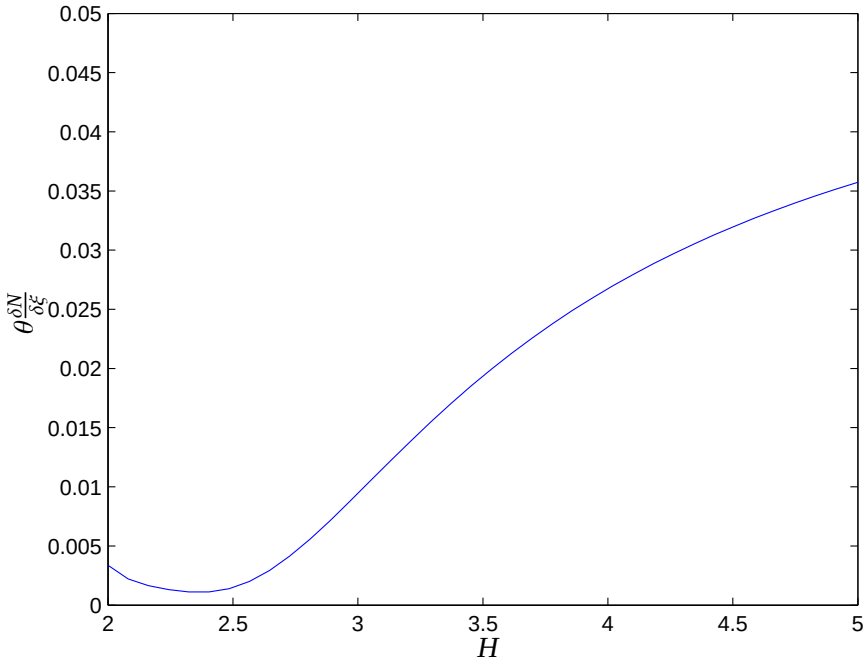

Figure 4.7: $\theta\frac{\delta N}{\delta\xi}$ and H for the Drela method

at least one frequency is still unstable) but that the dominant frequency that was responsible for the maximum amplification has a much lower amplification ratio now, and the -now largest- amplification ratio is lower than the former maximum value. It will be clear that this allows only for very small amount of damping of the amplification. This method uses a different $^{10}log(Re_{\theta_{crit}}) - H$ correlation as can be seen in figure 4.8. This method also has small discontinuities in the N-factor curve. These occur when a switch is made to an amplification curve of a different frequency in the calculation. In figure 4.9 these discontinuities can be seen in a calculation for an airfoil with a lower surface resembling a flat plate pressure distribution.

In the boundary layer iteration converges badly when this method is used. s interaction between the boundary layer iteration and transition calculation are to blame for this. This is resolved by letting the user define a N_{limit} value, at which the Van Ingen method switches to the Drela method that does converge. A drawback is that the transition prediction is then influenced by Drela's method, but the difference can be small, depending on the difference between N_{crit} (at which transition occurs) and N_{limit} (at which the methods are switched). Typical value for the N_{limit} at a N_{crit} of 9 is 7-8. Later in this report an alternative to this fixed N_{limit} value is given to get N_{limit} closer to N_{crit}.

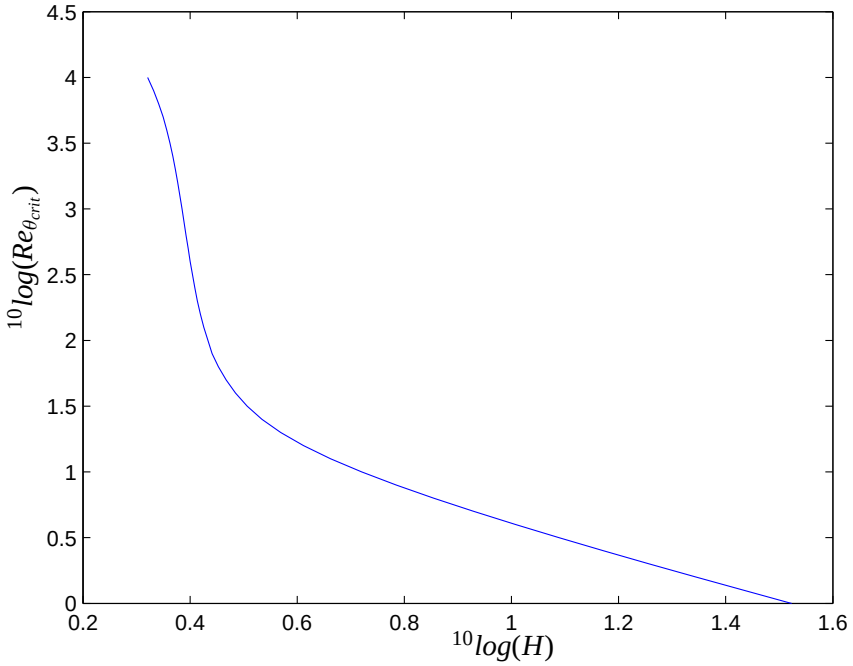

Figure 4.8: $^{10}log(Re_{\theta_{crit}})$ and $^{10}log(H)$ for the Van Ingen method

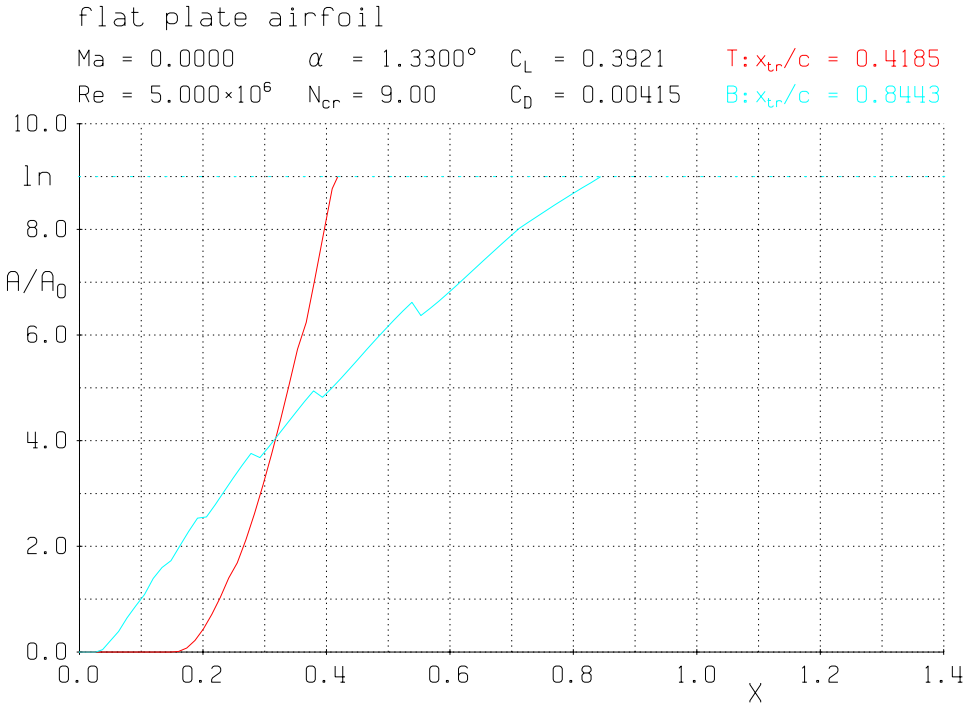

Figure 4.9: discontinuities in Van Ingen method

Chapter 5

Modifications to

In the previous chapter the existing form of was discussed. In the present chapter the implementation of the improved e^N-method and the necessary modifications that were made to will be discussed.

5.1 General principles of adapting code

As mentioned in section 1.5 the approach of adapting the code is such as to ensure user friendliness and functionality. In addition there is the desire to create a code understandable by future programmers who will adapt and use this code. To ensure these objectives are met, one has to take certain measures and adopt some programming habits.

- make as little changes as possible in the original program
- not impede the working of already present functionalities of the program
- keep the general structure and style of programming already present intact, this will help to keep a good overview
- include comments, this makes the intended effect of the code clear, and as a bonus makes the programmer him- or herself conscious of the need and function of that specific part of the code.
- the code added to is -contrary to customary practice- not condensed. With the condensing of code it is meant that the programmer will minimize the amount of code used to describe a program. This deteriorates the readability of the code to others, and often in a dramatic way. As it can be expected that other users will use or at least read this code (i.e. for implementation in MSES) no such condensation effort is made.
- make the user interface easy and transparent

- have the program produce warnings when special algorithms are used, but at the same time prevent the user from being flooded with warnings and remarks.

These principles were observed throughout the process, but despite the intention to keep the changes as small as possible, quite some changes had to be made. As all programming was done in 77 some language specific principles apart from the general principles can be formulated:

- use variable and subroutine names no more than 6 characters long. This is a 77 standard to ensure portability. Many 77 compilers can also handle longer variable names nowadays, but it is nonetheless needed to ensure all compilers can compile the programme
- use variable declarations. can handle implicit variable declarations but this is prone to error and deteriorates readability

In total over 2000 lines of new code were added to an estimated existing 30.000 lines of code of . Each addition into the existing code is marked by a statement like:

```
C-----Modified by Jeroen Bongers(7-Nov-2005): start
```

to mark the start of the modified code and ended by:

```
C-----Modified by Jeroen Bongers(7-Nov-2005): end
```

to mark the end of the modified code and to give the date of the last (major) modification. This way the code will be more easily readable. Because was published under the GNU General Public License [57], when or if is to be published or publicly released, the source code of the adapted program needs to be made public. It should be noted that under the GNU General Public License it is not obligatory to publicly release modified versions of a program. In such a public release, in the program and its source code it needs to be made clear what changes were made by which developers. To this requirement now complies by having every change marked in this manner.

5.2 Flowchart

In figure 5.1 a flowchart with the called subroutines is shown. It is divided into 3 zones: a blue zone, a red zone and the rest. The red zone represents subroutines that were made from scratch, the blue zone represents subroutines that were extensively modified, and the other subroutines were only very slightly modified or not modified at all. The figure that is shown starts with the subroutine which stands for the viscous calculation routine. Starting from this the subroutines will be briefly described and briefly the most important modifications made to it are mentioned.

- is the subroutine that is responsible for all viscous calculations. It checks the final convergence of the global Newton iterations. This is also the reason for it being extensively modified, as some work was done to improve convergence. This will be described in detail in section 5.3.3. Also some warning messages for the user were added.

- is the subroutine that fills the global Newton method with the boundary layer coefficients. It is also responsible for calling the marching boundary layer iteration routines. Together with the two boundary layer marching routines(and) it calls the routine to check for transition.

- is the subroutine that initializes the boundary layer. This routine will use a prescribed value for u_{e_i} to march through the boundary layer while iterating at each station for a converged solution. This subroutine checks for transition at each interval, at each iteration.

- is the subroutine that does the actual marching through the boundary layer while iterating at each station and continuously checking for transition. It also makes the boundary layer coefficients for the global Newton iteration. The iteration limit for every boundary layer interval was changed from 25 to 26 for convergence reasons. For more details about this see section 5.3.3

- is the subroutine that checks every boundary layer interval for transition by calling the amplification rate of change ($\frac{dN}{dx}$) routine . If transition is found in the current interval it will iterate in this interval to find the exact location of the transition point. In this iteration again is called. Added are the different mechanisms to improve on convergence. For more details about this see section 5.3.3

- is included here as it calls to . It is meant to set up global Newton coefficients for the boundary layer. In the laminar part also some amplification rate of change ($\frac{dN}{dx}$) calculations are necessary, and therefore it call on .

- is the subroutine that calculates the amplification rate from (Drela method), (Van Ingen method) or (improved e^N-method). Changes made here are to accommodate the Improved e^N-method. Also some calculations for the convergence improvement functions are added, as are functions to be used in plotting some variables connected to the transition prediction.

- is the subroutine that is responsible for the Drela method of transition prediction. The flowchart does not go into details of this routine any further.

- is the subroutine responsible for the Van Ingen transition prediction. The flowchart does not go into details of this routine further either.

- is the subroutine that was created newly for the improved e^N-method. It calculates the N-factor and derivative $\frac{dN}{dx}$ (needed for use in) at the current boundary layer interval.

- is the subroutine that finds the $Re_{\theta_{crit}}$ value for the current value of H from a splined function. Together with , , , and it is given in grey to show these routines belong to a group that all call the subroutines and . Plots of these splined function can all be found in chapter 3.

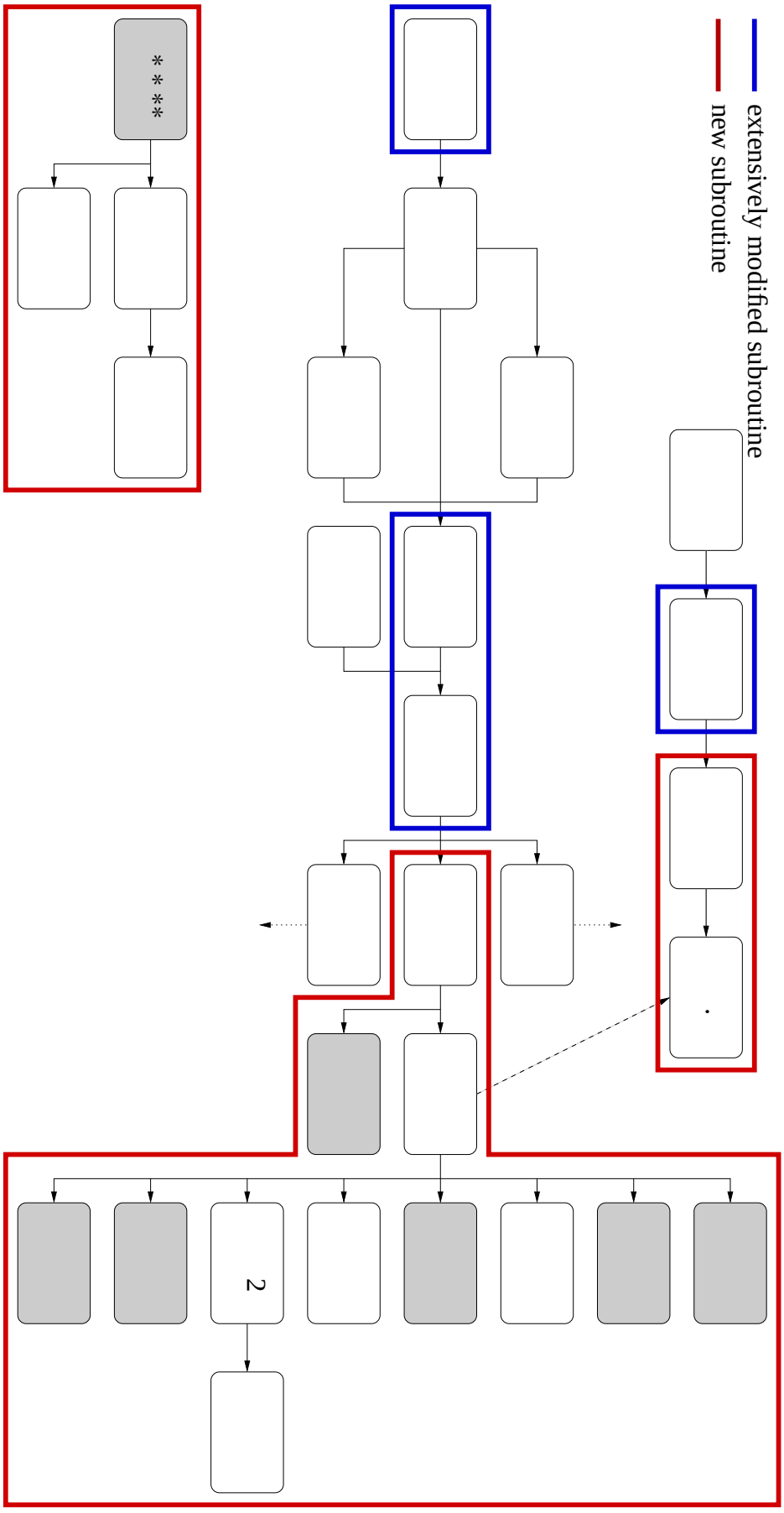

Figure 5.1: Flowchart of transition related subroutines in

- is the most important subroutine, it interpolates the data stored in . and creates an interpolated (sometimes extrapolated) stability diagram which is used to calculate the amplification rate for 601 frequencies at the current value for Re_θ.
- is the subroutine that finds the value for $\left(\frac{\omega\theta}{U}\right)_{scaled}$ for the current value of Re_θ.
- is the subroutine that finds the value of T_{maxmax} for the current value of $Re_{\theta_{crit}}$.
- is the subroutine that does a nearest neighbour interpolation to find the nine stability diagram crossections from the database that are nearest to the current Re_θ and $Re_{\theta_{crit}}$. Between these nine crossections is interpolated using a 2D Lagrange method.
- is the subroutine that finds the value of r_{top} for the current value of $Re_{\theta_{crit}}$.
- is the subroutine that performs a standard 1 Lagrange interpolation.
- 2 is the subroutine that performs the 2 Lagrange interpolation to interpolate the nine splines that describe the crossections through the relevant stability diagrams.
- is the subroutine that finds the value of the slope of $axis$ for extrapolation uses.
- is the subroutine that finds the value of $^{10}log(F_{top})$ for the current value of $Re_{\theta_{crit}}$.
- is the main routine that starts the program.
- is the subroutine that initializes all global parameters needed in xfoil. Some parameters needed for the improved e^N-method were included as well as a call to the subroutine.
- is the subroutine that does nothing more than include that large data file . .
- . is not a subroutine but included here for completeness. It holds all data connected to the stability diagrams, such as T, $axis$ and T_{max}.
- $*****$ is the collection of , , , , and .
- is the subroutine that gets the correct spline for the subroutine that calls it to find its needed variable.
- is the subroutine that evaluates splines. It is a slightly modified version of the routine given in [7]. The difference lies in that spline definitions are not uniform. The original ppvalu was made to also calculate derivatives of splines. The coefficients of these splines are thereto multiplied by an extra constant. As splines were used that lacked these extra constants, this subroutine was changed accordingly.
- is a subroutine needed by and taken from [7].

5.3 Implementation of improved e^N

The two main subroutines in the implementation of the Van Ingen Improved method are and . These are supported, as can be seen in figure 5.1, by a multitude of smaller subroutines. In the following these two main subroutines and their functions will be explained.

5.3.1

is a subroutine that is called many times, as a call occurs at each boundary layer interval at each iteration by some two to four subroutines. These intervals are divided in 2 stations, station #1 and station #2, where the first is upstream of the last. The routines function is to calculate the $\frac{dN}{dx}$ value in each interval for use in routine . This $\frac{dN}{dx}$ is the rate of change of the total N-factor, and necessary for use in . To do this calculates the $Re_{\theta_{crit}}$ from H using the correlation seen in figure 3.10. It will then check whether $Re_\theta \geq Re_{\theta_{crit}}$ to see if any amplification is present. If this is not the case and the N-factor is equal to zero, further calculation is skipped. The N-factor that was zero will remain zero. If either there is amplification or the N-factor has a non-zero value already it calls subroutine . This is to receive a vector 601 entries long which contains the values of T for that specific $Re_\theta - Re_{\theta_{crit}}$ combination for 601 different frequencies. Each frequency has its own amplification rate, be it negative (stable), zero (neutral), or positive (unstable) and is multiplied by the local nondimensional speed U, and by 10^6 to make TU. The specific level of N for each frequency is calculated for this interval in 3 different ways.

- If the frequency was stable at station #1, and remains so, the amplification factor will be set at zero.
- If the frequency was unstable at station #1 the following formula is used, irrespective of the value of T at station #2, as it is applicable to unstable and stable values for station #2.

$$dN = dxRe_c \cdot 10^{-6}(TU_1 + TU_2) \tag{5.1}$$

  Notice that damping is also permitted if either (or both) TU values are negative.

- If the frequency was stable at station #1 and will become unstable at station #2 a different formula is used to let the N-factor grow from the (in T) linearly interpolated root.

$$dN = \frac{1}{2}(dx_2 - dx_1)Re_c \cdot 10^{-6}\frac{TU_2^2}{TU_2 - TU_1} \tag{5.2}$$

Then the dominant frequency is selected. The selection is based on which frequency has the largest cumulative amplification factor at that interval. This means that the N-factor for each specific frequency at the previous interval is included. A frequency that is being damped in the current interval can still have an overall higher level of amplification due to high levels of amplification in previous intervals, and be the dominant frequency. Finally $\frac{dN}{dx}$ is calculated according to:

$$\frac{dN}{dx} = \frac{N_2 - N_1}{x_2 - x_1} \tag{5.3}$$

To increase the calculation speed the variables from station #1 and #2 are saved for future use. If iteration is going on in the same interval, the #1 values can be re-used without calculation effort. If the iteration is continued into the next interval, the #2 values will be the new #1 values. In all other cases both the #1 and #2 values will be calculated anew.

5.3.2

is intended to supply with the vector of T for the current $Re_\theta - Re_{\theta_{crit}}$ for 601 frequencies. This is done using the approach described in section 3.3. To this end the $\left(\frac{\omega\theta}{U}\right)_{scaled}$ and T_{maxmax} are determined first ($Re_{\theta_{crit}}$ is already known from H). Then using the nearest neighbour interpolation the 9 closest stability diagrams in r and $Re_{\theta_{crit}}$ direction will be determined. After that the 2 lagrange interpolation coefficients are derived from two times applying the 1 Lagrange method. (The 1 Lagrange interpolation is given in equation 3.25.) First the 1 Lagrange interpolation is used along $Re_{\theta_{crit}} = constant$, and then along $r = constant$. Now it is possible to apply these 9 interpolation coefficients to the spline coefficients of the stored stability data to create interpolated splines. This can be applied to splines describing T, $axis$ and T_{max}. However, not always there are 9 close datapoints but in that case some coefficient will be set to zero. On points outside $0 \leq r \leq 2.5$ (see figure 3.24) only one stability diagram dataset is used from each case (as the other have interpolation coefficient zero). See figures 5.2 and 5.3 for the situations with 9 available stability diagrams and with only 3 available stability diagrams. For more information on when which inter- or extrapolations are used the reader is referred to section 3.3.

There are warnings issued whenever some extrapolation is used whenever the current value of $Re_{\theta_{crit}}$ and Re_θ fall outside of the region given by $0 \leq r \leq 2.5$ and $2.216 \leq H \leq 35.944$. Also because of the working of the the program, a limit is put on the value of $Re_{\theta_{crit}}$, so it will not go higher than 4.3643 (the value corresponding with $H = 2$). The situation can occur that due to boundary layer suction the laminar value for H comes below 2. This is considered an unphysical situation and should therefore be regarded as erroneous. However this situation can sometimes occur when high boundary layer suction velocities are used, and to avoid crashing the program a $Re_{\theta_{crit}}$ value is used of 4.3643 letting the user decide whether or not to use the results.

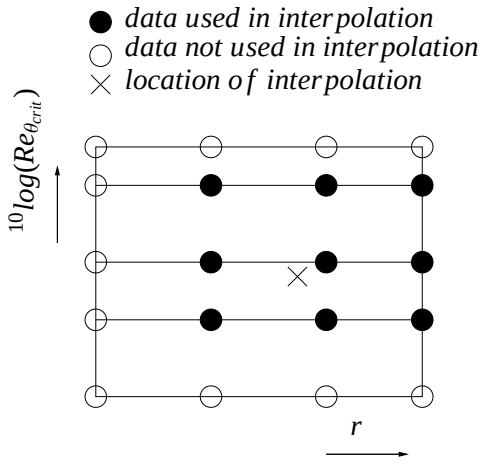

Figure 5.2: interpolation in 9 points

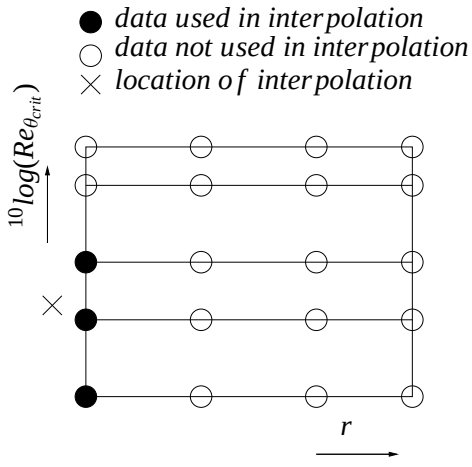

Figure 5.3: interpolation in 3 points

5.3.3 Convergence

The convergence of the boundary layer solution in is quite important and also strictly defined. If an airfoil does not meet the convergence standards, it will be not be possible to use the results in a drag polar or $C_l - C_d$ graph for instance. Therefore a solution that is nearly converged, is of no more use to the user than a solution quite some way from convergence. As was mentioned before, the Van Ingen method implemented by Ferreira [14] and adapted by Broers [1] is troubled by convergence problems. These are not caused by the method itself, but caused by interaction with the boundary layer iterations in . The problems were at the time solved by skipping to the Drela method when the N-factor nears N_{crit}. This is a reliable method that unfortunately results in a kink in the N-factor graph due to the difference in both methods. The error due to this is smaller as the value at which the switch in methods is made is nearer to N_{crit}. After the implementation of the improved e^N method it is found that similar convergence problems occur with this method. During the iterations in the boundary layer, often the H value oscillates heavily, especially at the start of iterations. As the improved e^N-method is sensitive to the H factor and allows for both damping and amplification of the N-factor this oscillating behaviour has a large impact on the predicted transition location. Due to the strong reaction of the N-factor to the changing H it can often be difficult to reach a converged solution as the transition point keeps changing position with every iteration as the boundary layer variables change. The problem occurs close to and in the transition interval as the changes in boundary layer variables are largest there due to switching between laminar and turbulent flow. One change was made in the boundary layer iteration routine that was helpful in lessening the oscillation of the shape factor H. This was to change the iteration limit for each interval from 25 to 26. It was found that all "extreme" H values occurred on odd-numbered iterations. This phenomenon is quite odd as the calculation is expected to converge on a solution, but apparently the solution is allowed to jump, but only on odd numbered iterations. The H values are still used if all iterations have finished and no converged boundary layer solution is found in that interval. Unless they seem absurd to , as then a extrapolation from the former interval is used, the non converged variables are used. These values seem agreeable for the Drela transition routine but it does not mean they do not hamper the convergence using the improved e^N-method. To counter this, the iteration limit was set to 26 which helps achieving convergence, but still more needed to be done. Several options were considered:

- Using the switching method as it exists
- Try to improve on the switching method by letting the N_{switch} get closer to N_{crit}.
- Fix the transition point put at the closest node
- Lower convergence demands by accepting larger errors in boundary layer variables.
- Use the forcing routine existing in to influence the movement of the transition point during iterations.

The first method was rejected as the Drela method to which is switched, cannot predict damping and because of the kink in the N-factor curve the result is ambiguous. The second method was tried to see whether getting the switching point close enough to the transition point would yield better results. Some success was obtained by implementing a predictor that calculates whether transition is likely to

occur in the next interval. If that is the case, a switch in methods is made. However in many cases the predictor needs to predict transition several intervals ahead for the switched method to work. A ”safety factor” can be changed by the user to have this switch occur earlier. The predictor is very basic, it predicts the expected level of the N-factor in the next interval assuming the next interval has the same value for $\frac{dN}{dx}$ as well as the same length as the current interval (in x). If for the next interval the predicted N-factor is higher than the N_{crit} value the switch is made. The user can specify this so-called safety factor with which the predicted rise in N-factor is multiplied. For instance: if a value of 2 is used, the prediction will be usually 2 intervals early with predicting transition (provided the both $\frac{dN}{dx}$ and dx do not change) and a switch is made 2 intervals in advance of the real transition interval. An example can be seen in figure 5.4. In this figure one can see the predicted N-factor. N_3 is

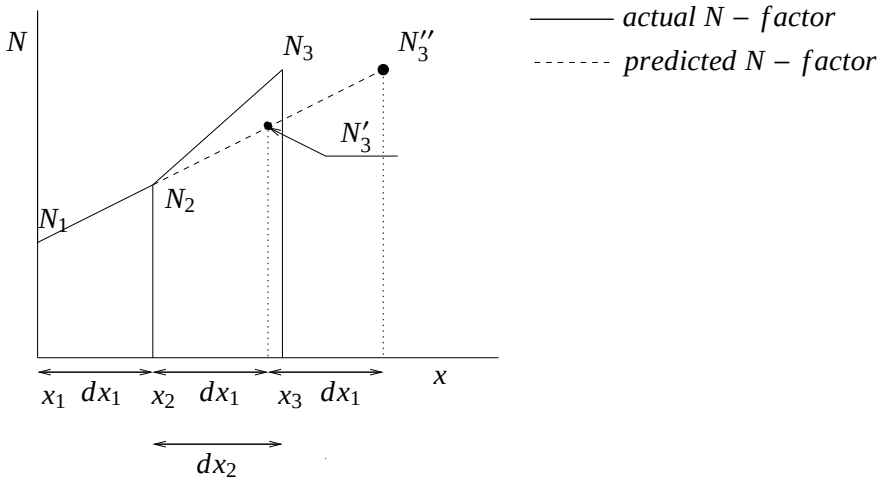

Figure 5.4: Safety factor prediction method

the actual N-factor that occurs at x_3 and the N_3' value is the predicted value for a safetyfactor of one. If however the safety factor is taken to be 2, the predicted rise in N-factor is multiplied by two and N_3'' will be the predicted value for x_3. (here the safety factor of two is represented by adding another interval dx_1) This method works and is implemented in but as it cannot predict damping in or past the area where the switch is made this was not found to be sufficient. However for the (older) Van Ingen method it is beneficial and is kept for use with this method.

Putting the transition point into the nearest node would probably not resolve the problem. The problem lies not so much in finding the transition point with every iteration but in fixation it in one location, so it becomes independent of the iterations when found. Together with lowering the convergence criteria putting the transition in a node was thought to have negative effects on the accuracy and both methods were therefore discarded.

The last method of using the forcing routine to influence convergence was considered promising. The forcing method in is a way to manually force transition at a point. If upstream of that point free transition is found, this is the transition location found. With this method, the manual forcing can still be used as was the case before. The forcing is used in 2 different ways to improve convergence:

- if the transition point in iteration i, called x_{t_i} is within 0.01% of the chord ($1 \cdot 10^{-4} \frac{x}{c}$) of the last transition point $x_{t_{i-1}}$ and no convergence is achieved, the method forces the transition to be on

this point. Then this transition point is fixed and within a few iterations usually convergence is achieved.

- if the transition point x_{t_i} is no more than 10% of the chord apart from $x_{t_{i-1}}$, and no more apart than 2% of the chord from $x_{t_{i-2}}$ (essentially when the x_t is "jumping" with every iteration between two stations maximum 10% apart and movement from these two locations of transition limited to 2%) a special treatment is used. (The maximum distance of 10% of the chord is necessary for separation bubbles, where convergence is a problem with all of the three transition methods.) When the points x_{t_i} and $x_{t_{i-1}}$ are more than 2% of the chord apart the most downstream location will be forced forward at 0.5% of the chord every iteration until the difference between them is no smaller than 2% of the chord. This is shown in figure 5.5 (every iteration this special treatment is used counts as a step in figure 5.5). Usually the transition point will be found in front of the forcing point and convergence will be reached, if not and the transition points are no more than 2% apart a slower rate of moving the downstream point closer is used. It can only then move at a rate of $\frac{1}{4}$ of the distance between the two points until they are within a distance of 0.01% of the chord at which the first forcing mechanism forces the two point on one point. The latter situation is not expected to occur in practice.

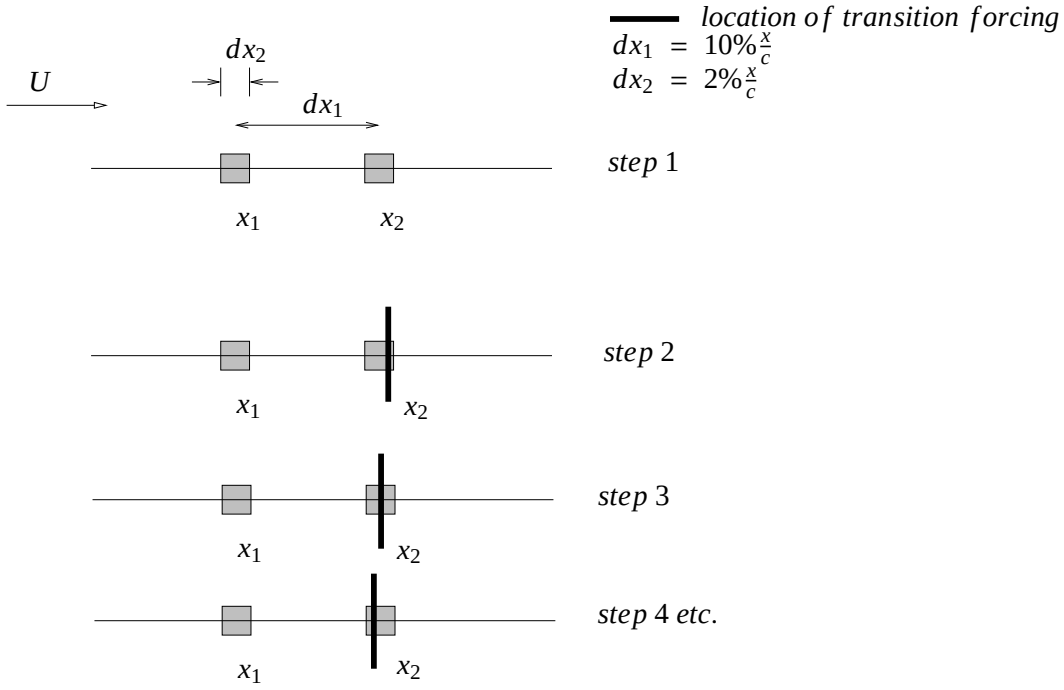

Figure 5.5: Forcing method

In the vast majority of cases in which this forcing method is used, the disturbing of an infinite loop in which the iteration can get caught, is usually enough to ensure convergence 'on the basis of a free transition point. In allowing the forcing of the transition point to move only 0.5% of the chord, it is guaranteed that the error in transition point due to this forcing is no more than this 0.5% of the chord. This is within the accuracy of the choice for N_{crit} and other errors due to (empirical) relations in the program. Some example calculations are given in table 5.1. Note that these airfoils were run with 360 panels in for accuracy reasons (see also 6.3). In this table one can see the

range of non-converged solutions transition points of the method without the forcing method and the converged solution transition points of the forcing method. In all cases the transition as calculated using the forcing method was of the free type, which means the converged transition point was found to be in front of the forcing point. The differences in most cases are small, perhaps except in the case of NACA0018, where a large separation bubble was present that gives a longer range for the non-converged transition points. In the cases where the non forcing method converges (NACA0012 and the lower surface of NACA1912) there is no difference between the methods. This reinforces the thought that the forcing method has no significant effect on the transition location, only on the convergence.

Table 5.1: Transition points for different convergence improvements

airfoil	transition ($\frac{x}{c}$) forcing method		transition ($\frac{x}{c}$) without forcing method
NACA0012	top:	0.4913	0.4890 - 0.4937*
$\alpha = 1, Re_c = 1 \cdot 10^6$	bottom:	0.6749	0.6738 - 0.6754 *
Flat plate airfoil	top:	0.4271	0.4271 *
$\alpha = 1.33, Re_c = 5 \cdot 10^6$	bottom:	0.8819	0.8817 - 0.8825 *
NACA4415	top:	0.7016	0.6998 - 0.7045 *
$\alpha = 1, Re_c = 1 \cdot 10^5$	bottom:	1.000	1.000 *
$NACA64_2$-A-215	top:	0.5567	0.5567 - 0.5568 *
$\alpha = 0, Re_c = 2.75 \cdot 10^6$	bottom:	0.5469	0.5469 *
NACA1912	top:	0.0572	0.0571 *
$\alpha = 5, Re_c = 1 \cdot 10^6$	bottom:	0.7762	0.7757 - 0.7768 *
NACA0018	top:	0.6393	0.6389 - 0.6406 *
$\alpha = 2, Re_c = 1 \cdot 10^5$	bottom:	0.8761	0.8696 - 0.8872 *

* = non-converged solution (2 values denote the maximum range of non converged solutions obtained)

Chapter 6

Validation

6.1 Test Airfoils

Before the validation phase can be started some test airfoils need to be chosen. The test airfoils need to represent all flow phenomena that can occur on airfoils in which the improved e^N-method is expected to be used. In this light 7 cases are tested, using 4 different airfoils. These are mentioned in table 6.1. Some other cases were considered in addition to the ones mentioned in table 6.1. These cases were mainly theoretical cases such as the Rheinboldt strip suction and a flat plate with boundary layer suction. These cases are shown in this section, but further analysis was abandoned as their results are considered unphysical due to a wrong handling of the boundary layer by 's boundary layer equations. This conclusion is however of such importance that these cases were included in section 6.2. Some applications of the Improved e^N-method to more "theoretical flows" can be found in [53].

Table 6.1: Studied Airfoils

name airfoil	Re_c	α	suction used
NACA0012	$1 \cdot 10^6$	3°	no
NACA0012	$1 \cdot 10^6$	0°	no
NACA0012	$1 \cdot 10^6$	0°	yes, between 25% $\frac{x}{c}$ and 55 % $\frac{x}{c}$,$base \cdot 1$
NACA0012	$1 \cdot 10^6$	0°	yes, between 25% $\frac{x}{c}$ and 55 % $\frac{x}{c}$,$base \cdot 2$
NACA0018	$1 \cdot 10^5$	2°	no
"Flat Plate Airfoil"	$5 \cdot 10^6$	1.33°	no
$NACA64_2$-A-215 airfoil	$2.75 \cdot 10^6$	0°	no

Of the testcases NACA0012 is used because it is so well studied and gives a classic pressure distribution of an adverse pressure gradient on the suction side of the airfoil and a partly favourable pressure gradient on the pressure side. This airfoil is first studied with an angle of attack of 3° and then with a zero angle of attack. At zero angle of attack also suction on the upper airfoil side is used, in between 25% $\frac{x}{c}$ and 55 % $\frac{x}{c}$ with a strength as calculated by the first iteration of the routine present

in in the menu. The base suction distribution is given in equation 6.1 and taken from Broers [1].

$$\frac{v_0}{U_\infty} = \frac{1}{0.2205} \frac{1}{\frac{U}{U_\infty}} \frac{d(\frac{U}{U_\infty})}{d(\frac{x}{c})} \frac{Re_\theta}{Re_c} \tag{6.1}$$

In this equation as a first iteration the Re_θ is assumed constant over the area to which the suction is applied. It is a first attempt to achieve laminar flow in the area it is used in. Here its objective was solely to test a realistic suction distribution so no more iteration cycles are used and this basic suction distribution is used right away. The case in which it is doubled represents a case in which heavy suction is used, where theoretically the N-factor will become zero again. The NACA0012 airfoil was also calculated with the single and the double amount of suction provided by . Both suction distributions are shown in figures 6.5 and 6.6. The pressure distributions of all three of the NACA0012 cases are shown in figures 6.1 to 6.4. In the $C_p - x$ figures 6.1 to 6.14 the dotted lines represents the inviscid solution by , the red line represents the upper surface viscous solution and the blue line represents the lower surface viscous solution.

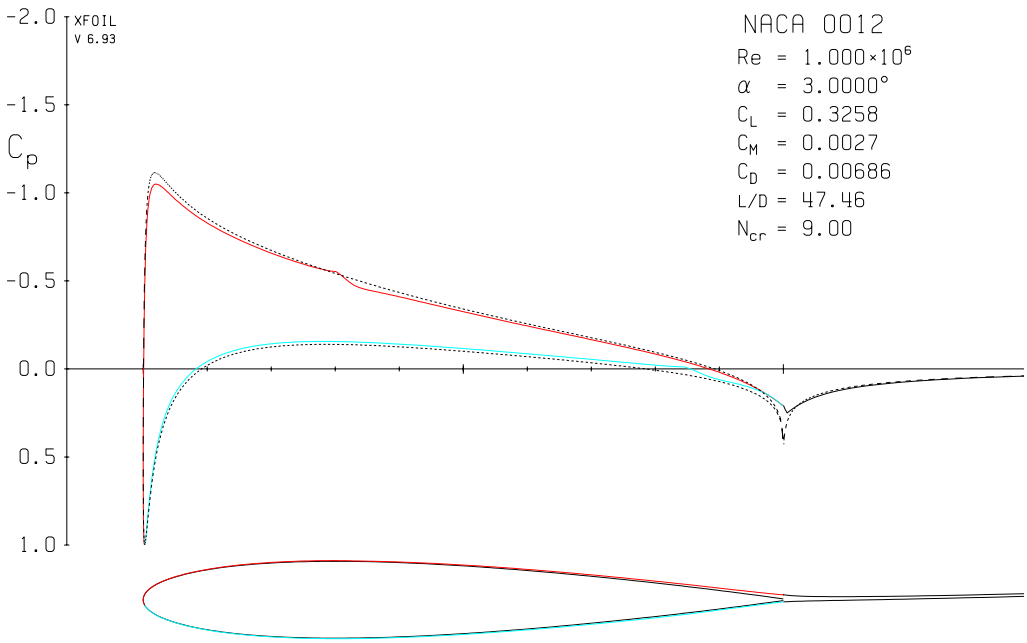

Figure 6.1: C_p NACA0012 for $\alpha = 3°$, $Re_c = 1 \cdot 10^6$, no suction

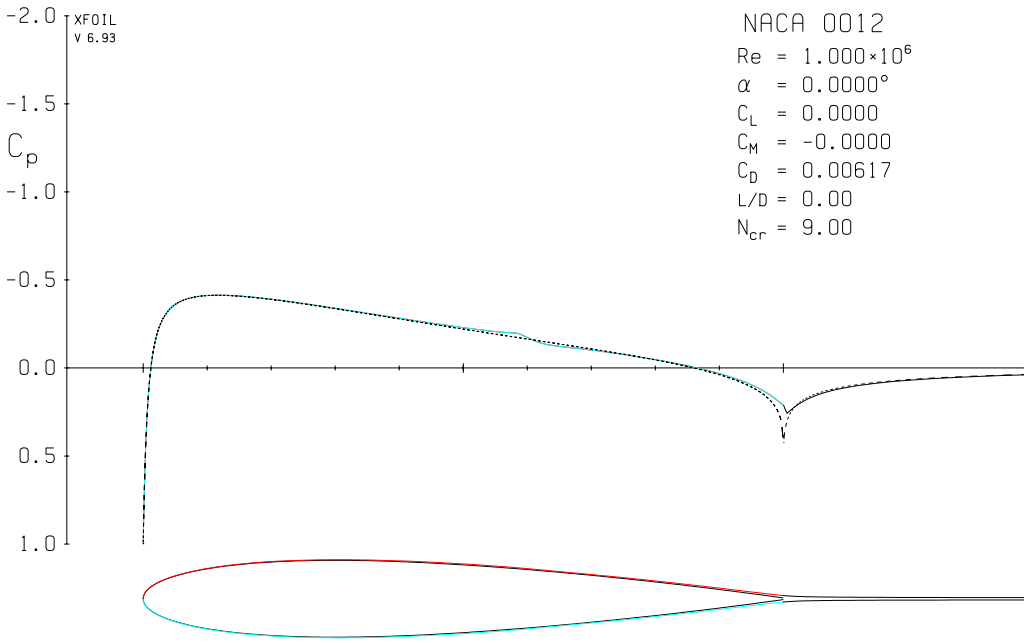

Figure 6.2: C_p for NACA0012 at $\alpha = 0°$, $Re_c = 1 \cdot 10^6$, no suction

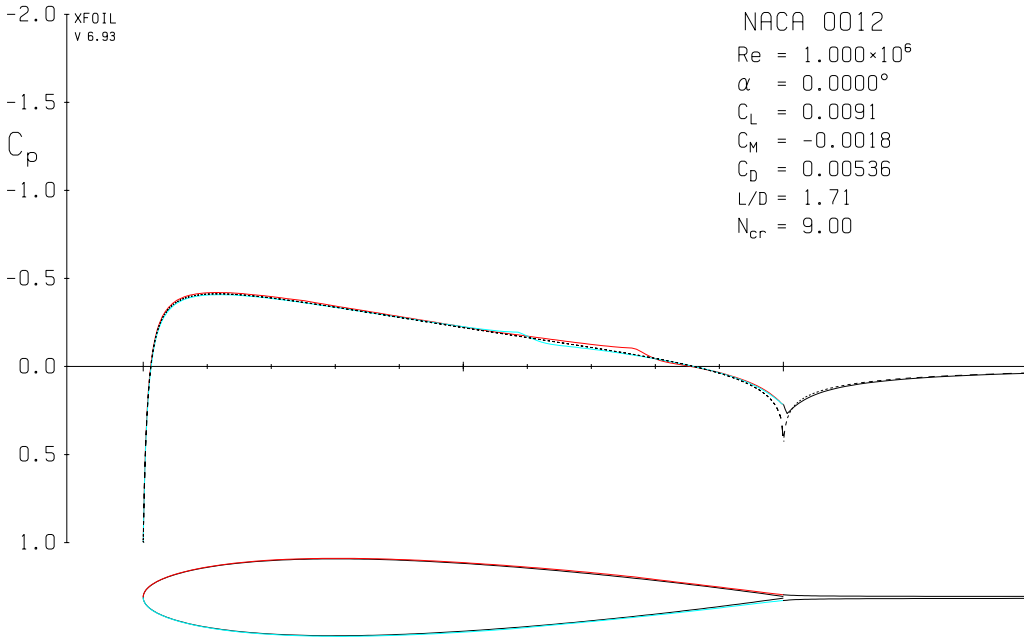

Figure 6.3: C_p for NACA0012 at $\alpha = 0°$, $Re_c = 1 \cdot 10^6$, base suction

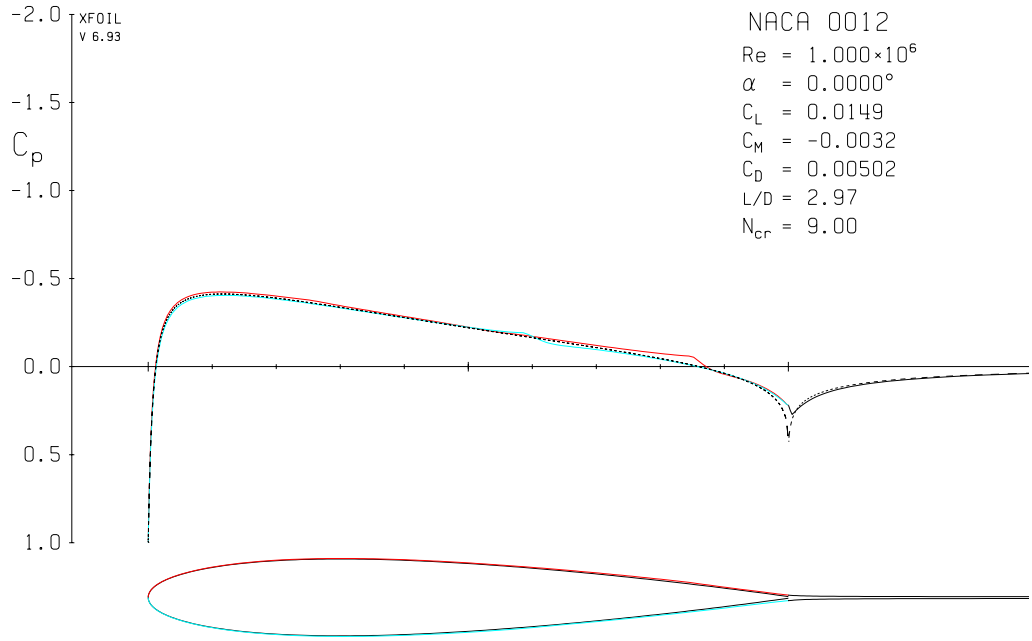

Figure 6.4: C_p for NACA0012 at $\alpha = 0°$, $Re_c = 1 \cdot 10^6$, $2 \cdot$ base suction

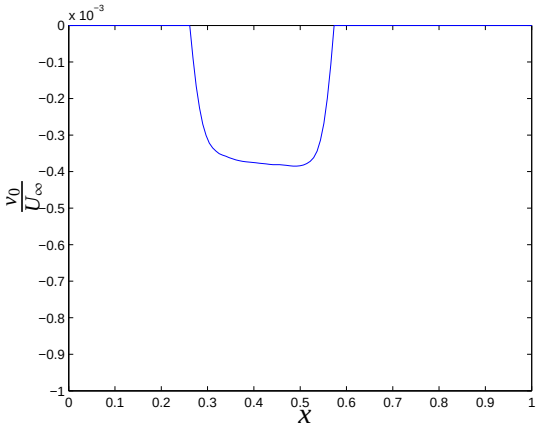

Figure 6.5: suction distribution *base* for NACA0012 $\alpha = 0°$, $Re_c = 1 \cdot 10^6$

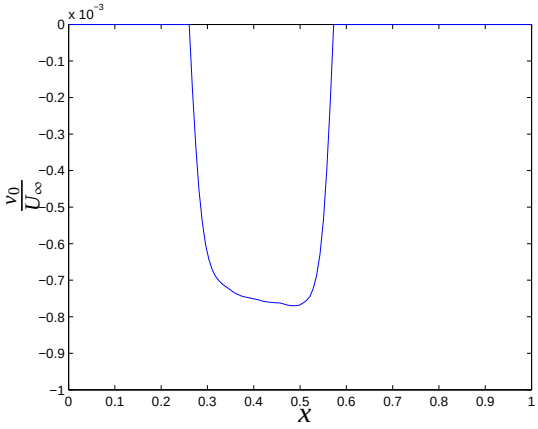

Figure 6.6: suction distribution $2 \cdot$ *base* for NACA0012 $\alpha = 0°$, $Re_c = 1 \cdot 10^6$

NACA0018 was used to check the handling of large separated flow areas. Its pressure distribution is shown in figure 6.7. At the low Reynolds number large areas of separated flow will occur. This can be seen in figure 6.8 where the skin friction is shown.

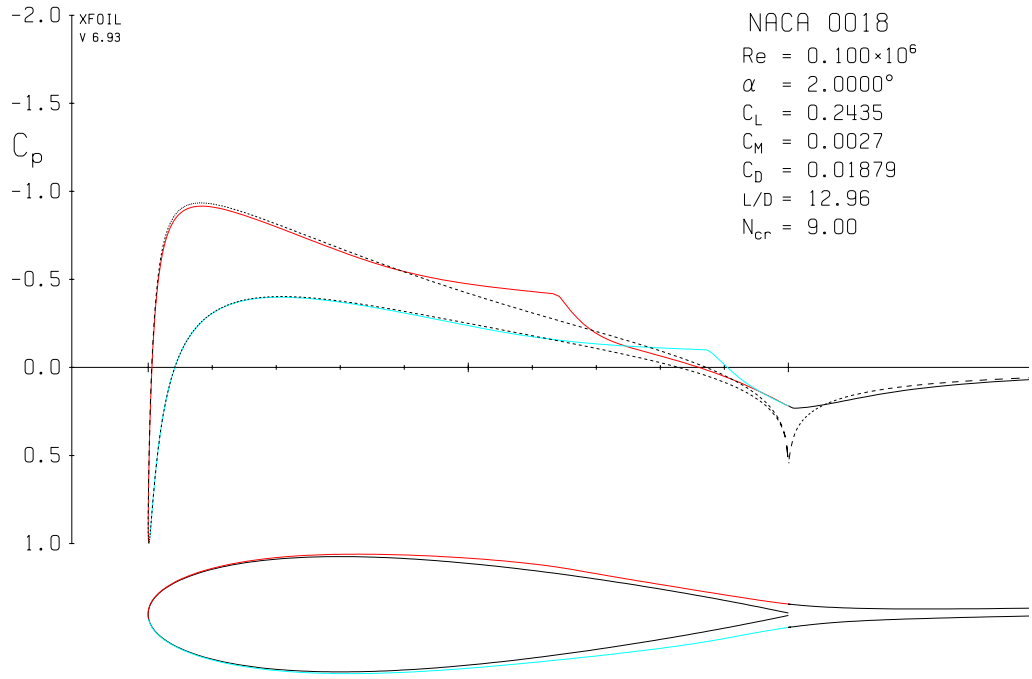

Figure 6.7: C_p for NACA0018 at $\alpha = 2°$, $Re_c = 1 \cdot 10^5$

The ”flat plate airfoil” is an airfoil which has an almost flat plate pressure distribution on the lower surface at an angle of attack of 1.33° and is taken from [14]. The airfoil's resemblance to a flat plate flow is checked in a few ways. The pressure distribution can be found in figure 6.9. This shows apart from the very start at the leading edge and the area close to the trailing edge a pressure coefficient of zero (although any constant pressure would suffice), as it would need to be to resemble a flat plat boundary layer. Also the development of the momentum thickness represented by Re_θ is compared in figure 6.10 and 6.11 to the Re_θ according to Blasius:

$$\frac{\theta}{x} = \frac{0.664}{\sqrt{Re_x}} \tag{6.2}$$

Apart from the very start as already mentioned the agreement is good. When one studies the shape factor in figure 6.12 at first it seems to be quite close to 2.591, the value for the Blasius solution. However on close inspection the shape factor seems to be 2.56, thus a little short of 2.591. Later on the consequences of this are shown. As to the reason this value is not closer to the flat plate value, one must look at equations 4.10 to 4.19. In these laminar boundary layer equations nor in the closure relations a pressure coefficient of 0 is guaranteed to yield a shape factor of 2.591. As already seen in figure 6.10, the momentum thickness θ is in good agreement with the flat plate value, so a difference in shape factor must originate in the displacement thickness δ^*.

As the last airfoil NACA64_2-A-215 was used, as it is an airfoil studied in Van Ingens dissertation and

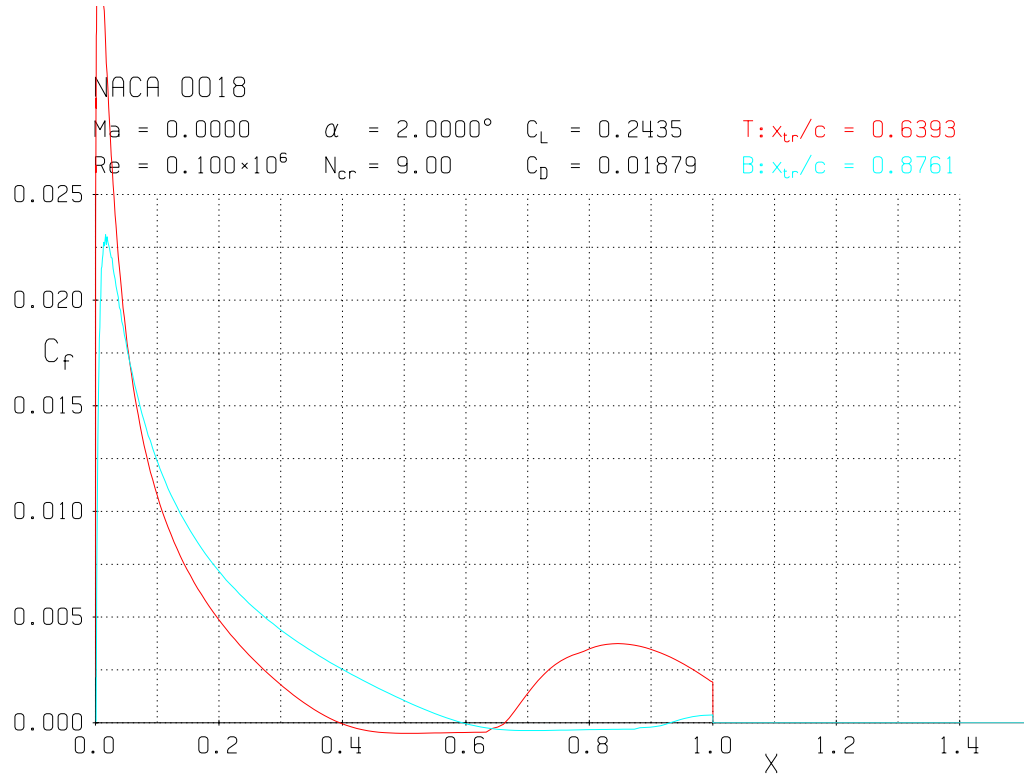

Figure 6.8: C_f for NACA0018 at $\alpha = 2°$, $Re_c = 1 \cdot 10^5$, upper surface (red), lower surface (cyan)

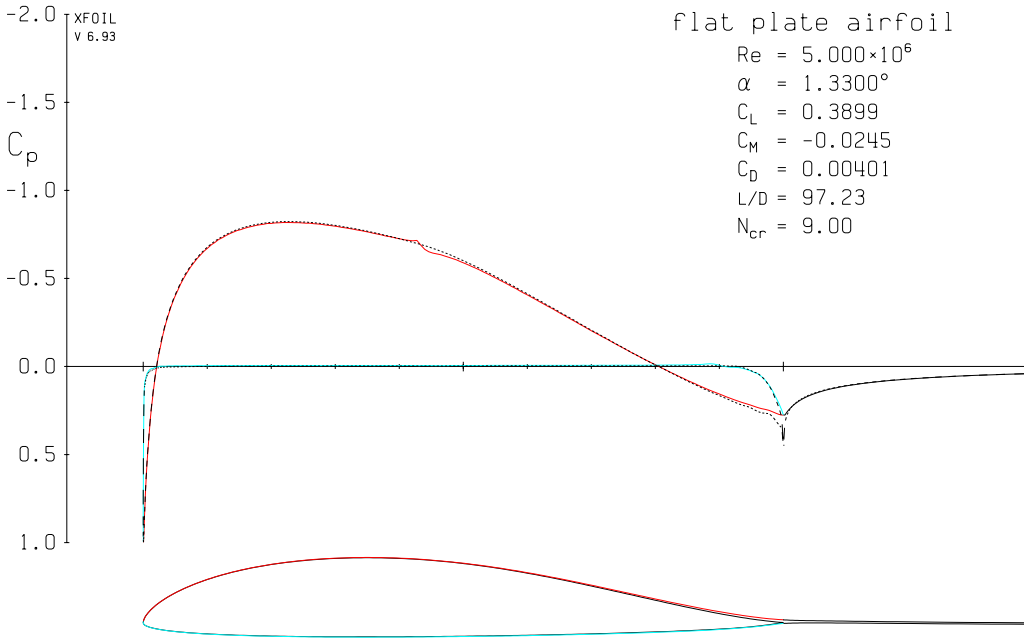

Figure 6.9: C_p for "flat plate airfoil" at $\alpha = 1.33°$, $Re_c = 5 \cdot 10^6$

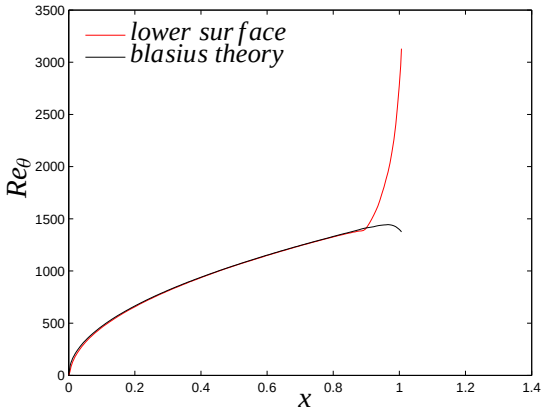

Figure 6.10: Comparison of Re_θ for the "flat plate airfoil" and the Blasius solution

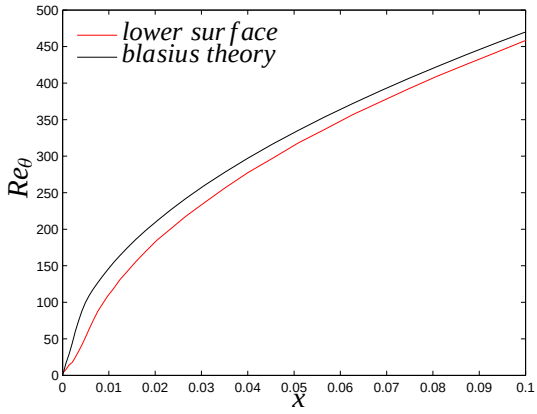

Figure 6.11: Zoomed in comparison of Re_θ for the "flat plate airfoil" and the Blasius solution

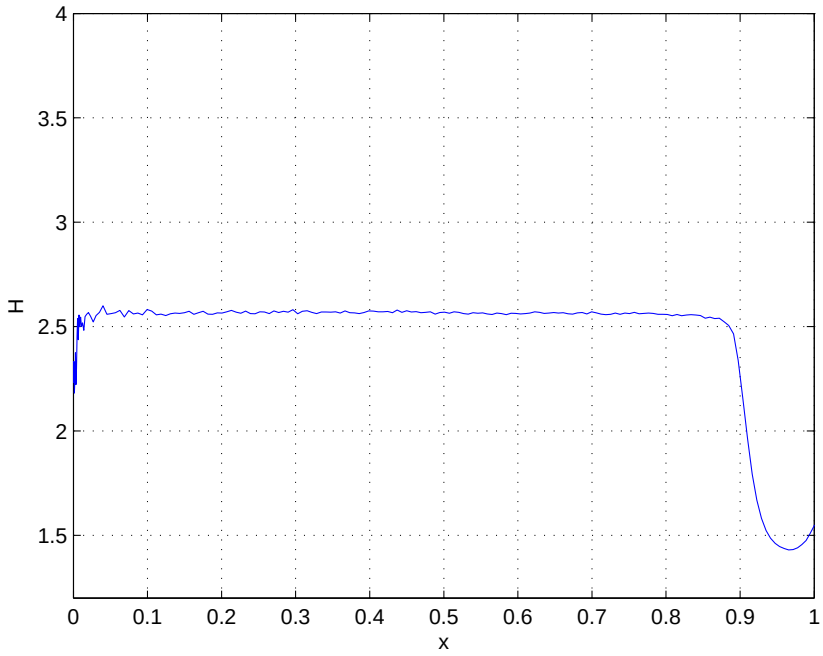

Figure 6.12: H for flat plate airfoil at $\alpha = 1.33°$,$Re_c = 5 \cdot 10^6$

for which some data are available. Unfortunately the data gathered in the windtunnel is influenced by the large size of the model. Therefore no good comparison could be made between calculated data and measured data and from here onwards only calculated data is used. The airfoil pressure distribution according to the data in [51] is shown in figure 6.13. This pressure distribution is only the calculated inviscid distribution that clearly shows bumps on the upper surface near the nose, and at around 60% of the chord on the lower surface. The reason for this behaviour is that the nose is not well defined and has a dimple. In Van Ingens research [51] the same phenomenon was found in the windtunnel model made up from these coordinates, and it was resolved by smoothing out the surface. The same is done on the numerical model in . The oscillatory behaviour on the lower surface however was not found on the windtunnelmodel. This because it stems from a numerical feature of the airfoil. The NACA64_2-A-215 has a straight line on the lower surface from 59% of the chord to the trailing edge which produces a small kink in the curvature of the airfoil profile. Due to this kink, the 2^{nd} derivative is no longer continuous. Due to this effect the vorticity is forced to a higher value. This bump in the pressure distribution was also removed by making the airfoil smoother at that spot. The corrections made on the NACA64_2-A-215 result in the new pressure distribution seen in figure 6.14.

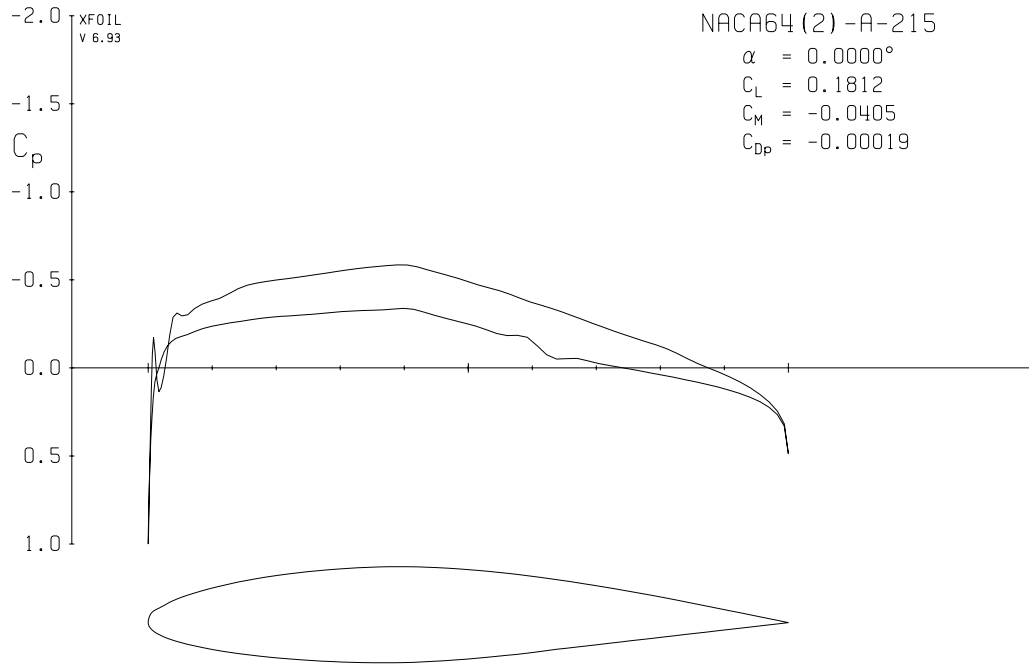

Figure 6.13: C_p for uncorrected NACA64_2-A-215 at $\alpha = 0°$, $Re_c = 2.75 \cdot 10^6$

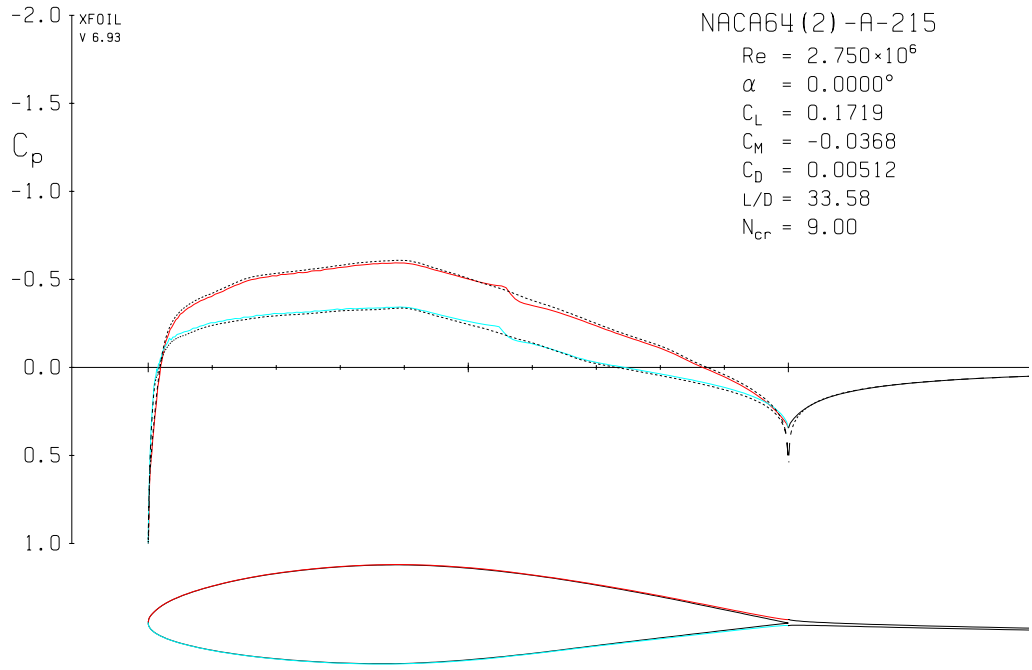

Figure 6.14: C_p for corrected NACA64$_2$-A-215 at $\alpha = 0°$, $Re_c = 2.75 \cdot 10^6$

6.2 Abandoned Test Cases

The dropped test cases are the Rheinboldt strip suction and high suction velocity employed on a flat plate. As can only handle airfoils and can handle no single flat plate, the ”flat plate airfoil” is used in both cases. Other approaches in getting a flat plate boundary layer have proven unsuccessful, because either no constant C_p distribution could be achieved or because a very thin plate results in poor numerical accuracy in . The Rheinboldt strip suction proved to be unpractical for as the very high suction velocity employed over a small strip prevented convergence of the boundary layer solution. This leaves only the flat plate with high suction velocity, with the suction not as high so as to prevent convergence. The suction is only applied to the lower surface of the ”flat plate airfoil”.In figure 6.15 the pressure distribution is shown, in figure 6.16 and in figures 6.17 to 6.20 the shape factor and the N factor are given. It must be stressed that the solution with a laminar shape factor of less than 2 is considered unphysical, and that therefore this solution cannot be considered to be correct. It is instructive nonetheless in showing the faulty behaviour of the boundary layer routines in . This test case is abandoned for the rest of the calculations as the boundary layer variables seem to be erroneous.

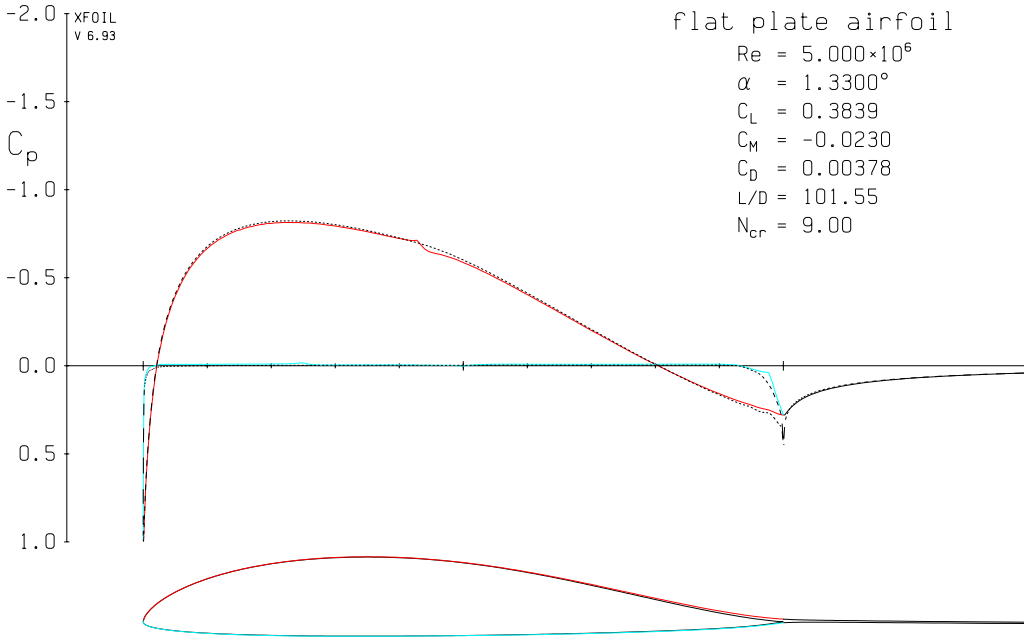

Figure 6.15: C_p for flat plate suction airfoil at $\alpha = 1.33°$, $Re_c = 5 \cdot 10^6$

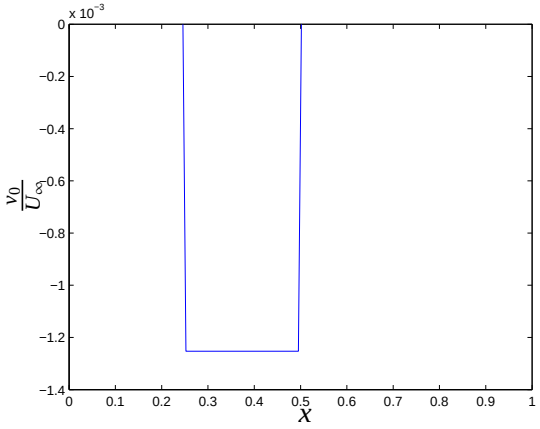

Figure 6.16: v_0 for flat plate suction airfoil at $\alpha = 1.33°$, $Re_c = 5 \cdot 10^6$

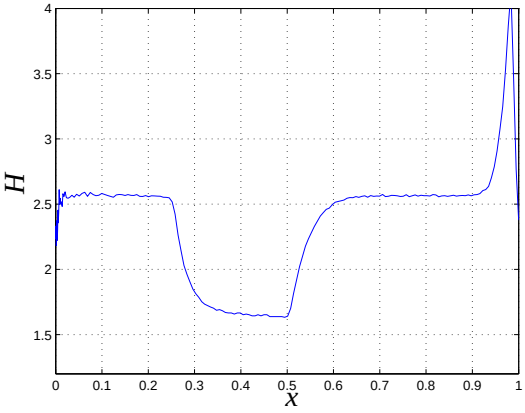

Figure 6.17: H for flat plate suction airfoil at $\alpha = 1.33°$, $Re_c = 5 \cdot 10^6$, lower surf.

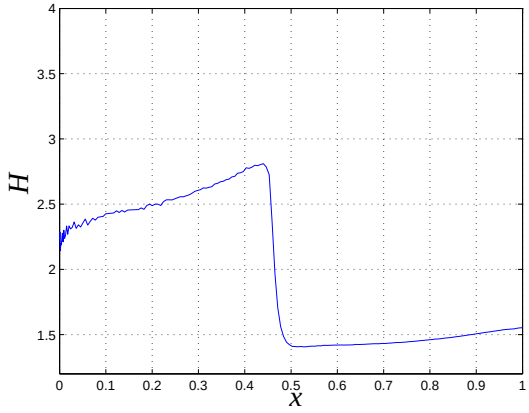

Figure 6.18: H for flat plate suction airfoil at $\alpha = 1.33°$, $Re_c = 5 \cdot 10^6$, upper surf.

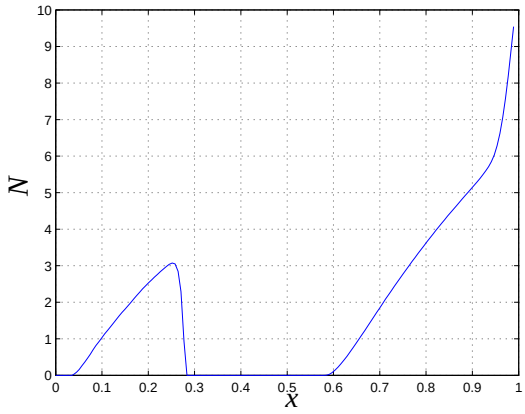

Figure 6.19: N for flat plate suction airfoil at $\alpha = 1.33°$, $Re_c = 5 \cdot 10^6$, lower surf.

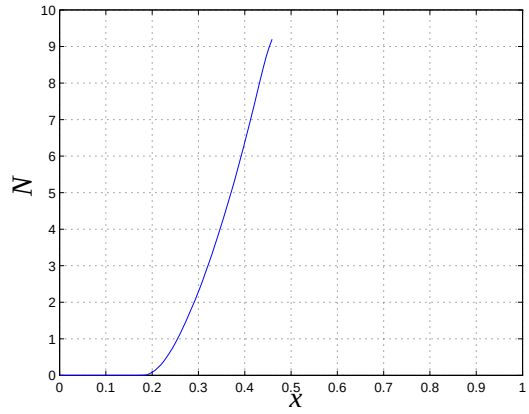

Figure 6.20: N for flat plate suction airfoil at $\alpha = 1.33°$, $Re_c = 5 \cdot 10^6$, upper surf.

6.3 Grid convergence

Before any airfoils were calculated using , a grid convergence study was made. The default number of panels for nowadays is 160 panels (originally it was 120, later changed into 140 and then to 160), which is supposed to give a high resolution solution. As a comparison will be made of different transition methods the objective is to isolate as much as possible other factors that can influence the transition calculation. The panel density is one of the factors that can have an influence on transition. To reduce the contribution of the error in transition location as much as possible a grid convergence study is made of the airfoils that are used. The results of this can be seen in figures 6.21 to 6.34. As the scale of the figures differs a lot arrows are added that give approximately 1% of chord length. Notice that for the suction surfaces (figures 6.26 and 6.28) the convergence is especially bad.

The panelling of the airfoils is given in appendix B.

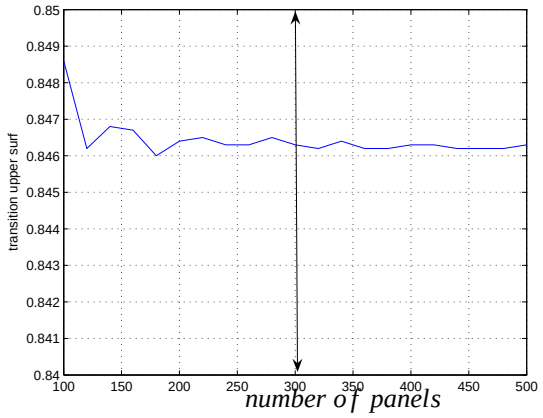

Figure 6.21: $x_{transition}$ lower surface for NACA0012 $\alpha = 3°$, $Re_c = 1 \cdot 10^6$

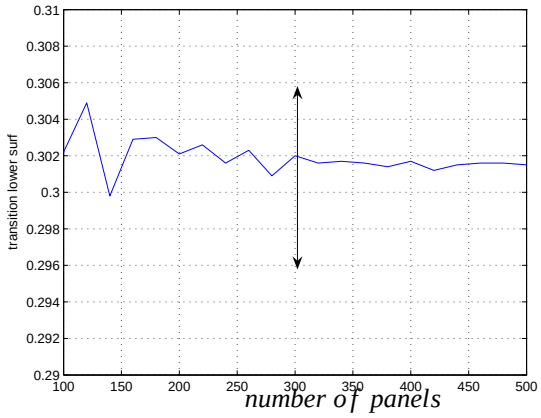

Figure 6.22: $x_{transition}$ upper surface for NACA0012 $\alpha = 3°$, $Re_c = 1 \cdot 10^6$

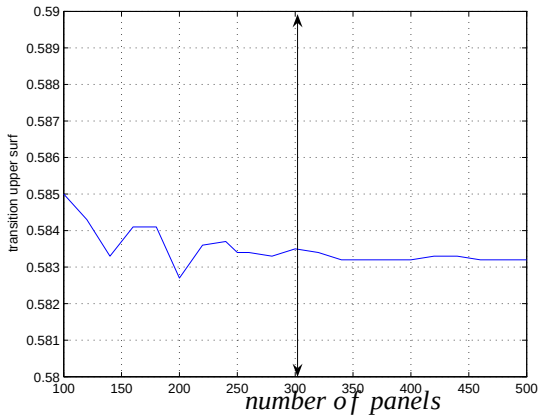

Figure 6.23: $x_{transition}$ lower surface for NACA0012 $\alpha = 0°$, $Re_c = 1 \cdot 10^6$, no suction

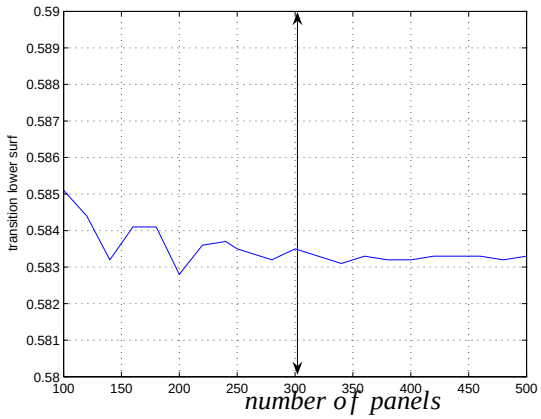

Figure 6.24: $x_{transition}$ upper surface for NACA0012 $\alpha = 0°$, $Re_c = 1 \cdot 10^6$, no suction

As can be seen in figures 6.21 to 6.34 the transition location sometimes varies quite a bit in the region

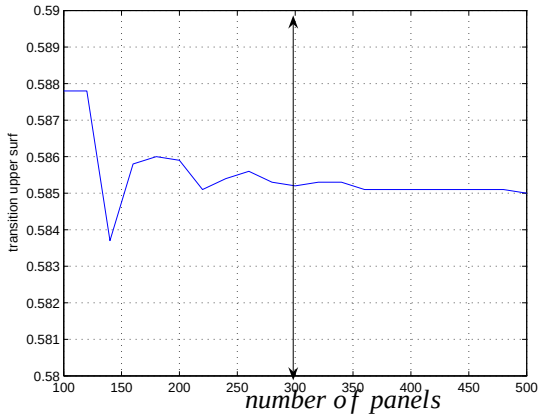

Figure 6.25: $x_{transition}$ lower surface for NACA0012 $\alpha = 0°$, $Re_c = 1 \cdot 10^6$, suction *base*

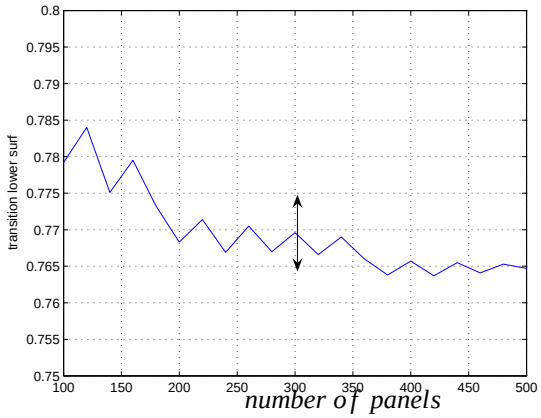

Figure 6.26: $x_{transition}$ upper surface for NACA0012 $\alpha = 0°$, $Re_c = 1 \cdot 10^6$, suction *base*

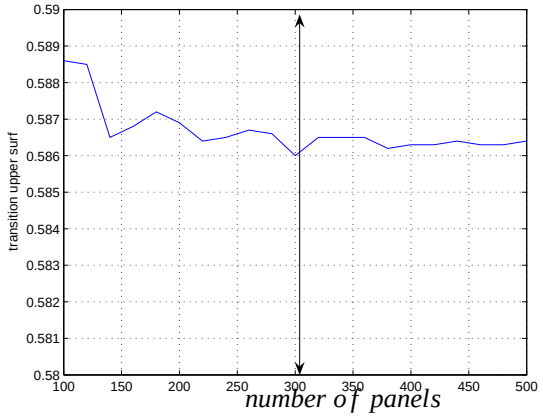

Figure 6.27: $x_{transition}$ lower surface for NACA0012 $\alpha = 0°$, $Re_c = 1 \cdot 10^6$, suction $2 \cdot base$

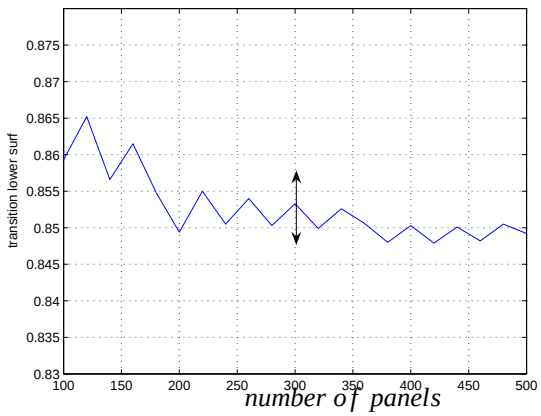

Figure 6.28: $x_{transition}$ upper surface for NACA0012 $\alpha = 0°$, $Re_c = 1 \cdot 10^6$, suction $2 \cdot base$

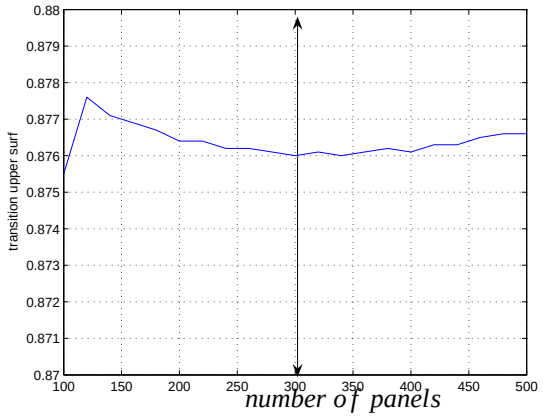

Figure 6.29: $x_{transition}$ lower surface for NACA0018 $\alpha = 2°$, $Re_c = 1 \cdot 10^5$

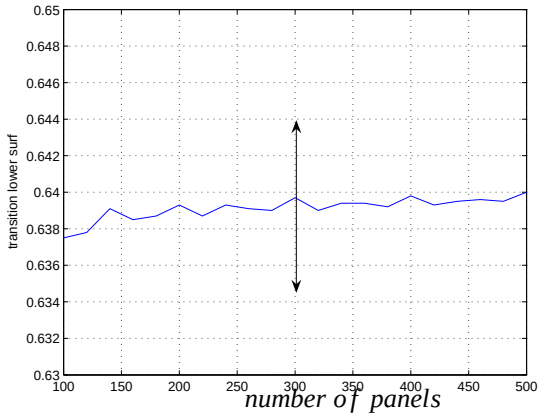

Figure 6.30: $x_{transition}$ upper surface for NACA0018 $\alpha = 2°$, $Re_c = 1 \cdot 10^5$

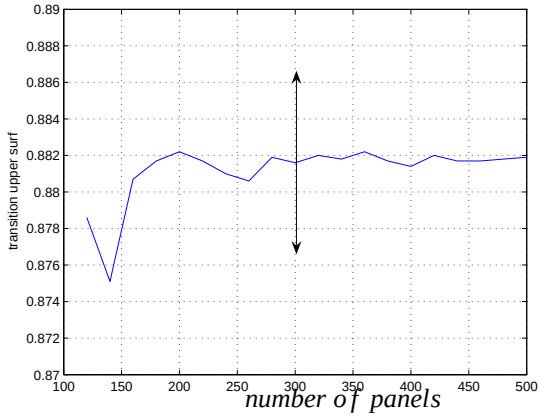

Figure 6.31: $x_{transition}$ lower surface for flat plate airfoil$\alpha = 1.33°$, $Re_c = 5 \cdot 10^6$,

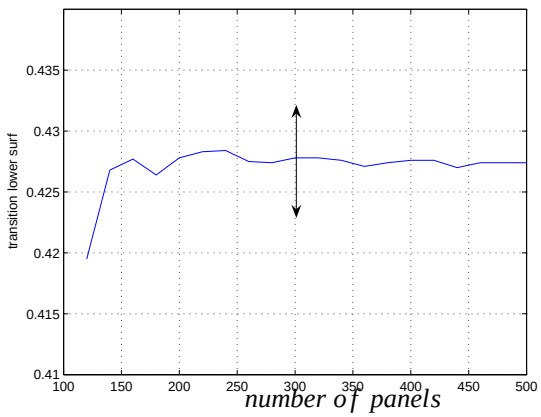

Figure 6.32: $x_{transition}$ upper surface for flat plate airfoil $\alpha = 1.33°$, $Re_c = 5 \cdot 10^6$

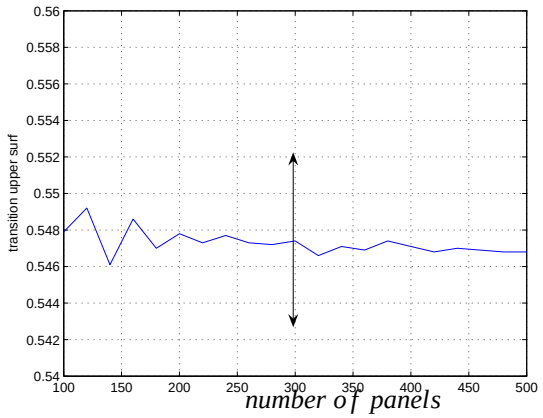

Figure 6.33: $x_{transition}$ lower surface for NACA64$_2$-A-215 $\alpha = 0°$, $Re_c = 2.75 \cdot 10^6$

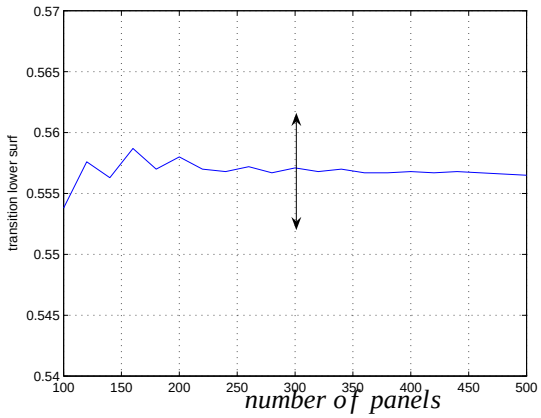

Figure 6.34: $x_{transition}$ upper surface for NACA64$_2$-A-215 $\alpha = 0°$, $Re_c = 2.75 \cdot 10^6$

with less than 200 panels. The oscillations vary in size from airfoil to airfoil. But for all airfoils the oscillations are small at around 360 panels, and therefore this is the number of panels used for all airfoils. The error in transition location due to the panelling of the airfoil is no more than $0.0025\frac{x}{c}$ (or 0.25% of the chord) in any of the evaluated cases (having 360 panels) and is considered small with regard to the other errors present in the total handling of the airfoil and the transition method and will from here on be neglected.

6.4 Validation of transition method

In the case of the improved e^N-method the validation is done by a select group of airfoils given in table 6.1. These airfoils are selected in such a way that most flow phenomena usually encountered in airfoils are represented, such as favourable and adverse pressure gradients, large separated flow areas and boundary layer suction. These airfoils (upper and lower surface) were calculated using a total of 360 panels. Then the N-factor as calculated by with the implemented improved e^N-method is compared to the routine of the improved e^N-method as made by Van Ingen. As input for the routine the boundary layer variables (H, Re_θ, $\bar{u}$) as they were calculated by were used. In figures 6.1 to 6.40 the results for the NACA0012 at $\alpha = 3°$ and $Re_c = 1 \cdot 10^6$ are shown. Figure 6.1 gives the pressure distribution, figures 6.35 and 6.36 give the shape factor for the lower and upper surface, figures 6.37 and 6.38 give the ${}^{10}log(Re_\theta)$ and ${}^{10}log(Re_{\theta_{crit}})$ for the lower and upper surfaces, and figures 6.39 and 6.39 give the N-factor for the upper and lower surfaces as calculated by the routine implemented into (in red) and the routine (in blue). For the other airfoils only the figure of the pressure distribution and the N-factor are shown, but in appendix C all figures are shown for all test case airfoils.

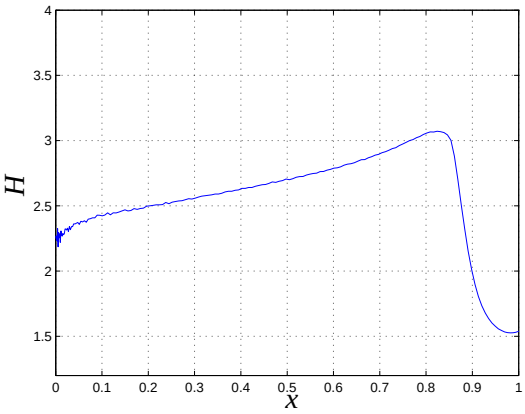

Figure 6.35: H for NACA0012 $\alpha = 3°$, $Re_c = 1 \cdot 10^6$, lower surf.

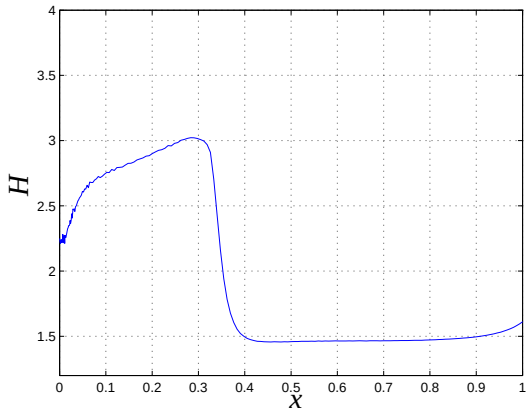

Figure 6.36: H for NACA0012 $\alpha = 3°$, $Re_c = 1 \cdot 10^6$, upper surf.

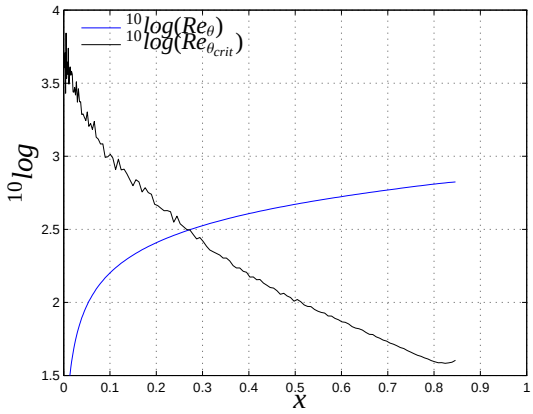

Figure 6.37: Re_θ and $Re_{\theta_{crit}}$ for NACA0012 $\alpha = 3°$, $Re_c = 1 \cdot 10^6$, lower surf.

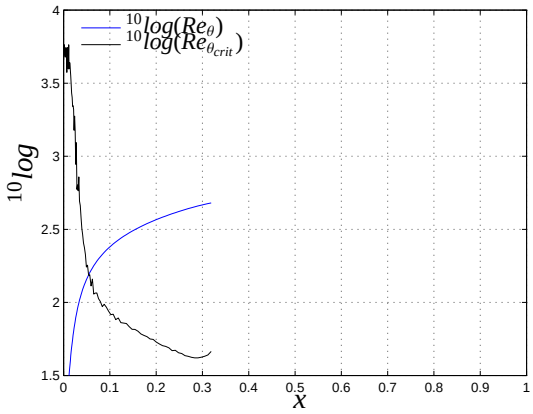

Figure 6.38: Re_θ and $Re_{\theta_{crit}}$ for NACA0012 $\alpha = 3°$, $Re_c = 1 \cdot 10^6$, upper surf.

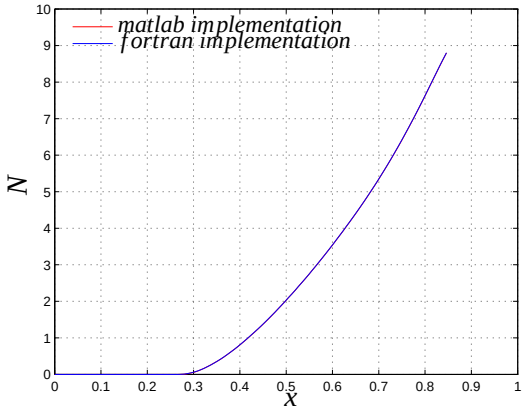

Figure 6.39: N for NACA0012 $\alpha = 3°$, $Re_c = 1 \cdot 10^6$, lower surf.

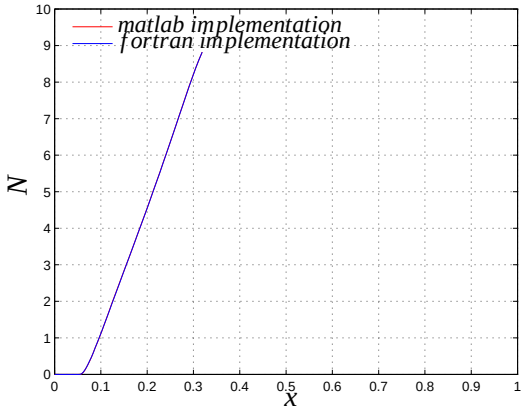

Figure 6.40: N for NACA0012 $\alpha = 3°$, $Re_c = 1 \cdot 10^6$, upper surf.

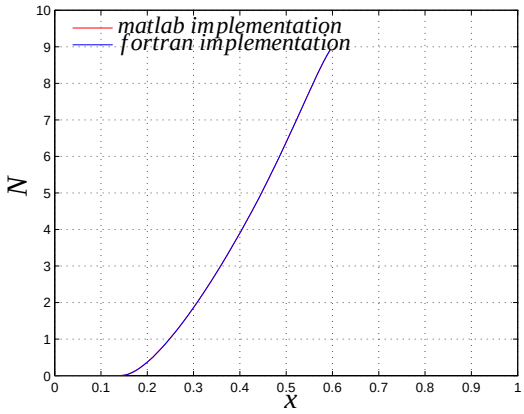

Figure 6.41: N for NACA0012 at $\alpha = 0°$, $Re_c = 1 \cdot 10^6$, no suction, lower surf.

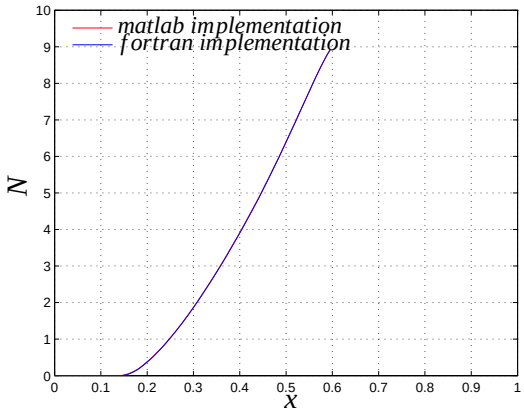

Figure 6.42: N for NACA0012 at $\alpha = 0°$, $Re_c = 1 \cdot 10^6$, no suction, upper surf.

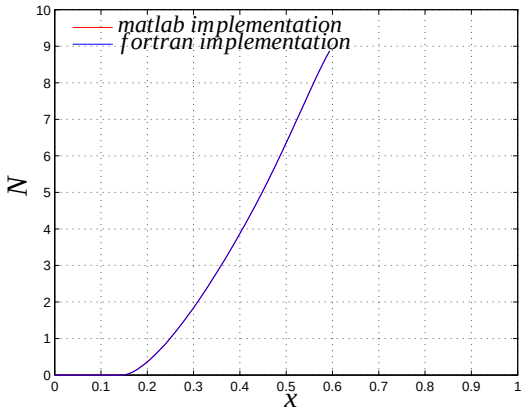

Figure 6.43: N for NACA0012 at $\alpha = 0°$, $Re_c = 1 \cdot 10^6$, base suction, lower surf.

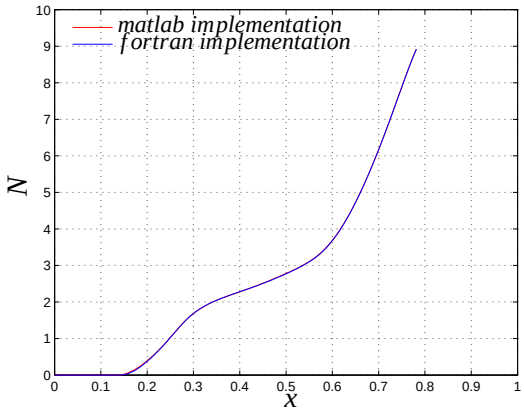

Figure 6.44: N for NACA0012 at $\alpha = 0°$, $Re_c = 1 \cdot 10^6$, base suction, upper surf.

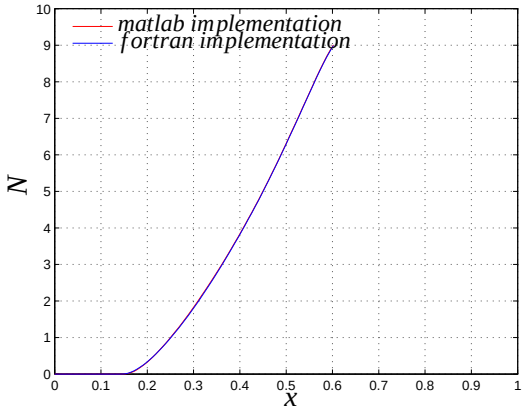

Figure 6.45: N for NACA0012 at $\alpha = 0°$, $Re_c = 1 \cdot 10^6$, $2 \cdot$ base suction, lower surf.

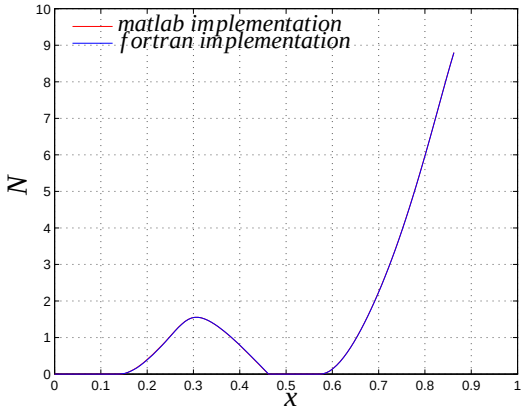

Figure 6.46: N for NACA0012 at $\alpha = 0°$, $Re_c = 1 \cdot 10^6$, $2 \cdot$ base suction, upper surf.

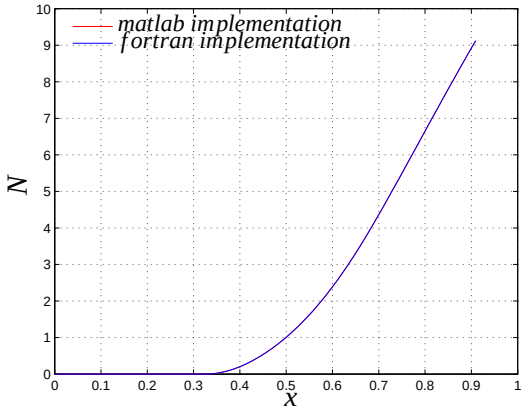

Figure 6.47: N for NACA0018 at $\alpha = 2°$, $Re_c = 1 \cdot 10^5$, lower surf.

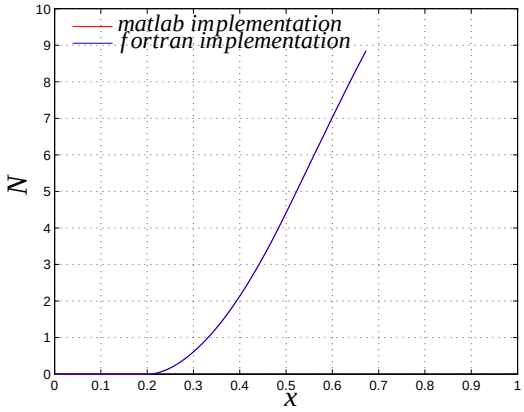

Figure 6.48: N for NACA0018 at $\alpha = 2°$, $Re_c = 1 \cdot 10^5$, upper surf.

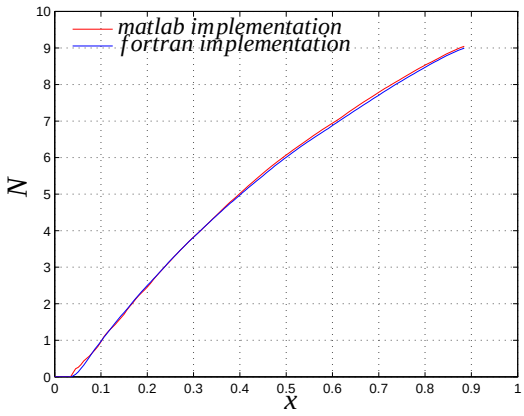

Figure 6.49: N for flat plate airfoil at $\alpha = 1.33°$, $Re_c = 5 \cdot 10^6$, lower surf.

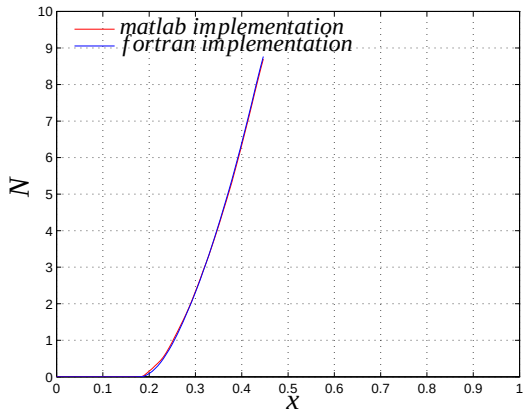

Figure 6.50: N for flat plate airfoil at $\alpha = 1.33°$, $Re_c = 5 \cdot 10^6$, upper surf.

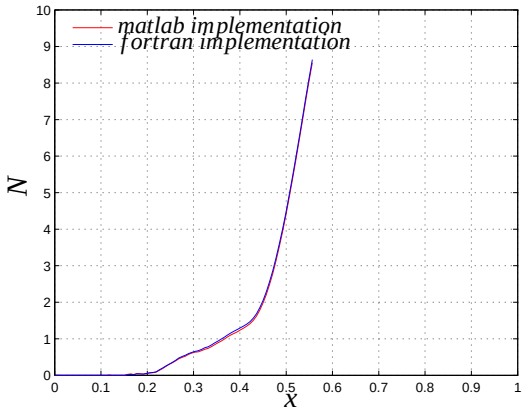

Figure 6.51: N for NACA64$_2$-A-215 at $\alpha = 0°$, $Re_c = 2.75 \cdot 10^6$, lower surf.

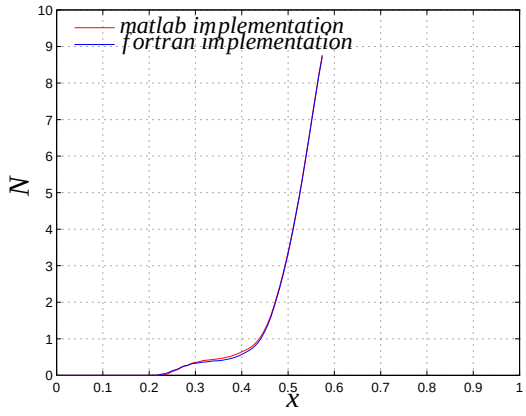

Figure 6.52: N for NACA64$_2$-A-215 at $\alpha = 0°$, $Re_c = 2.75 \cdot 10^6$, upper surf.

As can be seen in all cases both N-factor calculations give excellent agreement. Mostly only the red lines are visible in the diagrams as they lie on top of the blue ones. With the agreement for all upper and lower boundary layers of the testcases it is assumed that both methods will yield the same results as long as the same input variables are used. Thus in proving that the database method as implemented in correctly depicts the data as calculated by Arnal in [4], also proves the implementation to depict this data correctly. Proof of this can be found in [53], which was not yet published at the time this thesis was written, but a draft version was made available to the author in which this proof could be found. Assuming the Arnal data is correct, the method as implemented in and uses correct solutions of the Orr-Sommerfeld equation for use in its e^N-method. The only question mark left is whether the one parameter approach for the stability diagrams is valid. Some supporting arguments have been given in section 3.2, but no decisive argument has been found yet. If the working hypothesis of a single parameter approach should hold, the validity of this method is achieved as the validation of the e^N-method has been done already by many authors (i.e. [39], [50]) in the past. However the validation is then only valid for the area in which data from Arnal is available. The zones of extrapolation cannot so easily be proven to be valid, but in chapter 3 some sound arguments are given to assume their validity.

Chapter 7

Results of the finite difference boundary layer calculation

As a separate check the finite difference method boundary layer calculation was done on the pressure distribution output of . This means only the u_e on every panel is used for the finite difference boundary layer calculation. The reader has to keep in mind that there is no further interaction between the boundary layer variables as calculated by the finite difference method and the pressure distribution coming from . The pressure distribution from is however the final converged solution where the boundary layer interaction is taken into account. The difference due to leaving out the interaction with the boundary layer in the finite difference method can be considered small, as the only possible influence would be the effect of the difference between the boundary layer solution from and the finite difference method. The working of the finite difference method is described in section 2.4. The results of these calculations done with the finite difference method can be seen in figures 7.1 to 7.28. In these figures only the shape factor and the N-factor is shown, as the Re_θ values are in very good agreement and for these cases can be found in appendix C. Also a comparison is made with the N-factor calculation using the and the finite difference calculated boundary layers.

Figures 7.19 and 7.20 do not go up to $N = 9$ because there is separation occurring which causes the finite differences method to stop the calculation. As can be seen in the figures the shape factor as calculated using the finite differences method is different in many cases. The finite difference method is believed to be more accurate and therefore the laminar boundary layer formulation as used in and is often underestimating or overestimating the shape factor. This is a serious observation, as this implies that the transition position as calculated by and can be quite a bit from the actual location. This has not such a big impact if there is a steep rise in N-factor but can be quite dramatic when the N-factor does not rise so steep. This is very clear in figure 7.23 where the transition point differs more than 20% of the chord. The sensitivity of the N-factor to the shape factor can now also be clearly seen. Observing figures 7.21 to 7.24 the conclusion is drawn that when the shape factor and the Re_θ are the same also the N-factor will be the same. This implies that the only disturbing factor in the difference seen in these figures is due to the difference in H.

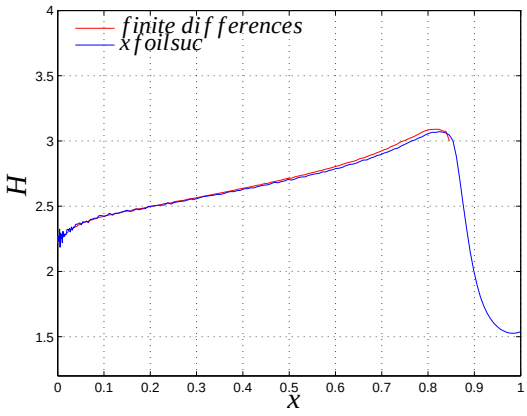

Figure 7.1: H at lower surface for NACA0012 $\alpha = 3°$, $Re_c = 1 \cdot 10^6$

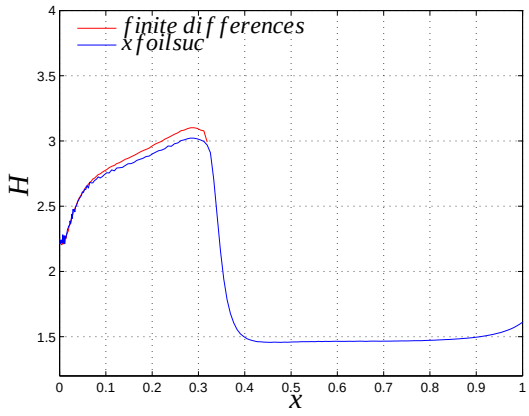

Figure 7.2: H at upper surface for NACA0012 $\alpha = 3°$, $Re_c = 1 \cdot 10^6$

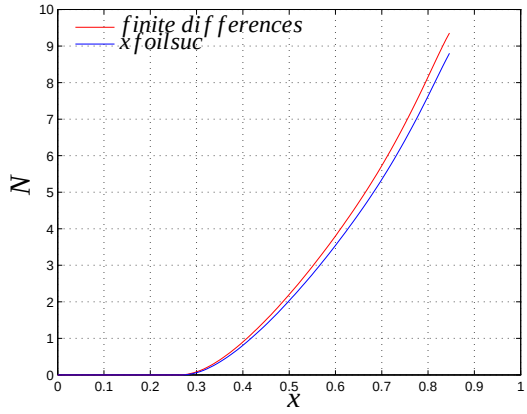

Figure 7.3: N at lower surface for NACA0012 $\alpha = 3°$, $Re_c = 1 \cdot 10^6$

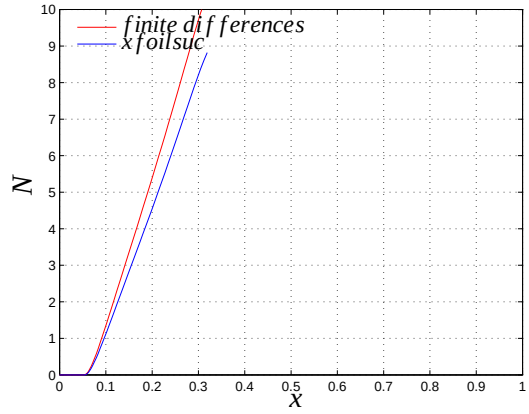

Figure 7.4: N at upper surface for NACA0012 $\alpha = 3°$, $Re_c = 1 \cdot 10^6$

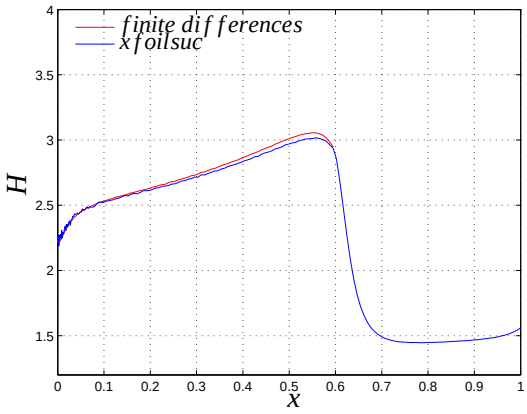

Figure 7.5: H at lower surface for NACA0012 $\alpha = 0°$, $Re_c = 1 \cdot 10^6$, no suction

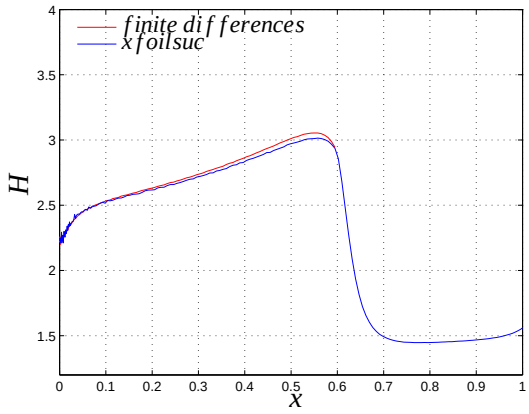

Figure 7.6: H at upper surface for NACA0012 $\alpha = 0°$, $Re_c = 1 \cdot 10^6$, no suction

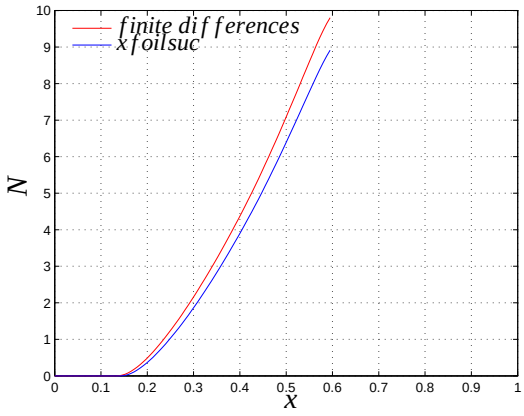

Figure 7.7: N at lower surface for NACA0012 $\alpha = 0°$, $Re_c = 1 \cdot 10^6$, no suction

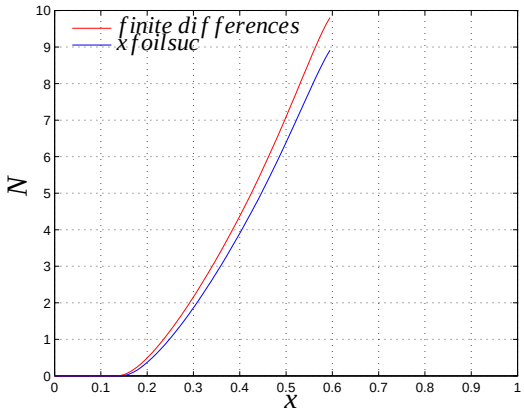

Figure 7.8: N at upper surface for NACA0012 $\alpha = 0°$, $Re_c = 1 \cdot 10^6$, nosuction

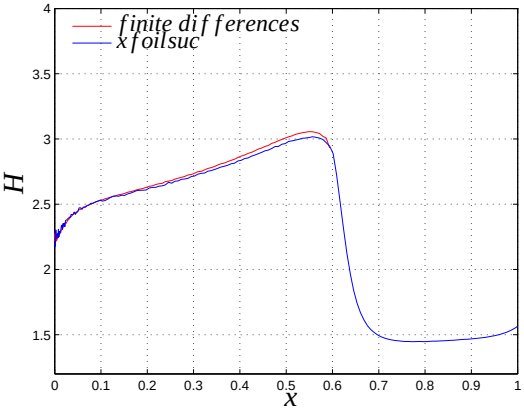

Figure 7.9: H at lower surface for NACA0012 $\alpha = 0°$, $Re_c = 1 \cdot 10^6$, suction *base*

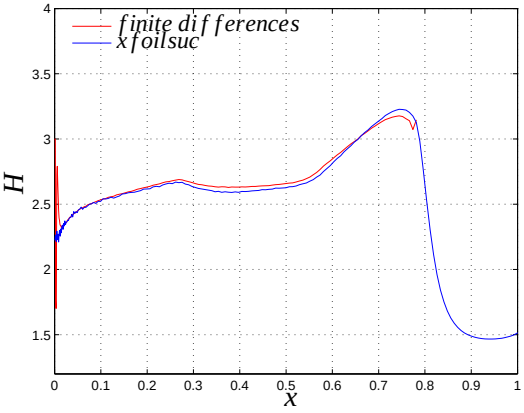

Figure 7.10: H at upper surface for NACA0012 $\alpha = 0°$, $Re_c = 1 \cdot 10^6$, suction *base*

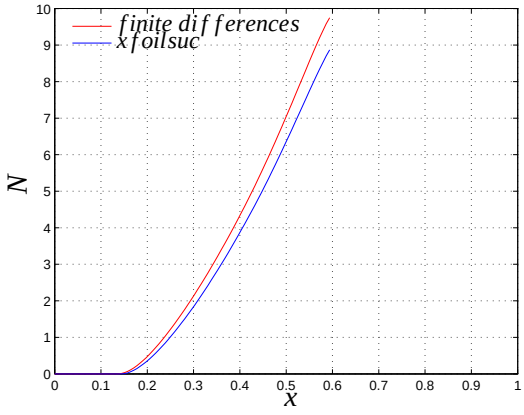

Figure 7.11: N at lower surface for NACA0012 $\alpha = 0°$, $Re_c = 1 \cdot 10^6$, suction *base*

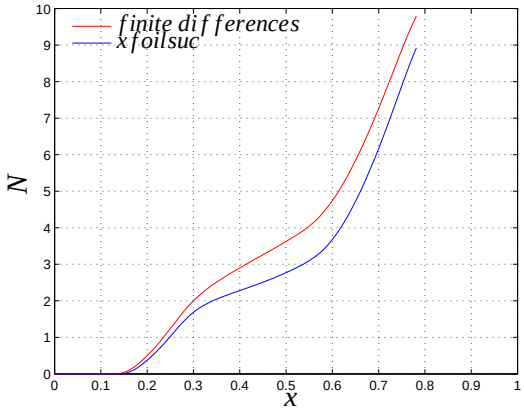

Figure 7.12: N at upper surface for NACA0012 $\alpha = 0°$, $Re_c = 1 \cdot 10^6$, suction *base*

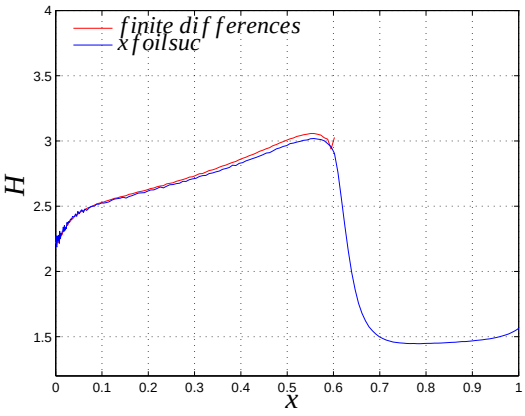

Figure 7.13: H at lower surface for NACA0012 $\alpha = 0°$, $Re_c = 1 \cdot 10^6$, suction $2 \cdot base$

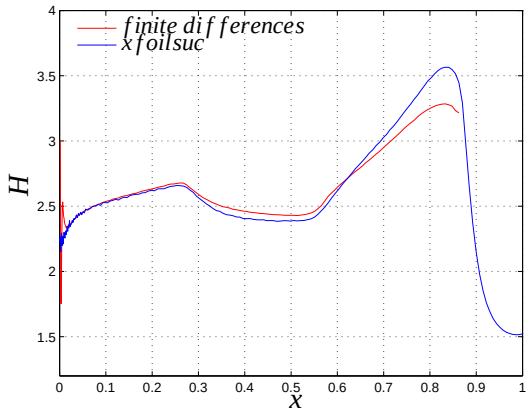

Figure 7.14: H at upper surface for NACA0012 $\alpha = 0°$, $Re_c = 1 \cdot 10^6$, suction $2 \cdot base$

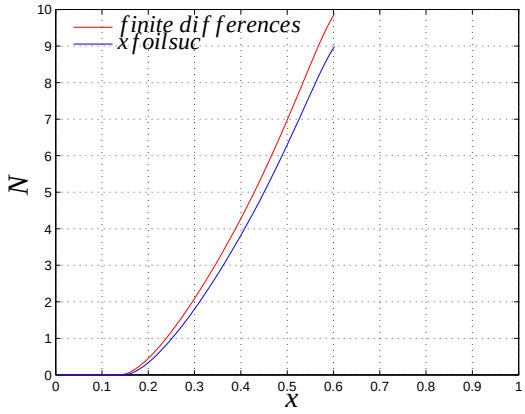

Figure 7.15: N at lower surface for NACA0012 $\alpha = 0°$, $Re_c = 1 \cdot 10^6$, suction $2 \cdot base$

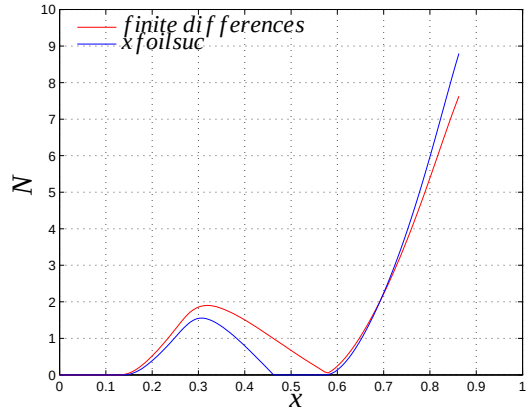

Figure 7.16: N at upper surface for NACA0012 $\alpha = 0°$, $Re_c = 1 \cdot 10^6$, suction $2 \cdot base$

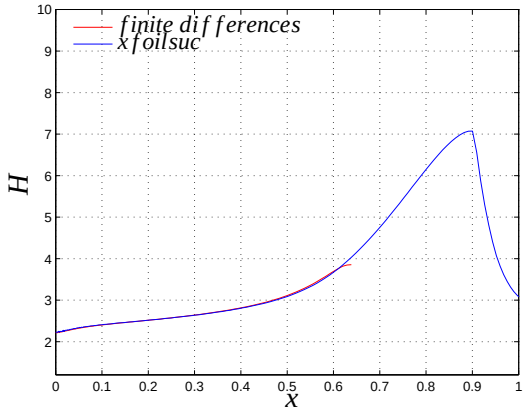

Figure 7.17: H at lower surface for NACA0018 $\alpha = 2°$, $Re_c = 1 \cdot 10^5$

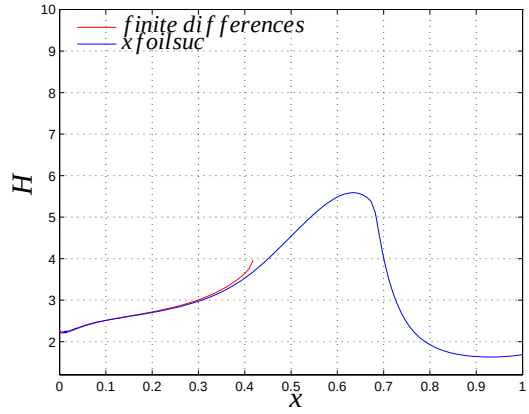

Figure 7.18: H at upper surface for NACA0018 $\alpha = 2°$, $Re_c = 1 \cdot 10^5$

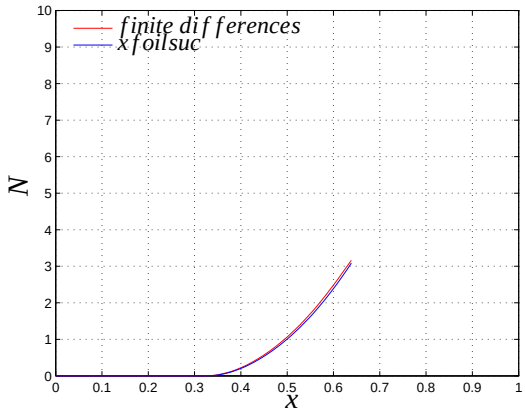

Figure 7.19: N at lower surface for NACA0018 $\alpha = 2°$, $Re_c = 1 \cdot 10^5$

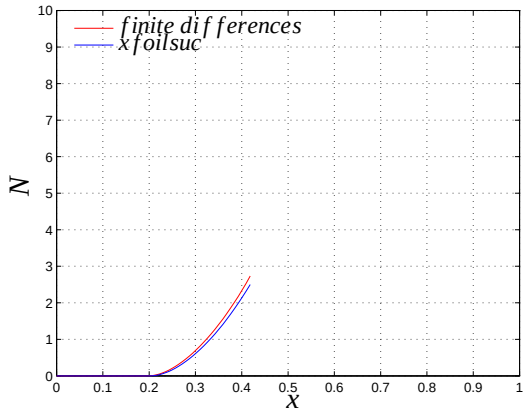

Figure 7.20: N at upper surface for NACA0018 $\alpha = 2°$, $Re_c = 1 \cdot 10^5$

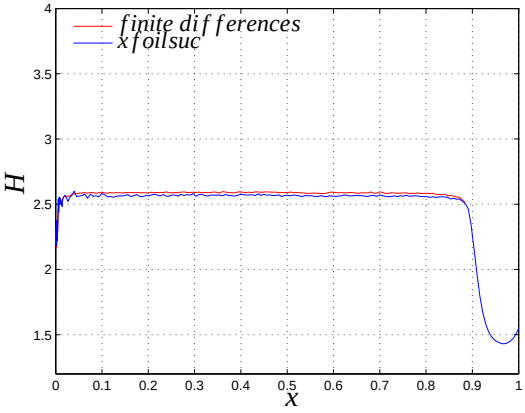

Figure 7.21: H at lower surface for flat plate airfoil $\alpha = 1.33°$, $Re_c = 5 \cdot 10^6$

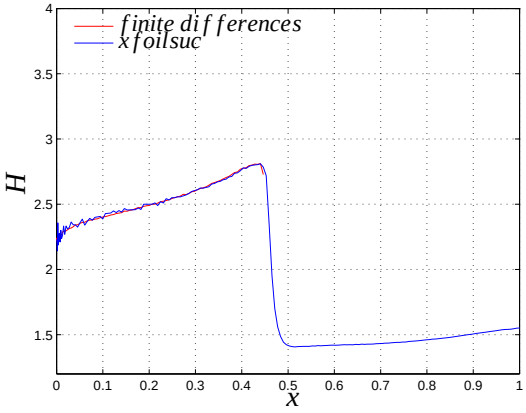

Figure 7.22: H at upper surface for flat plate airfoil $\alpha = 1.33°$, $Re_c = 5 \cdot 10^6$

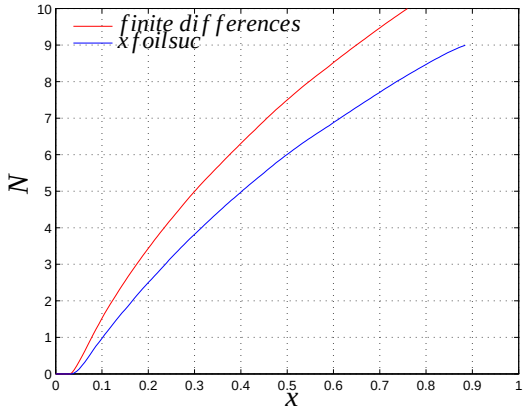

Figure 7.23: N at lower surface for flat plate airfoil $\alpha = 1.33°$, $Re_c = 5 \cdot 10^6$

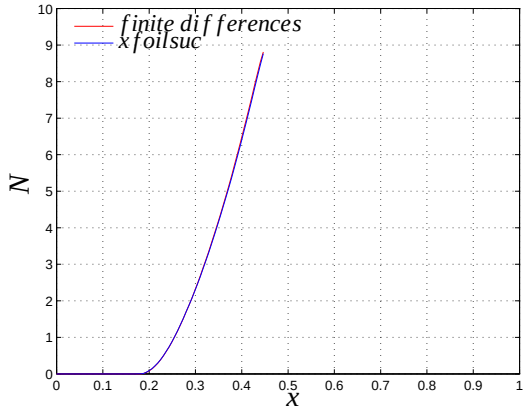

Figure 7.24: N at upper surface for flat plate airfoil $\alpha = 1.33°$, $Re_c = 5 \cdot 10^6$

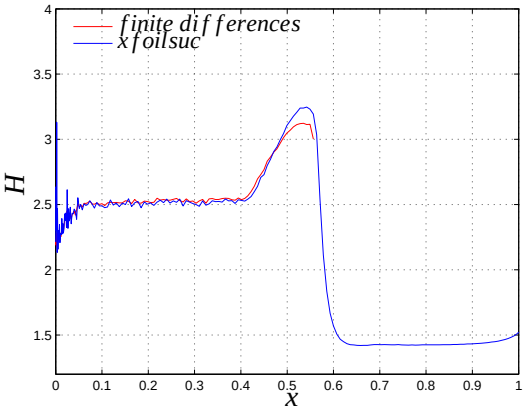

Figure 7.25: H at lower surface for naca 64_2-A-215 $\alpha = 0°$, $Re_c = 2.75 \cdot 10^6$

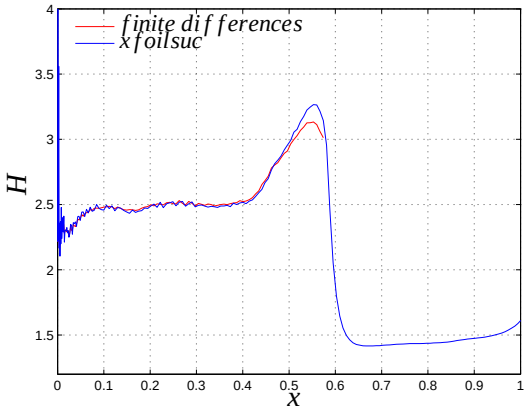

Figure 7.26: H at upper surface for naca 64_2-A-215 plate airfoil $\alpha = 0°$, $Re_c = 2.75 \cdot 10^6$

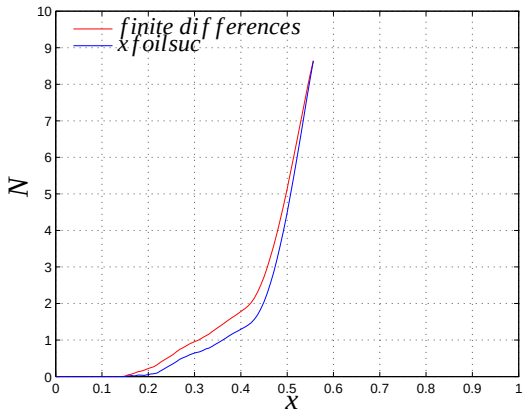

Figure 7.27: N at lower surface for naca 64_2-A-215 $\alpha = 0°$, $Re_c = 2.75 \cdot 10^6$

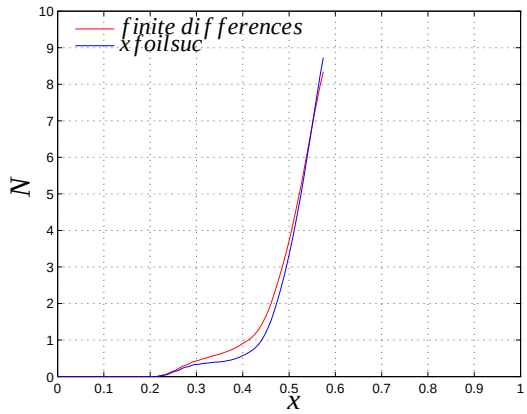

Figure 7.28: N at upper surface for naca 64_2-A-215 $\alpha = 0°$, $Re_c = 2.75 \cdot 10^6$

Chapter 8

Transition method comparison

After the evaluations of the panelling and the laminar boundary layer equations, now the different transition methods present in will be evaluated. First the different curves for the $^{10}log(Re_{\theta_{crit}}) - ^{10}log(H)$ are compared in figure 8.1.

The Drela method, the Van Ingen method and the improved e^N-method are compared with the seven test cases used earlier (mentioned in table 6.1). The results for the seven test cases are presented in figures 8.2 to 8.8.

Figure 8.2 shows N for NACA0012 with $\alpha = 3°$, $Re_c = 1 \cdot 10^6$. The Van Ingen and the Improved e^N-method show very similar behaviour, except the part upward of $N = 8$ where the Van Ingen method switches to the Drela method. The Drela method displays a similar trend but with an offset to the other two methods. The same holds for figure 8.3 where N for NACA0012 with $\alpha = 0°$, $Re_c = 1 \cdot 10^6$ and without suction is displayed. Figure 8.4 is interesting as it employs suction(the $1 \cdot base$ distribution) on a NACA0012 with $\alpha = 0°$, $Re_c = 1 \cdot 10^6$. All three transition methods predict a similar trend for the N-factor.

When the suction velocity is doubled a different graph can be seen, shown in figure 8.5. Very clearly the advantage of improved e^N-method can be seen. Both the Van Ingen and the Drela method fail in predicting damping of the N-factor whereas this is predicted by the improved e^N-method. The fact that the Improved e^N-method has a somewhat steeper curve in the second unstable part offsets partly the differences in the different methods predicted point of transition. Figure 8.6 gives again a similar trend predicted by all three methods, albeit that the Drela method has an offset as usual to the other two methods. The flat plate airfoil N-factor displayed in figure 8.7 shown again a similar trend but an offset for the Drela method and the kink in the Van Ingen method which makes the transition point nearly the same to that of the Improved e^N-method. The same pattern is seen in figure 8.8.

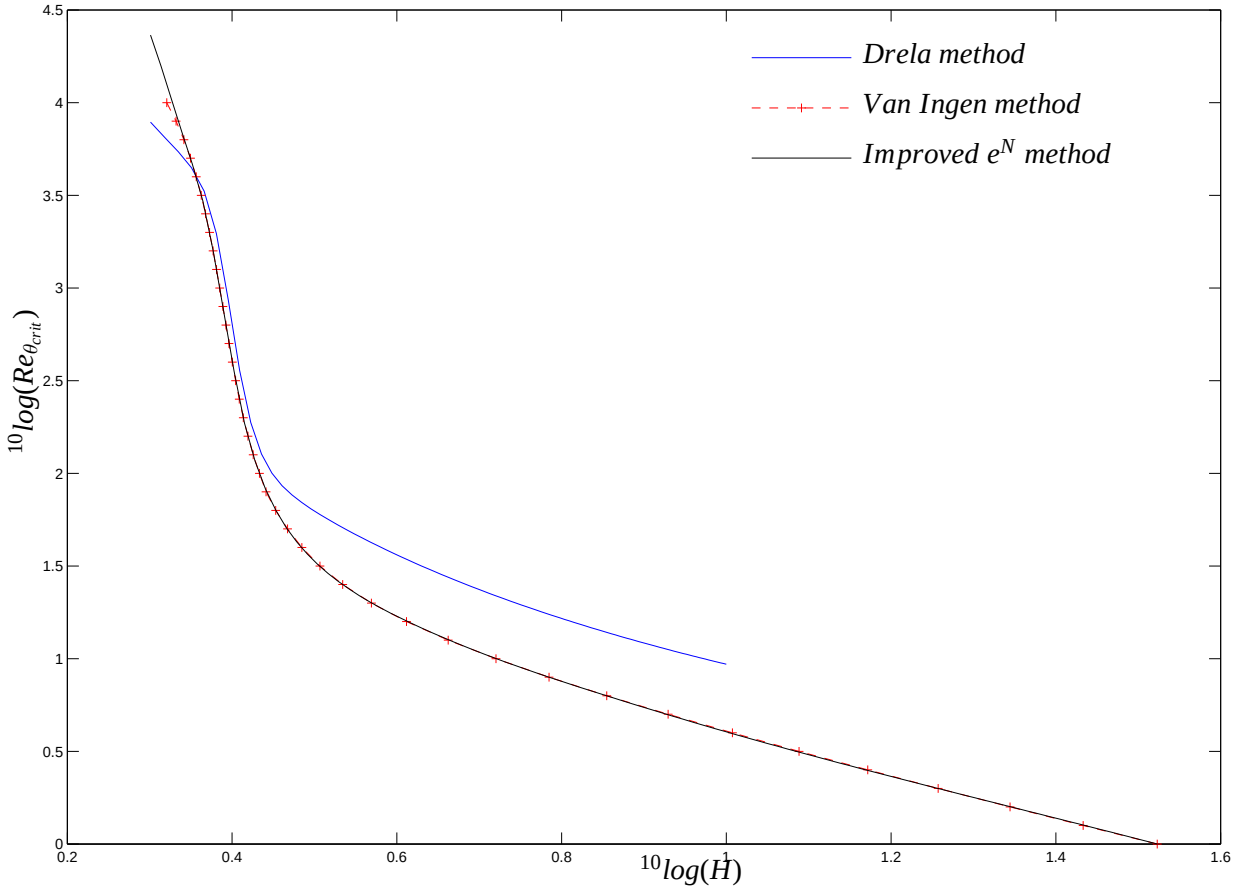

Figure 8.1: $^{10}log(Re_{\theta_{crit}}) - ^{10}log(H)$ for all three transition methods

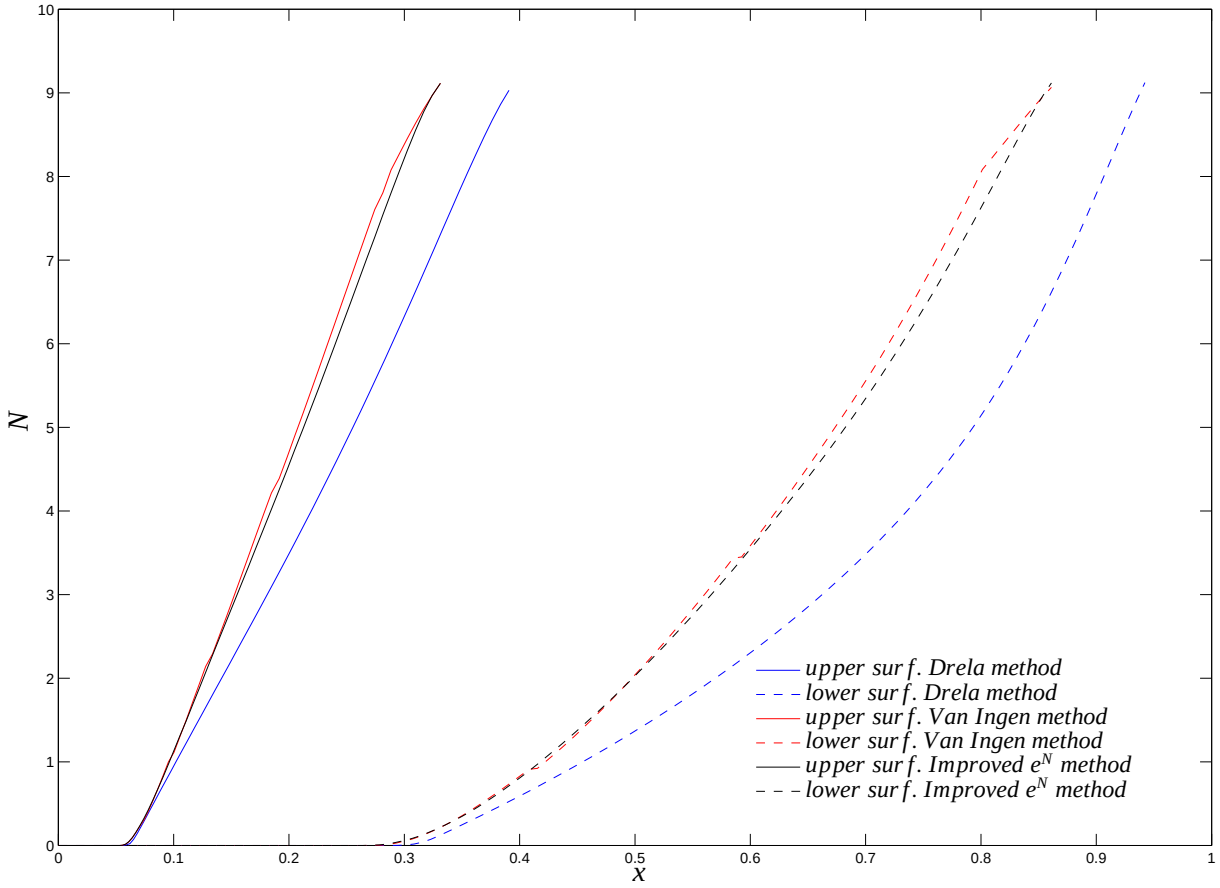

Figure 8.2: N for NACA0012 $\alpha = 3°$, $Re_c = 1 \cdot 10^6$

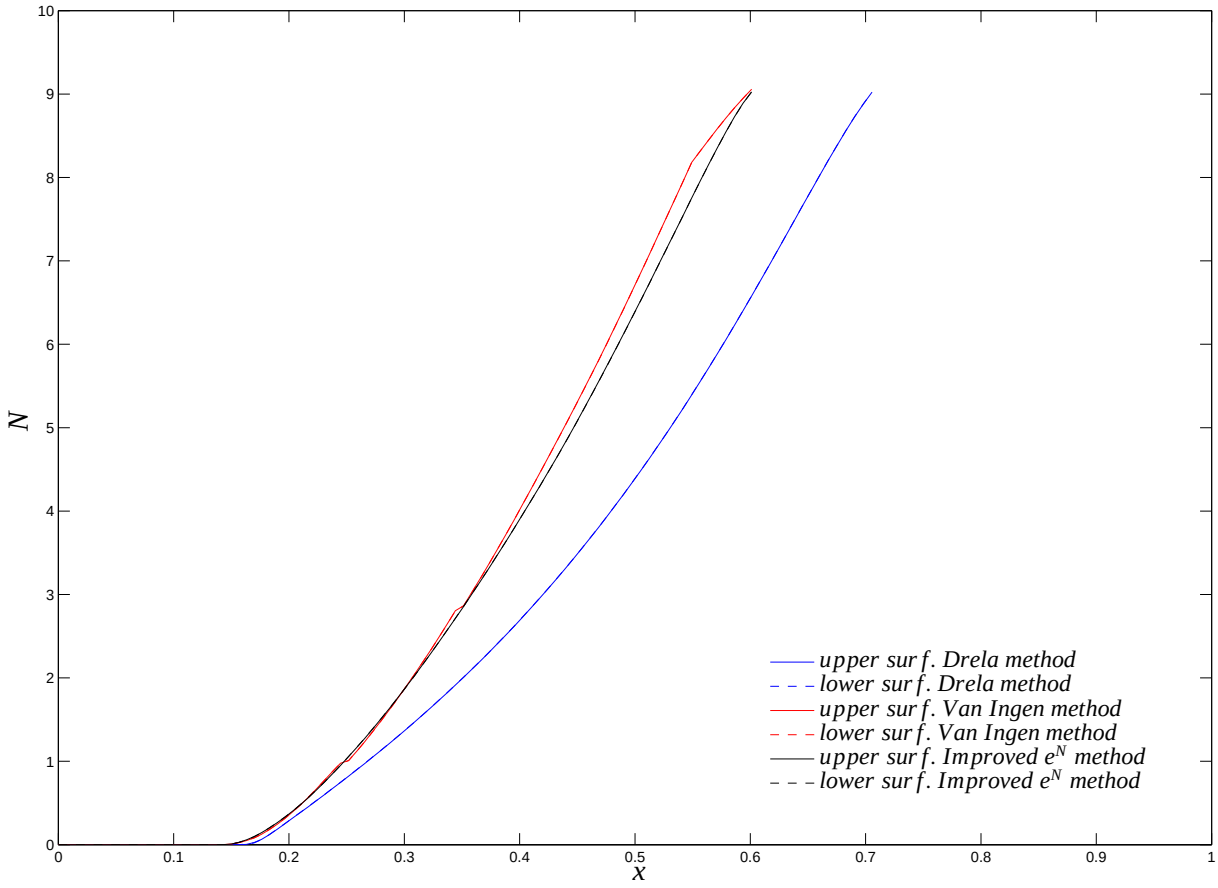

Figure 8.3: N for NACA0012 $\alpha = 0°$, $Re_c = 1 \cdot 10^6$, no suction

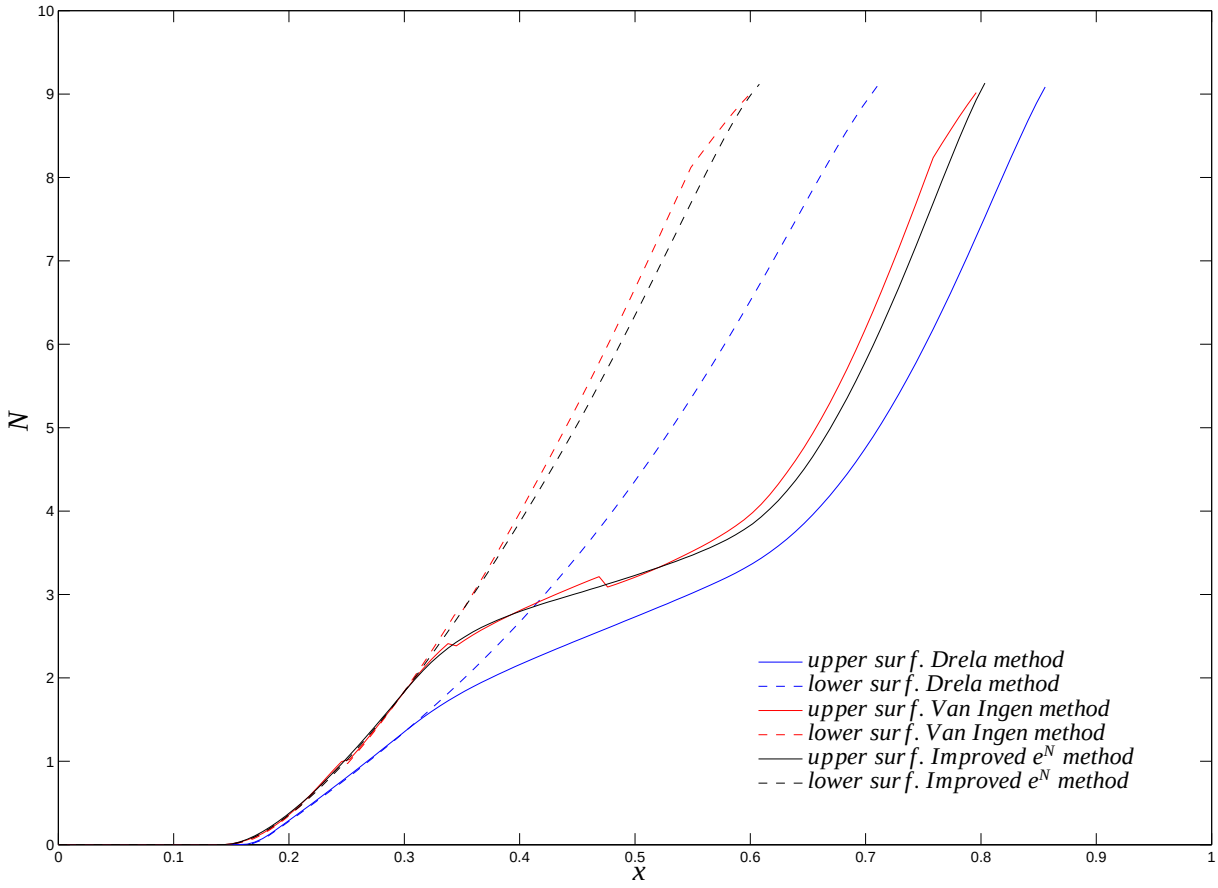

Figure 8.4: N for NACA0012 $\alpha = 0°$, $Re_c = 1 \cdot 10^6$, suction *base*

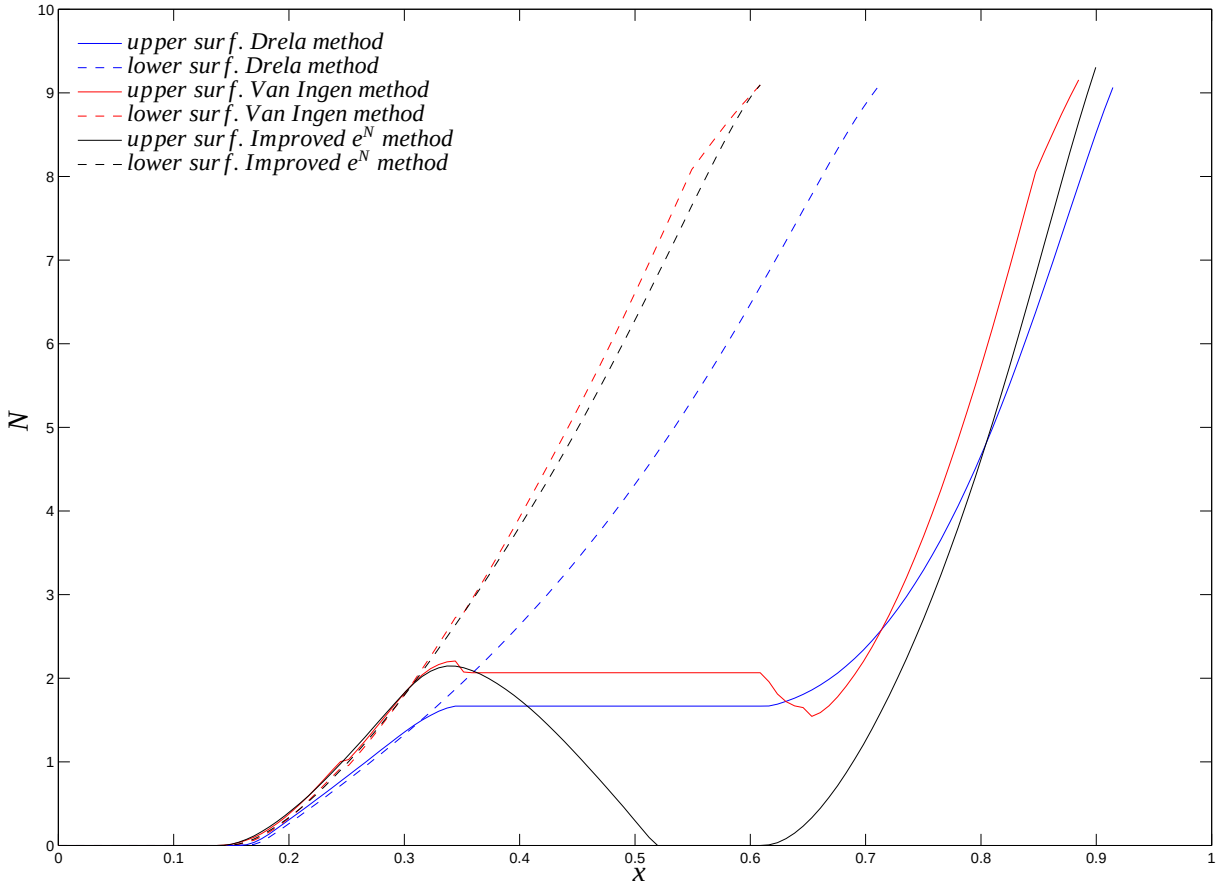

Figure 8.5: N for NACA0012 $\alpha = 0°$, $Re_c = 1 \cdot 10^6$, suction $2 \cdot base$

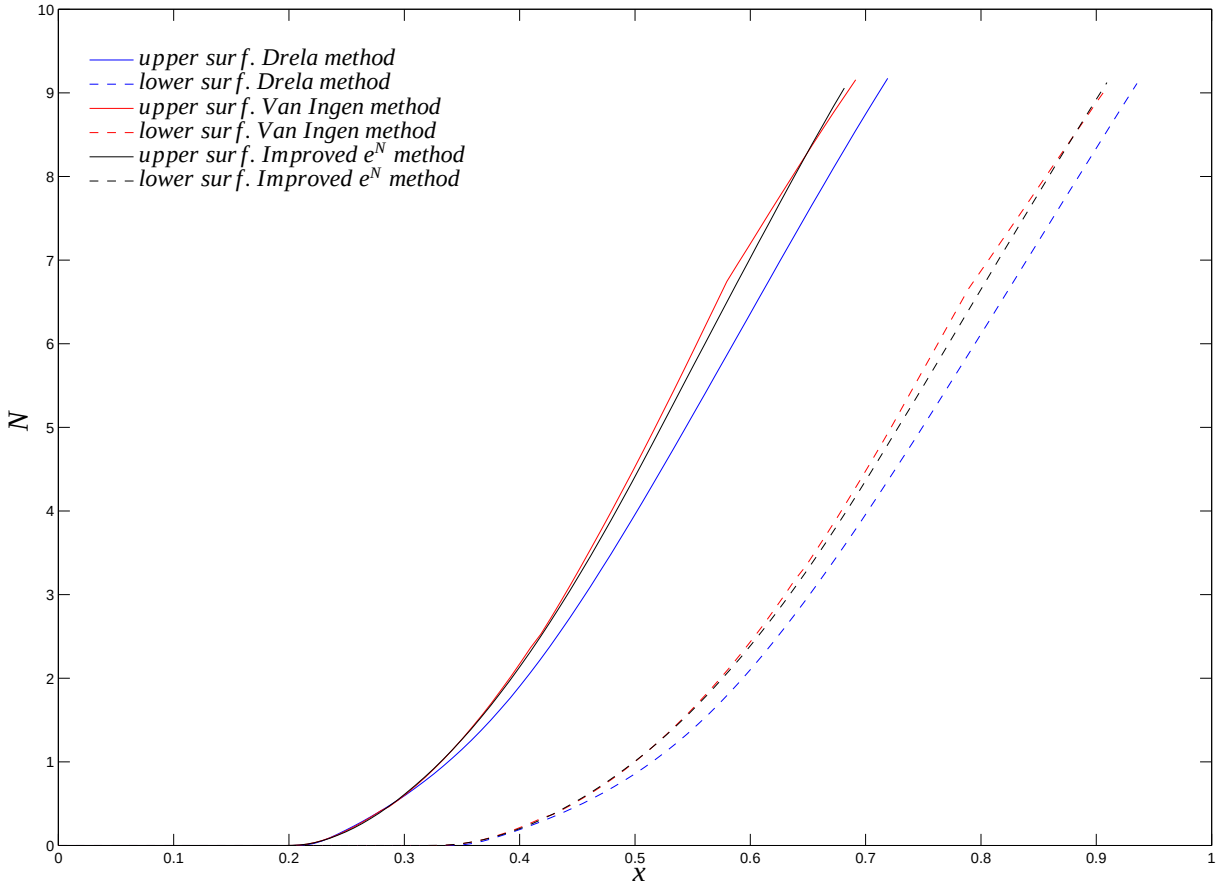

Figure 8.6: N for NACA0018 $\alpha = 2°$, $Re_c = 1 \cdot 10^5$

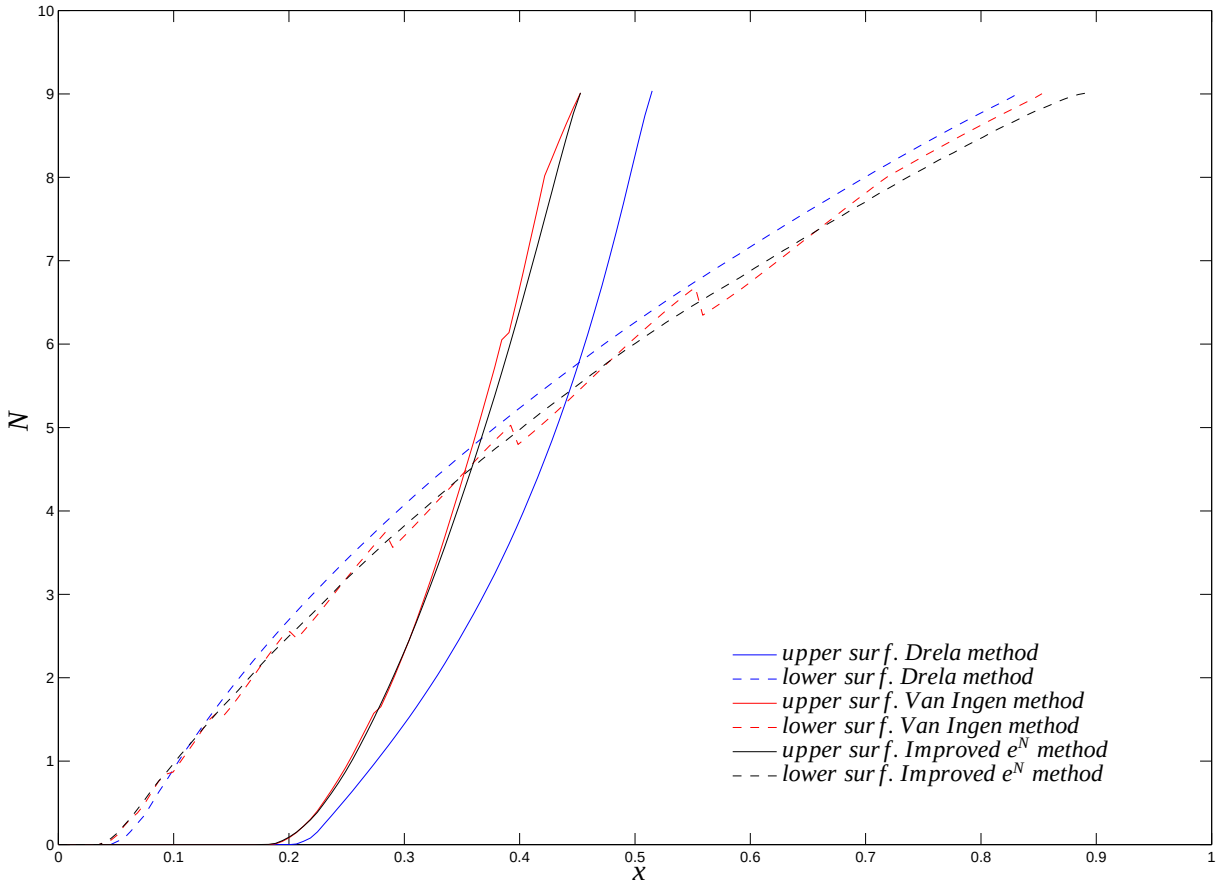

Figure 8.7: N for flat plate airfoil $\alpha = 1.33°$, $Re_c = 5 \cdot 10^6$

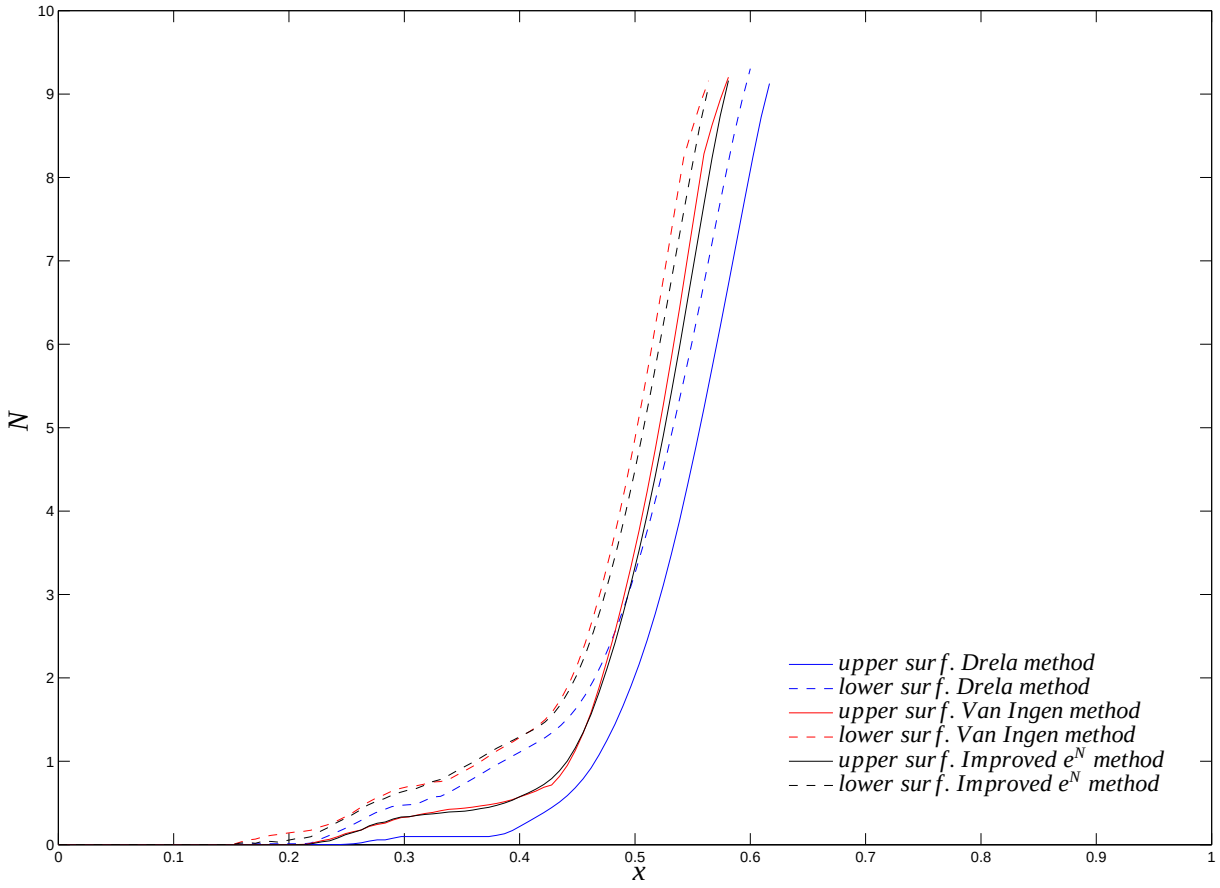

Figure 8.8: N for NACA64$_2$-A-215 $\alpha = 0°$, $Re_c = 2.75 \cdot 10^6$

Chapter 9

Case study DU99 airfoil

The DU99 airfoil is a 14.7% thick airfoil designed for the standard class sailplane ASW-28. It is quite well suited for use with boundary layer suction to extend the laminar boundary layer on the upper surface as the upper surface already has a long laminar boundary layer. This airfoil is planned to be provided with boundary layer suction to serve as demonstration wing. Transition is forced on both the upper (at 95% c) and lower (at 85% c) surface to avoid laminar separation. Up to these locations strong suction can prevent laminar separation, but at the upper trailing edge no suction can be used downstream of 95% c and at the lower surface a flap will be present from 85% onwards. A case study is performed on the DU99 airfoil to study the effect of the Improved e^N-method transition point prediction on the performance of the airfoil. Also a suction distribution is designed for this airfoil to achieve better performance. The DU99 airfoil with the panel distribution used is shown in figure 9.1. For this airfoil 360 panels were used on the surface for all calculations to minimize differences in the comparisons due to the panelling.

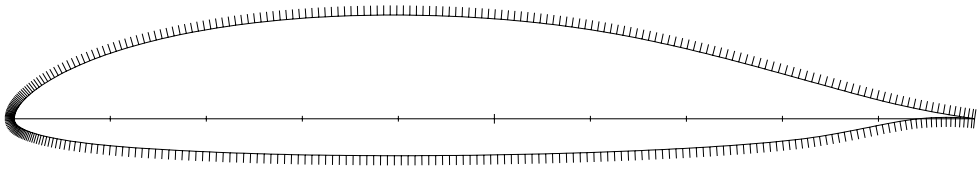

Figure 9.1: DU99 airfoil with the 360 panel grid

9.1 Performance without suction

First the performance polars are calculated using all three transition prediction methods present in , being the Drela method, the Van Ingen method and the newly implemented Improved e^N

method. These polars can be seen in figure 9.2.

It can be seen that both the Van Ingen method and the Improved e^N-method behave very similar. This was to be expected as the methods differ not greatly except for the ability of the Improved e^N-method to calculated damping of the N-factor and the ability to calculate more frequencies than the Van Ingen method so the N-factor curve is smoother. Both the Van Ingen and the Improved e^N-method predict transition earlier (up to 10 % c) than the Drela method at adverse pressure gradient situations.

9.2 Suction distribution

For the DU99 a suction distribution is designed. A Reynolds number of $1.05 \cdot 10^6$ and $M = 0$ was used. The variation of Reynolds with C_l is such that $Re\sqrt{C_l}$ is constant. This corresponds with a stationary flight situation, where the flight speed varies but that the total lift remains equal. In Broers [1] it is shown as a practical result that for $Re\sqrt{C_l}$ constant, the v_0 distribution for this situation is practically constant for $C_l > 0$. This way the suction velocity can be scaled by $\frac{1}{U_\infty \sqrt{C_l}}$ so that:

$$\frac{v_0(x)}{U_\infty \sqrt{C_l}} \approx constant \tag{9.1}$$

Because the v_0 distribution is not exactly constant a suction distribution needs to be calculated for several values of C_l, after which the most demanding C_l value determines the suction distribution. For this airfoil two suction distributions for the upper surface were calculated. The first by using the built in command in for a first suggestion for a suction distribution to keep a flow laminar (command *base*). The suction distribution was then modified by hand to avoid boundary layer separation. This resulted in a suction distribution as shown in figure 9.3. As can be seen the suction distribution runs from 50% to 95% of the chord. This resulted in the polars calculated with all three transition methods shown in figure 9.4.

The suction distribution shown in figure 9.3 is somewhat irregular. As the airfoil will be built at some later stage and provided with boundary layer suction a more smooth and regular suction distribution is preferred to ease the construction and suction control mechanism. Along with this it is possible to extend the start of the suction distribution forward. This makes it possible to redesign the suction distribution and to make it a simpler one. The new suction distribution is shown in figure 9.5. In figure 9.6 both suction distributions are plotted in one figure. A new performance polar was calculated using the second suction distribution, again using all three transition methods and it is shown in figure 9.7.

A comparison is made of the polar without suction (cyan curve), and with suction distributions no.1 (blue curve) and suction distribution no.2 (magenta curve) in figure 9.8 . The advantages of boundary layer suction are very clear in this figure. In the low drag bucket region the profile drag of the airfoil is reduced by about 50% to 75%. This excludes suction drag, because this is dependant on the efficiency of the suction system, and possible ejection of the air taken in by the suction system. Even when transition point occurs just in front of the start of the suction distribution (at around $C_l = 0.9$ for the second suction distribution) and the turbulent boundary layer is present in the suction part, the drag is still a lot less than the non suction case through the effect of suction on the turbulent boundary layer. Also the $C_{l_{max}}$ is with suction around 1.7 instead of 1.4 without suction. So for the DU99 airfoil

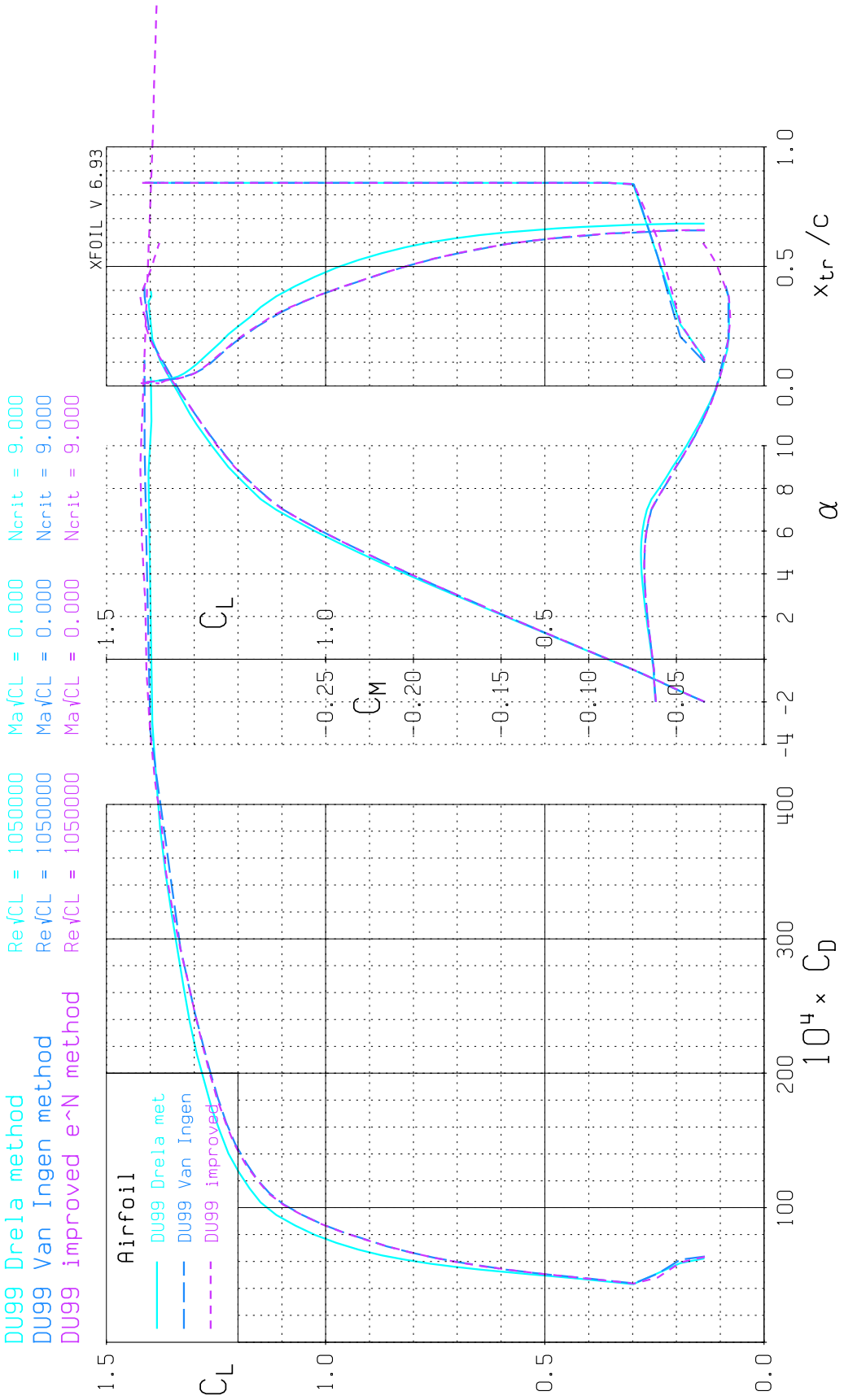

Figure 9.2: DU99 polar without suction

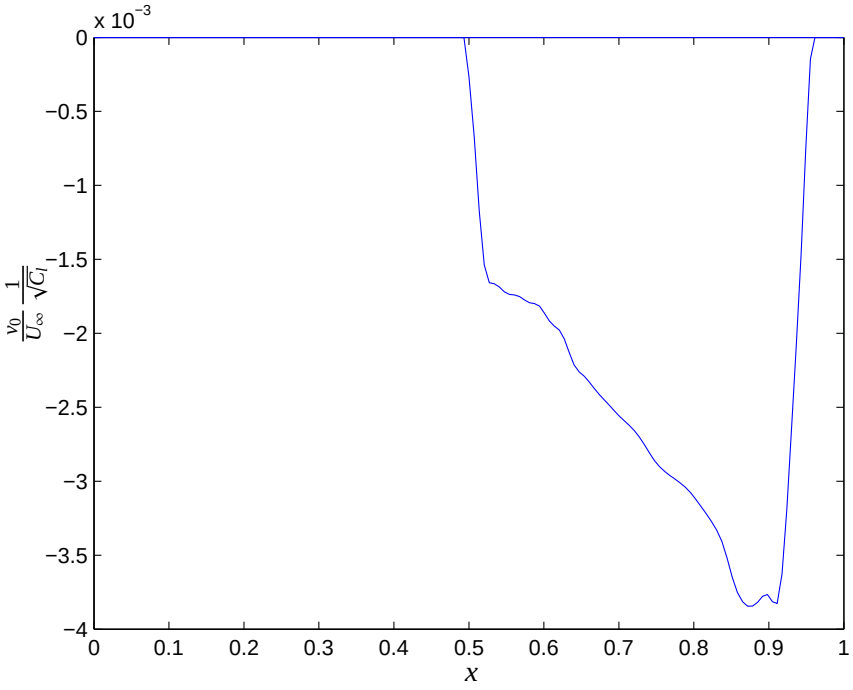

Figure 9.3: DU99 suction distribution no. 1

a carefully designed suction distribution can dramatically reduce drag and increase lift by delaying both transition and laminar and turbulent separation. Therefore this airfoil is very well suited for windtunnel testing and verifying the calculations.

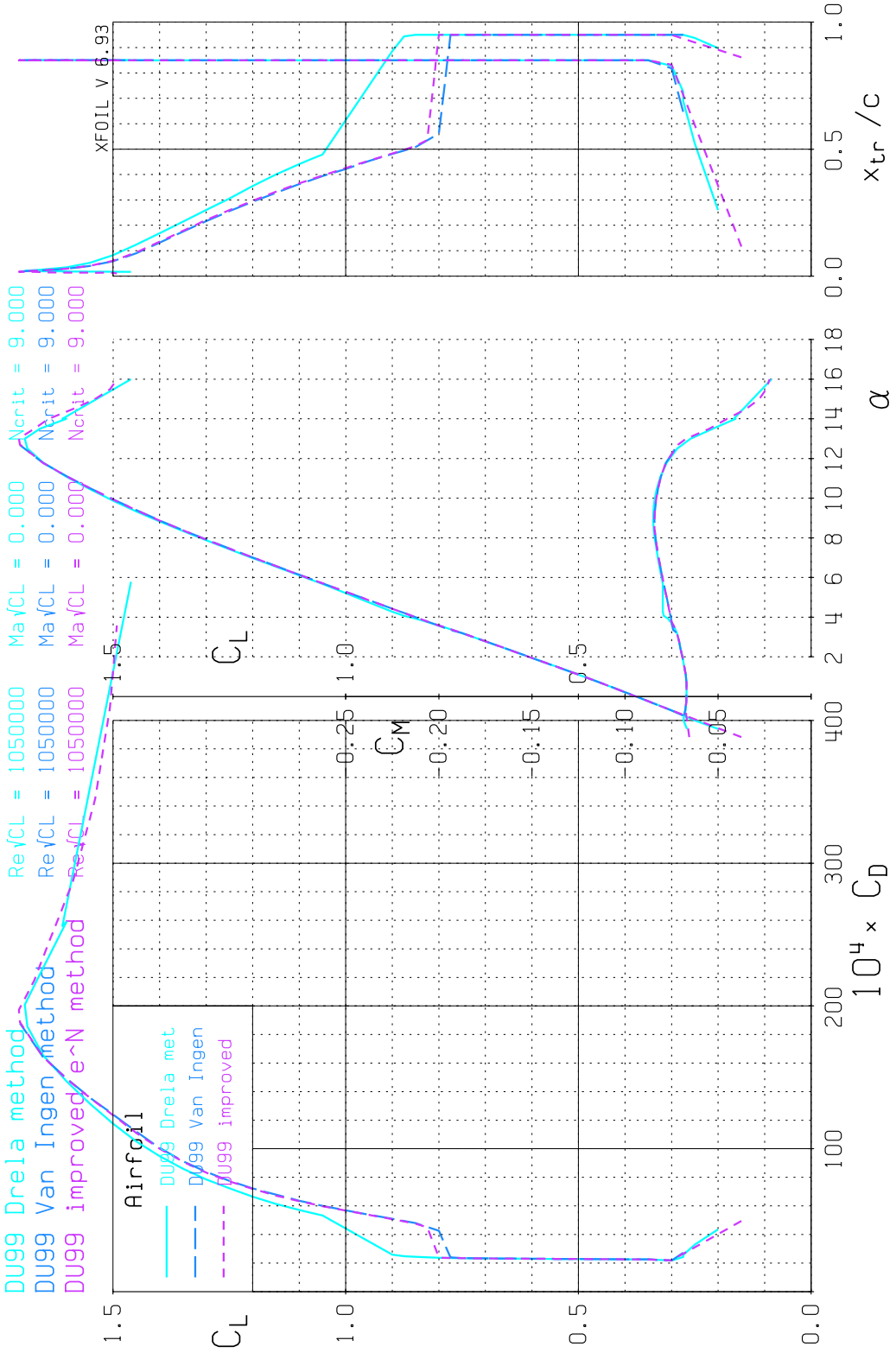

Figure 9.4: DU99 polar with suction distribution no. 1

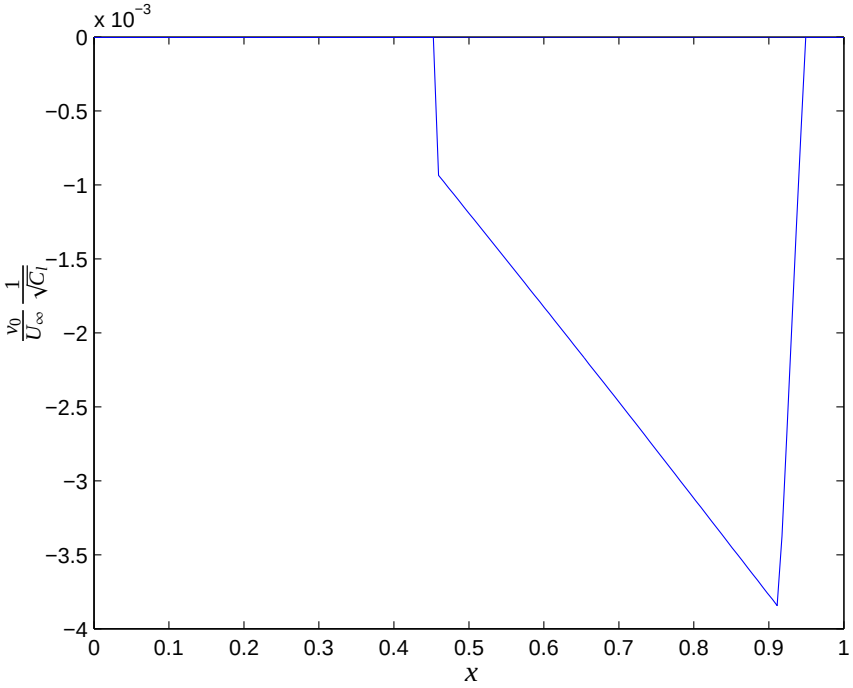

Figure 9.5: DU99 suction distribution no. 2

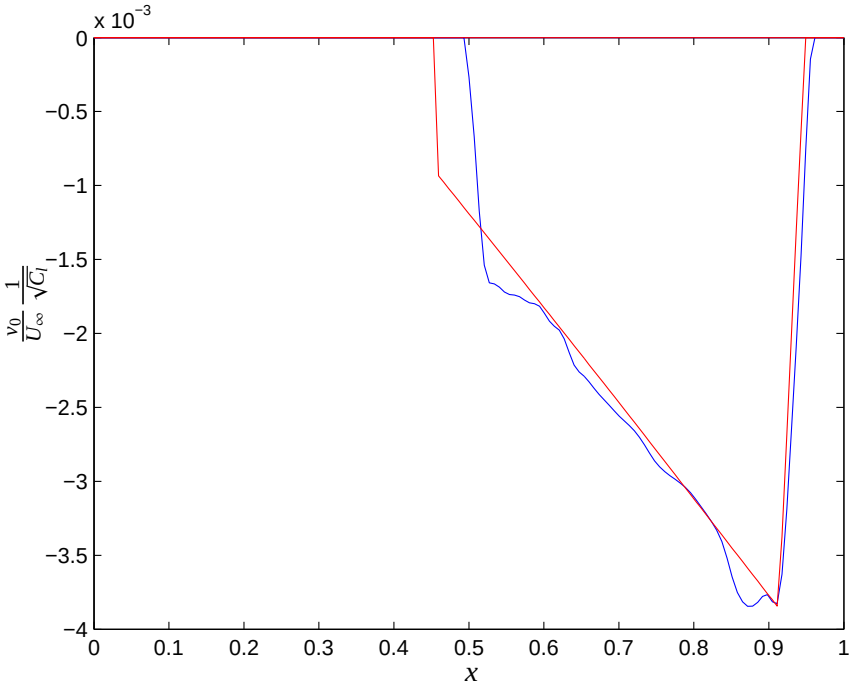

Figure 9.6: DU99 suction distribution no. 1 & 2

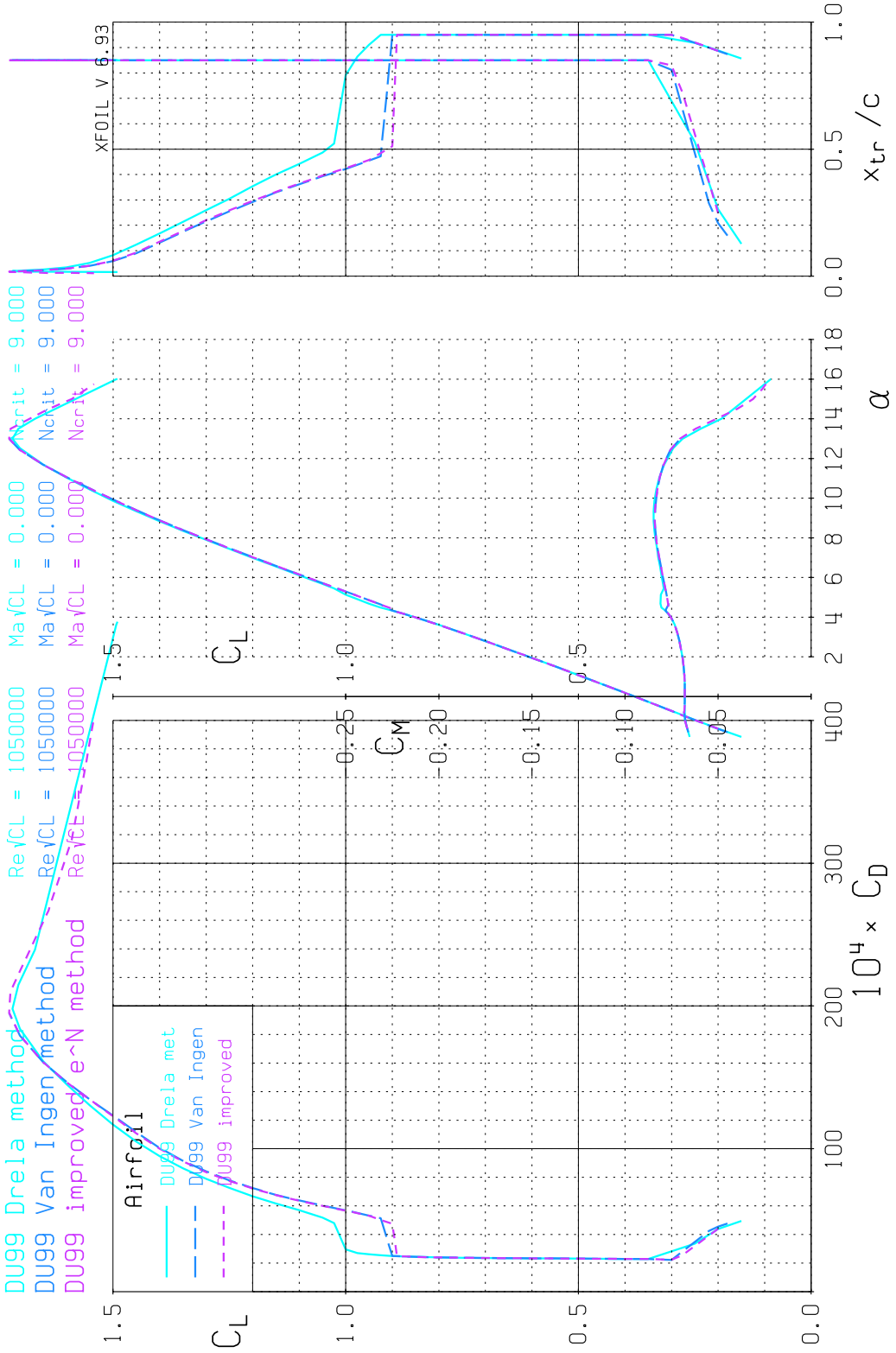

Figure 9.7: DU99 polar with suction distribution no. 2

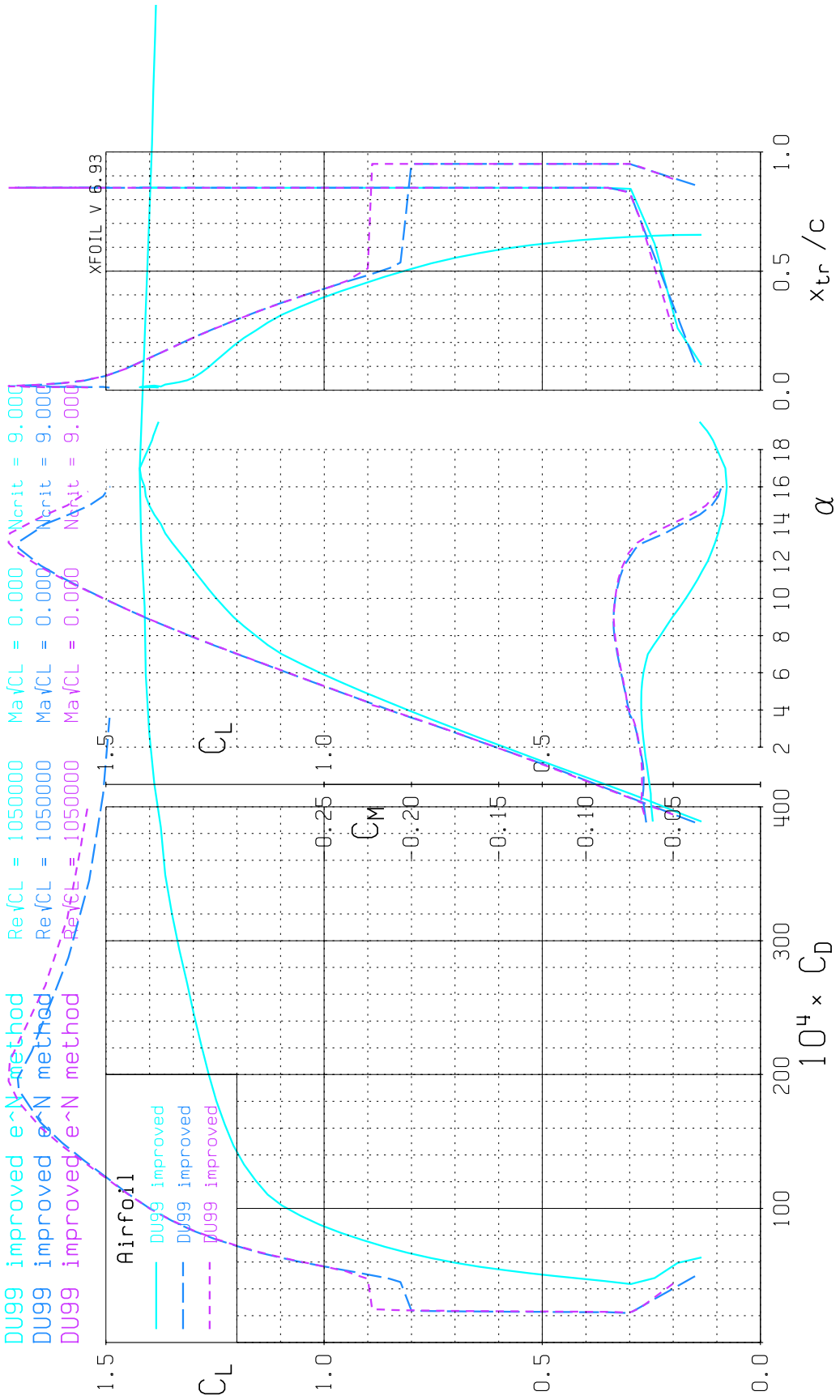

Figure 9.8: DU99 polar, without suction, and both suction distributions

Chapter 10

Conclusions and Recommendations

10.1 Conclusions

From this study some conclusions can be drawn with regard to the objectives laid out in section 1.4: *To implement an improved transition region prediction method in that achieves reliable results for boundary layers on airfoils with and without boundary layer suction.* A reliable transition prediction method was implemented in in the form of the improved e^N-method, and it can calculate both amplification and damping of the N-factor. Some measures to ensure converging of the boundary layer calculation in were necessary. These measures use the forcing routine already present in to interrupt infinite loops can otherwise be caught in. These measures do not significantly influence the location of transition.

Without boundary layer suction the results of this method are very similar to the Van Ingen method implemented earlier in , as long as the N-factor is strictly increasing. Compared with the Drela method for non-suction boundary layers, the improved e^N-method shows a steeper curve for the N-factor all cases except the flat plate airfoil, where the gradient is similar. When boundary layer suction is applied, only the improved e^N-method can predict damping of the N-factor. This is of great value when designing airfoils specifically meant for use with boundary layer suction to delay transition and boundary layer separation to reduce drag.

In analyzing the grid convergence it was found that the default value of 160 panels is for many cases not a dense enough distribution and 360 panels were used to ensure the influence of the panelling on the transition locations could be neglected.

The laminar boundary equations of and were found to differ significantly from the results made with a finite differences method. It is believed the laminar boundary equations or its closure relations in and are somewhat inaccurate with regard to the shapefactor. As this influences the transition location calculation highly this is a serious observation. Connected with this is the fact that for high suction velocities a laminar shapefactor of less than 2 is given by . Finding the cause of this was thought to be outside the scope if this study, but the observation deserved

to be mentioned here.

The DU99 airfoil is suited well for use with boundary layer suction. Drag reductions (excluding suction drag) are between 50% and 75% in the low drag bucket. Outside the low drag bucket the drag reductions are also significant. Also using boundary layer suction a $C_{l_{max}}$ of 1.7 can be achieved, compared with a $C_{l_{max}}$ of about 1.4 for the case without suction.

10.2 Recommendations

A few recommendations for future study can formulated after this study.

- It would be interesting to verify the working hypothesis about the asymptotic suction boundary layer having a stability diagram very similar to that of the stagnation point with calculations. This could be done by making or using an Orr-Sommerfeld equations solver and calculating the stability diagram of the asymptotic suction boundary layer and comparing it to the stability diagram of the stagnation point.
- A study in determining the actual frequencies responsible for the dominant amplification of disturbances beforehand would increase the efficiency of the method, because a large range of frequencies(601) is used to try all possible dominant frequencies are included in the calculations, but in some cases the number of frequencies in the unstable area is too small for an accurate description of the amplification rate curve.
- A detailed study should be made into the laminar boundary layer calculation of and - as they were found to differ from results using a finite differences method and in suction cases allow a shapefactor of less than 2 to appear.
- Connected with the previous suggestion is the recommendation to study the lack of convergence in due to s handling of the interaction of the boundary layer iterations and the transition calculation.
- A grid convergence study should be done for each profile that is to be extensively analyzed using or . Especially when using suction, results can vary much with the number of panels used.

Appendix A

User Guide Transition

This user guide is a short guide for users working with and who want to use the (full) Van Ingen or the improved Van Ingen transition method. This last transition prediction is valid for boundary layers with and without suction. This short guide is split in two sections: one concerning the choice of transition method ( ) and another with the convergence improvement ( ) usually needed in for the two above mentioned methods.

Warning A warning beforehand is needed here, as this user guide may be separately used from the thesis it is appended to. In testing it was found out that the boundary layer formulations in allow for a shape factor of less than 2 when suction is used. It is believed that this is *NOT* correct, and that only values above H = 2 should be trusted.

A.1

The command stands for TRansition MEthod and can be found in de menu. When entering the command a short menu will appear giving the user 3 choices:

1. 2nd order Drela method
2. Van Ingens e^N method
3. Improved Van Ingens e^N method

A.1.1 2nd order Drela method

This method is an improved version of 's first transition method, the 1st order Drela method. This 2nd order method is more accurate than the 1st order method but is essentially the same. It is

an envelope method that is based on self-similar Falkner-Skan velocity profiles. From H = 5 onwards non-similar profiles are used for better accuracy in separated flow situations. This transition method cannot cope with damping of TS instability (as can occur with boundary layer suction) and has the implicit disadvantages of envelope methods (although alleviated by the use of non-similar profiles for H > 5) but is the best converging method of all three and therefore needs no help in finding a converged solution that both other methods need.

A.1.2 Van Ingens e^N method

The (full) Van Ingen method implemented in 2002 in was meant to be able to account for damping TS instabilities, as can occur when using boundary layer suction. This it is able to do, but to a very limited amount only. This is because the calculation is stopped whenever a Re_θ lower than $Re_{\theta_{crit}}$ is found. The N-factor is kept constant when this happens. The only damping can come from the dominant frequency that, even though it is being damped, stays dominant. At least one other frequency needs to be unstable, to keep the calculation going. The method is a full e^N semi-empirical method which uses Re_θ and the H factor to calculate the present N factor. In the boundary layer iteration converges badly when this method is used. s interaction between the boundary layer iteration and transition calculation are to blame for this. There are 2 solutions to this convergence problem, both boiling down to the same: namely to switch slightly before transition to Drela's method. This can be done by using the Nlimit or the safety factor method. See A.2.2 and A.2.1. The Nlimit method is the default method for this transition method.

A.1.3 Improved Van Ingens e^N method

The improved Van Ingen e^N method is invented by Van Ingen in 2005. This improved method is able to cope with amplifying and damping TS instabilities, which makes it possible to use boundary layer suction. This is of great importance to , in which already the boundary layer formulation was adapted to handle normal velocities on the wall. Using this routine will enable the user to design airfoils using boundary layer suction with accurate transition predictions. However also when this method is used in the boundary layer iteration converges badly. Again s interaction between the boundary layer iteration and transition calculation is to blame. The before mentioned solutions of switching to the Drela method can be used, however in cases of boundary layer suction a third method is preferred which is known as the forcing method. See A.2.3. The default method is the forcing method for this transition method.

A.2

This is the convergence method selection. This command opens a small menu featuring 4 options:

1. Safety factor method, uses predicted N to switch

2. Nlimit, fixed N limit method
3. Forcing xt at calculated xt coordinate
4. No convergence improvement

A.2.1 Safety factor method

The safety factor uses the $\frac{dN}{dx}$ value multiplied by the (current) dx value. This is then multiplied by the 'safety factor' and added to the current N-factor. If this value is larger than the specified N at which transition is assumed the method switches to the Drela method. This way the method switches at the latest possible interval, so that the deviation due to the difference in method is small. The safety factor can be changed from its default value of 1. separately for each side, or for both sides at once. The higher the safety factor, the earlier switching occurs. In the iteration output the values for the switching interval on each side are displayed to be compared to the transition interval. Some caution is advised when using this method in a situation where the n factor will rise steep only to go down further on. During a steep rise the predicted value can be quite large, especially when boundary layer suction is used, and too early switching occurs. (especially the suction cases are dangerous as the Drela method to which is switched cannot cope with damping of TS instabilities) will give the interval in which is switched during iterations, so the user kan adapt the 'safety factor' value accordingly.

A.2.2 Nlimit method

The Nlimit has a similar working as the safety factor but is more direct. The Nlimit value is the value above which the transition method is switched to the Drela method. This value can also be separately set for each side, or both sides at once. The default setting is 8. will give the interval in which is switched during iterations, so the user kan adapt the Nlimit value accordingly.

A.2.3 Forcing method

The forcing method can only be used with the improved Van Ingen method and works quite differently from the methods mentioned above. If the transition point is fixed and does not move more than $0.0001\ \frac{x}{c}$ the transitionpoint is forced to that spot. In forcing the transition there, convergence will be easier achieved. To combat the infinite loops in which can get stuck, this method also checks whether two consecutive values for the transition point are closer than $0.1\ \frac{x}{c}$ and also checks whether these points are not too volatile. The maximum distance they are allowed to move in an iteration is $0.02\ \frac{x}{c}$. If this is established the downstream transition point (as long as the distance between the points is at least $0.02\ \frac{x}{c}$) is forced $0.005\ \frac{x}{c}$ forward. Transition can still occur freely in front of this downstream point, but not after. This process goes on untill both transition points (the upstream and downstream one on one side) are closer than $0.02\ \frac{x}{c}$ or the values 'merge' to 1 transition point at which convergence occurs (due to the first forcing case or naturally). In the case of the two points

being close, the downstream one is forced forward $\frac{1}{4}$ of the distance between them every time untill the two points match at a free or forced transition point. This way the accuracy is never more off than 0.5% of the chord and convergence is good, even in separated flows.

A.2.4 No convergence improvement

This option is to disable all the convergence improving options.

Appendix B

Airfoil Grids

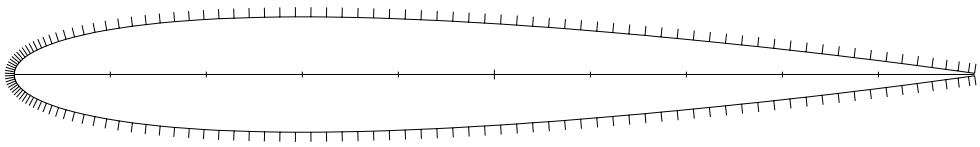

Figure B.1: NACA0012 with 160 panels

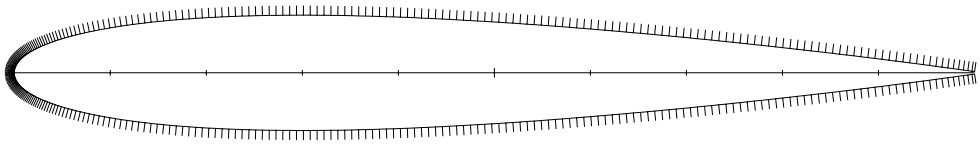

Figure B.2: NACA0012 with 360 panels

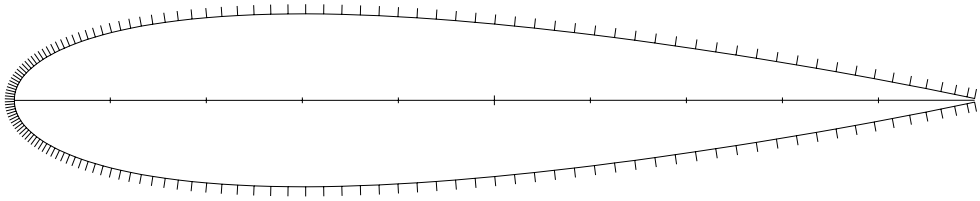

Figure B.3: NACA0018 with 160 panels

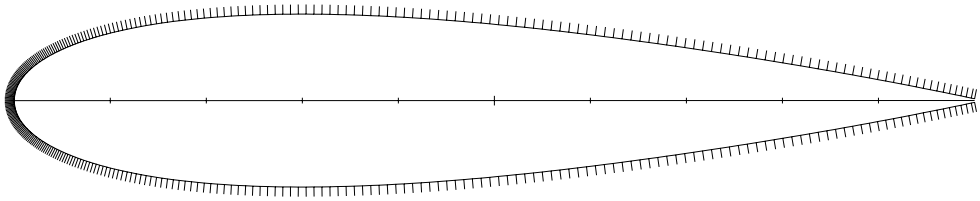

Figure B.4: NACA0018 with 360 panels

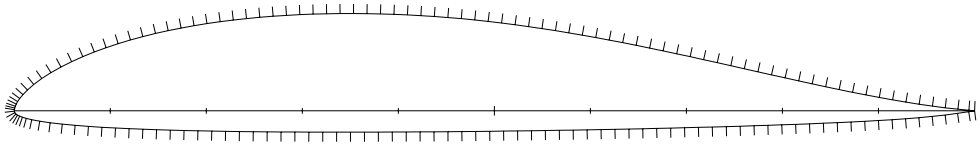

Figure B.5: Flat plate airfoil with 160 panels

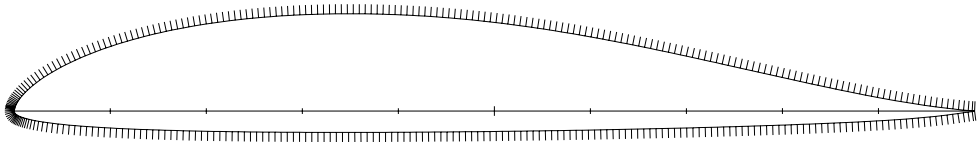

Figure B.6: Flat plate airfoil with 360 panels

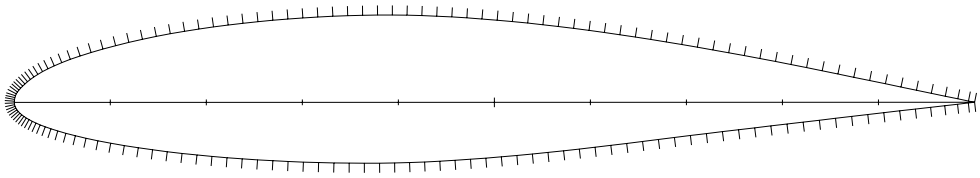

Figure B.7: NACA 64_2-A-215 with 160 panels

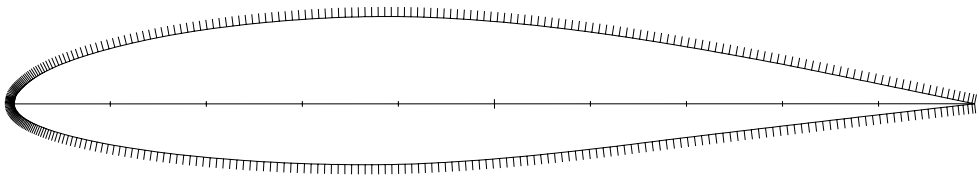

Figure B.8: NACA 64_2-A-215 with 360 panels

Appendix C

Validation figures

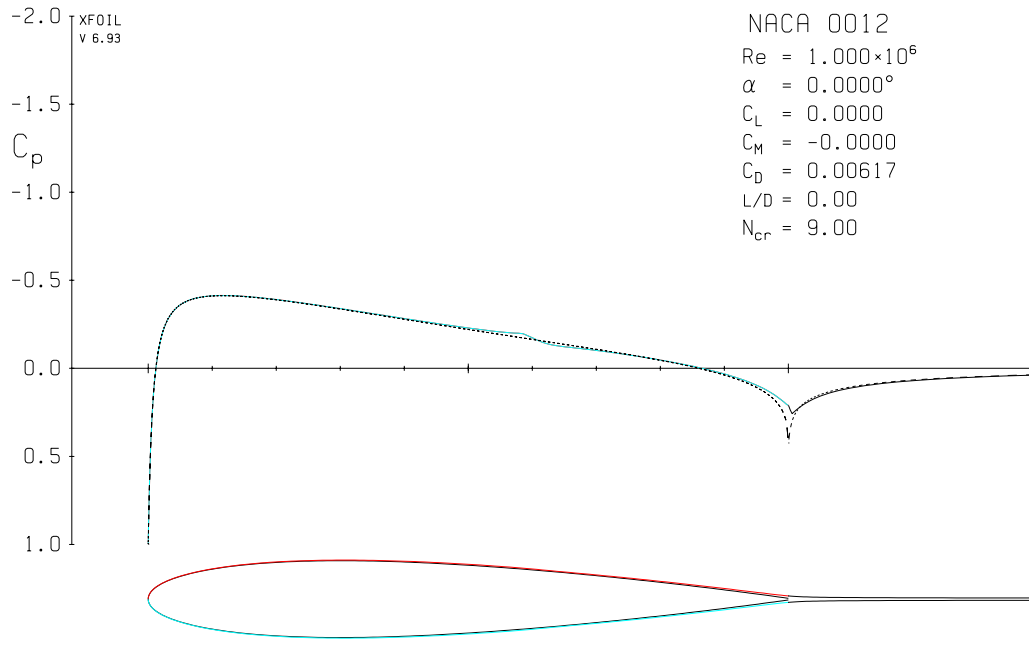

Figure C.1: C_p NACA0012 for $\alpha = 0°$

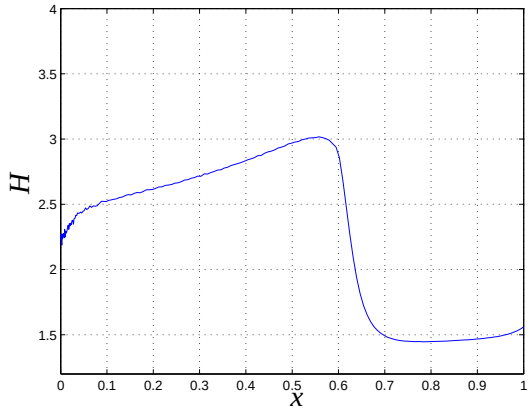

Figure C.2: H for NACA0012 $\alpha = 0°$,$Re_c = 1 \cdot 10^6$, no suction, lower surf.

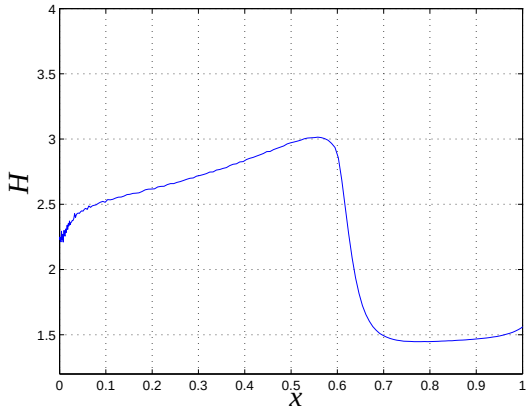

Figure C.3: H for NACA0012 $\alpha = 0°$,$Re_c = 1 \cdot 10^6$, no suction upper surf.

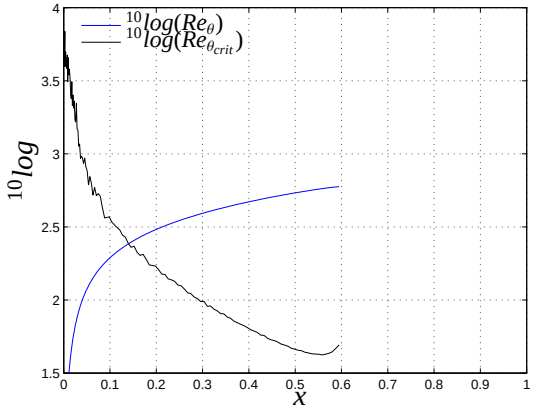

Figure C.4: Re_θ and $Re_{\theta_{crit}}$ for NACA0012 $\alpha = 0°$,$Re_c = 1 \cdot 10^6$, no suction, lower surf.

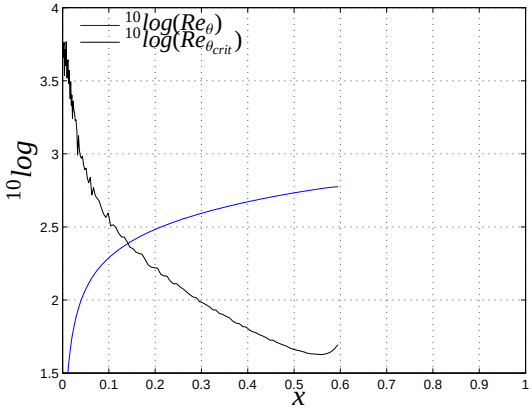

Figure C.5: Re_θ and $Re_{\theta_{crit}}$ for NACA0012 $\alpha = 0°$,$Re_c = 1 \cdot 10^6$, no suction, upper surf.

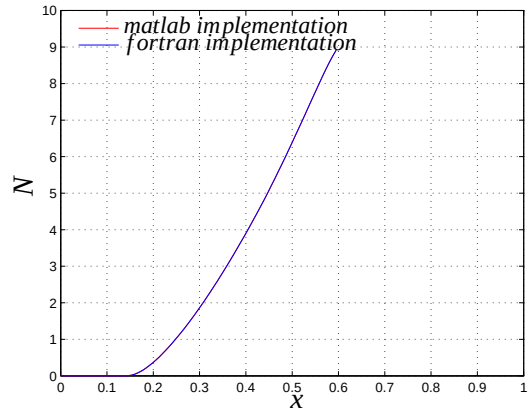

Figure C.6: N for NACA0012 at $\alpha = 0°$,$Re_c = 1 \cdot 10^6$, no suction, lower surf.

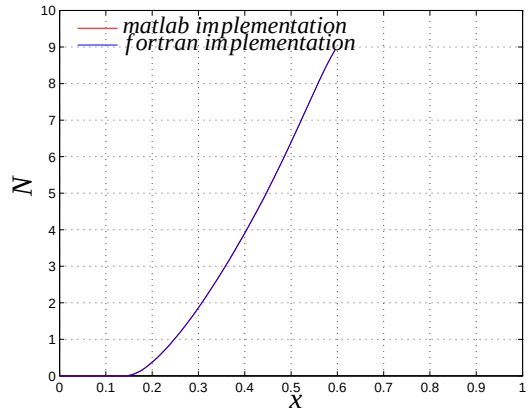

Figure C.7: N for NACA0012 at $\alpha = 0°$,$Re_c = 1 \cdot 10^6$, no suction, upper surf.

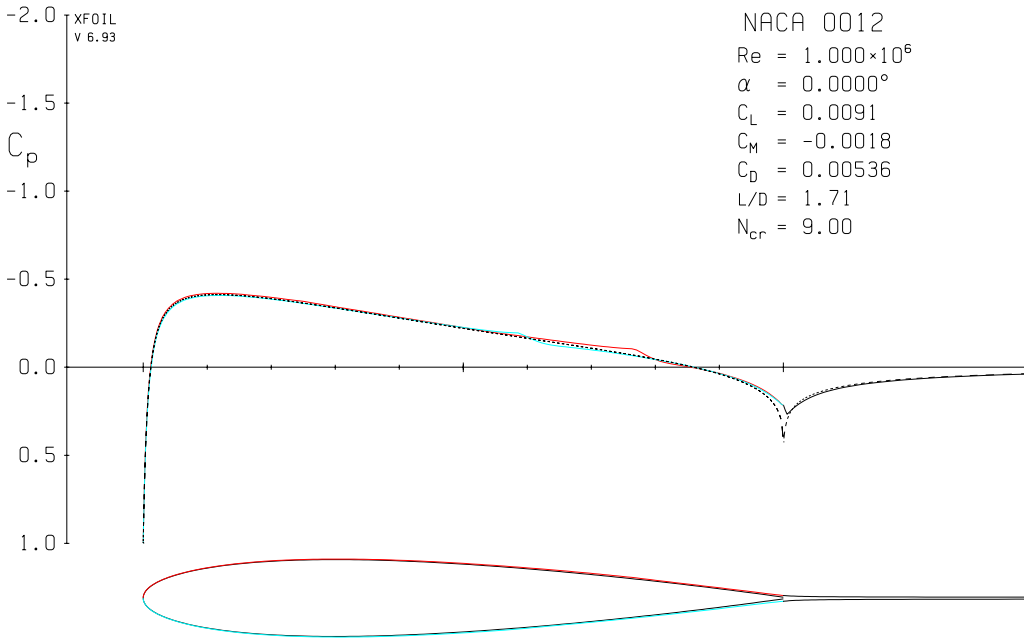

Figure C.8: C_p for NACA0012 at $\alpha = 0°$,$Re_c = 1 \cdot 10^6$, base suction

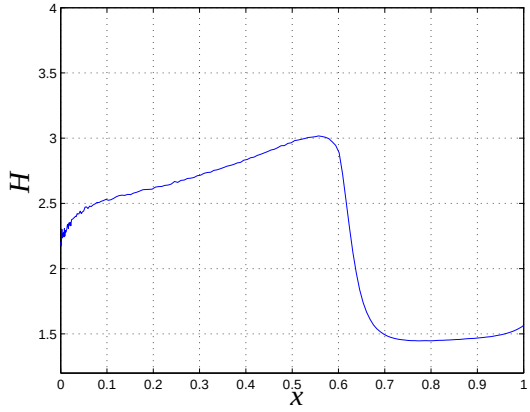

Figure C.9: H for NACA0012 at $\alpha = 0°$,$Re_c = 1 \cdot 10^6$, base suction, lower surf.

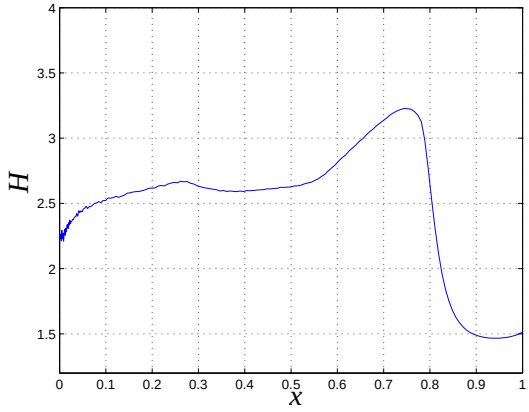

Figure C.10: H for NACA0012 at $\alpha = 0°$,$Re_c = 1 \cdot 10^6$, base suction, upper surf.

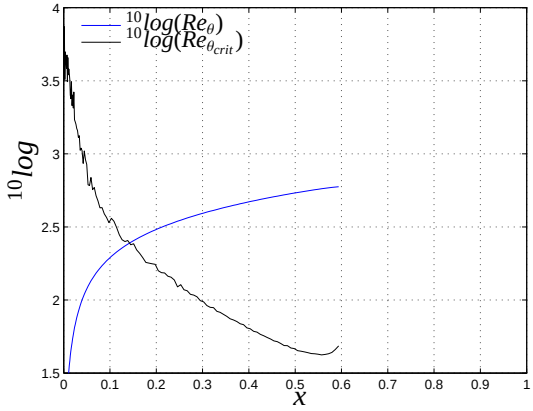

Figure C.11: Re_θ and $Re_{\theta_{crit}}$ for NACA0012 at $\alpha = 0°$,$Re_c = 1 \cdot 10^6$, base suction, lower surf.

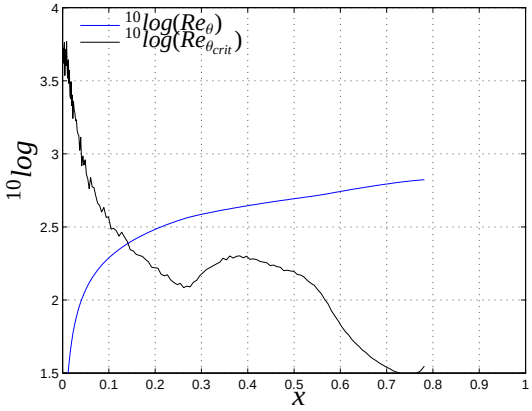

Figure C.12: Re_θ and $Re_{\theta_{crit}}$ for NACA0012 at $\alpha = 0°$,$Re_c = 1 \cdot 10^6$, base suction, upper surf.

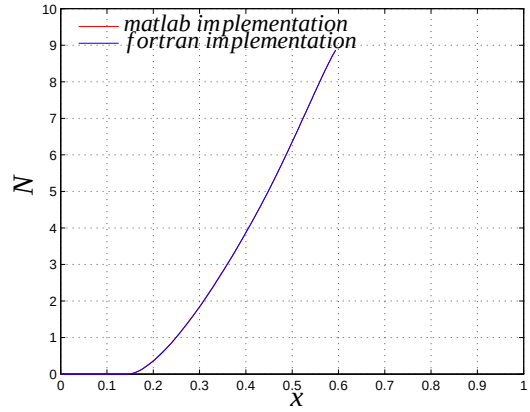

Figure C.13: N for NACA0012 at $\alpha = 0°$,$Re_c = 1 \cdot 10^6$, base suction, lower surf.

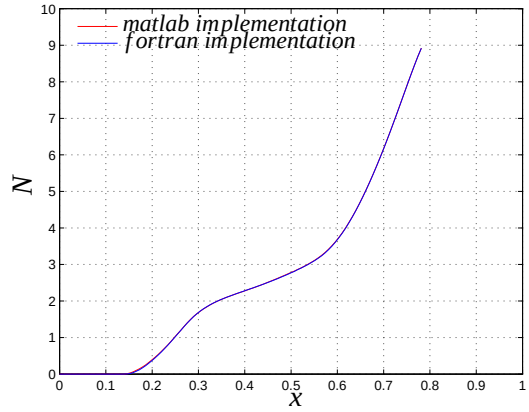

Figure C.14: N for NACA0012 at $\alpha = 0°$,$Re_c = 1 \cdot 10^6$, base suction, upper surf.

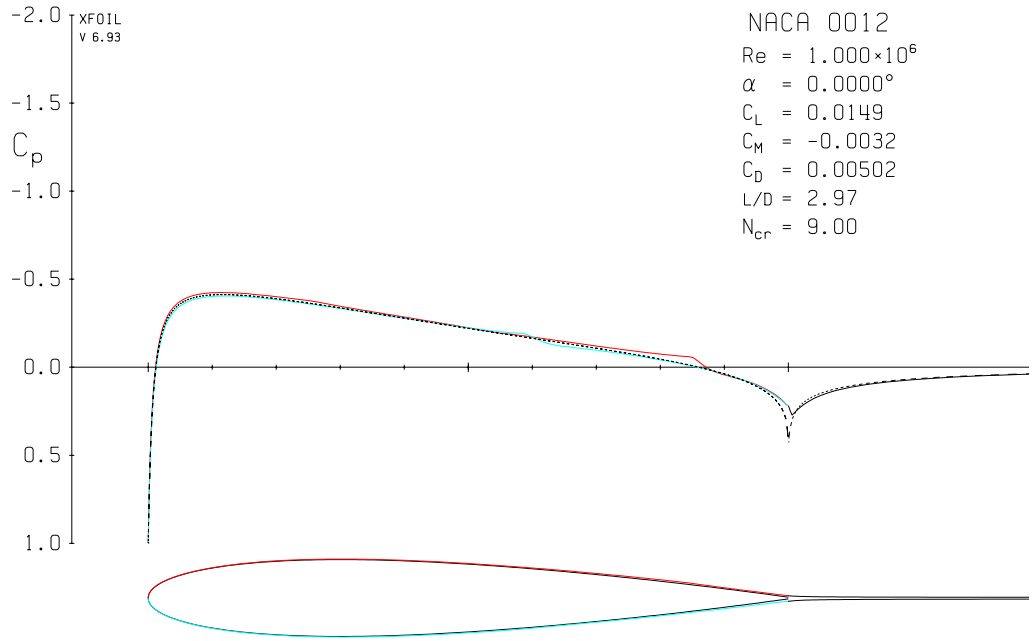

Figure C.15: C_p for NACA0012 at $\alpha = 0°$,$Re_c = 1 \cdot 10^6$, 2·base suction

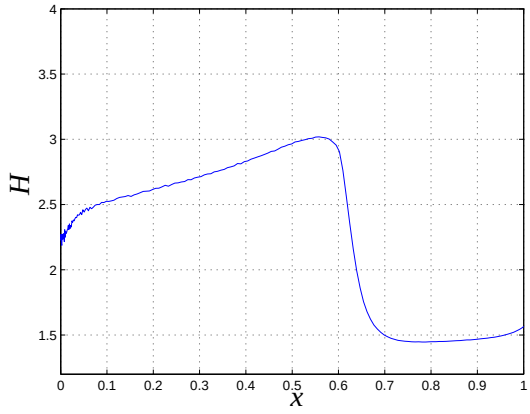

Figure C.16: H for NACA0012 at $\alpha = 0°$,$Re_c = 1 \cdot 10^6$, 2·base suction, lower surf.

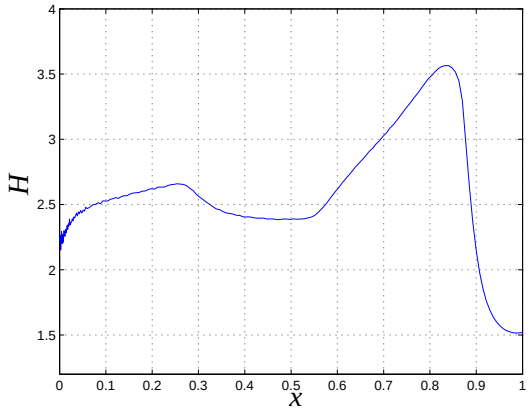

Figure C.17: H for NACA0012 at $\alpha = 0°$,$Re_c = 1 \cdot 10^6$, 2·base suction, upper surf.

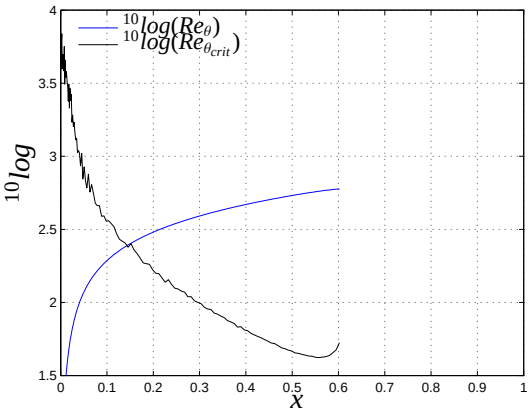

Figure C.18: Re_θ, $Re_{\theta_{crit}}$ for NACA0012 at $\alpha = 0°$,$Re_c = 1 \cdot 10^6$, 2·base suction, lower surf.

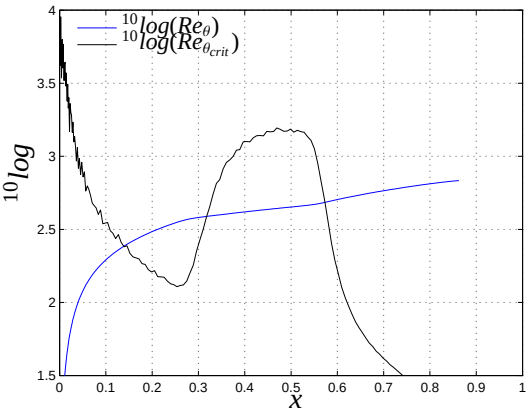

Figure C.19: Re_θ, $Re_{\theta_{crit}}$ ffor NACA0012 at $\alpha = 0°$,$Re_c = 1 \cdot 10^6$, 2·base suction, upper surf.

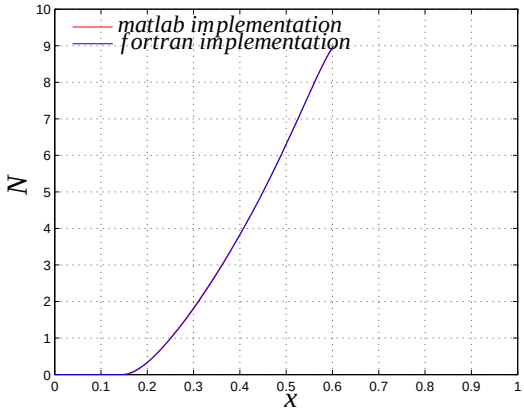

Figure C.20: N for NACA0012 at $\alpha = 0°$,$Re_c = 1 \cdot 10^6$, 2·base suction, lower surf.

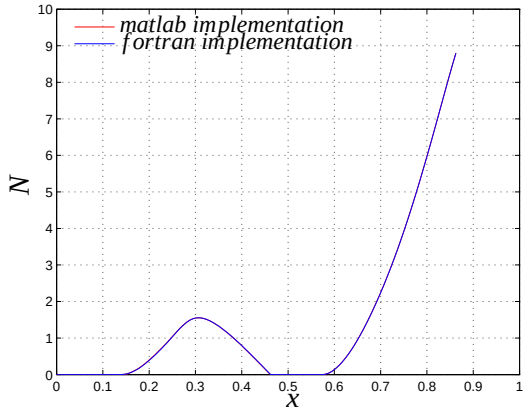

Figure C.21: N for NACA0012 at $\alpha = 0°$,$Re_c = 1 \cdot 10^6$, 2·base suction, upper surf.

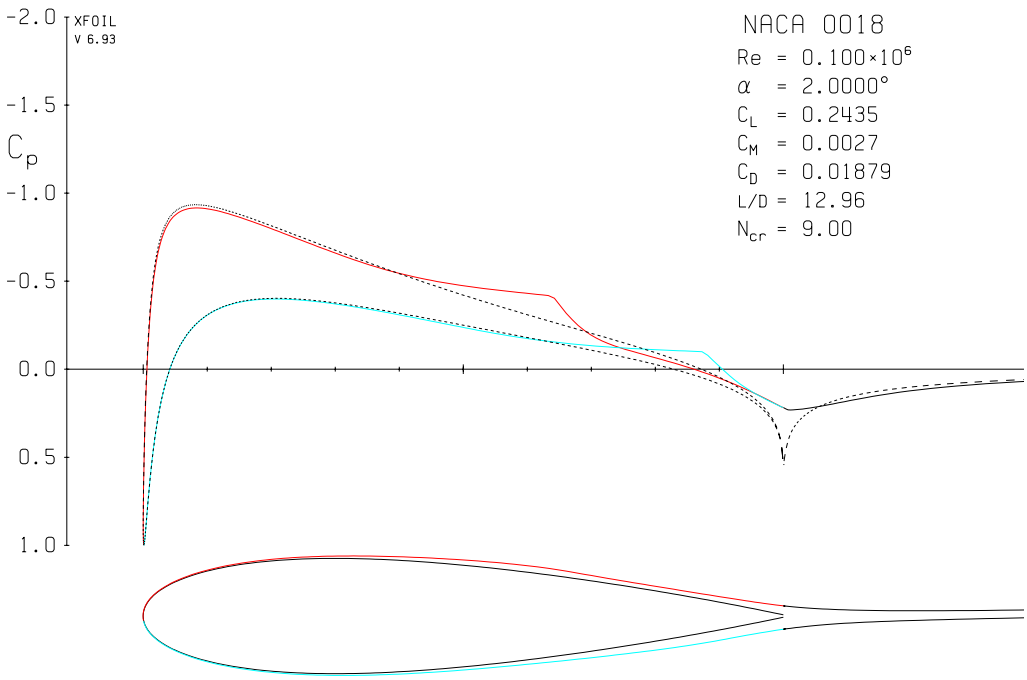

Figure C.22: C_p for NACA0018 at $\alpha = 2°$,$Re_c = 1 \cdot 10^5$

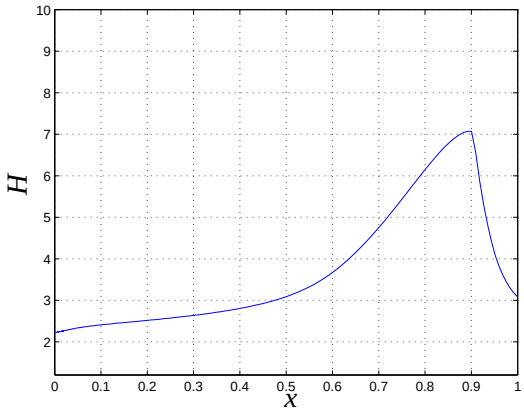

Figure C.23: H for NACA0018 at $\alpha = 2°$,$Re_c = 1 \cdot 10^5$, lower surf.

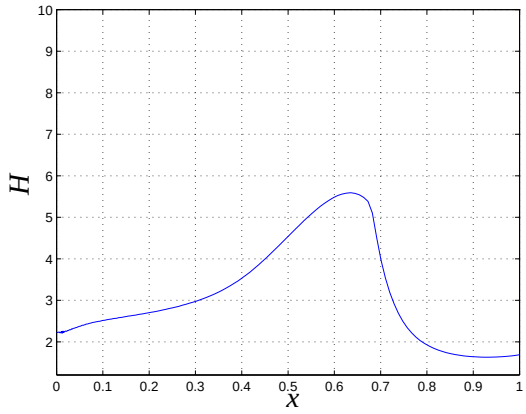

Figure C.24: H for NACA0018 at $\alpha = 2°$,$Re_c = 1 \cdot 10^5$, upper surf.

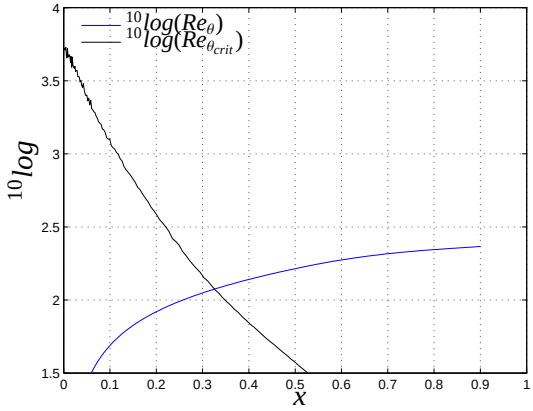

Figure C.25: Re_θ and $Re_{\theta_{crit}}$ for NACA0018 at $\alpha = 2°$,$Re_c = 1 \cdot 10^5$, lower surf.

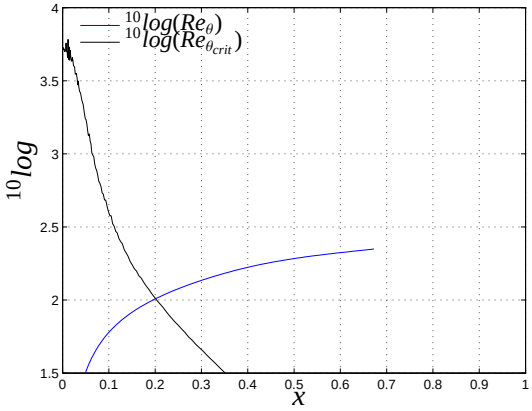

Figure C.26: Re_θ and $Re_{\theta_{crit}}$ for NACA0018 at $\alpha = 2°$,$Re_c = 1 \cdot 10^5$, upper surf.

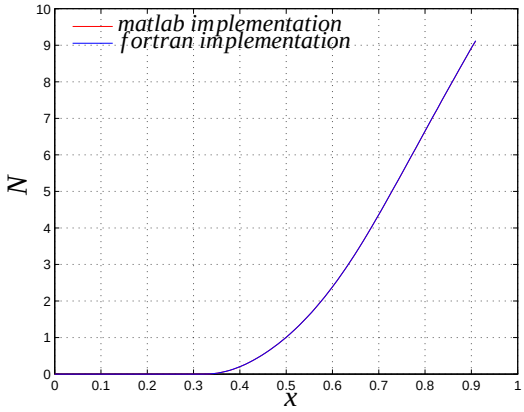

Figure C.27: N for NACA0018 at $\alpha = 2°$,$Re_c = 1 \cdot 10^5$, lower surf.

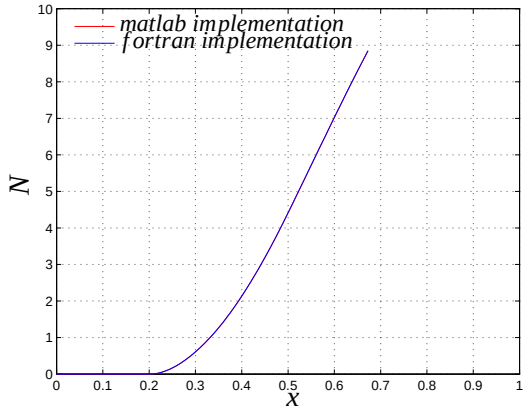

Figure C.28: N for NACA0018 at $\alpha = 2°$,$Re_c = 1 \cdot 10^5$, upper surf.

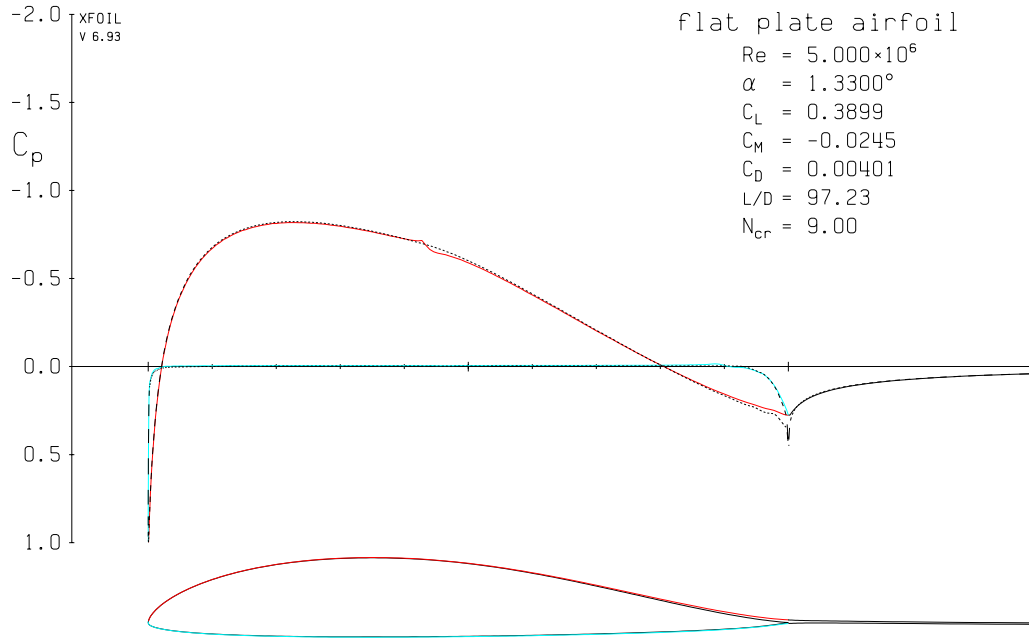

Figure C.29: C_p for flat plate airfoil at $\alpha = 1.33°$,$Re_c = 5 \cdot 10^6$

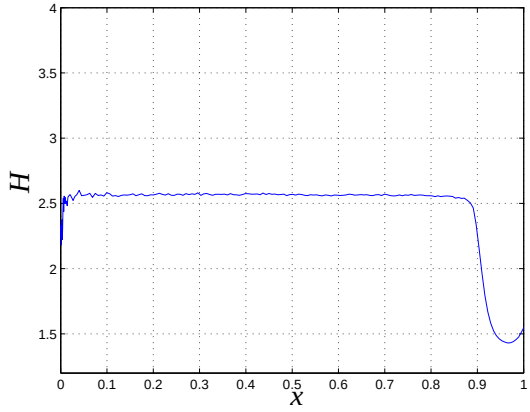

Figure C.30: H for flat plate airfoil at $\alpha = 1.33°$,$Re_c = 5 \cdot 10^6$, lower surf.

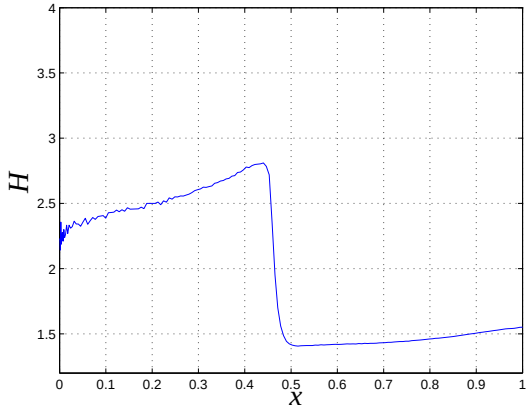

Figure C.31: H for flat plate airfoil at $\alpha = 1.33°$,$Re_c = 5 \cdot 10^6$, upper surf.

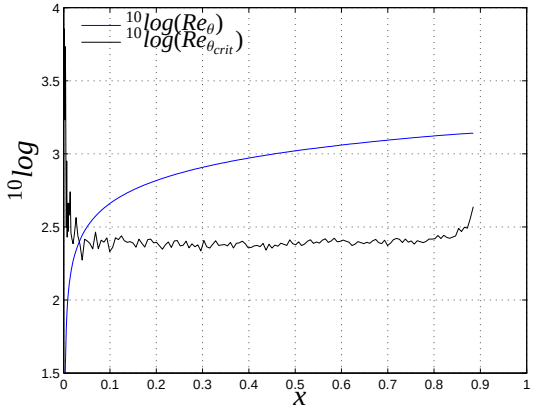

Figure C.32: Re_θ and $Re_{\theta_{crit}}$ for flat plate airfoil at $\alpha = 1.33°$,$Re_c = 5 \cdot 10^6$, lower surf.

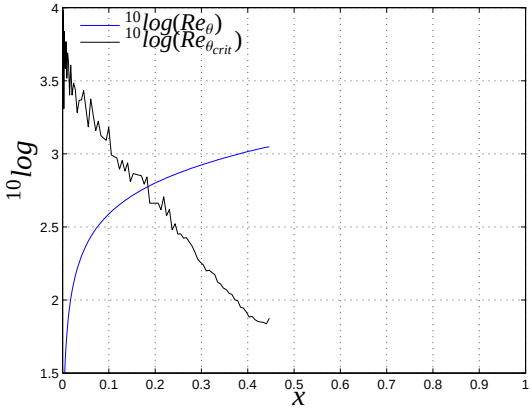

Figure C.33: Re_θ and $Re_{\theta_{crit}}$ for flat plate airfoil at $\alpha = 1.33°$,$Re_c = 5 \cdot 10^6$, upper surf.

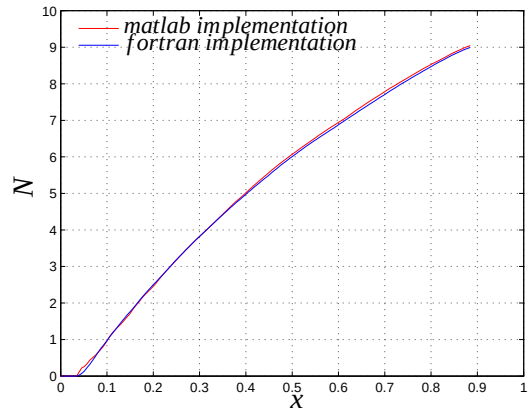

Figure C.34: N for flat plate airfoil at $\alpha = 1.33°$,$Re_c = 5 \cdot 10^6$, lower surf.

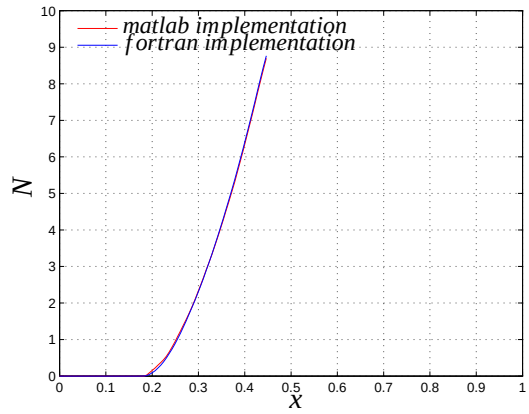

Figure C.35: N for flat plate airfoil at $\alpha = 1.33°$,$Re_c = 5 \cdot 10^6$, upper surf.

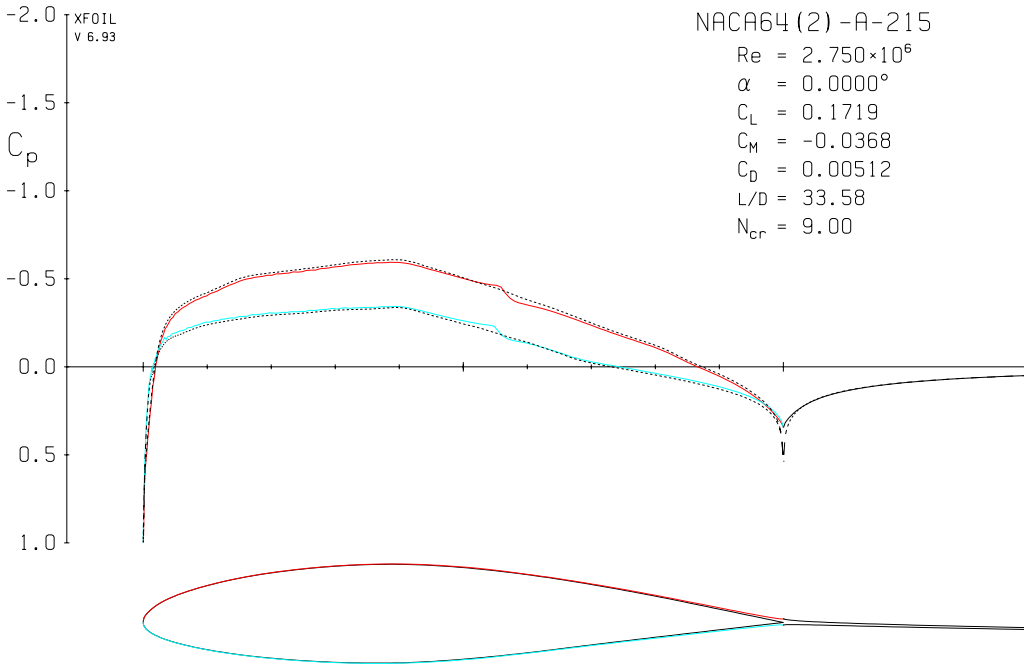

Figure C.36: C_p for NACA64$_2$-A-215 at $\alpha = 0°$,$Re_c = 2.75 \cdot 10^6$

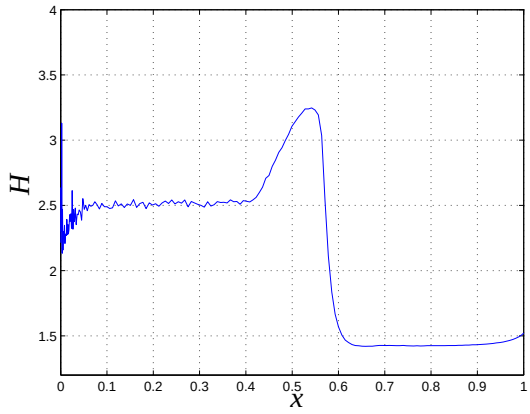

Figure C.37: H for NACA64$_2$-A-215 at $\alpha = 0°$,$Re_c = 2.75 \cdot 10^6$, lower surf.

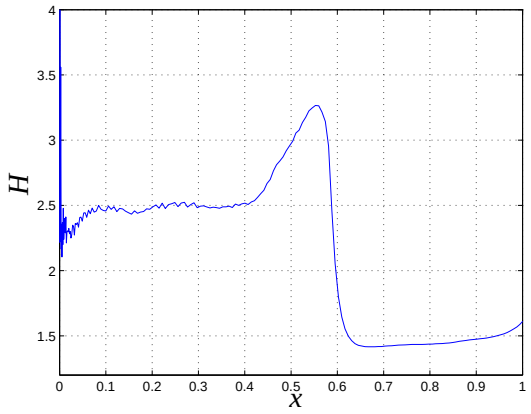

Figure C.38: H for NACA64$_2$-A-215 at $\alpha = 0°$,$Re_c = 2.75 \cdot 10^6$, upper surf.

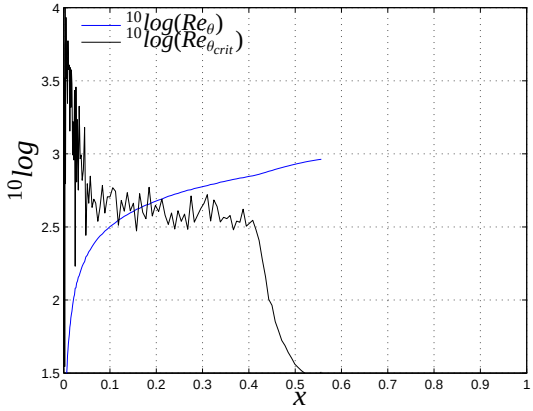

Figure C.39: Re_θ and $Re_{\theta_{crit}}$ for NACA64$_2$-A-215 at $\alpha = 0°$,$Re_c = 2.75 \cdot 10^6$, lower surf.

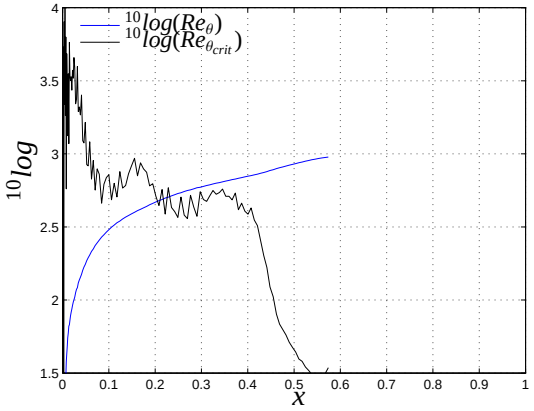

Figure C.40: Re_θ and $Re_{\theta_{crit}}$ for NACA64$_2$-A-215 at $\alpha = 0°$,$Re_c = 2.75 \cdot 10^6$, upper surf.

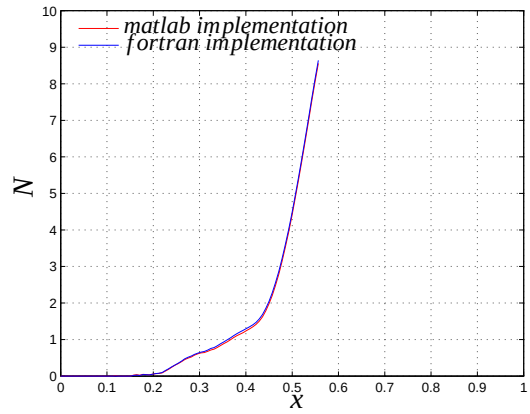

Figure C.41: N for NACA64$_2$-A-215 at $\alpha = 0°$,$Re_c = 2.75 \cdot 10^6$, lower surf.

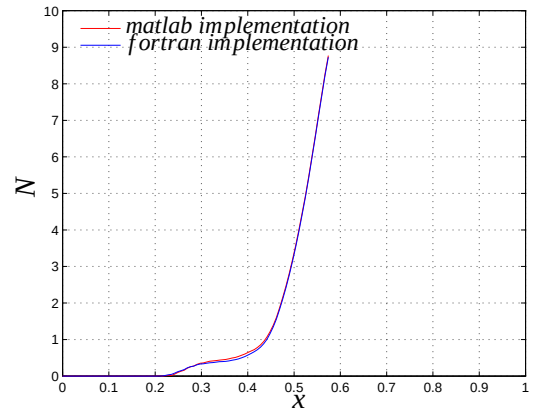

Figure C.42: N for NACA64$_2$-A-215 at $\alpha = 0°$,$Re_c = 2.75 \cdot 10^6$, upper surf.

Bibliography

[1] Broers, R.S.W.: *Extending XFOIL and xSoaring for suction-type boundary layer control calculations*,Delft University of Technology, (2004)

[2] Anderson, J.D. jr.: *Fundamentals of Aerodynamics*, McGraw-Hill, (1991)

[3] Anderson, J.D. jr.: *Computational Fluid Dynamics*, McGraw-Hill, (1995)

[4] Arnal, D.: *Diagrammes de stabilité des profils de couche limite auto-semblables, en ecoulement bidimensionnel incompressible, sans et avec courant de retour*, ONERA Rapport Technique OA Nr 34/5018, (1986)

[5] Blasius, H.: *Grenzschichten in Flu̇ssigkeiten mit kleiner Reibung*, Z. Angew. Math. Phys. vol. 56, (1908)

[6] Schlichting, H.: *Grenzschichtteorie*, G. Braun, third edition, (1958)

[7] De Boor, C.: *A practical guide to splines*, Springer Verlag, (1978)

[8] Dini, P.: *A simplified e^N method for separated boundary layers*, AIAA-91-3285, (1991)

[9] Drela, M. and Giles, M.B.: *Viscous-inviscid analysis of transonic and low reynolds number airfoils*, AIAA 86-1786-CP, (1986)

[10] Drela, M. and Giles, M.B.: *Two-dimensional transonic aerodynamic design method*, AIAA Journal, 25(10) Oct. (1987)

[11] Drela, M. and Giles, M.B.: *Ises: A two-dimensional viscous aerodynamic design and analysis code*, AIAA 87-0424, (1987)

[12] Drela, M.: *XFOIL: An Analysis and Design System for Low Reynolds Number Airfoils*, Conference on Low Reynolds Number Airfoil Aerodynamics, University of Notre Dame, (1989)

[13] Drela, M.: *Improvements in Low Reynolds Number Airfoil Flow Predictions with ISES and XFOIL*, CFD Lab., Dept. of Aeronautics and Astronautics, MIT, (1990)

[14] Ferreira, C.: *Implementation of Boundary Layer Suction in X-Foil and Applicationof Suction Powered by Solar Cells at High Performance Sailplanes.*, Delft University of Technology, (2002)

[15] Gaster, M.: *A Note on the Relation between Temporally-Increasing an Spatially-Increasing Disturbances in Hydrodynamic Stability*, J. Fluid. Mech. vol 14., (1962)

[16] Görtler, H.: *A new series for the calculation of steady laminar boundary layer flows*, J. Math. Mech. 6, (1957)

[17] Guerriero, V.: *Design of a Sailplane Wing with Solar Powered Suction*, Delft University of Technology, (2002)

[18] Hartree, D. R.: *On an equation occuring in Falkner and Skan's approximate treatment of the equations of the boundary layer*, Proc. Camb. phil. Soc. vol. 19, (1937)

[19] Henkes, R.A.W.M., Van Ingen, J.L.: *Transitional Boundary Layers in Aeronautics*, Roy. Neth. Acad. of Arts and Sciences, (1995)

[20] Herbert, Th.: *Parabolized Stability Equations*, Ann. Rev. Fluid Mech. vol. 29, (1997)

[21] T.H. Hughes, Reid, W.H.: *On the stability of the asymptotic suction boundary-layer profile*, J. Fluid Mech., (1965)

[22] Jelsma, E.: *Aanpassing en uitbreiding van xSoaring en xSoaring-flap*, Delft University of Technology, (1997)

[23] Kümmerer, H.: *Numerische Undersuchungen zur Stabilität ebener laminarer Grenzschichtströmungen*, Dissertation Technische Hochschule Stuttgart, (1973)

[24] Liepmann, H.W.: *Investigations on Laminar Boundary Layer Stability and Transition on Curved Boundaries*, NACA Wartime Report W107 (ACR3H30) (1943), See also NACA Technical Memo 1196 (1947) and NACA Report 890 (1947)

[25] Lin, C.C.:*The theory of hydrodynamic stability*, Cambridge University Press, (1955)

[26] Navier, C. L. M. H.: *Mémoire sur les lois du mouvement des fluides*, Mem. Acad. R. Sci. Paris, vol. 6, (1823)

[27] Orr, W.M.F.: *The Stability or Instability of Steady Motions of a Perfect Fluid and of a Viscous Liquid*, Proc. Roy. Irish Aced. Sect. A. (1907)

[28] Prandtl, L.: *Über Flüssigkeitsbewegung bei sehr kleiner Reibung*, Proc. Third Internat.Math. Cong. Heidelberg, (1904), Translation published under NACATechnical Memo. 452

[29] Pretsch, J.: *Die Stabilität einer ebenen Laminarströmung bei Druckgefälle und Druckanstieg*, Jb. dtsch. Luftfahrtforsch. 1, (1941)

[30] Pretsch, J.: *Die Anfachung instabiler Störungen in einer laminaren Reibungsschicht*, Jb. dtsch. Luftfahrtforsch., (1942)

[31] Pretsch, J.: *Die laminare Grenzschicht bei starkem Absaugen und Ausblasen.*, Untersuch. Mitt. dtsch. Luftfahrtf. No. 3091, (1944)

[32] Pretsch, J.: *Grenzen der Grenzschichtsbeeinflussung*, Z. angw. Math. Mech. 24 (1944)

[33] Pretsch, J.: *Berechnung der Stabilitätsgrenze von Grenzschichtprofilen und der Anfachung von Störungen.*, (1945)

[34] Reynolds, O.: *On the Experimental Investigation of the Circumstances Which Determine Whether the Motion of Water Shall be Direct or Sinuous, and the Law of Resistance in Parallel Channels,* Philos. Trans. Roy. Soc. London. Ser. A, (1883)

[35] Rosenhead, L.: *Laminar Boundary Layers*, Oxford University Press, (1961)

[36] Schlichting, H.: *Zur Entstehung der Turbulenz bei der Plattenstromung*, Nachtr. Ges. Wiss. Göttingen. Math.-Phys. Kl. II. (1933)

[37] Schlichting, H.: *Grenzschichtteorie,* third edition, G. Braun Verlag, Karslruhe, (1958)

[38] Schubauer, G.B. and Skramstad, H.: *Laminar Boundary Layer Oscillations and Transition on a Flat Plate*, J. Res. Nat. Bur. Standards, vol. 38, (1947)

[39] Smith, A.M.O. and Gamberoni, N.: *Transition, Pressure Gradient and Stability Theory*, Douglas Aircraft Report ES-26388, (1956)

[40] Sommerfeld, A.: *Ein Betrag zur hydrodynamischen Erklärung der turbulenten Flüssigkeitsbewegungen*, Proc. Fourth Internat. Cong. Math. Rome, (1908)

[41] Squire, H.B.: *On the stability of Three-Dimensional Distribution of Viscous Fluid Between Parallel Walls*, Proc. Roy. Soc. ser. A. vol. 142 (1933)

[42] Steffens, K.: *Investigation on the pressure loss over the suction skin and the maximum suction-threshold*, Delft University of Technology, (2005)

[43] Stewartson, K.:*Further solutions of the Falkner-Skan equation*, Proc. Camb. phil. Soc. vol. 50, (1954)

[44] Stokes, G. G.: *On the Theories of Internal Friction of Fluids in Motion*, Trans. Cambridge Phil. Soc., vol 8., (1845)

[45] Taghavi, H., Wazzen, A.R.: *Spatial stability of some Falkner-Skan profiles with reversed flow*, Physics of Fluids, vol 17, no 12, (1974)

[46] Taylor, G.I.: *Statistical theory of turbulence. V. Effect of turbulence on boundary layer.* Proc. Roy. Soc. London, Ser. A. vol. 156, no 888. (1936)

[47] Terry, E.L.N.: *Extension of xSoaring*, Delft University of Technology, (2002)

[48] Terry, E.L.N.: *Extension of the aerodynamic design program MSES for the simulation of boundary layersuction*, Delft University of Technology, (2004)

[49] Tollmien, W.: *Über die Entstehung der Turbulenz*, Nachr. Ges. Wiss. Göttingen Math.-Phys. Kl. II, (1929)

[50] Van Ingen, J.L.: *A suggested semi-empirical method for the calculation of the boundary layer transition region*, VTH-74, Delft University of Technology, (1956)

[51] Van Ingen, J.L.: *Theoretical and Experimental Investigations of Incompressible Laminar Boundary Layers with and without Suction*Delft University of Technology, (1965)

[52] Van Ingen, J.L.: *An Introduction to Boundary Layer Flows for Aeronautical Engineering Students*. Report LR-656, Also published under :*Grenslaagstromingen A* Dictaat LR-19a, Delft University of Technology, (1991)

[53] Van Ingen, J.L., This article will be on Van Ingens 50 year involvement with the e^N-method, and will include a new database method. A draft version was consulted by the present author as no definitive version was available. *title not known yet*, (2006)

[54] Wazzan, A.R., Okamura, T.T., Smith, A.M.O.: *Spatial and temporal stability charts for the Falkner-Skan boundary layer profiles*, DAC 67086, McDonnel Douglas Corp. (1968)

[55] Whitfield, D.L.: *Integral Solution of Compressible Turbulent Boundary Layers Using Improved Velocity Profiles*, Arnold Air Force Station, AEDC-TR-78-42, (1978)

[56] White, F.M.: *Viscous Fluid Flow*, McGraw-Hill, (1991)

Internet references

[57] http://www.gnu.org/copyleft/gpl.html

[58] http://www.mathworks.com/products/matlab/

[59] http://raphael.mit.edu/xfoil/